Doctoral Dissertation
Doctoral Program in Chemical Engineering (35th Cycle)

Development and advanced characterization of Cu-based catalysts for the electro and photo-electrocatalytic CO_2 reduction

Maddalena Zoli

******

Supervisors:
Prof. Supervisor Nunzio Russo
Prof. Co-Supervisor Simelys Hernández
Prof. Co-Supervisor Angelica Monica Chiodoni

Doctoral Esamination Committee:

Dr. Fatwa F. Abdi, Reviewer
Dr. Miriam Diaz de los Bernardos Sánchez

Politecnico di Torino

Declaration

I hereby declare that the contents and organization of this dissertation constitute my own original work and does not compromise in any way the rights of third parties, including those relating to the security of personal data.

Maddalena Zoli

Turin, June 2023

* This dissertation is presented in partial fulfillment of the requirements for **Ph.D. degree** in the Graduate School of Politecnico di Torino (ScuDo).

Acknowledgements

The work presented in this Ph.D. thesis has been developed within the Ph.D programme in Chemical Engineering, XXXV° cycle - Politecnico di Torino.

An acknowledge is due to the Italian regional project SATURNO – Bioeconomy (Piedmont Region 2019–2022, https://saturnobioeconomia.it/).

This work has received funding from the European Union's Horizon 2020 Research and Innovation Action programme under the Project SunCoChem (Grant Agreement No 862192).

The generous resources provided by Helmholtz-Zentrum Berlin für Materialien und Energie, specifically addressed to Solar Fuels Institute in the person of Dr. Fatwa F. Abdi, during the Ph.D. student research abroad period are also acknowledged.

Abstract

Carbon dioxide (CO_2) emissions into the atmosphere are both natural, as a product of terrestrial bio-geochemical cycles, and anthropogenic, mainly as the result of the combustion of fossil fuels. While the former ones are balanced by natural processes, CO_2 originating from anthropogenic activities remains into the atmosphere causing the entrapment of the radiation from the Earth and the consequent warming of the planet. The CO_2 concentration in the atmosphere is increasing every year from the 50s to now, until current levels exceeding 415 ppm. A renewable and green approach to CO_2 recovery is increasingly necessary to minimize the worrying impact of these emission to the environment. A growing research effort in the field of electrochemical and photo-electrochemical reduction of CO_2 is one of the current response from scientists and engineers. The implemented strategy is to introduce CO_2 as a raw material into a circular economy loop to synthesize high-added-value products, fulfilling at the same time the enduring growth in global fuel demand. The challenges to cope with in the catalytic conversion of CO_2 into fuels are huge. Thermodinamically, CO_2 is a fully oxidized, inert, and extremely stable molecule, thus its conversion to other C-based molecules results difficult without a substantial energy input. In this work the focus is on electrochemical and photo-electrochemical processes. The electricity can drive the water splitting reaction to generate protons (H^+) necessary for CO_2 hydrogenation. The process of electrocatalytic CO_2 reduction implies the usage of an external electric field as the main energy source to induce redox reaction on electrodes. The photons-assisted process, instead, refers to the generation of electrons by photo-excitation of a semiconductor photoelectrode by a light source, and the consequent migration of these photo-excited electrons to the electrode surface under the guidance of external applied potential to accomplish the catalytic reduction of CO_2. The possibility to conduct the reaction under mild conditions, and the simple control on the reaction via the tuneable external bias, are common to both techniques, making them more suitable than other methods since can directly exploit renewable energy sources such as sunlight. Currently, the selective production of desired chemicals is a challenging topic, because the redox potentials are similar for different reaction pathways. The CO_2 reduction reaction (CO_2RR) path is mainly focused on the production of molecules like CO (the syngas production is also taken into consideration) and formic acid, for which the transfer of $2e^-$ is required. The ability to obtain, among others, the aforementioned products with a high activity belongs to the Cu and Cu-based compounds reactivity, which are the ones investigated during this work.

Various catalysts for electro and photo-electrocatalytic CO_2RR have been designed, synthetised, characterised and tested in different setup in order to choose the best for carrying out the reaction and maintaining its stability over time. Working within Italian regional (SATURNO-Bioeconomy) and European (SunCoChem) Projects has meant that the effort was always direct to the more scalable synthetic route for the catalysts (*i.e.,* standardization of synthesis). In Chapter 3, a bimetallic PdCu aerogel was studied in electrocatalytic systems. Particular care in the choice of the more suitable synthesis path was taken, then the obtained catalyst showed a good syngas production ($CO:H_2 \sim 1$) with Faradaic Efficiency (FE) values of 38 and 42% respectively, and a FE = 3.5% for Ethanol. Then the scale-up of the cell for the CO_2RR was accomplished and by applying higher potentials the selectivity of C-compounds raised up to 40%. In Chapter 4, the investigation on Sn as a protective agent on Cu_2O started, focusing on making an efficient and stable photo-electroctalyst. The first synthesis attempt was performed via co-precipitation, having in mind its ease and scalability. The role of light in the formation of C-compounds and H_2 hindering was observed at different current density values applied. Then, the study on Cu_2O and SnO_2 proceeded and Chapter 5 deals with another synthethic approach, namely the creation of core-shell nanoparticles. Photo-electrocatalytic characterization confirmed the enhancement in performance with respect to the previous catalyst design, with improved photo-activity and better results in terms of Formic acid FEs. Given the raising interest in long-term stability, the Cu:Sn ratio was varied in order to accomplish a thicker protective layer onto the Cu_2O core. A deep characterization of the new set of catalysts was carried out at the Helmholtz-Zentrum Berlin facilities. In particular, carriers mobility was studied via Time Resolving Microwave Conductivity (TRMC) analysis, and the lifetime of electrons at the surface photoelectrode-electrolyte was evaluated thanks to a novel approach for CO_2RR such as IMVS (Intensity-Modulated Photovoltage Spectroscopy). Insights of these advanced characterization methods are discussed in Chapter 6, and finally resulted in a tendency of mainly producing C_1 compounds with the increasing amount of Sn. The rationalization of this effect led to the application of a very low Cu:Sn ratio in the standardization of the synthesis of core-shell Cu_2O-SnO_2 catalyst. After assessing the stability of the CO and H_2 production after a 5-hour lasting chronoamperometric test, the metallic catalyst was functionalised with supramolecular Ru/Re complexes developed by partners of the Suncochem Project. The modified catalyst was tested in the same conditions and the comparison of the performance (in terms of photo-activity and FE) are shown in Chapter 7.

Contents

1. Introduction....1
1.1 Climate change and the greenhouse effect....1
1.2 Fossil fuels demand....4
1.3 CO_2 Conversion....6
1.4 Electrochemical methods....9
1.4.1 Electrocatalytic (EC) CO_2RR....12
1.4.2 Photo-electrocatalytic (PEC) CO_2RR....15
1.5 Regional and European Projects to face the CO_2 presence in atmosphere....16
1.6 Aim of the work....17
2. Materials and Methods....20
2.1 Materials used as CO_2 reduction catalysts....20
2.1.1 Copper....21
2.1.2 Palladium....23
2.1.3 Tin....24
2.2 Characterization Techniques....25
2.2.1 Physical Properties....25
2.2.2 Chemical Properties....27
2.2.3 PEC Properties....34
2.3 Setup of CO_2R catalytic tests....40
2.3.1 RDE setup for EC CO_2RR....40
2.3.2 PEC setup for CO_2RR....41

2.4 Products analysis 43
3. Bimetallic Pd-Cu based Aerogels for electrocatalytic CO_2 reduction. 44
3.1 Chemistry of aerogels and xerogels 45
3.1.1 Synthesis via sol-gel process 46
3.1.2 Drying methods 48
3.2 Noble metal-based aerogels and xerogels 50
3.2.1 Synthesis strategies 52
3.2.2 Gelation mechanism investigation 53
3.2.3 Characterization studies 56
3.2.4 Applications 57
3.3 State of the art on Pd and Cu based aerogels 57
3.4 Pd-Cu xerogel synthesis methods 60
3.4.1 Reagents 60
3.4.2 Synthesis procedure 60
3.4.3 Comparison between different drying methods 62
3.5 Catalyst characterization 63
3.5.1 Comparison of drying methods: XRD and N_2 physisorption 63
3.5.2 XPS analysis 65
3.5.3 Advanced characterization: TEM ex-situ and in-situ 65
3.6 Electrocatalytic CO_2 reduction test 67
3.6.1 Comparison between PdCu_HV and PdCu_SC 68
3.6.2 Pd_3Cu_1 CO_2 reduction test 71
3.7 Scaling up: design of a GDE cell set-up 74
3.7.1 Electrocatalytic CO_2 reduction test in the new GDE set-up 75
3.8 Conclusions 78
4. Co-precipitation synthesis of Cu_2O-SnO_2 catalyst for the photoelectrochemical CO_2 conversion 79
4.1 Ultrasound-assisted co-precipitation synthesis 80

4.2 Cu_2O-SnO_2 design of a novel catalyst 82
4.3 Cu_2O-SnO_2 synthesis method 85
4.3.1 Reagents 85
4.3.2 Synthesis procedure 85
4.3.3 Synthesis reproducibility 86
4.3.4 Electrodes preparation 87
4.4 Catalyst characterization 88
4.4.1 Catalyst morphology 88
4.4.2 Copper oxidation state 91
4.4.2 Before PEC test electrodes characterization 94
4.5 PEC CO_2 reduction test 95
4.5.1 Setup and protocol 95
4.5.2 PEC results and discussion 96
4.5.3 After PEC test electrodes characterization 102
4.5.4 EIS analysis 104
4.6 Conclusions 105
5. Core-shell Cu_2O-SnO_2 photo-electrocatalyst for the CO_2RR: comparison with co-precipitation and new features 107
5.1 Core-shell nanoparticles (CSNs) 109
5.2 Core-shell synthesis method 110
5.2.1 Reagents 111
5.2.2 Synthesis method 111
5.3 Catalyst characterization 112
5.3.1 Cu_2O Nanocubes characterization 112
5.3.2 Cu_2O-SnO_2 characterization 115
5.4 PEC CO_2 reduction test 118
5.4.1 Core-shell Cu_2O-SnO_2 PEC results 119
5.4.2 Comparison: Cu_2O-SnO_2 co-precipitation vs. core-shell 121

5.4.3 Screening of 5 core-shell samples....123
5.4.4 EIS analysis....127
5.5 Conclusions....135
6. Advanced characterization of core-shell samples via TRMC and IMVS....137
6.1 Carriers mobility....138
6.2 Time-Resolved Microwave Conductivity....140
6.2.1 Fundamentals....141
6.2.2 Experimental apparatus....143
6.2.3 Experimental procedures....146
6.2.4 Results and discussion....147
6.3 Light Intensity Modulated Impedance Spectroscopy....155
6.3.1 Intensity modulated photocurrent spectroscopy....156
6.3.2. Intensity modulated photovoltage spectroscopy....157
6.3.3 Experimental apparatus and procedures....158
6.3.4 Results and discussion....159
6.4 Conclusions....161
7. Functionalization of Cu_2O-SnO_2 catalyst with Ru-Re based hybrid supramolecular complexes....163
7.1 Ru-Re supramolecular complexes....164
7.2 Cu_2O-SnO_2 Synthesis standardization....166
7.2.1 Reagents and instruments....167
7.2.2 Synthesis method....168
7.3 Characterization and reproducibility....170
7.3.1 Reproducibility and dependence with flow rate....171
7.3.2 Core-shell catalysts characterization....173
7.4 Preliminary PEC results....177
7.5 Catalyst functionalization....181
7.6 Stability test of modified catalysts....184

7.7 Conclusions 188
8. Summary and Conclusions 191
9. References 195
10. Appendix 226
A1. Bare Carbon Paper PEC CO_2RR tests 226
A2. Co-precipitation obtained Cu_2O PEC CO_2 reduction test 228
A3. Cu_2O Nanocubes, preliminary synthesis study 231
A4. IMVS plots 233
A5. Characterization of Cu_2O-SnO_2 core-shell catalysts obtained with the standardized synthesis 235

List of Figures

Figure 1.1 – Schematic representation of the global mean energy budget of the Earth. Published in Contribution of Working Group I to the Sixth Assessment Report of the Intergovernmental Panel on Climate Change [1], adapted by [2]. Copyright © 2014, The Authors under the terms of the Creative Commons CC BY license [3]. 2

Figure 1.2 – Global Warming Potential (GWP) weighted global greenhouse gas emissions in 1970-2004. CO_2, CH_4, N_2O, HFCs, PFCs, and SF_6 from all sources are included. The two CO_2 emissions categories reflect CO_2 emissions from energy production (the upper part of the picture on the right) and land use changes (the bottom part of the picture on the left). Source: Climate Change 2007: The Mitigation of Climate Change Contribution of Working Group III to the IPCC Fourth Assessment Report, page 4 [5]. 3

Figure 1.3 – Share of primary energy from fossil fuels (OurWorldInData.org/energy), adapted from [11]. Copyright 2022 Our World in Data under Creative Commons By License [3]. 5

Figure 1.4 – Schematic of several possible reaction pathways of electrochemical CO2 reduction reaction toward methane, ethylene, and ethanol, respectively. Reprinted with permission from [54]. Copyright © 2021, American Chemical Society. 14

Figure 2.1 – Schematic representation of: (a) Bragg's Equation (Equation 8), and (b) the goniometer system. 28

Figure 2.2 - (a) Processes that result from X-ray bombardment of a surface include emission of a photoelectron on the left and emission of an Auger electron on the right; (b) Energy level diagram illustrates the basic XPS equation (Equation 10) schematically. 31

Figure 2.3 – Schematic picture of a traditional three-electrode cell for ECSA analysis in an RDE (Rotating Disk Electrode) system. 37

Figure 2.4 – Equivalent circuit used to model the PEC system. 40

Figure 2.5 – Schematic picture of *H-type* cell in RDE setup. 41

Figure 2.6 – Schematic picture of the PEC *H-type* cell. 42

Figure 2.7 – Schematic setup for the development of photo-electrocatalytic tests. 43

Figure 3.1 – Schematic representation of typical sol-gel synthesis procedure. 47

Figure 3.2 – (a) Scheme of the reaction for the formation of the PdCu aerogel; (b) Hydrogel sample (black) synthesized in laboratory deposited on the bottom of the tube; (c) Image of the set-up made for working in parallel on multiple tubes onto the heating plate for the reaction. 61

Figure 3.3 – FESEM image and related EDX analysis of the atomic percentages of the elements of interest and contaminants for the catalyst sample (a) before and (b) after the clean-up procedure. 62

Figure 3.4 – XRD pattern of (a) HV sample and (b) SC sample. 64

Figure 3.5 – FESEM images of catalyst deposited on: (a) chip, and on silicon substrate (b) before and (c) after thickness optimization.....66

Figure 3.6 – TEM characterization of PdCu catalyst: (a,b): BFTEM, (c) High Resolution TEM, (d) SAED, (e) EDX spectrum, (f-h) FESEM image and EDX maps for Pd and Cu.....67

Figure 3.7 – RDE test of CO_2 reduction for the two catalysts: PdCu_HV blue line and PdCu_SC red line; (a) Cyclic Voltammetry performed in CO_2 ; (b) Linear Sweep Voltammetry performed in CO_2-environment; (c) Chronoamperometry test performed at –1.6V vs. Ag/AgCl.....69

Figure 3.8 – Comparison of Faradaic Efficiencies for gaseous and liquid products detected after a two-hours chronoamperometry at an applied potential value of –0.9 V vs. RHE for both the catalysts (PdCu_SC in the left part of the graph and PdCu_HV in the right one). 71

Figure 3.9 – RDE test of CO_2 reduction for the final Pd_3Cu_1 catalyst; (a) Cyclic Voltammetry performed in CO_2; (b) Linear Sweep Voltammetry performed in CO_2-environment; (c) Chronoamperometry test performed at –0.9V vs. RHE.72

Figure 3.10 – Comparison of Faradaic Efficiencies for gaseous and liquid products detected after a two-hours chronoamperometry at an applied potential value of –0.9 V vs. RHE for the two the catalysts (Pd_3Cu_1 in the left part of the graph and PdCu_HV in the right one). 73

Figure 3.11 – Scaled-up 100 cm^2 GDE electrochemical cell of Saturno project: (a) Exploded view of the cell assembly; (b) side view of the constructed cell. 75

Figure 3.12 – Results of electrocatalytic CO_2 reduction test carried out in in a continuous flow electrochemical system: (a) Linear sweep voltammetry under CO_2 flow; (b) Chronopotentiometric curves; (c) Photo of the electrode after the test in the inset and (d) selectivity of CO_2 reduction products at different applied current densities (–10, –50, and –133 mA cm^{-2}) for the Pd_3Cu_1 catalyst-tested electrode. 77

Figure 4.1 – (a) Energy band bending of a p-type semiconductor in contact with an electrolyte, and (b) staggered band heterojunction in a typical p-n junction. 84

Figure 4.2 – (a) XRD pattern and (b) Tauc's Plots of the repeated samples (S1-5). 87

Figure 4.3 – XRD pattern of the Cu_2O-SnO_2 powder catalyst. 88

Figure 4.4 – (a) Bright-Field TEM low magnification image and (b) representative Bright-field TEM image; (c) the corresponding electron diffraction pattern and (d,e) High-Resolution TEM images with corresponding Fast Fourier Transform (FFT). 89

Figure 4.5 – FESEM images of the catalyst obtained at different magnification scale (c,d,e). 90

Figure 4.6 – Tauc's Plot for determining the material Band Gap. 92

Figure 4.7 – XPS results of catalyst powder analysis: (a) high resolution $Cu2p_{1/2}$ and $Cu2p_{3/2}$ and abundance of copper oxidation states obtained from $Cu2p_{3/2}$ deconvolution procedure (not reported); (b) CuLMM spectra and Modified Auger Parameter value; (c) Cu_2O-SnO_2 Valence Band spectrum, linearly fitted in order to extrapolate the valence band maximum (VBM) position (red line), and (d) Sn3d doublet. 93

Figure 4.8 – PEC test of CO_2 reduction; (a) Cyclic Voltammetry performed in N_2 and CO_2 ; (b) Linear Sweep Voltammetry performed in CO_2-environment with chopped light; (c) Linear Sweep Voltammetry curves carried out in dark (blue line) and in light (green line) pointing out the different final *J* value due to light influence. (d) Chronoamperometry test performed at –250mV, pointing out the stability of the photocurrent density (red dots). 96

Figure 4.9 – Gaseous product evolution and summary of faradaic efficiencies for main products; values have been obtained in aqueous based electrolyte (0.1M $KHCO_3$) after 30 minutes long chronopotentiometries at different applied values of current density *J*, in particular: (a) –0.25 mA cm^{-2} , (b) –0.50 mA cm^{-2} , (c) –1 mA cm^{-2} , (d) –1.5 mA cm^{-2} , (e) –3 mA cm^{-2} , (f) –10 mA cm^{-2}. 98

Figure 4.10 – FEs of gas and liquid products detected after a 2-hours Chronopotentiometry in 0.1M $KHCO_3$ aqueous electrolyte at (d) –1 mA cm^{-2} and (e) –3 mA cm^{-2}. For each current density value, the products are reported both for the test without and under illumination. 100

Figure 4.11 – (a) XRD pattern of Carbon Paper (electrodes support) (red line) and the electrode with the Cu_2O-SnO_2 catalyst after the test under light conditions (green line). In the inset the peaks attributed to the catalyst are reported and labelled; (b) XPS High-Resolution spectra of two electrodes one after a test in dark (blue line) the other after a test in light (yellow line), focusing on the copper peaks. 103

Figure 4.12 – EIS analysis results: (a) values of rate-defining resistance R3, (b) characteristic time T3 obtained via fitting operations. 105

Figure 5.1 – Characterization of Cu_2O nanocubes; in particular: (a) XRD pattern, and (b) (c) SEM images at two different magnification. 113

Figure 5.2 – Tauc Plot for the Cu_2O nanocubes band gap energy determination. 114

Figure 5.3 – Calibration lines of: (a) Cu and (b) Sn for the ICP-OES detection of metal amounts into catalytic samples. 115

Figure 5.4 – XRD of core-shell samples; from the top: CS3, CS5, CS11, CS65, CS200. The graph placed lower down the figure reports the relative intensities of the Cu_2O and SnO_2 peaks (green and blue lines, respectively).....117

Figure 5.5 – Morphology (a) image obtained by FESEM and Tauc method calculations (b) for E_g determination, for the sample CS65. 118

Figure 5.6 – Photo-electrocatalytic tests carried out in N_2-saturated environment (blue lines) and CO_2-saturated one (red lines). In particular (a) CV of a bare Cu_2O catalyst, (b) CV of the core-shell Cu_2O-SnO_2 one at the same conditions. (c) LSV of the bare Cu_2O catalyst and (d) LSV of the core-shell Cu_2O-SnO_2 at the same conditions. 120

Figure 5.7 – Comparison of co-precipitation and core-shell Cu_2O-SnO_2 results; in particular: (a) LSV curves and (b) CA curves of the CP (green) and CS (orange) samples, together with Cu_2O samples obtained via co-precipitation (light green) and core-shell synthesis (red). 122

Figure 5.8 – Results of PEC tests on the 5 different core-shell samples; in particular: (a) LSV curves, (b) chronoamperometry test, both in light/dark chopped conditions, (c) chronopotentiometry curves lasting 2-hours, obtained at an applied current density of –3 mA cm^{-2}, (d) Faradaic efficiency results of the 6 samples after the chronopotentiometry test, related to the Sn atomic percentage within each sample (purple rhombus). 125

Figure 5.9 – Nyquist plots related to one of the core-shell samples sample measured at different potentials vs. Ag/AgCl in CO_2-saturated electrolyte in tests enlightened by the solar radiation (the points are experimental data). 128

Figure 5.10 – Nyquist plot of three different catalyst, (a) Cu_2O, (b) CS5, and (c) CS3, obtained during the "*pre*" and "*post*" campaign of measurement carried out at –1.5 V vs. Ag/AgCl in CO_2-saturated environment both in dark and light conditions. 130

Figure 5.11 – Equivalent resistance R3 trends of (a) all the samples, (b) co-precipitation sample, (c) Cu_2O, (d) CS200, (e) CS65, (f) CS11, (g) CS5, and (h) CS3; open symbols represent the "*pre*" measurements while solid ones, that are labelled "*post*", represent the one executed after the chronoamperometry. R3 values were calculated through a fitting procedure using the equivalent electrical circuit shown in Figure 2.4 134

Figure 6.1 – Scheme of the experimental setup and illustration of the measurement principle of cavity-based TRMC. 145

Figure 6.2 – UV-Visible spectra of core-shell and bare Cu_2O samples air-brushed onto a quartz substrate. 147

Figure 6.3 – Plots of maximum of carriers mobility vs. time for each analyzed sample at 450 nm; in particular: (a) Cu_2O, (b) CS200, (c) CS65, (d) CS11, (e) CS5, and (f) CS3. Both the axes are given in a logarithmic scale. 148

Figure 6.4 – Plots of maximum of carriers mobility vs. time for each analyzed sample at 500 nm; in particular: (a) Cu_2O, (b) CS200, (c) CS65, (d) CS11, (e) CS5, and (f) CS3. Both the axes are given a logarithmic scale. 149

Figure 6.5 – Plots of maximum of carriers mobility vs. time for each analyzed sample at 560 nm; in particular: (a) Cu_2O, (b) CS200, (c) CS65, (d) CS11, (e) CS5, and (f) CS3. Both the axes report a logarithmic scale. 150

Figure 6.6 – Maximum TRMC signal $(\phi\Sigma\mu)_{max}$ vs. incident laser pulse intensity for core-shell samples and bare Cu_2O one in all the different excitation wavelengths. 151

Figure 6.7 – Trends of maximum mobility values $(\phi\Sigma\mu)_{max}$ detected at λ = 450 nm (pink bars), 500 nm (orange bars), and 560 nm (purple bars) for all the core-shell and the bare Cu_2O samples. The laser light intensity was chosen to be 10^{12} photons per pulse. The Sn amount within each sample is showed in the right-Y axis. 152

Figure 6.8 – β and γ values for each samples obtained as the slopes of the linear fit applied to the decay curves obtained at each wavelength; in particular: (a) CS200, (b) CS65, (c) CS11, (d) CS5, (e) CS3, (f) the average values of β and γ for each sample related to the Sn amount (%) within each sample, and (g) the correlation between the average β with the C-compounds selectivity as showed in Chapter 5. 155

Figure 6.9 – Schematic diagram of the setup for intensity modulated photovoltage/photocurrent spectroscopy (IMVS/IMPS). 159

Figure 6.10 – The effects of different Sn amount into the 5 core-shell samples on f_{IMVS} values; results of both the experiment types were showed in the plot: blue points are referred to the test with no bubbling while the red ones are proper of the CO_2 bubbling experiment. 160

Figure 7.1 – Schematic representation of the instruments and reagents involved in the (a) first part of the synthesis and (b) its second part. 168

Figure 7.2 – Colour changes: (a) $CuCl_2$ solution, (b) NaOH addition, (c) L-ascorbic acid addition – green, (d,e,f,g) L-ascorbic acid addition – mustard yellow, (h,i) L-ascorbic acid addition – orange. 169

Figure 7.3 – XRD characterization of the Cu_2O samples; (a) spectra of the Cu_2O samples, (b) (100) peak/(200) peak ratio, and (c) mean crystallite size per flow rate. 172

Figure 7.4 – ECSA values of Cu_2O sample obtained with different L-ascorbic acid flow rates. 173

Figure 7.5 – Characterization of the Cu_2O_100_SnO_2_100, in particular: (a) FESEM images of Cu_2O_100, and (b) of Cu_2O_100_SnO_2_100, performed at the same magnification to observe the differences due to the external shell, (c) XPS survey spectrum and, (d) Sn3d region of the XPS spectrum of Cu_2O_100_SnO_2_100. 176

Figure 7.6 – Band structure for the Cu_2O-SnO_2 core-shell samples. 176

Figure 7.7 – LSV curves of the three different Cu_2O-SnO_2 samples, with a zoomed region of the plot present in the inset. 178

Figure 7.8 – Results of chronopotentiometry test on the three Cu_2O_SnO_2 samples: (a) chronopotentiometry curves registered at $J_{applied}$ = –3 mA cm^{-2}, and gaseous products evolution of (b) Cu_2O_60_SnO_2_60, (c) Cu_2O_100_SnO_2_100, and (d) Cu_2O_60_SnO_2_60, detected by a μGC. 179

Figure 7.9 – Gaseous products evolution during three different chronopotentiometry tests on Cu_2O_100_SnO_2_100, in particular reported at: (a) $J_{applied}$ = –1 mA cm^{-2} for 1 hour, (b) $J_{applied}$ = –5 mA cm^{-2} for 1 hour, and (c) $J_{applied}$ = –3 mA cm^{-2} for 5 hours. 180

Figure 7.10 – Schematic representation of the Ru and Re complexes used in this work. 182

Figure 7.11 – Functionalization of the Cu_2O-SnO_2 nanoparticles with VTES schematic representation. 182

Figure 7.12 – Electropolymerization of the molecular complexes scheme. .183

Figure 7.13 – FESEM images and EDX analysis of: (a) Cu_2O-SnO_2-RuRe1, and (b) Cu_2O-SnO_2-RuRe2. 184

Figure 7.14 – Results of the photo-electrocatalytic tests on the three modified Cu_2O_100_SnO_2_100 samples; (a) LSV curves, (b) 300 minutes chronopotentiometry curves, applying –3 mA cm^{-2} as the current density under simulated sunlight, and the gaseous products behaviour during the test of (c) Ru+Re sample, (d) RuRe1, and (e) RuRe2 ones, and (f) Faradaic efficiency values of the three samples obtained after the tests. 187

Figure A.1 – PEC test of a bare carbon paper based electrode; (a) Cyclic Voltammetry performed in N_2 and CO_2 ; (b) Linear Sweep Voltammetry performed both in N_2 and CO_2-environment with chopped light (2sec); (c) Chronoamperometry test performed at –250mV, chopped light each 1 minute (d).

FEs of gas and liquid products detected after a 2-hours Chronopotentiometry in 0.1 M $KHCO_3$ aqueous electrolyte in two different environment (N_2 on the left and CO_2 on the right part of the graph) at two different current density values (–1 mA cm^{-2} and –3 mA cm^{-2}). All the tests were carried out under illumination....227

Figure A.2 – XRD pattern of the bare Cu_2O catalyst.....228

Figure A.3 – Comparison of bare Cu_2O (red line) and Cu_2O-SnO_2 (green line) PEC CO_2 reduction results; (a) Cyclic Voltammetry performed in CO_2; (b) Linear Sweep Voltammetry performed in CO_2-environment with chopped light (2sec), in the inset there is an enlargement of the photoactivity evidence revealed from the curve; (c) Chronoamperometry test (10 minutes) performed at –250mV, chopped light each 1 minute for bare Cu_2O (red); (d). FEs of gas and liquid products detected after a 2-hours Chronopotentiometry under illumination in 0.1 M $KHCO_3$ aqueous electrolyte in CO_2-environment of bare Cu_2O at two different current density values (–1 mA cm^{-2} and –3 mA cm^{-2}). 229

Figure A.4 – Reported yields percentage for the Cu_2O produced nanoparticles. 232

Figure A.5 – IMVS plots obtained with an applied bias of 1 V and varying the amplitude from 100 to 200 and 300 mV. Experiments carried out without CO_2 bubbling. The samples analyzed were: (a) CS200, (b) CS65, (c) CS11, (d) CS5, and (e) CS3. 233

Figure A.6 – IMVS plots obtained with an applied bias of 1 V and varying the amplitude from 100 to 200 and 300 mV. Experiments carried out with CO_2 bubbling. The samples analyzed were: (a) CS200, (b) CS65, (c) CS11, (d) CS5, and (e) CS3. 234

Figure A.7 – Electrocatalytic surface area analysis of Cu_2O bare samples, in particular: (a) Cyclic voltammetries of Cu_2O core samples and, (b) linear fitting of the current densities mean value obtained for Cu_2O samples.....235

Figure A.8 – XPS analysis of the samples, in detail: (a) Cu_2O survey spectra, to be compared with (b) Cu_2O-SnO_2 survey spectra (both the images reported various samples obtained with different delivery velocities), and (c) HR Cl2p peak with flat background highlighted in the box for the various Cu_2O-SnO_2 samples. 236

List of Tables

Table 1.1 – Standard Equilibrium Potentials vs Reversible Hydrogen Electrode for the Electrochemical Reduction of CO_2, adapted from [41]. 10

Table 3.1 – Critical points of selected solvents* 49

Table 3.2 – Comparison of the results obtained from N_2 physisorption analysis of the two as-prepared samples. 64

Table 3.3 – Technical specifications required for the design of the 100 cm^2 GDE electrochemical cell of the Saturno project. 74

Table 4.1 – Crystallite sizes of the samples, calculated via Scherrer Equation, band gap, molar composition of the two metals of interest (Cu and Sn), and Cu:Sn ratio calculated via ICP analysis together with their standard deviation value. 86

Table 4.2 – Comparison table of elements atomic percentage in EDX and XPS. 91

Table 5.1 – Measured Cu and Sn bulk concentrations in Cu_2-SnO_2 catalysts. In the sample name CS*X*, *X* stands for the molar ratio between Cu and Sn, as reported in the last column. 116

Table 5.2 – Photocurrent gain of the 6 samples analyzed via chronoamperometry test at –200 mV vs. OCP in chopped light mode and CO_2-saturated environment. 126

Table 5.3 – Values of impedance (R) obtained from the plots reported in Figure 5.10 for three different catalysts. 131

Table 7.1 – Volumes and concentrations of the reagents solutions. 168

Table 7.2 – Average of approximated amounts of Ru and Re onto the electrodes surface, analyzed by EDX and correlated by atomic percentages. 184

Table A.1 – Molarity and volumes of the reagents involved for the synthesis. 231

Table A.2 – Atomic percentage of Cu, O, Sn, C and Cl in $Cu_2O_SnO_2$ samples obtained with different delivery velocities. 237

Glossary of terms and abbreviations

μ-GC	micro-Gas Chromatograph
3D	Three-dimensional
AC	Alternating Current
APD	Ambient Pressure Drying
at.%	Atomic Percentage
BE	Binding Energy
BET	Brunauer, Emmett, Teller
BFTEM	Bright Field Transmission Electron Microscopy
BJH	Barrett-Joyner-Halenda
CA	Chronoamperometry
CAGR	Compound Annual Growth Rate
CB	Conduction Band
CBM	Conduction Band Maximum
CCU	Carbon Capture and Utilization
CE	Counter Electrode
CEM	Cation Exchange Membrane
CO_2RR	CO_2 Reduction Reaction
CP	Chronopotentiometry
CPEs/Q	Constant Phase Elements
CSNs	Core-shell Nanoparticles
CV	Cyclic Voltammetry
C_μ	Chemical Capacitance
DC	Direct Current
DFT	Density Functional Theory
DLC	Double Layer Capacitance
DMS	Direct Methanol Synthesis
D_p	Total Pore Diameter
DSSC	Dye-Sensitized Solar Cell
E	Potential
E^0	Standard Potential
EC	Electrocatalytic
ECSA	Electrochemical Surface Area
EDS/EDX	Energy-Dispersive X-ray Spectroscopy
E_g	Band Gap
EIS	Electrochemical Impedance Spectroscopy
eV	electron Volt
fcc	face-centered-cubic
FE	Faradaic Efficiency
FESEM	Field Emission Scanning Electron Microscopy

FFT	Fast Fourier Transform
FRA	Frequency Response Analyzer
FTO	Fluorine Doped Tin Oxide
FWHM	Full Width at Half Maximum
GDE	Gas Diffusion Electrode
GHGs	Global Greenhouse Gases
GWP	Global Warming Potential
HAADF-STEM	High-Angle Annular Dark-Field Scanning Transmission Electron Microscopy
HER	Hydrogen Evolution Reaction
HPLC	High-Performance Liquid Chromatograph
HR	High Resolution
HRTEM	High-Resolution Transmission Electron Microscopy
ICP	Inductively Coupled Plasma
ICP-OES	Inductively-Coupled Plasma Optical Emission Spectrometry
IMPS	Intensity Modulated Photocurrent Spectroscopy
IMVS	Intensity Modulated Photovoltage Spectroscopy
IPCC	Intergovernmental Panel on Climate Change
J	Current Density
KE	Kinetic Energy
k_{inj}	Charge Transfer Constant
k_{rec}	Recombination Rate Constant
LED	Light Emitting Diod
LSV	Linear Sweep Voltammetry
M	Molar
MDR	Methane Dry Reforming
MFC	Mass Flow Controller
ND	Neutral Density
NGFS	Network for Greening the Financial System
NIR	Near-Infrared
NMAs	Noble Metal Aerogels
NMFs	Noble Metal Foams
NPs	Nanoparticles
OAm	oleylamine
OCV	Open Circuit Voltage
OER	Oxygen Evolution Reaction
OPO	Optical Parametric Oscillator
ORR	Oxygen Reduction Reaction
P_c	Critical Pressure
PCET	Proton-Coupled Electron-Transfer
PEC	Photo-electrocatalytic
PEcats	Photo-electrocatalysts

PFCs	Perfluorinated Compounds
ppm	Parts per million
R	Resistor
RDE	Rotating Disk Electrode
RDS	Rate-Determining Step
RE	Reference Electrode
Re_{CAT}	Rhenium CO_2 Reduction Catalyst
RHE	Reversible Hydrogen Electrode
R_{rec}	Recombination Resistance
RuRe1	Supramolecular Ru-Re complex
RuRe2	Binuclear Ru-Re complex
Ru_{VLA}	Ruthenium Visible Light Absorber
RWGS	Reverse Water Gas Shift reaction
SAED	Selected Area Electron Diffraction
S_{BET}/SSA	Specific Surface Area
$scCO_2$	Supercrytical Drying
SEM	Scanning Electron Microscopy
SEs	Secondary Electrons
SR	Sabatier Reaction
T_c	Critical Temperature
TEM	Transmission Electron Microscopy
TPER	Transparent Photo-electrocatalytic Reactor
TRMC	Time-Resolved Microwave Conductivity
UV-Vis	UV-visible spectroscopy
VB	Valence Band
VBM	Valence Band Maximum
VC	Vulcan Carbon
VD	Vacuum Drying
V_p	Total Pore Volume
vs.	versus
VTES	Vinyltriethoxysilane
WE	Working Electrode
wt.%	Weight Percentage
XPS	X-ray Photoelectron Spectroscopy
XRD	X-Ray Diffraction
μ	Carrier Mobility
λ	Wavelength
τ	Characteristic Lifetime

Chapter 1

Introduction

Chapter 1 aims to explore the complex relationship between climate change, fossil fuel demand, and CO_2 conversion. Through electrochemical methods, this research seeks to identify new strategies for mitigating the impacts of greenhouse gas emissions. By examining these topics in depth, this work looks to contribute to a better understanding of the challenges facing our planet and the potential solutions that may help address them.

1.1 Climate change and the greenhouse effect

The Earth's climate has always undergone gradual and cyclic alterations, resulting in alternating warm and cold periods due to a variety of natural factors that have yet to be fully understood. Climate change is a significant alteration in average weather conditions, such as increased warmth, humidity, or dryness, over several decades or more. This longer-term trend distinguishes climate change from natural weather variability. The global concern over climate change is due to the significant impact that such shifts, particularly the sudden ones, have on society, mainly regarding economic activities and human health. These sudden climate changes are often not accompanied by rapid adaptations by society. The causes of climate change are rooted in the mechanics of the Earth's climate system and radiative balance. When energy from the sun is reflected off the Earth and back into space (mostly by clouds and ice) or when the Earth's atmosphere releases energy, the planet cools. In parallel, the planet warms when the Earth absorbs the sun's energy or atmospheric gases prevent heat released by the Earth

from radiating into space. That is the basic mechanism of the so-called "greenhouse effect". In the greenhouse effect, shortwave solar radiation passes through the atmosphere and reaches the Earth's surface, where it gets absorbed. When the Earth re-emits the radiation, it shifts toward long-wavelength infrared radiation, which does not easily pass through the atmosphere. Instead, the atmosphere absorbs this infrared radiation, particularly greenhouse gases such as CO_2, methane, and water vapor. As a result, the atmosphere heats up.

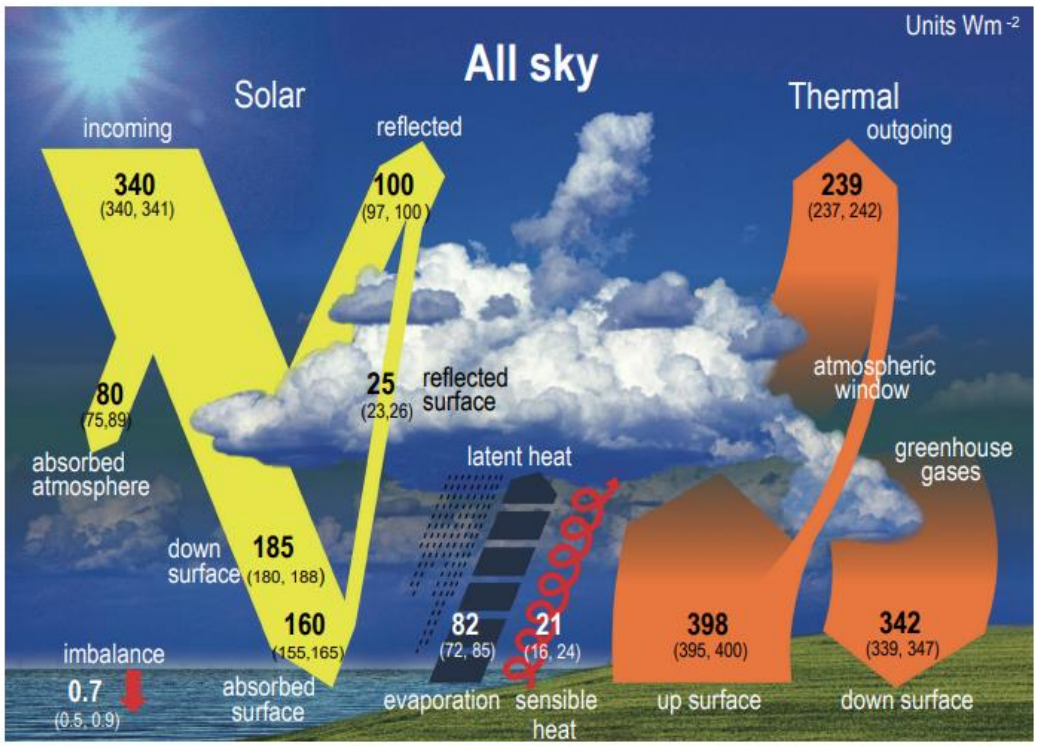


Figure 1.1 – Schematic representation of the global mean energy budget of the Earth. Published in Contribution of Working Group I to the Sixth Assessment Report of the Intergovernmental Panel on Climate Change [1]**, adapted by** [2]**. Copyright © 2014, The Authors under the terms of the Creative Commons CC BY license** [3]**.**

Figure 1.1 summarizes these energy transfers. The top of the diagram represents the top of the atmosphere, the bottom indicates the Earth's surface, and the atmosphere is supposed to be in the middle. The solar radiation components are on the left side of the picture, while the terrestrial ones are on the right side. Numbers indicate best estimates for the magnitudes of the globally averaged energy balance components in W m^{-2}, and their uncertainty ranges are given in parentheses (5–95% confidence range), representing climate conditions at the beginning of the 21st century. The main greenhouse gases currently present in the

Earth's atmosphere are water vapor (H_2O), carbon dioxide (CO_2), methane (CH_4), nitrous oxide (N_2O), and ozone (O_3) [4]. Global greenhouse gas (GHG) emissions have been growing since pre-industrial times, with an increase of 70% between 1970 and 2004, as reported in Figure 1.2 [5]. The abundance of long-lived greenhouse gases could be a primary driver of our changing climate [6,7]. In recent years, there has been a growing scientific interest in how human activities have impacted and intensified climate change over the past centuries. To confirm the hypothesis, in 2007, the Intergovernmental Panel on Climate Change (IPCC) published a report concluding that climate change was "very likely" to be caused by humans [5].

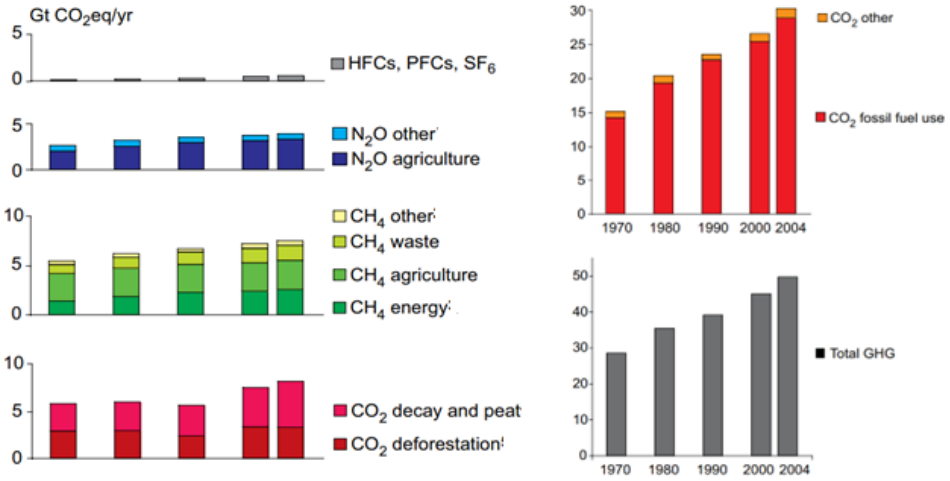


Figure 1.2 – Global Warming Potential (GWP) weighted global greenhouse gas emissions in 1970-2004. CO_2, CH_4, N_2O, HFCs, PFCs, and SF_6 from all sources are included. The two CO_2 emissions categories reflect CO_2 emissions from energy production (the upper part of the picture on the right) and land use changes (the bottom part of the picture on the left). Source: Climate Change 2007: The Mitigation of Climate Change Contribution of Working Group III to the IPCC Fourth Assessment Report, page 4 [5].

The latest IPCC report published in 2022 reiterated that "human-induced climate change is causing dangerous and widespread disruption in nature and is affecting the lives and livelihoods of billions of people, despite efforts to reduce the risks." [8]. This worrying scenario shows why it is extremely important to act right now.

1.2 Fossil fuels demand

How are humans affecting climate change? An answer could be found in the rising fossil fuel demand. Fossil fuels have been a key factor in technological, social, economic, and human progress. These fuels, including coal, oil, and gas, have and continue to hold a significant position in the global energy landscape. Currently, the question "What share of primary energy comes from fossil fuels?" leads to a worrying answer. In 2019, around 84% of global primary energy came from coal, oil, and gas. Figure 1.3 shows that in 2020, fossil fuels accounted for over 80% of all energy used in the United States, and in general, this can be considered true worldwide. The EU economy is highly dependent on fossil fuels, representing nearly three-quarters of its total energy consumption. The principal drawbacks of their use are that they are non-renewable resources and their combustion processes result in huge CO_2 emissions, together with other GHGs, in the atmosphere leading to the terrifying effects described in Section 1.1. In Europe in 2022, the emissions coming from the chemical industries accounted for around 8% of the total world's emissions. The contribution of the United States is more than double (13.4%), while China leads the ranking of CO_2 emissions with a value of 31% [9]. Despite that it is clear that the risk is high, the demand is continuously growing due to the need for chemical feedstocks in manufacturing consumer goods (personal care items, food preservation, fertilizers, and furnishing). Urgent actions are needed to reduce the consumption of fossil fuels and shift to green energy sources, to fight the massive risks to ecosystems and humans. According to the Network for Greening the Financial System (NGFS), this share must be reduced to around 30% to reach net-zero emissions by 2050 [10]. For the EU, the reduction will have to be even greater. That will require wide-ranging structural changes in energy production.

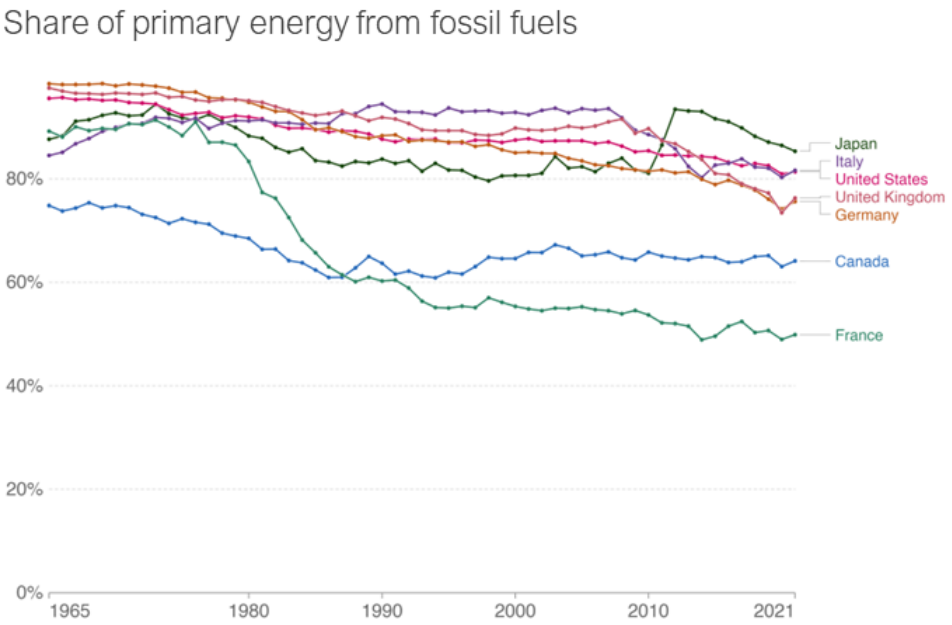


Figure 1.3 – Share of primary energy from fossil fuels (OurWorldInData.org/energy), adapted from [11]. Copyright 2022 Our World in Data under Creative Commons By License [3].

Current policies to reduce or at least slow down the growth of CO_2 and other greenhouse gas emissions will positively impact future warming. There are two fundamental areas we need to focus on: energy (this encompasses electricity, heat, transport, and industrial activities) and food and agriculture (which includes agriculture and land use change). Transitioning to low-carbon alternatives is crucial to address these problems and create a more sustainable energy future. The key strategies for reducing reliance on fossil fuels and decreasing emissions include [12]:

i. Decreasing energy consumption through increased efficiency
ii. Substituting fossil fuels with cleaner alternatives, such as renewable energy sources
iii. Capturing and storing carbon dioxide emissions

The optimal way to decrease greenhouse gas emissions is utilizing renewable energy sources, such as solar, wind, and hydroelectric. Most of these sources are not as economically viable or reliable as fossil fuels, particularly natural gas. While some renewables are already competitive in existing markets, others teeter on the line between needing support and being competitive. Instead, others clearly

cannot survive at their current technology level. In addition, the variability of these resources may limit their ability to consistently supply a stable and reliable source of electricity to the grid without proper management and integration. Several studies [13,14] have found that reaching the goal of 100% renewable energy systems is not feasible in short- to medium-term. Fossil fuels will likely continue to play a major role in the eventual transition to a zero net emissions energy future. As a result, carbon capture and utilization (CCU) has been proposed to help decarbonize the energy sector.

1.3 CO_2 Conversion

The CO_2 concentration in the atmosphere has been increasing every year since the 50s, at the beginning of industrial acceleration, until now, when it exceeds 410 ppm. The current expectative is the increase to 800–1000 ppm at the end of the 21st century [15]. The present CO_2 level in the atmosphere is higher than at any time during the last 6,500,000 years, for which trustworthy data was extracted from ice cores [16]. Openly emerged the needing for a reliable approach to the huge presence of CO_2 in the atmosphere. The purpose is to introduce CO_2 as a raw material into a circular economy loop to synthesize high-added-value products, joining at the same time the steady growth in global fuel demand. In this way, using CO_2 to produce fuels sustainably can be adopted to substitute traditional fossil fuels. The conversion of atmospheric CO_2 into low-carbon fuels or small-molecule organic compounds has the potential to decrease CO_2 emissions and serve as a means of energy storage. That has significant implications for addressing energy shortages and reducing global environmental pollution [17,18]. CCU represents a novel economic opportunity that enables stakeholders to utilize captured CO_2 as a raw material for producing fuels and value-added products through other processes. CO_2 has gained attention as a promising and renewable carbon source due to its economic and safe availability. This gas can be used as a C_1 building block to create various organic chemicals, materials, and carbohydrates, making it an attractive feedstock for various industries [19,20]. Not only does utilizing CO_2 as a feedstock aid in mitigating the effects of global climate change caused by rising CO_2 emissions, but it also presents an exciting challenge for catalytic and industrial development, opening up new opportunities and concepts for research and application [21]. The thermodynamic stability of CO_2 makes its conversion challenging, as it has a high Gibbs energy ($\Delta G^0 = -400$ kJ/mol) that requires a substantial amount of energy to be overcome [22,23]. The conversion of CO_2 into a different form represents a significant challenge, as it

entails an alteration in the carbon oxidation state. As a rule, such a process is endergonic and endothermic, necessitating a considerable energy input. It is worth noting that CO_2 is the most oxidized state of carbon, with +4 as the oxidation number, meaning that its conversion to more energetic chemicals requires electron transfers to lower it. Huang and Tan [24] classified different forms of CO_2 valorisation into two main categories. Physical processes involve using CO_2 in its untransformed state, while the chemical and biological processes imply the transformation of CO_2 conversion molecule into high-added values products.

Chemical processes for CO_2 conversion towards high-added value substances can be divided into several categories:

- thermocatalytic hydrogenation [25]
- photocatalytic conversion [26]
- electrocatalytic reduction [27]
- photo-electrocatalytic methods [28].

From this list, the first two techniques will be described below, as they were not the subject of study in this thesis work, while the other two will be discussed in more detail in the following paragraphs.

Thermocatalytic methods are promising for the conversion of CO_2 into synthetic fuels and chemicals because they provide quick reaction rates and, as a result, enable large-scale manufacturing [29]. However, that is high energy consumption process. Four significant processes that exhibit high potential for large-scale implementation in the industry are: methane dry reforming (MDR), as represented by Equation 1; reverse water gas shift reaction (RWGS), Equation 2; Sabatier reaction (SR), Equation 3; and direct methanol synthesis (DMS), Equation 4 [29].

Equation 1 – Methane dry reforming

$$CO_2 + CH_4 \rightleftharpoons 2CO + 2H_2$$

Equation 2 – Reverse water gas shift

$$CO_2 + H_2 \rightleftharpoons CO + H_2O$$

Equation 3 – Sabatier reaction

$$CO_2 + 4H_2 \rightleftharpoons CH_4 + 2H_2O$$

Equation 4 – Direct methanol synthesis

$$CO_2 + 3H_2 \rightleftharpoons CH_3OH + H_2O$$

To make the processes sustainable, H_2 as a reactant should come from a renewable source (*e.g.*, water electrolysis using solar and wind energy). Efficient heat supply or removal, depending on the endothermicity of each reaction, and catalyst deactivation are challenges that must be addressed with innovative reactor designs and inexpensive, highly-active, and stable nanostructured catalysts. Heterogeneous catalysis, typically based on low-cost transition metals (*e.g.*, Ni, Cu, Cr, Fe), is widely used in thermocatalytic processes [30,31]. Moreover, thermocatalytic conversion using heterogeneous catalysis has already been widely implemented on an industrial scale, making these processes promising for large-scale implementation. Despite the potential advantages of thermocatalytic CO_2 conversion, some several significant drawbacks and challenges must be addressed for the technology to become commercially viable. One major challenge is the high energy demand required to drive the endothermic reactions, which results in significant operating costs. Another issue is the availability of cheap and abundant feedstocks, such as methane, which limits the scalability of the process. Additionally, the development of highly active and stable catalysts is crucial for the success of the technology, as catalyst deactivation can occur due to poisoning, sintering, or carbon deposition. Finally, the overall process needs to be designed in a way that minimizes the environmental impact and ensures the sustainability of the process.

Switching the focus to another CO_2 conversion approach, photocatalytic CO_2 reduction is an environmentally friendly technology that utilizes solar energy for converting CO_2 into fuel and chemicals [32]. Utilizing solar energy as the sole energy input to convert CO_2 into fuel and chemicals is considered a great advantage of the technique, making it renewable because of its abundant energy source. Additionally, the process does not require any additional energy and has no adverse environmental effects. Therefore, it can be considered a clean and sustainable technology. In this process, the three principal steps are [33]:

i. light absorption,
ii. charge separation,
iii. surface reaction,

that are the three principal steps, similar to natural photosynthesis. The first step involves photon energy exciting electrons from the valence band (VB) to the

conduction band (CB), creating positively charged holes. VB is the highest energy level occupied by electrons involved in bonding, while CB is usually empty and is the lowest unoccupied energy band. The semiconductor photocatalyst should have an appropriate band gap structure to make these electrons and holes energetically favourable for subsequent reactions [34]. In the second step, photogenerated carriers can undergo several major processes, such as in-band transitions, charge transfer, or electron-hole recombination. Finally, the redox reaction can use electrons or holes that reach the catalyst's surface. The photogenerated electrons in CB participate in CO_2RR. Photocatalytic reduction generally occurs on the surface of semiconductors where there exist energy bands. For successful photoreduction of CO_2, the photocatalyst must have a suitable VB and CB to enable electron transfer from the photocatalyst to CO_2. The band gap energy and CB and VB positions of different photocatalysts are related to possible solar fuels and standard reduction potentials. Despite the potential of CO_2 photoreduction [35], the process currently faces a significant limitation due to low conversion efficiency. Several key factors contribute to this limitation, including a mismatch between the semiconductor absorption ability and the solar spectrum, the poor separation efficiency of charge carriers, the low solubility of CO_2 in water (approximately 33 μmol in 1 mL of water at 100 kPa and room temperature [34]), back reactions during CO_2 reduction, and competition from the water reduction reaction to hydrogen [36].

A growing research effort in electrochemical methods (specifically: electrocatalytic and photo-electrocatalytic reduction of CO_2) is the current response from physical scientists and engineers.

1.4 Electrochemical methods

The general reaction occurring for the CO_2 reduction is shown in Equation 5:

Equation 5 – General CO_2RR

$$CO_2 + H_2O \rightarrow C_xH_yO_z + mO_2$$

In the electrochemical devices, it is possible to break this broad process into the two half-reactions shown in Equation 6 and Equation 7.

Equation 6 – Cathodic reaction: CO_2RR

$$xCO_2 + yH^+ + ne^- \rightarrow C_xH_yO_z + mH_2O$$

Equation 7 – Anodic reaction: Hydrogen Evolution Reaction (HER)

$$2H^+ + 2e^- \rightarrow H_2$$

The complete utilization of the CO_2RR electrochemical process is hindered by three main obstacles [37]:

i. Chemical inertness of CO_2 molecule, which is a result of the significant difference in the bonding energies of the constituent atoms [38,39].

Specifically, the C=O double bond has a bonding energy of 187 kcal/mol, whereas the O=O double bond and C−C single bond have bonding energies of 116 kcal/mol and 145 kcal/mol, respectively. The higher bonding energy of CO_2 implies that more energy is required to activate the molecule for the reaction pathway.

ii. Competition with the hydrogen evolution reaction (HER) [40].

The HER is more favourable than CO_2RR because it requires a lower overpotential energy and involves only two electron transfer steps. In contrast, CO2RR requires multiple steps to produce high-value products such as propanol. Table 1.1 shows the equilibrium potentials (V) versus the reversible hydrogen electrode (RHE) (at 1 bar, 25 °C, pH = 0) for the electrochemical reduction of CO_2 to commonly reported products.

Table 1.1 – Standard Equilibrium Potentials vs Reversible Hydrogen Electrode for the Electrochemical Reduction of CO_2, adapted from [41]**.**

Reaction	E^0 [V vs. RHE]	Product
$2H_2O \rightarrow O_2 + 4H^+ + 4e^-$	1.23	Oxygen Evolution Reaction (OER)
$2H^+ + 2e^- \rightarrow H_2$	0	Hydrogen Evolution Reaction (HER)

$CO_2 + 2H^+ + 2e^- \rightarrow CO + H_2O$	–0.10	Carbon Monoxide
$CO_2 + 2H^+ + 2e^- \rightarrow HCOOH$	–0.12	Formic Acid
$CO_2 + 6H^+ + 6e^- \rightarrow CH_3OH + H_2O$	0.03	Methanol, MeOH
$CO_2 + 8H^+ + 8e^- \rightarrow CH_4 + 2H_2O$	0.17	Methane
$2CO_2 + 12H^+ + 12e^- \rightarrow C_2H_5OH + 3H_2O$	0.09	Ethanol, EtOH
$2CO_2 + 12H^+ + 12e^- \rightarrow C_2H_4 + 4H_2O$	0.08	Ethylene
$3CO_2 + 18H^+ + 18e^- \rightarrow C_3H_7OH + H_2O$	0.10	Propanol, PrOH
$CO_2 + e^- \rightarrow CO_2^-$	–1.9	CO_2 Radical Anion*

* The E_0 value for the formation of the $CO_2^{\bullet-}$ radical is the only taken from [42].

While some products have more positive equilibrium potentials than HER, their sluggish kinetics and high overpotentials limit their performance. Significantly, the activation energy of the CO_2 molecule to form the CO_2 radical anion, which is often the first elementary electron transfer step in a CO_2RR besides the rate-determining step (RDS), only proceeds at a very negative applied potential (–1.9V [42]). Accordingly, in the development of electrocatalysts for the CO_2RR, it is vital to lower the kinetic energy barriers and improve energy efficiency.

iii. Poor selectivity of CO_2RR towards higher value product streams.

The wide range of products shown in Table 1.1, that resulted from CO_2RR, including CO, CH_3OH, C_2H_4, and C_2H_5OH, among others, contribute to this poor selectivity.

The electrochemical pathway is widely acknowledged as a more advantageous alternative to the thermochemical route due to various reasons. For instance, it facilitates a one-step reaction process that does not necessitate high temperatures or pressures [43]. Consequently, the implementation of electrochemical routes would entail lower infrastructure expenses. Additionally, the electrochemical pathway enables the reduction of CO_2 in compact, portable units, thereby permitting the decentralized production of chemicals.

In this work, two approaches to CO_2 electrochemical reduction have been studied and then applied:

i. Electrocatalysis;
ii. Photo-assisted electrocatalysis under sun-simulated illumination.

The next paragraphs will briefly introduce the theoretical insights, the different kinds of cells/reactors, and the status of the art on the catalysts that are able to accomplish the reaction.

1.4.1 Electrocatalytic (EC) CO_2RR

The CO_2 electrochemical conversion has several advantages as a method for generating valuable chemicals and fuels. These include mild reaction conditions, the ability to control reaction rates and product selectivity through the applied potential, and wide scalability due to modular electrolyzer designs. The coupling of CO_2 electroreduction with renewable energy sources is a promising strategy for increasing the utilization of renewable energy in the fuel and chemical industries. CO_2RR is a three-phase chemical reaction that could involve diffusion, adsorption, activation, cleavage, eventually dimerization, and product desorption [44,45]. A variety of factors contribute to the complexity of CO_2RR, including the use of heterogeneous catalysts, different reaction mechanisms, electrolysis conditions, and target products. Early research revealed for most EC CO_2R reactions the formation of the $CO_2^{\bullet-}$ radical [46]. Table 1.1 shows that the standard potential for producing this radical species is relatively high compared to other products. Therefore, this causes high cell overpotentials (the difference between the theoretical thermodynamic potential for the desired product and the real

applied potential), which are usually reported as huge challenges. Because EC CO_2RR possesses thermodynamic potentials similar to those of HER [47], from a kinetic perspective, it is preferable for the entire system to carry out the competitive HER. This makes the H_2 production hard to suppress and CO_2R less effective in terms of Faradaic Efficiency (FE) and selectivity. Typically, CO_2RR starts to occur at low overpotentials for a two-electron-transfer reaction with a suitable electrocatalyst, and the two-electron-transfer products, CO or HCOOH, can follow different pathways. Schematic routes for the possible reactions are represented in Figure 1.4. The intermediate *COOH is important for CO formation through proton-coupled electron-transfer (PCET) reactions, while *OCOH is likely the intermediate for formate [48]. Catalysts strongly determine the reaction pathway selectivity of these two species. However, for multi-electron ($>2e^-$) transferred products, CO_2RR kinetics become slower, resulting in larger overpotentials and lower selectivity. Furthermore, multi-electron-transfer pathways can have different reaction mechanisms and subsequent product selectivities [49]. Theoretical methods have been employed to guide CO_2RR experiments, while C_1 and C_2 product pathways have been studied using a solvation method [50,51]. *CO–COH is formed by coupling *CO and *COH at a neutral pH, but the dimerization of *CO to form *CO–CO is a critical pathway toward C_2 products at alkaline pHs. Further selectivity on ethylene and ethanol can involve surface-adsorbed H_2O. *CO has been suggested as an essential intermediate in multi-electron-transfer reductions, and the density and capability of CO adsorption active sites in electrocatalysts are important. Several experimental results have reported the combined effects of both *CO surface density and adsorption energy [52,53]. Therefore, it is crucial to design and adjust the active sites on heterogeneous electrocatalysts for CO_2RR in a rational manner.

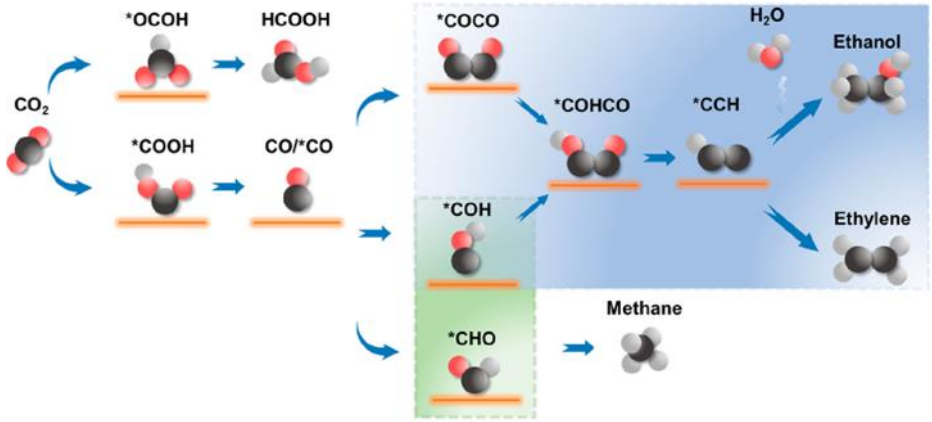


Figure 1.4 – Schematic of several possible reaction pathways of electrochemical CO2 reduction reaction toward methane, ethylene, and ethanol, respectively. Reprinted with permission from [54]**. Copyright © 2021, American Chemical Society.**

The electrocatalytic process involves cathodic and anodic reactions in two separate compartments, separated by a membrane, to prevent the oxidation of the reduced products generated in the cathodic compartment. An external power supply is employed to drive the non-spontaneous proton-electron transfer reaction, converting electrical energy into the chemical energy of the resulting products. This technology is compatible with the current water electrolysis technology, allowing water to be used as a source of protons (H^+). In aqueous electrolytes (*i.e.,* $NaHCO_3$ or $KHCO_3$ solutions), the water and carbon dioxide reduction processes take place simultaneously at the cathode due to the proximity of their CO_2/CO potential (–0.53 V vs. NHE, Normal Hydrogen Electrode, at pH = 7) [55]. In addition, the electricity needed could be generated from photovoltaics.

As seen in Table 1.1, CO_2 can be converted into a great variety of products. The difficulty in this field is the preparation of catalysts with high reactivity towards specific target products, considering the many possible products. The electronic structure of a catalyst surface plays a significant role in determining the overpotential and selectivity of the CO_2RR by directly affecting the binding energies of reaction intermediates. The geometric structure is often linked to the density and arrangement of catalytic sites, which can affect, among others, product selectivity and current density. In this context, using nano-scaled heterogeneous catalysts is an attractive way to perform EC CO_2 reduction. The use of nanostructured catalysts instead of conventional electrodes greatly improves the reactivity of the surfaces by increasing the number of reactive sites

available for catalysis. Researchers have investigated the use of nano-structured metal (mono- or bimetallic) and metal oxides as catalysts. The morphology and composition control of supported nano-catalysts lead to higher reactivity and selectivity [56]. Nanostructured catalysts offer high grain boundaries and larger numbers of active sites because of their high surface areas [57]. They also provide a higher proportion of coordinately unsaturated surface sites, which can play a remarkable role in CO_2 electroreduction.

1.4.2 Photo-electrocatalytic (PEC) CO_2RR

PEC CO_2 reduction process entails using a semiconductor photoelectrode to generate electrons through photoexcitation, which are then guided by an external applied potential to the electrode surface where they perform the reduction of CO_2 [58,59]. Applying an external electric field promotes the directional transfer of photogenerated electrons and holes, thus increasing the separation efficiency of these carriers and enhancing the redox ability. Furthermore, by applying an appropriate bias voltage, the redox potentials can be adjusted even if the band position of the photocatalyst is not favourable for CO_2 reduction and H_2O oxidation [60]. It is worth noting that semiconductors do not have a continuous distribution of energy levels like, metals. The valence band and the conduction band do not overlap. The distance between the highest occupied energy level (valence band maximum VBM) and the lowest unoccupied energy level (conduction band minimum CBM) is called the energy band gap, and its value corresponds to the least energetic electromagnetic wave capable of exciting an electron from the VBM enough to jump and occupy the CBM [61]. An ideal photocatalyst must possess two essential characteristics: a narrow bandgap and a robust redox capability. A narrow bandgap enables the catalyst to broaden its photoresponse and increase its range of solar light absorption. Furthermore, a higher conduction band potential coupled with a lower valence band potential is more thermodynamically favourable for conducting reduction and oxidation reactions. However, these attributes are crucial yet mutually exclusive [58,62]. The PEC reduction of CO_2 can integrate the advantages of electrocatalysis, which directly uses renewable electricity and water, e^- and H^+ sources, respectively, to convert CO_2 [58,63]. The utilization of solar energy and the avoidance of high-temperature and high-voltage reduction environments to promote charge separation and improve solar conversion efficiency leads to a broad application prospect [61,64]. The resulting PEC system can promote carrier separation by tuning the overpotential and acting on the catalytic reaction efficiency by realizing

fast electrons and proton transfer. The key to achieve PEC reactions is to employ materials capable of performing both light absorption and electro-catalysis of the desired reaction. A good photo-electrocatalyst should present a narrow bandgap and strong redox ability. Natural photosynthesis heavily inspires that idea and tries to adapt the same concept to CO_2 reduction. As such, it had even been referred to as "artificial photosynthesis" when it was first conceived. Like in natural photosynthesis, photo-generated electrons and holes can be used to drive chemical reactions rather than being collected for electricity. That allows solar energy to be harvested and turned into chemical energy (solar fuel), which is then stored in chemical bonds. Artificial photosynthesis is the name given to this multi-step process that replicates the action of natural photosynthesis [65].

1.5 Regional and European Projects to face the CO_2 presence in atmosphere

The work presented in this thesis was performed within two main Projects. A brief explanation of the objectives and contextualization of both projects is provided below.

The Italian regional SATURNO-Bioeconomy project aims to develop an integrated platform for the chemical, biochemical, technological, and methodological conversion of urban organic waste into raw materials for various sectors, including industrial chemistry and waste, fuels and automotive, agriculture, industrial biochemistry and biotechnology, and cement. The platform targets as well the recovery and conversion of carbon dioxide through the development, application, and validation of innovative methodologies. This approach creates a practical example of a circular economy at the urban level, focusing on recovering and reusing carbon dioxide and developing new processes and products. The project also aims to validate technologies currently being studied to reduce carbon dioxide emissions, capture CO_2, and reuse it for other purposes. In particular, the conversion of CO_2 to methanol through biochemical, thermochemical, and electrochemical processes is tested and validated, and the production of alcohols (*i.e.,* acetone, butanol, and ethanol) through biochemistry are evaluated. In particular, the task in which our group was involved investigated of the synthesis of some materials for the EC CO_2RR to alcohols and other high-value-added products. In Chapter 3, the work developed within the SATURNO Project was presented.

The SunCoChem European Project focused on using CO_2 from environmentally damaging waste material to make valuable chemical compounds. SunCoChem responds to the demand of the EU Chemical Industry for highly competitive and integrated solutions enabling the production of energy and high-value chemicals from solar energy, water, and carbon dioxide while remaining carbon neutral. Photo-electrocatalysts (PEcats) can help solve this challenge by creating competitive systems that transform sunlight, water, and carbon dioxide into useful products. It is still difficult to find PEcats to scale the process from lab to industrial operations. An important obstacle to sustainability is the intensification of the solar to chemical energy conversion process. These procedures built into devices resembling fake leaves are anticipated to propel the carbon-neutral production of chemicals in the EU in the coming decades. Given the potential of using CO_2 to create chemicals or fuels, and once the difficulties in treating such a molecule are known, the SunCoChem CO_2 revalorization aims at developing a competitive and modular self-biased tandem photo-electrocatalytic reactor (TPER) to efficiently produce oxo-products from CO_2, water, and sunlight integrating CO_2 capture and conversion in a single unit. In the framework of the general Project, the tasks in which our group is involved within this thesis aim to optimize the catalyst and the electrolyte for PEC CO_2 reduction to CO, in the cathodic compartment. The work related to the optimization of the PEcats involved in the cathodic part of the reactor was reported in Chapters 4 and 5. Then, the advanced analysis of the obtained catalysts was reported in Chapter 6 and finally the functionalization of the catalysts was described in Chapter 7.

1.6 Aim of the work

This thesis investigated the performance of Cu-based catalyst materials in the EC and PEC CO_2 conversion processes. There were 5 main goals:

1. Prepare a reproducible and scalable electrocatalyst material composed of Pd and Cu.

Chapter 3 explores the literature useful for describing the characteristics of the aerogel/xerogel class of materials, the procedure of synthesis and the testing of the Pd/Cu-based materials for the EC CO_2R to valuable products in a double chambers cell. The final part of the Chapter focuses on evaluating the electrocatalytic performances of the aerogel materials even in a scaled-up setup to produce high energy density chemicals (*e.g.,* current density higher than 100 mA cm^{-2}) from the electrocatalytic CO_2 conversion.

2. Design, synthesise, and test a reproducible and scalable photo-electrocatalyst material composed of Cu and Sn.

The first part of Chapter 4 and 5 aims to develop a photo-electrocatalyst for the CO_2 reduction to CO + H_2 (syngas) and other high-added values products. Two synthetic methods were followed: co-precipitation and core-shell synthesis. - In addition, Chapter 5 also reports a study about the selectivity of the reaction according to the amount of SnO_2 as the shell material. The assessment of the reproducibility and the characterization of the obtained materials, composed of Cu_2O and SnO_2, and the studies which led to the final design of the catalysts were also debated.

3. Evaluate the electrocatalytic activity of the Cu-Sn materials to C_{1+} products from the PEC CO_2 conversion and assessment of the light influence within the selectivity.

The second part of Chapters 4 and 5 highlight the PEC tests carried out with the obtained catalysts. Different kinds of tests are reported, aiming to investigate catalysts' performance in a double chamber cell, enlightened by a solar simulator. Moreover, the tests carried out under solar simulator lighting are compared with those without the simulated illumination, and a shift of the selectivity towards multicarbon products was observed. In the final part of both Chapters, an EIS (Electrochemical Impedance Spectroscopy) test overview assesses the better behaviour of the samples when enlightened, for both the types of catalysts created, by investigating the trend of the R3 resistance associated with the equivalent circuit, which describes the system.

4. Provide an advanced analysis of the best Cu-Sn-based photo-electrocatalysts to understand their carriers behaviour.

Chapter 6 gives the theoretical fundamentals of the two techniques used for deepening understand the carriers' mobility inside the samples. In particular, the core-shell sample underwent TRMC (Time-Resolved Microwave Conductivity) and IMVS (Intensity Modulated Photovoltage Spectroscopy), resulting in characteristics of the samples related to the higher or lower amount of SnO_2 in them. As far as we know from what is published in the literature, this is among the first works regarding IMVS analysis on materials used as the cathodic part of a PEC reactor for the CO_2RR.

5. Functionalization of the best Cu_2O-SnO_2 catalyst with Ru-Re-based supramolecular complexes to enhance the long-term stability and the selectivity towards 1:1 CO/H_2 syngas.

Chapter 7 first deals with the synthesis standardization for the best Cu:Sn ratio photo-electrocatalyst, as discussed in the previous Chapters. The relationship between the reagents' flow rate into the synthesis reactor and the properties of the resulting materials is studied. After the characterization and a preliminary set of PEC tests, the most promising catalyst was functionalized via electropolymerization by attaching different kinds of supramolecular compounds Ru/Re-based onto its surface. The stability test carried out on the modified catalyst shows the maintenance of the performance over time and the obtainment of a very promising syngas mixture with a proper $CO:H_2$ ratio, useful for eventual future applications (*i.e.,* hydroformylation reactions).

Chapter 2

Materials and Methods

Chapter 2 comprehensively describes the elements used as catalysts, the characterization techniques employed during the experimental work, and the experimental setups utilized for carrying out the experiments. This Chapter presents a detailed account of the specific materials and techniques used to conduct the research. It provides theoretical insight into the methodologies employed to achieve the desired results. By outlining the procedures and techniques employed in the study, this Chapter serves as a valuable resource for understanding the experimental design and conducting similar research in the future.

2.1 Materials used as CO_2 reduction catalysts

The standard reduction potential for reducing CO_2 in an aqueous solution (at pH = 7, 1 M electrolyte, 25 °C, 1 atm) into products such as CO or formate falls within the range of –0.2 V to +0.2 V (compared to RHE). However, the reaction can only occur at a more negative voltage due to the high overpotential required to overcome energy barriers during conversion pathways. Variations in the electrolyte medium and cell configuration can affect the performance of the CO_2RR. Nevertheless, the electrocatalyst plays a significant role.

The effectiveness of a catalyst and its design are the most important factors in determining the overall performance of a cell. This Section will review the

properties of elements mainly used in this work as electrocatalysts and photo-electrocatalysts: Cu, Pd, and Sn.

2.1.1 Copper

The classification of metal materials for use in the electrochemical reduction of CO_2 was first established in the 1980s and 1990s through the work of Hori *et al*. [66]. They found that certain metals, including Ni, Fe, Pt, and Ti, were not suitable for CO_2 reduction since they mainly perform water splitting. Other metals, such as Pb, Hg, Tl, In, Sn, Cd, and Bi, could primarily reduce CO_2 to formic acid (HCOOH) or formate ($HCOO^-$). However, only Au, Ag, Zn, Pd, Ga, and Cu were able to reduce CO_2 to multiple hydrocarbons, aldehydes, and alcohols. Among those, copper (Cu) was the best catalyst material to reduce CO_2 to multi-carbon products in electrochemical applications. This classification has formed the foundation of contemporary research in this field. Cu is a highly conductive metal with various properties that make it an attractive choice as a catalyst in the electrocatalytic and photo-electrocatalytic reduction of CO_2. It is a widely recognized heterogeneous catalyst capable of effectively converting CO_2 into valuable hydrocarbons, aldehydes, and alcohols [41]. In fact, Cu is the only pure metal capable of reducing CO_2 to products that require more than two electron transfers (referred to as "further reduced products" or " $>2e^-$ products") with high Faradaic efficiency [41]. Recently, a large interest has been devoted to copper oxide-based materials for their various applications and their ability to reduce CO_2 to valuable products with a relevant activity [43,67]. While many researchers have believed that metallic Cu is the active site for catalysis, recent studies suggest that certain oxidation states of Cu species can enhance CO_2RR performance to C_{2+} products [68]. Research on oxide-derived Cu electrodes has shown that oxygen centres of copper oxide surfaces and Cu^+ oxide sites provide favourable binding sites and modulate reactivity, significantly influencing product distribution. In general, Cu-based catalysts exhibit moderate binding energies of important intermediates like CO on the surface, which helps to initiate the formation of subsequent important intermediates leading to C_{2+} products. This intrinsic catalytic nature of Cu is attracting significant attention in the research community for CO_2 reduction to multi-carbon products compared to other catalytic materials. A study on polycrystalline Cu revealed broadly divergent selectivities for over 16 products. Among them, 12 were C_2 or C_3 products [69], indicating the complex nature of the reaction but highlighting the potential future use of CO_2 as a starting molecule on Cu-based materials for various chemical

syntheses. The applied potential leads to compositional and structural changes in copper due to the greater possibility of exceeding the redox potential of active species under real-time operating environments. The oxidation state and structural evolution of polycrystalline Cu varied at various applied voltages, and Cu_2O could be converted to metallic Cu and Cu(111) reconstructed to Cu(100) at larger cathodic potentials [70]. The copper capability to shift its oxidation state could bring a peculiar advantage, studied via computational studies by Chang, Li, and Tsai [71]. The discovery showed that a CO molecule can be adsorbed at an under-coordinated site on a CuO surface and then couple with a neighbouring CO molecule. This process is most likely to occur on an Ov-Cu_4O_3 surface due to its mixed-valence property. The mixed-valence ions help stabilize the charge-separated $(OC)^{\delta+}(CO)^{\delta-}$ dimer through covalent interaction and electrostatic attraction. This finding may explain the experimentally observed C_2-formation catalysed by oxide-derived Cu.

However, the practical application of copper-based catalysts in electrocatalytic and photo-electrocatalytic CO_2 reduction has been limited so far by low current density, poor selectivity, and poor stability [72]. Therefore, developing efficient copper-based catalysts with high current density, C_{2+} selectivity, and stability has become a research focus in the EC and PEC CO_2 reduction field. Various strategies have been proposed, such as regulating morphology structure [73,74], defects, and surface/interface engineering [75], to enhance the activity and selectivity of copper-based catalysts.

Thus, the present study aims to investigate the use of Pd and Cu-based electrocatalysts, as well as Cu and Sn-based photo-electrocatalysts, for the specific CO_2 reduction reaction.

2.1.1.1 Cuprous oxide

Cuprous oxide (Cu_2O) is a p-type semiconductor with an excellent visible light absorption ability, as shown by its band gap of ~ 2 eV and a favourable conduction band position [76,77]. Thanks to its merits such as low-cost, non-toxicity, abundance, and easy synthesis, Cu_2O has been one of the most investigated transition metal oxide crystals [78]. It has an energy band structure suitable for CO_2 reduction to CO and C_1-compounds. It has been well-demonstrated for applications in photo-electrochemical and photovoltaic solar energy conversion. Cu_2O can be synthesized with several morphologies: normally, high index planes show high photo-activity, but for Cu_2O, it was observed that cubic morphology, has a higher selectivity in terms of CO_2

reduction instead of H_2 production from water by exposing low index facets [76]. The suitable positioning of its conduction and valence bands makes Cu_2O an ideal photocatalyst for CO_2RR to CO and C_1 compounds because its Fermi level has lower energy than the standard reduction potential of the CO_2/CO couple (E_0 = –0.105 V vs. NHE at pH=0) and CO_2/HCOOH couple (E_0 = –0.169 V vs. NHE at pH=0) [79]. Nevertheless, as commonly described for photoactive semiconductors, Cu_2O photo-stability is insufficient for their application in large-scale devices or facilities [80]. The main limitation is that the initial photoactivity of the catalyst decreases in a short time. An efficient charge transfer can prevent the possibility of self-photoreduction and oxidation.

2.1.2 Palladium

Palladium is a unique electroreduction catalyst due to its ability to absorb hydrogen and form palladium hydride (PdH) in aqueous electrolytes at potentials commonly used for electrochemical CO_2 reduction. It leads to activity trends that are not typical of other metallic catalysts. For example, Pd and Pt are both known to be poisoned by adsorbed CO, but Pd produces a mixture of H_2 and CO under CO_2 reduction conditions, while Pt only produces hydrogen. That suggests that the electrocatalytic performance of PdH may differ from that of metallic Pd. Previous studies have examined Pd as a CO_2 electroreduction catalyst in aqueous electrolytes, but PdH phase formation was not always explicitly identified, and the mechanism was not well understood [81,82]. The group of Tackett and co-workers [83] recognized that the surface-producing mixtures of H_2 and CO on Pd electrodes during CO_2 reduction were likely PdH instead of Pd and aimed to understand further the relationship between the active site and product distribution. Thus, unlike most metals, Pd changes phase during the CO_2. Regarding the CO_2 reduction mechanism, it has been fully demonstrated that the reaction kinetics for the generation of *COOH is faster on a palladium surface than on a copper surface because palladium has a stronger ability to adsorb CO_2. Therefore, combining palladium with copper can be an effective way to enhance CO_2 reduction. Theoretical calculations using density functional theory (DFT) have also indicated that a stepped copper-palladium CuPd(111) surface has a stronger capacity to adsorb and activate CO_2 compared to a plain Cu surface [84]. In addition, experiments have shown that CuPd alloy catalysts can effectively promote the activation of CO_2 and inhibit the formation of hydrocarbons on the catalyst surface, resulting in a higher selectivity for CO products [85].

2.1.3 Tin

Tin (Sn) is a well-known electrocatalyst for reducing CO_2 to produce useful chemicals and fuels. Sn-based electrocatalysts are typically prepared by depositing tin on various conductive substrates such as carbon and metal or alloying with other metals [86,87]. Feaster *et al*. [88] confirmed the efficient electrocatalyst role of Sn for the CO_2RR because of its appropriate binding energy for the intermediate *OCHO. In their study, the Sn electrode was selective toward hydrogen at the earlier overpotentials. However, it becomes selective to formate around –0.8 V vs RHE. Maximum FE to formate is observed around –0.9 V vs RHE before mass transport of CO_2 becomes the rate-limiting step for CO_2RR. They also discovered reasonable performance for producing CO (FE value of around 17% at –0.7 V vs. RHE), suggesting that tin is suitable for CO and HCOOH production. Furthermore, the practical application of Sn catalysts is less restricted by financial considerations (compared to Au and Ag), and toxicity concerns (especially Pb).

2.1.3.1 Tin Oxide

Tin oxide is an n-type direct band gap semiconductor with noticeable electron mobility (up to 250 $cm^2\ V^{-1}\ s^{-1}$ [89]) and intrinsic stability. Besides, in general, Sn-based materials are highly selective catalysts for the EC CO_2RR to formate [90,91], which is currently reported as one highly desirable bulk chemical in terms of economic and environmental benefits. Recent works highlight a strong dependence on the Sn oxidation state versus the selectivity of a specific product [92,93]. Baruch *et al*. [94] observed using in-situ infrared spectroscopy that the CO_2RR proceeds over metallic Sn surface via a surface-bound carbonate (*OCHO) intermediate interacting with Sn(II) oxyhydroxide species. Instead, Zeng *et al*. [95] investigated the role of Sn(IV) in SnO_2 coupled with Cu_2O as an electrocatalyst for syngas production. Sn could become a barrier to the further reduction of copper species, avoiding photo-electroactivity losses. According to the literature, another effect of the Sn presence in the precursors' solution is the diminishing of Cu_2O particle size [96,97], which can influence the adsorption/desorption of reaction intermediates and, consequently, the product distribution.

2.2 Characterization Techniques

Several physical, chemical, and (photo)-electrocatalytic properties of the materials described have been evaluated in this work. In this Section, the methods employed for this purpose are described.

2.2.1 Physical Properties

2.2.1.1 Transmission Electron Microscopy

The transmission electron microscope (TEM) provides information on morphology, structure, chemistry, and even the nature of bonds [98]. The TEM follows the same basic principles of light microscopes but uses electrons instead of light. The optimal resolution attainable for TEM images is many orders of magnitude better than a light microscope because the wavelength of electrons is much smaller than that of light. Thus, TEMs can reveal the finest details of internal structure - in some cases, as small as individual atoms. A high-energy beam of electrons is shone through a very thin sample. The interactions between the electrons and the atoms can be used to observe features such as the crystal structure and features in the structure like dislocations and grain boundaries. Regarding the instrument composition, the modern TEM comprises an illumination system, a specimen stage, an objective lens system, a magnification system, a data recording system(s), and the chemical analysis system [99]. The electron gun is the heart of the illumination system, which typically uses a LaB_6 thermionic emission source or a field emission source. The illumination system also includes condenser lenses that are vitally important for forming a fine electron probe. The specimen stage is key to carrying out structural analysis because it can be used to perform in situ observations of phenomena induced by annealing, electric field, or mechanical stress, giving the possibility of characterizing the physical properties of individual nanostructures. The objective lens is the heart of a TEM which determines the limit of image resolution. The magnification system consists of intermediate and projection lenses, giving a magnification of up to 1.5 million. Finally, the chemical analysis system is the energy-dispersive X-ray spectroscopy (EDS) to quantify the chemical composition of the specimen. EDS relies on counting X-rays emitted from the beam-illuminated specimen region as a function of the photon energy, and it is probably the most precise microanalysis technique in TEM. Chemical analysis can also be performed. TEM can be used to study the growth of layers, their composition, and defects in semiconductors. High resolution can be used to

analyze the quality, shape, size and density of quantum wells, wires, and dots. It is also possible in TEM to measure the diffraction patterns of single particles using a method called Selected area electron diffraction (SAED). In SAED, the user can select an area of the sample with a small aperture, and only the electron diffraction pattern from that area will be measured.

Technical details: Transmission electron microscopy (TEM) characterization was performed on an FEI Tecnai G2 F20 S-Twin instrument operated at 200 kV acceleration voltage. The catalyst was dispersed in high-purity ethanol, sonicated, and drop-casted on Au holey carbon TEM grids.

2.2.1.2 Brunauer, Emmett, Teller

The most commonly used method for measuring surface area is the Brunauer, Emmett, Teller (BET) method, which involves measuring the amount of nitrogen adsorbed on the surface and in micropores [100]. Other organic gases, such as ethylene glycol monoethyl ether, can also be used for this measurement. However, nitrogen is more effective because can access smaller pores. The BET measurement balances adsorption and desorption, and the possibility of multiple adsorbed layers is considered. The BET model is based on the following assumptions: i) the rate of adsorption is equal to the rate of desorption in each layer; ii) the heat of adsorption from the second layer is constant and equal to the vapor condensation heat; iii) when the pressure equals the saturation pressure, the vapor condenses as a liquid and the number of adsorbed layers is infinite. It is possible to determine the number of moles of adsorbed material in the monolayer (nm) and the equivalent surface area using the BET method.

Technical details: the Specific Surface Area (S_{BET}), the total pore volume (V_p) and the total pore diameter (D_p) were measured by using N_2 physisorption at –196 °C (Micromeritics Tristar II 3020, v1.03, Micromeritics Instrument Corp., Norcross, GA, USA, 2009) on samples previously outgassed at 200 °C for 2 h.

2.2.1.3 Scanning Electron Microscopy

Scanning electron microscopy (SEM) is an electron microscope that uses a focused beam of electrons to interact with a sample, producing an image of its topography and relative composition. When the beam of electrons comes in contact with the sample, it generates secondary electrons (SEs), backscattered electrons, and characteristic X-rays, which are then detected by specialized detectors and displayed on a monitor. A typical SEM system consists of an

electron source, a column containing electromagnetic lenses, an electron detector, a sample chamber, and a computer display. The process of forming an SEM image is mainly related to detecting signals resulting from the interactions between the electron beam and the scanned sample. SEM has a resolution of 10 nm. Therefore, smaller particles must be analyzed with more sophisticated techniques [101]. Field emission scanning electron microscopy (FESEM) operates according to the same principles as SEM, but it uses a field emission electron source rather than a thermionic electron source. In FESEM, the electron beam is emitted by a potential gradient rather than thermal energy. This difference allows FESEM to produce higher quality images with higher resolution and a wider range of imaging capabilities compared to SEM (reaching a resolution up to 2-3 nm).

Technical details: FESEM measurements were carried out by Zeiss MERLIN, Gemini-II column, Oberkochen, Germany. Scanning electron microscopy (SEM) analyses were performed using a FEI (Hillsboro, OR, USA) model QUANTA INSPECT 200LV microscope.

2.2.2 Chemical Properties

2.2.2.1 X-Ray Diffraction

X-ray diffraction (XRD) is one of the most important materials characterization techniques, capable of analyzing crystal structures and atomic spacing [102]. For each analyzed substance, it is possible to obtain a complete description of its structure. However, the possible presence of amorphous phases should be considered in interpretation. X-ray diffraction is based on constructive interference of monochromatic X-rays and a crystalline sample. X-rays are generated via a cathode ray tube (mainly made of Cu), filtered to produce a collimated monochromatic radiation directed towards the sample (Figure 2.1a).

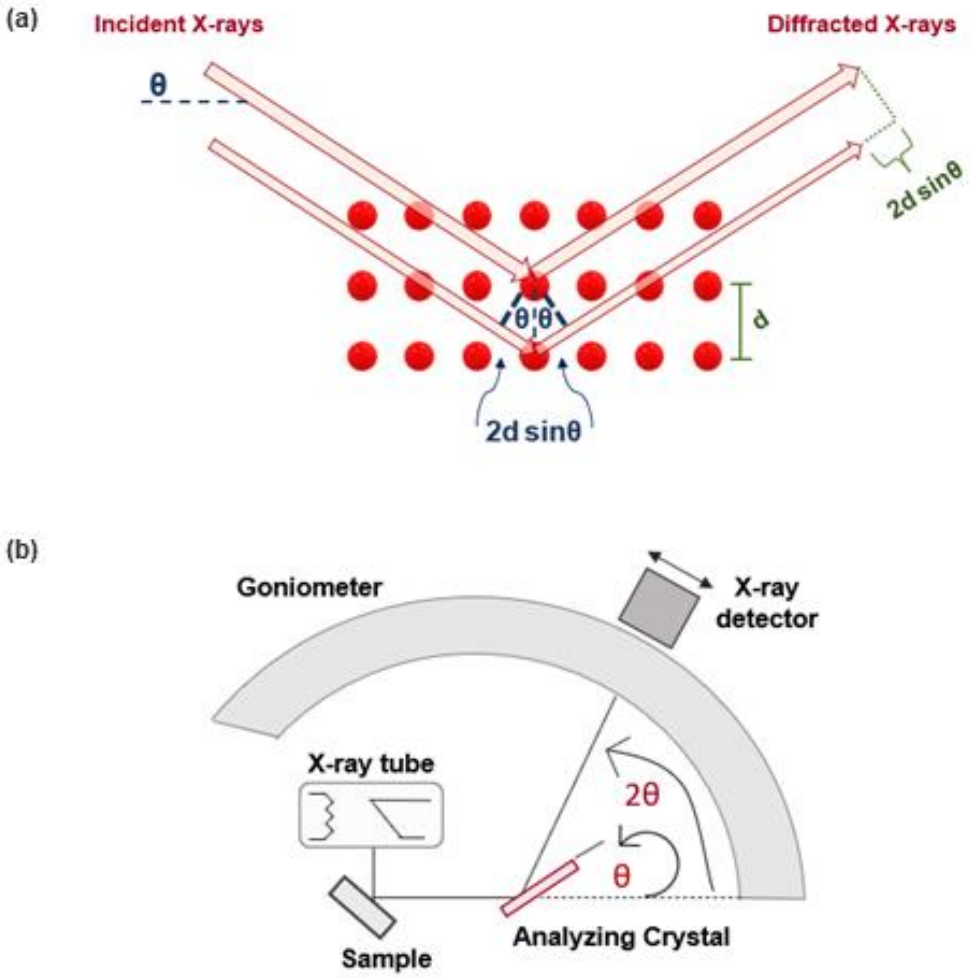


Figure 2.1 – Schematic representation of: (a) Bragg's Equation (Equation 8), and (b) the goniometer system.

The scattered X-rays from the sample interfere with each other either constructively or destructively. It means that detectors can read-out a signal only at angles where constructive interference occurs. The dots in the figure correspond to the building blocks of crystalline material. Due to its crystalline nature, the atoms are arranged regularly, thus periodically. The incident X-ray beam is scattered at different planes of the material. The resulting diffracted X-rays, therefore, have a different optical path length to travel. The magnitude of this path length only depends on the distance between the crystal planes and the incident angle of the X-ray beam. This is summarized in the famous Bragg's Law:

Equation 8 – Bragg equation

$$n\lambda = 2d\ sin\vartheta$$

where n is an integer, λ is the wavelength of the X-rays, d is the interplanar spacing generating the diffraction and θ is the diffraction angle. Because of the wavelength is known in XRD experiments and the angles at which constructive interference occurs are measured, the use of the Bragg equation allows for determining the distance between the lattice planes of the material. The resulting measure is called a "diffractogram". This is a plot of X-ray intensity on the *y*-axis versus the angle 2θ (which is defined as the angle between the incident and the diffracted beam) on the *x*-axis. Conversion of the diffraction peaks to d-spacings allows the identification of the compound because each compound has a set of unique d-spacings. Typically, this is accomplished by comparison of d-spacings with standard reference patterns. When amorphous materials are analyzed with XRD they do not show the typical sharp peaks centred in a certain θ. Amorphous materials' spectra consist of broad features or halos however centred on the typical angles [103]. In an X-ray diffractometer, the geometry is fixed. The sample rotates in the path of the collimated X-ray beam at an angle θ while the X-ray detector is mounted on the arm to collect the diffracted X-rays and rotates at an angle of 2θ (Figure 2.1b). The instrument used to maintain the angle and rotate the sample is named "goniometer". Usually, an X-Rays diffractometer consists of three basic elements: an X-ray tube, a sample holder, and an X-ray detector. As said, X-rays are generated in a cathode ray tube by heating a filament to produce electrons, accelerating the electrons toward a target by applying a voltage, and bombing the target material with electrons. When electrons have such that energy to dislodge inner shell electrons of the target material, characteristic X-ray spectra are produced and registered. As the sample and detector are rotated, the intensity of the reflected X-rays is recorded. When the geometry of the incident X-rays impinging on the sample satisfies the Bragg law, constructive interference occurs and a peak in intensity is shown in the diffractogram. A detector records and processes this X-ray signal and converts the signal to a count rate which is then output to a device.
The analysis of the peaks using the Scherrer equation (Equation 9) makes it possible to calculate the crystallite size of each phase present in the sample.

Equation 9 – Scherrer Equation

$$\textbf{crystallite size}\ (\text{Å}) = \frac{\mathbf{k\lambda}(\text{Å})}{\mathbf{FWHM\ cos\ \theta}}$$

Where k is a constant (0.94), λ is the X-Ray wavelength in Å, $FWHM$ is the full width at half maximum of the diffraction peak, and θ is the diffraction angle of the analyzed peak.

The reported XRD analyses are led under standard conditions in the following Chapters: Cu anode, K-Alpha$_1$ wavelength 1.5405980 Å, K-Alpha$_2$ wavelength 1.5444260 Å, K-Alpha$_2$/K-Alpha$_1$ ratio of 0.500, without monochromator. Furthermore, XRD technique is extremely sensitive (up to 1% w/w).

Technical details: The crystalline phase evaluation was investigated by X-ray diffraction (XRD) on a Panalytical PW 3040 X'Pert equipped with a Cu anode for the Kα radiation generation at 40 kV operating voltage in the 2θ range of 10-100° with a scanning step of 0.013° and a Cu radiation wavelength Kα = 1.54018 Å.

2.2.2.2 X-ray photoelectron spectroscopy

X-ray photoelectron spectroscopy (XPS) is a powerful analytical technique used to study the chemical and electronic structure of the surface of a material. When X-rays are directed at the surface of a sample, they excite the outermost electrons of the atoms, and the kinetic energy of the emitted electrons is measured. This information can be used to identify the elemental composition, chemical state, and bonding of the material's surface. XPS is highly sensitive to the surface of a material and can provide information at the atomic level, making it useful for various applications, including the study of catalysts, electronic devices, and biological systems. The technique is based on the photoelectric effect, first observed in the late 19th century and later described by Albert Einstein. For the analysis, a sample is exposed to soft X-rays with energies lower than ~6 keV. The kinetic energy of the resulting emitted electrons is then analyzed, see Figure 2.2a. The photoelectron that is emitted is produced when the energy of the X-ray is transferred to a core-level electron of the sample. The equation can describe this process:

Equation 10 – Transfer of the X-ray energy to a core level electron

$$h\nu = BE + KE + \Phi_{spec}$$

where $h\nu$ is the energy of the X-ray, BE is the binding energy of the electron (how strongly it is bound to the atom or orbital it is associated with), KE is the kinetic energy of the emitted electron, and Φ_{spec} is a constant known as the

spectrometer work function. The binding energy of an electron is a characteristic of the material and does not depend on the X-ray source used to emit it. However, the kinetic energy of the emitted photoelectrons will vary depending on the X-ray source, as described by the equation above. Any electron with a binding energy less than the energy of the X-ray source should be emitted and detected in an XPS experiment.

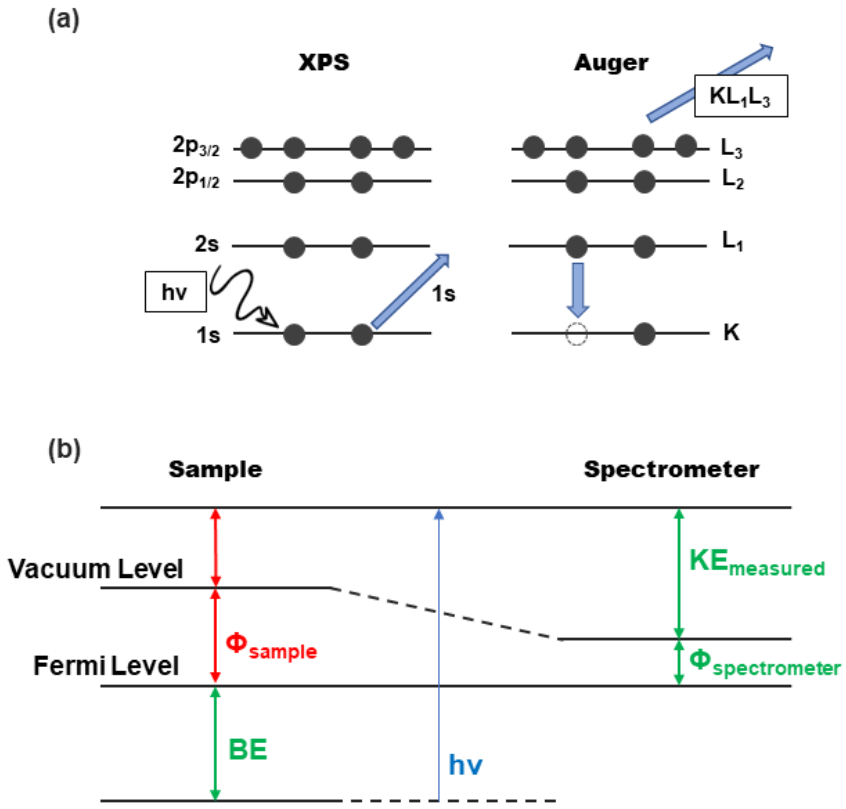


Figure 2.2 - (a) Processes that result from X-ray bombardment of a surface include emission of a photoelectron on the left and emission of an Auger electron on the right; (b) Energy level diagram illustrates the basic XPS equation (Equation 10) schematically.

When an XPS core electron is lost, it leaves behind a "hole" in the core. This excited, ionized state can relax by filling the hole with an electron from a valence orbital. This process releases energy, which can be emitted in one of two ways, X-ray fluorescence or the emission of an Auger electron (the latter is represented in Figure 2.2b). The interest is on Auger electrons, detected in the electron spectrum and often used in XPS for qualitative analysis. The kinetic energy of the Auger electron is dependent on the binding energies of specific orbitals in the atom it

originated from, which are independent of the X-ray source energy. This means that the kinetic energy of the Auger electron is also independent of the X-ray excitation energy. However, the binding energy of the Auger electrons does change when different X-ray sources are used for excitation. The fact that the binding energy of photoelectrons is constant with the X-ray source, while the binding energy of Auger electrons changes, can be useful when there is an overlap between Auger lines and photoelectron lines in the spectrum.

Technical details: A PHI 5000 Versaprobe X-ray photoelectron spectrometer (Physical Electronics, Chanhassen, MN, USA), equipped with a monochromatic Al K-alpha X-ray source (1486.6 eV), was used to check the catalyst surface chemical composition. A circular spot of 100 μm in diameter was selected to gather the photoelectron signal for both the high resolution (HR) and the survey spectra. The semi-quantitative atomic concentration and fitting procedures were acquired using CasaXPS 2.3.23 dedicated software (Casa Software Ltd., Wilmslow, UK).

2.2.2.3 Energy-dispersive X-ray spectroscopy

Energy-dispersive X-ray spectroscopy (EDS, EDX, or XEDS) is a technique used to identify the elemental makeup of a sample. It involves exposing the sample to a beam of X-rays or charged particles, which excites the electrons within the sample and causes them to emit X-rays of a characteristic energy [104]. The energy of the emitted X-rays can be measured using an energy-dispersive spectrometer, which allows the elemental composition of the sample to be determined. EDS is often used in conjunction with SEM to analyze the surface of samples. EDX can provide both qualitative and quantitative information about a sample [105].

Technical details: The atomic composition of the samples was investigated by means of Energy-dispersive X-ray spectroscopy. The instruments used were the same described in Section 2.2.1.3 for FESEM and SEM analysis.

2.2.2.4 UV-visible spectroscopy

UV-Visible spectroscopy (UV-Vis) is a technique used to study the absorption of the light by a sample. It can be used to identify, characterize, and quantify a wide range of molecular compounds, and is often used in non-destructive measurements [106]. Absorption of light occurs on a sample when the energy of the incoming light is equal to the energy difference between a

molecule's ground and excited states. This passing of an electron from the ground state to an excited state is known as an electronic transition. The absorption of light by a sample can be described by Planck's equation (Equation 11), which shows that the longer the wavelength of the absorption band, the less energy is needed to excite the electrons.

Equation 11 – Plank Equation

$$E = h\nu = {}^{hc}/_{\lambda}$$

where E is the energy required to promote an electron from the ground to excited state, h is Planck's constant, ν is the wavenumber, c is the speed of light, and λ is the wavelength. The absorption bands are indicative of the molecular structure of the sample and can shift in wavelength and intensity depending on the molecular interactions and environmental conditions. UV-vis spectroscopy can be used to measure the reflectance of a sample. Reflectance is the sum of two types of reflection: specular and diffuse. Specular reflection is light reflected at the same angle as the incident beam, while diffuse reflection is light reflected in a different direction. An integrating sphere is a device that can be used to measure reflectance. It consists of a spherical cavity with a highly reflective inner surface, usually coated with a material (such as barium sulfate). When light enters an integrating sphere, it undergoes multiple reflections until a detector detects it. The presence of a sample can change the optical path of the light, which can be problematic when trying to measure transmittance. An integrating sphere is useful in these cases because it allows the measurement of reflectance regardless of the position or size of the light beam received by the detector. Finally, it is worth to note that the Tauc relation [63,64], reported in Equation 12, was chosen to calculate the optical band gap energy:

Equation 12 – Tauc relation

$$\alpha h\nu = A\,(h\nu - E_g)^n$$

where α is the absorption coefficient (dimensionless unit), $h\nu$ is the photon energy in eV, A is a constant related to the mass of electrons and holes, E_g is the band gap energy, measured in electron Volt (eV), and the value of n depends on the type of transition (n = 1/2 for allowed direct transition and 2 for allowed indirect transition).

Technical details: A Varian Cary 5000 spectrophotometer was used in the diffuse reflectance mode with an integrating sphere to obtain UV-Vis absorption spectra of the samples.

2.2.2.5 Inductively coupled plasma

Inductively coupled plasma (ICP) is a type of plasma source that is often used in analytical chemistry for atomic spectroscopy. It is a high-temperature, electrically conductive gas that can be created by ionizing a gas using high-frequency electromagnetic fields. In an ICP system, the plasma is generated by an induction coil surrounding the plasma torch, which is a tube through which the gas flows. The high-frequency electromagnetic fields created by the induction coil cause the gas to become ionized, creating the plasma [107]. One of the main advantages of ICP is its ability to produce high-temperature plasmas (up to 10,000 K) that can atomise and ionise a wide range of elements. This makes it a useful tool for analyzing samples with a wide range of compositions. ICP is often used in combination with other techniques to analyze samples for a variety of applications (*i.e.,* environmental testing, food safety, and materials analysis).

Technical details: The molar amount of metals in the several catalysts was evaluated via inductively coupled plasma, with an iCAP 7600 DUO (Thermo Fisher Scientific).

2.2.3 PEC Properties

This Section provides a description of the electro- and photo-electrocatalytic characterization techniques carried out in this work. The following Sections will report the description of the equipment used and the setup where the tests were carried out.

2.2.3.1 Testing protocol

The chosen protocol for the tests, in order to characterize the (photo-)electrocatalytic activity of the catalysts, involved:

- cyclic voltammetry (CV),
- linear sweep voltammetry (LSV),
- chronoamperometry (CA),
- chronopotentiometry (CP).

CV provides, as a technique, an initial estimation of the voltage/current characteristics and enables the testing of catalyst stability through repetition of the voltage sweeps. Moreover it helps the assessing of the suitability of the catalyst for the CO_2RR by comparing the activity in CO_2 and in N_2 environment. The LSV curves show the behaviour of the photocurrent density as a function of the applied potential in the system. They were carried out in chopped light mode, that is toggling a lamp shutter between open/closed position at a regular time interval, and often were repeated several times during the test to check on photoactivity changes. The CA curves show the behaviour of the photocurrent density over time at a fixed potential. This measurement was implemented for to evaluate mid-term stability of the sample photoactivity, the recording was typically taken for 10 minutes, across which light shutter was toggled every minute. Finally, in CP the current density value is kept constant and the voltage between the working and reference electrode is measured. These measurements were extended for two hours, and both gaseous and liquid products were analyzed. More details about these analyses will be provided in the next Sections. Specific attention was dedicated to assessing the test protocol, especially in terms of applied potential range on the working electrode, to be as conservative as possible with species covering the electrode and to avoid undesirable and uncontrolled reduction of the photoactive species.

2.2.3.2 Electrochemical Surface Area

The electrochemical surface area (ECSA) measures the electrochemically active area, which is the total surface area accessible to the electrolyte and relies on the double-layer capacitance [108,109]. The measurement is performed in the potential region where only the electrical double-layer charging occurs, resulting in only capacitive current with no contribution from faradaic processes. This region, called the double layer region, is near the Open Circuit Voltage (OCV) and does not involve any oxidation or reduction process at the electrode-electrolyte interface. Characterizing each sample in this region is essential to determine the reproducibility of the synthesis method. The primary source of error in this procedure is the value of the reference capacitance, which can differ among materials, and it is not guaranteed that there exists a reference capacitance value for each material. However, the double-layer region, where there is no current passage through the electrode, reduces the possibility of surface state changes. Moreover, this method is non-destructive and can measure the total surface area available to the electrolyte for electrochemical reactions [110]. The current depends on the potential scan rate and increases as the scan rate increases [111].

By changing the scan rates, it is possible to collect the necessary current values to estimate the surface area. The surface area is also described as dependent on the measured current in a diffusion-controlled process. The current depends on the rate at which the analyte diffuses to the electrode [112].

The schematic setup of the tests is reported in Figure 2.3. The experimental procedure begins with determining the OCV, followed by recording voltammetric curves within a narrow potential range of OCV±0.05 V to eliminate faradaic contributions. Each scan rate (5 mV/s, 10 mV/s, 25 mV/s, 50 mV/s, 75 mV/s, 100 mV/s, 150 mV/s, and 200 mV/s) is repeated five times. The current density at the OCV potential is recorded, and the absolute value of this current density is averaged using Equation 13.

Equation 13 – Average of absolute *J* values

$$J\ (OCV)(\frac{mA}{cm^2}) = \frac{|J(OCV)_{ox}| + |J(OCV)_{red}|}{2}$$

A plot originates by reporting the average values (corresponding to each scan rate) vs. the scan rate. In the absence of capacitive contributions, this plot is linear and the slope can be used to determine the double-layer capacitance of the sample, as per Equation 14 [113]. The glassy carbon area used for the experiment is 0.1963 cm^{-2}.

Equation 14 – Double Layer Capacitance

$$DLC\ (\mu F) = slope\left(\frac{mA}{cm^2} \cdot \frac{s}{mV}\right) \cdot glassy\ carbon\ A\ (cm^2) \cdot 10^6$$

By determining the double layer capacitance per unit area of a reference electrode that has a precisely planar surface and the same composition as the sample being studied (where the value of $(DLC\ )_{ref}$ is 28 uF cm^{-2} for a Cu planar film), it becomes feasible to compute the electrochemical surface area (as per Equation 15) and consequently the surface roughness factor (as per Equation 16) [114].

Equation 15 – Electrocatalytic surface area

$$ECSA\ (cm^2) = \frac{DLC}{DLC_{ref}}$$

Equation 16 – Roughness factor

$$roughness\ factor\ = \frac{ECSA}{glassy\ carbon\ area}$$

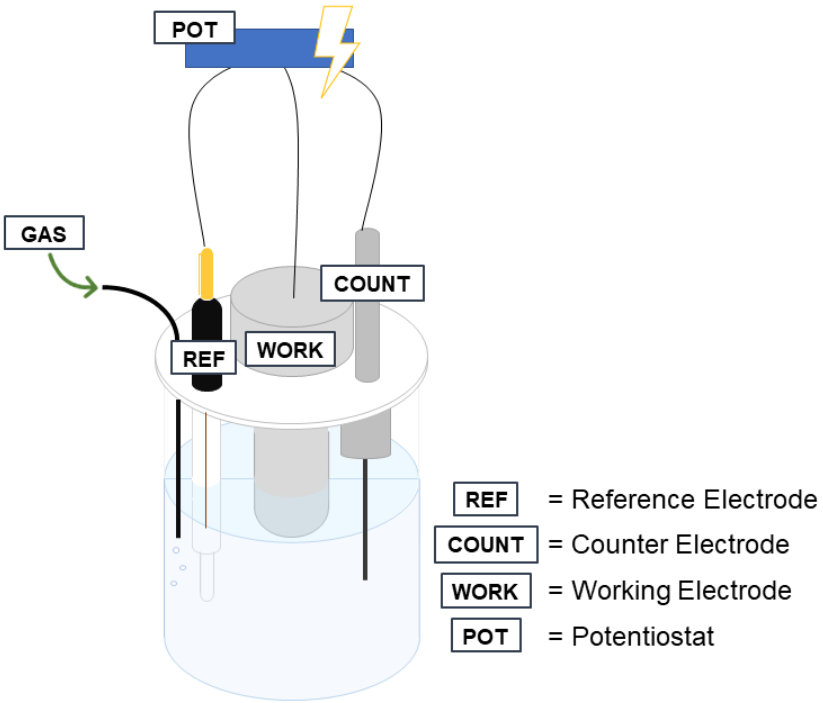


Figure 2.3 – Schematic picture of a traditional three-electrode cell for ECSA analysis in an RDE (Rotating Disk Electrode) system.

2.2.3.3 Electrochemical Impedance Spectroscopy

Electrochemical impedance spectroscopy (EIS) is a powerful analytical technique used to study the electrochemical behaviour of various systems, such as batteries, fuel cells, and corrosion processes. It measures the electrical impedance, or resistance to the flow of an alternating current, at different frequencies within the electrochemical system. In EIS, a small AC voltage of frequency f, with a small amplitude, is applied to the cell. The voltage can be represented as in Equation 17,

Equation 17 – Cell voltage

$$V_{cell}\ =\ V_0\ sin\ (2\pi f t)$$

and the current, I_{cell}, will also exhibit an oscillating behaviour with the same frequency but a different phase due to the cell impedance. It is crucial to ensure linearity, causality, and stability of the system before conducting a valid spectroscopic experiment. The impedance is generally the complex representation of the cell resistance to the flow of the alternating current. It is represented, in general, by Equation 18.

Equation 18 – General Impedance

$$Z_{cell} = \frac{V_{cell}}{I_{cell}} == Z_0(f)e^{j\phi(f)}$$

The measurements are performed using the same cell setup as traditional PEC measurements and potentiostats are well suited for three electrode systems. To obtain complex impedance values, a small sinewave signal is applied on top of a fixed DC voltage, and the frequency of the small signal is swept across many orders of magnitude while the oscillating current value is measured. The system then calculates impedance as a complex value. The key point of the technique is to interpret the data and associate an equivalent circuit to model the cell behaviour, taking into account both the physical aspect of the conduction mechanism occurring in the cell and the shape of the data. Theoretical treatment of the data is then done, and once the equivalent circuit is decided, data sets can be fitted using custom equivalent circuits. This process provides a great deal of information that can be extracted from the fitted parameters' values and trends, as each of them is closely tied to a physical quantity. By analyzing the impedance data, important information such as the corrosion rate, charge transfer resistance, and time constants can be obtained, allowing for a better understanding of the underlying electrochemical processes and the performance of the system.

To obtain a single EIS measure, a small sine signal was superimposed over a DC bias voltage and its frequency was swept from 10^6 to 10^{-1} Hz. The potentiostat (PalmSense4) applies a voltage signal and measures the current to evaluate the system impedance. The impedance data obtained from an EIS measurement can be plotted in the complex plane to form a Nyquist plot, which provides a visual representation of the electrical behaviour of the system. In an EIS Nyquist plot, the *x*-axis represents the real part of the impedance and the *y*-axis represents the imaginary part of the impedance. The presence of a semicircle in the Nyquist plot indicates the presence of a time constant in the system, which can be related to various physical phenomena, such as diffusion, charge transfer,

and resistive processes. After collecting data, an equivalent circuit is chosen to fit the data based on the physical phenomena occurring in the cell and the data shape. To understand this process it is worth to have in mind the possible cell phenomena and some examples of common electrical circuit impedance trends. The PEC cell electrical behaviour was commonly modelled as a series of components, including:

- resistance from the potentiostat circuitry,
- impedance elements related to non-ideal charge conduction inside the catalyst material,
- impedance contributions due to charge transfer at the catalyst surface,
- a circuital element to model mass transport limitations in the electrolyte solution.

Modelling a real system is challenging due to the lack of ideal capacitors. To overcome this, Constant Phase Elements (CPEs or Qs) were introduced [115]. It could describe nonuniform current distribution on electrode surfaces related to the microscopic roughness of the electrode. Today, it is used as a substitute for capacitors in electrochemical systems or as an imperfect capacitor. The impedance value of the CPE is described by Equation 19,

Equation 19 – Impedance value of CPE

$$Z_{CPE} = \frac{1}{Q(j\omega)^n}$$

where Q coincides with the admittance value Q = 1/|Z| at ω = 1rad s^{-1} , ω is the angular frequency and n is a dimensionless parameter which takes values between 0 and 1 and is referred to as the constant phase. When n tends to 1, the CPE behaviour resembles that of an ideal capacitance with Q = C. If, on the other hand, n tends to 0, CPE impedance become independent from frequency values and its phase becomes 0, meaning that it behaves exactly like a resistor. The constant phase parameter can then be interpreted to indicate the balance between capacitive and resistive behaviour of the CPE. Figure 2.4 depicts the equivalent circuit used to model the system, which is composed of resistors (R) and constant phase elements (Q). The equivalent circuit consists of three elements arranged in series: R1 represents the resistance of the electrolyte, while R2 and R3, which are parallel to CPE1 and CPE2 respectively, represent the material electrical

resistance and the resistance to electron flow from the material surface to the surface molecules.

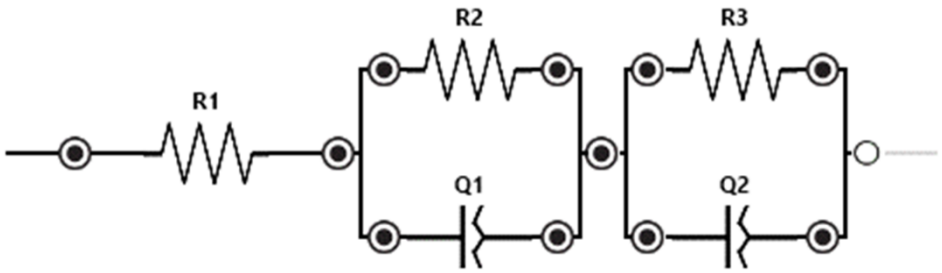


Figure 2.4 – Equivalent circuit used to model the PEC system.

ABC Chemistry "EIS Spectrum Analyser" free software was used to fit the data sets using the fragmentary analysis mode selecting the appropriate frequency range to rule out undesired effects. The chosen fitting algorithm is the Nelder-Mead method with the "amplitude" option. The equivalent circuit used to fit the data, was chosen following previous EIS analysis performed on similar systems [95,116]. These work highlighted the presence of two time-constants related to charge transport limitations inside the catalyst bulk and charge transfer phenomena at the catalyst/electrolyte interface. Mass transport limitations become influential at low frequencies (<1 Hz) while potentiostat cable impedances are prevalent at high frequencies (>10^5 Hz). Both phenomena make datasets strongly deviate from the modelling circuit and have therefore been excluded from fitting operations.

2.3 Setup of CO_2R catalytic tests

As previously described, this work focused on two approaches for the catalytic reduction of CO_2, the electrocatalytic and the photo-electrocatalytic. Below is reported a general setup for each of the experiments. If any changes were made, they will be described in the following paragraphs, along with a detailed description of the experiment itself.

2.3.1 RDE setup for EC CO_2RR

A rotating disk electrode (RDE) is a type of electrochemical cell used to study the kinetics of electrochemical reactions. It consists of a disk-shaped electrode mounted on a spindle and rotated at a constant speed. To conduct an electrochemical characterization of the samples, a conventional three-electrode

electrochemical system is utilized to test their catalytic activity at atmospheric pressure and room temperature. A glassy carbon rotating disk electrode, serving as the working electrode with an electrode area of 0.1963 cm^2, was utilized for depositing the catalysts, that was an ink. The counter electrode was a platinum wire, and the reference electrode was a silver/silver chloride electrode (Ag/AgCl, 3 M NaCl). A Biologic VSP-300 multichannel potentiostat and RRDE-3A rotator system were used to perform the electrochemical tests. The RDE system, is schematized in Figure 2.5. A solution containing the reactants is placed in the cell chamber around the electrode, and an electrical current is passed through the system. As the disk rotates, it comes in contact with the solution at different points, allowing the reaction to occur at the electrode surface. The technique is useful for studying the electrocatalysis of reactions eliminating the effects of mass transfer limitations.

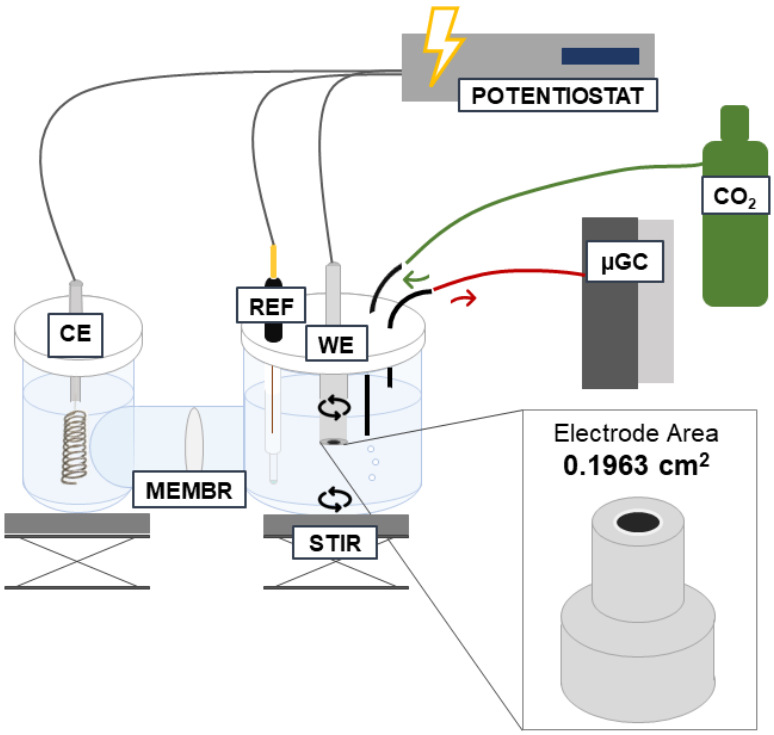


Figure 2.5 – Schematic picture of *H-type* cell in RDE setup.

2.3.2 PEC setup for CO_2RR

For the development of a photo-electrocatalytic CO_2 reduction test, an experimental set-up has been designed. A schematic image of the cell is reported

in Figure 2.6, instead, the general setup is shown in Figure 2.7. The double chamber cell (*H-type*) made in quartz is illuminated from the cathode side from the simulated AM 1.5G solar light provided by using a 450 W Xe lamp by Newport equipped with an AM 1.5 filter and a water filter model 6123NS, with a power density of 100 $mW \cdot cm^{-2}$. The cell was maintained at a fixed distance from the lamp to ensure the reproducibility of tests. Gaseous CO_2 flowed into the cell with a settled rate, and the exit from the cell was connected to a μ-GC for the online gas analysis. The experiments of photo-electrocatalytic CO_2 reduction were conducted in a three-electrodes configuration, including the prepared photocathode as the working electrode (WE), a Pt mesh counter electrode (CE) and an Ag/AgCl (3M KCl) reference electrode (RE). A multichannel potentiostat (VoltaLab PGZ 301 Dynamic Potentiostat) was used for the photo/electrochemical tests. The cell was filled with two different electrolyte solutions: 0.1M $KHCO_3$ in water as the catholyte, which was kept under stirring throughout the test, and 0.1M KOH as the anolyte. The two compartments were maintained separated by a previously activated bipolar membrane provided by Fumasep.

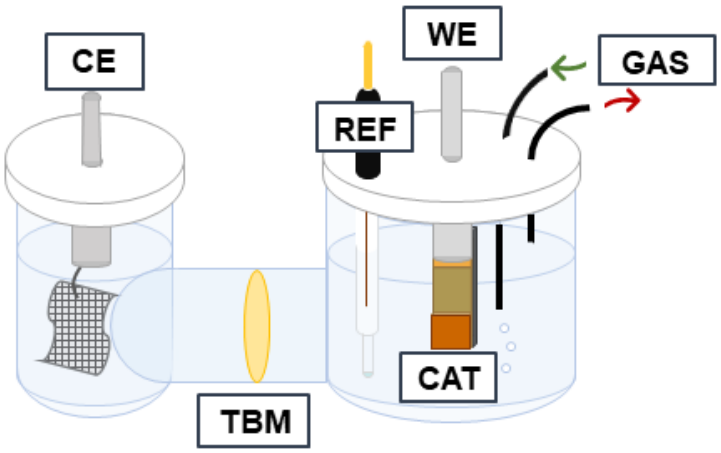


Figure 2.6 – Schematic picture of the PEC *H-type* cell.

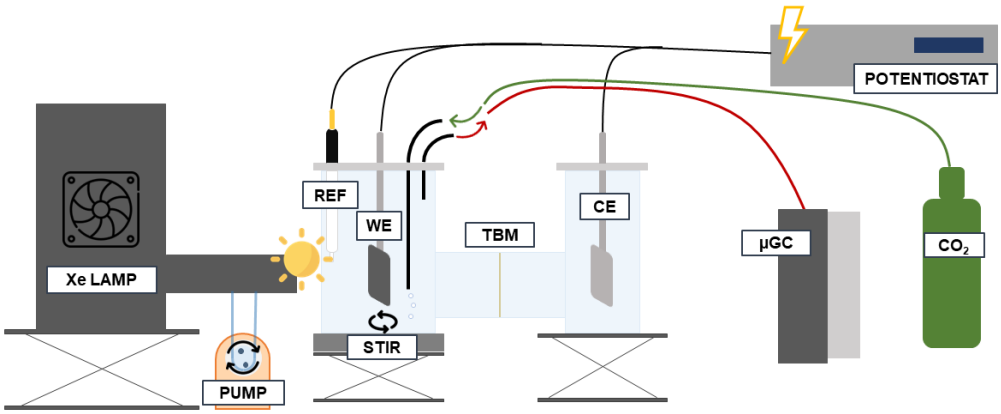


Figure 2.7 – Schematic setup for the development of photo-electrocatalytic tests.

2.4 Products analysis

During the measurements, a constant CO_2 flow rate was maintained to saturate the electrolyte and to take the gaseous products to the μGC (Varian 490 Micro GC equipped with a PPQ and Molsieve columns). Liquid products were analyzed by a high-performance liquid chromatograph (Shimadzu HPLC, Prominence model with detector RID-10A, SPD-M20A, ELSD-LT II and RF-20A by Shimadzu Europa GmbH, Duisburg, Germany) with a Photodiode-Array Detection (PDA) set at 208 nm by using a Rezex ROA (300 × 7.8 mm) column, with 5 mM H_2SO_4 (flow rate of 0.7 mL min^{-1}) as mobile phase and a Gas Chromatograph (Perkin Elmer GC, model Clarus 580) with a Mass Spectrometer (model Clarus SQ8 S) and Head Space (Turbomatrix 16) by PerkinElmer Italia Spa, Milan, Italy. The Faradaic efficiency for each product was calculated by using Equation 20:

Equation 20 – Faradaic Efficiencies

$$FE(\%) = \frac{z \cdot n \cdot F}{j \cdot A \cdot t} \cdot 100$$

where z represents the number of electrons exchanged at the cathode surface, n is the outlet molar flow rate of each product, j is the current density (mA cm^{-2}), t is the reaction time (s), F is the Faraday constant (C·mol^{-1}), and A is the active geometric area (cm^2).

Chapter 3

Bimetallic Pd-Cu based Aerogels for electrocatalytic CO_2 reduction.

Chapter 3 presents the successful synthesis and reproducibility of the PdCu catalyst for CO_2 electrochemical reduction tests in an RDE system. The catalyst was characterized by using various analytical techniques, including XRD, XPS, N_2 physisorption, TEM, and in-operando experiments. The electrocatalytic properties of the new material were investigated in a lab-scale cell developed by *Hysytech* for the SATURNO project. The CO_2 co-electrolysis was carried out at relevant reduction current densities, achieving a carbon compound selectivity of up to 40% with CO Faradaic efficiency of 38.84% and an ethanol yield of 3.41%. Potential theoretical and mechanistic explanations were identified through comparison with the literature to explain the selectivity of the reaction.

Contributions: The work presented in the following Chapter has been developed within the Italian regional SATURNO-Bioeconomy Project. Many of the analyses have been carried out in collaboration with partners from "Dipartimento di Scienza Applicata e Tecnologia" (DISAT) and "Istituto Italiano di Tecnologia" (IIT) for characterizing the prepared materials. In particular, Dr. Angelica Chiodoni and Dr. Katarzyna Bejtka supported the PhD student in the FESEM, XRD, TEM data collection and curation. XPS analysis have been carried out by Dr. Micaela Castellino, who took care of data collection and analysis. The student carried out the investigation and methodology of the synthesis of the catalysts. She also measured and analyzed the N_2 adsorption/desorption isotherms,

the data analysis, and the *H-type* cell electrocatalytic CO_2 reduction tests. The design and creation of the scaled-up cell have been performed by the partner *Hysytech.* The electrocatalytic CO_2 reduction test in this latter cell has been carried out by Dr. Hilmar Guzmán, in collaboration with Federica Zammillo.

3.1 Chemistry of aerogels and xerogels

According to a general definition, aerogels are materials in which the typical structure of the pores and the network is largely maintained while the liquid present into the porous structure is replaced by air [117]. This class of materials presents unique properties that are summarised in the following list [118]:

- Coherence,
- High porosity,
- Solidity,
- Very low mass density,
- Large inner surface area,
- Ability to self-organize forming monoliths.

The properties of a porous solid and its reactivity are strongly dependent on the kind, shape, and size of the pores. Some of the exclusive properties of aerogels arise from the peculiar arrangement of their solid network [119]. It is typically possible to detect branched mesopores, cylindrical and well-accessible structures for the aerogels. Aerogels present density values between 0.004 - 0.500 g cm^{-3}because of their high porosity (as a comparison, the density of air is 0.00129 g cm^{-3}) [117]. Their main ability is to combine chemical and physical properties of nanomaterials with those of the macroscale ones. Moreover, one of the most significant potentials is integrating the different constituents' specific properties in one resulting material. That makes aerogels hugely attractive in several applications, such as catalysis, thermistors, piezoelectric detectors, and sensors. A pioneer of the research in this field was Kistler in 1931 [120], studying silica and alike ones, even if their practical application was not completely explored until 1974 when Cantin *et al*. [121] reported on the use of silica aerogels as detectors in Cerenkov radiation. From that moment on, research about aerogels considerably expanded to create many classes of compounds dealing with inorganic, organic-inorganic hybrid, organic and carbon-based aerogels [117,122–124]. The most investigated materials that form fine aerogel superstructures are silica and other metal oxides with their mixtures. Together with the carbon aerogels doped with

noble metals, these have long been created by impregnation or sol-gel method [125]. Instead, the fabrication of pure metallic aerogels with metal support by the direct sol-gel method was more recently performed [126,127].

3.1.1 Synthesis via sol-gel process

To clarify the concept, solid particles suspended in a liquid with a very small, dispersed phase (1-1000 nm) are called sol. For them, gravitational forces are negligible, and interactions are dominated by short-range forces such as Van der Waals attraction and surface charges. There are two methods for preparing a sol: condensation and dispersion of particles. In the condensation, the nucleation growth of the particle up to their appropriate size occurs, while dispersion proceeds via the reduction of lager particles down to the proper colloidal dimensions. Even if the properties of the final particles depend on the rates of these processes, the formation of the sol is enhanced when the nucleation rate is higher and the crystal growth rate is lower. The control of the reaction for the formation of the sols is a crucial point. The resulting product is stable in terms of agglomeration and precipitation, only if several parameters, such as the polarity of the solvent, the strength of the reaction medium, and the temperature, are properly set. The gel is a semisolid very rich in liquid, which avoids the collapsing of the overall solid network [128]. Typically, it is possible to recognize three different steps for the preparation of aerogels:

i. the sol-gel transition (gelation)
ii. the network perfection (ageing)
iii. the transition from gel to aerogel (drying)

Usually, the process starts when the proper precursors needed for the aerogel fabrication are chosen and dispersed in a liquid (colloidal dispersion) until they form a continuous network of solid particles throughout the liquid, creating the gel [129]. In general, a gel is a three-dimensional solid network presenting pores filled with an extra substance, which is often a liquid, mainly water or alcohol. Hence, the resulting wet gels formed are called aquagels/hydrogels or alcogels. During the reaction, the transition from a colloidal solution (liquid) into a bi- or multiphase gel (solid) occurs, leading to the expression “sol-gel process”. During the gelation process, the free-flowing sol is transformed into a solid three-dimensional (3D) network, including the solvent. The exact point for the gelation is found when the viscosity presents a rapid rise and an elastic response to the stress. Typically, the gelation is more conveniently forced via a sudden change of

the pH of the solution, especially for the aerogel formation. The schematic diagram of the synthesis is shown in Figure 3.1. The dependence of the process with a high variety of parameters is underlined in the figure, such as the chemical composition of the precursors, their concentration and one of the additives, the temperature, and the pH [129–131].

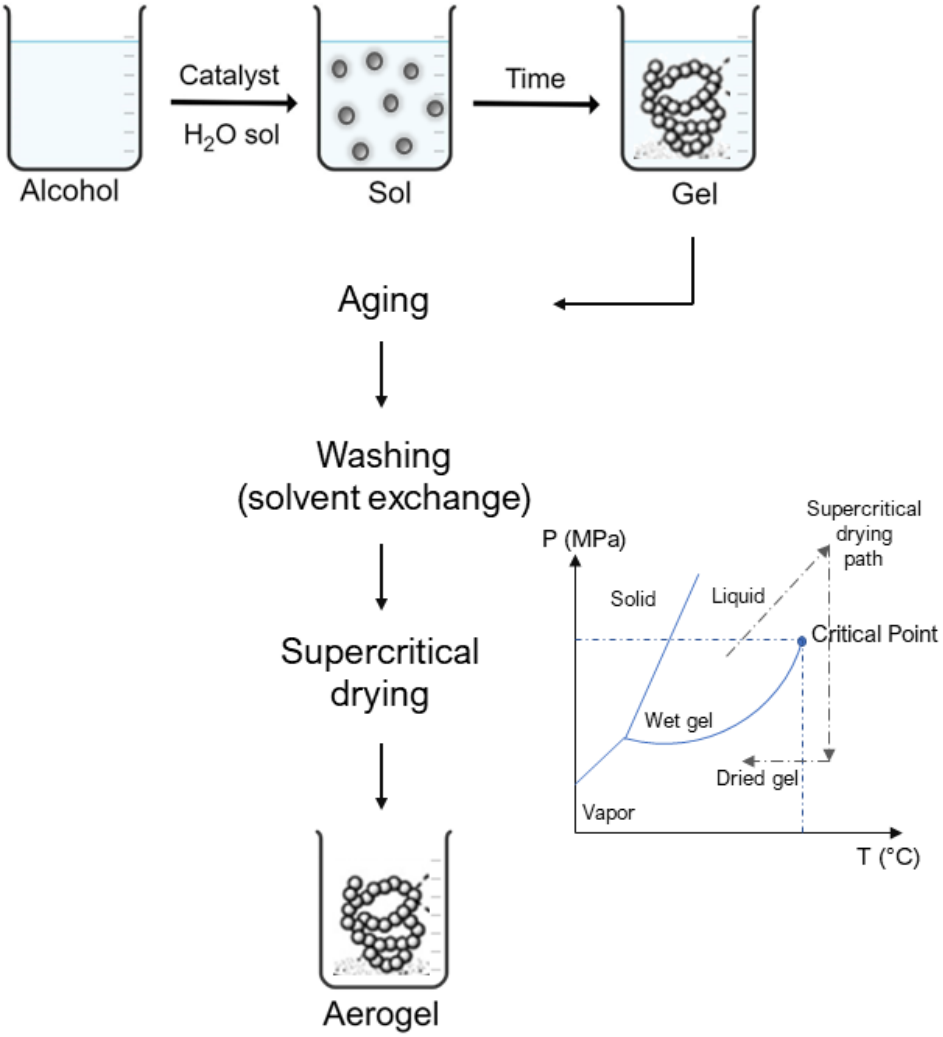


Figure 3.1 – Schematic representation of typical sol-gel synthesis procedure.

The sedimentation rates (Equation 21) could be calculated in order to evaluate better the formation of a uniform suspension of colloidal particles. Moreover, by assuming the sphericity of the particles, Stokes' law can be used, considering that η = viscosity of surrounding medium, r = radius of colloid particles, ρ' = density of the colloid particle, ρ = density of surrounding material.

Equation 21 – Sedimentation rate

$$dx/dt = [(4\pi r^3/3)(\rho' - \rho)g]/6\pi r\eta = [2r^2(\rho' - \rho)g]/9\eta$$

The gravitational force (g) can be considered negligible, and the interactions are prevailed by short-range ones, such as Van der Waals attraction and dipole driven. Moreover, the dispersed phase presents a very small inertia, enough to follow Brownian motion, which means a random walk throughout the other molecules of the suspended medium and chaotic collisions that transmit the momentum. Depending on the material, the transition from a colloidal dispersion to a gel could be carried out with or without a crosslinker. In general, crosslinking materials can enhance the interaction between the solid particles and promote gel formation [132]. Consequentially, the higher the degree of cross-linker added, the more rigid the gel structure, because of the great influence of crosslinkers on the mechanical conformation of the gel. Additional hardening could be requested after the gelation phase, such as network perfection, aiming to strengthen the aerogel network [133]. Ageing a gel before drying helps strengthen the network and thereby reduce the fracture risk [134]. After the gelation, the drying of the gel happens in order to minimize the surface tension within the pores of the solid network [129].

3.1.2 Drying methods

The last step of production for aerogels is drying. It consists of removing the liquid (mainly water or alcohol) from the pores of the structure. The process of drying a porous material can be divided into several stages. This last phase is the most critical in the aerogel synthesis process. At first, the body shrinks by an amount equal to the volume of liquid that evaporates, and the liquid-vapour interface remains at the exterior surface of the body. The second stage begins when the body becomes too stiff to shrink, and the liquid recedes into the interior, leaving air-filled pores near the surface. Even as air invades the pores, a continuous liquid film supports flow to the exterior, so evaporation continues to occur from the surface of the body. Different approaches can be used to dry the gels. The resulting materials are named differently, depending on the strategy chosen for the drying.

3.1.2.1 Supercritical drying

Since capillary forces produce shrinkage and cracking, Kistler and co-workers [120] thought that those problems could be avoided by removing the liquid from

the pores above the critical temperature (T_c) and critical pressure (P_c) of the liquid itself. The technique replaces the liquid with gas to isolate the solid component from the material without destroying the delicate nanostructured pore network. From the phase diagram, there is no longer any distinction between the liquid and vapour phases. The density becomes equal and there are no liquid-vapour interfaces and capillary pressure. Then, once the critical point is passed, the solvent is vented at a constant temperature (>T_c). Table 3.1 contains values of T_c and P_c for some relevant liquids. It is generally preferable that, instead of using flammable, explosive solvents, a safer, non-flammable solvent should be chosen, such as carbon dioxide. In this process (called supercritical CO_2, $scCO_2$), the solvent in a gel is replaced with liquid carbon dioxide by soaking. To achieve this, the organic solvent in the gel must be soluble in $scCO_2$. The liquid carbon dioxide can supercritically work at a much lower temperature (31.1° C) than an organic solvent without the risk of combustion. As a drawback, certain aerogels cannot be made with liquid carbon dioxide, such as certain metal oxides, because they react with carbon dioxide to form metal carbonates. Generally, aerogels made using supercritical drying from carbon dioxide may shrink up to 5%.

Table 3.1 – Critical points of selected solvents*

Substance	Formula	T_c (°C)	P_c (MPa)
Carbon Dioxide	CO_2	31.1	7.36
Freon 116	CF_3CF_3	19.7	2.97
Methanol	CH_3OH	240	7.93
Ethanol	C_2H_5OH	243	6.36
Water	H_2O	374	22.0

* Data collected by Tewari, Hunt and Lofftus, ref. [135]

3.1.2.2 Evaporative drying

Through this technique, the solvent that is entrapped in the gel is evaporated. The two possible approaches are ambient pressure drying (APD) or vacuum drying (VD). The treatment leads to the formation of a xerogel. The drying happens by increasing the temperature or decreasing the pressure, with a

consequent large shrinkage (and mostly destruction) of the initially uniform gel body and the collapse of the filigree. This phenomenon is due to capillary forces acting on the pore walls as the liquid retreats into the gel body.

3.1.2.3 Freeze-drying

Another way to avoid the presence of the liquid-vapour interface is to freeze the pore liquid and sublime the resulting solid under a vacuum to force it to abandon the structure. Again, the pore liquid is replaced by air without decisively altering the network structure or the volume of the gel body, even if the structure suffers changes as the growth of solvent crystals (most commonly water) leads to the fragmentation of the samples. This technique does not permit the preparation of monolithic gels because the growing crystals reject the gel network pushing it out of the way until it is stretched to the breaking point. Attempts to freeze-dry typically result in flakes or translucent bodies with large pores. The resulting material is called cryogel. Recently, following a communication written by Vareda and co-workers [136], researchers have begun to classify these materials less strictly. In fact, they reported that materials with aerogel-like properties could be currently obtained with drying approaches other than supercritical. Taking this into consideration, it should be possible to overcome the forcing definition for which aerogels are exclusively obtained via supercritical drying or have very narrowed intervals of some specific properties and to agree with Kistler's original definition: "an aerogel withstands the drying without significant changes in the gel's structure" [120].

3.2 Noble metal-based aerogels and xerogels

This chapter focuses on inorganic aerogel and xerogel, particularly those based on noble metals. Noble metal aerogels (NMAs) are a 3D cross-linked network nanostructures with ultralow density, large specific surface areas (SSAs), and abundant interconnected pores [137]. Because of the strong chemical stability and enhanced catalytic activity, noble-metal based nanomaterials have spread a huge interest in different fields, including heterogeneous catalysis and electrocatalysis, plasmonics and biological research [138,139]. They achieved a unanimous interest due to the process through which they are built and for the resulting properties toward future extension in the potential range of applications. In fact, since the 2000s, several efforts have been devoted to modifying already known oxide-based aerogels synthesis procedure with metallic nanoparticles (for example Pd) [140], to carry the catalytic properties of metals into the beneficial

porous structure of aerogels. Other kinds of mesoporous assemblies of active metal nanoparticles have been created by exploiting artificial opals or fungi as templates [140] or by interlinking gold nanoparticles with dithiols [141], and lipid nanospheres to palladium to create a superstructural hybrid nanomaterial made as necklace nanochains [142]. Finally, the formation of "supraspheres", that can be considered generically like aggregates, about hundreds of nanometers in size, in which nanoparticles of one or two different metals have been cross-linked with dithiols, was reported in 2007 [143]. Since then, a big breakthrough in the synthesis of NMAs was reported by Bigall and co-workers [126]. The metallic aerogel they presented first exhibited an average density two orders of magnitude lower than previously developed foams [144]. Another outstanding material property lies in the size range of single nanoparticles, reported as an order of magnitude smaller (5-20 nm) than the "supraspheres" formerly synthesized. The production of such noble-metal nanoparticle-based monometallic and bimetallic aerogels was a noteworthy step for self-supported monoliths characterized by huge catalytically active surfaces. In fact, no chemical cross-linkers have been used for their self- assembly process, making this latter one of the most important aspects of Bigall's work. For the first time, they obtained self-supported monoliths with the enormously high catalytically active surface. From then on, self-assembled porous nanostructures have been increasingly studied for their attractive properties. Their ability to assemble the individual building blocks into 3D structures is low cost and very facile, resulting in the creation of complex and multifunctional nanomaterials [145]. No need for a template is crucial to revealing the properties of the materials. Starting from the metal precursors only, collective, and extraordinary physicochemical properties could be developed during the self-assembled process due to the coupling effects. This grants NMAs performances are superior to the separated building blocks [146]. Thus, various highly porous and nanostructured NMAs have been realized, thanks to the well-established sol-gel synthesis method and the tunable composition and morphology of the resulting materials. Considering their huge advantages, such as the presence of more exposed and accessible active sites together with their high porosity, which promotes mass and electron transfers, and the capability of avoiding corrosion issues due to the absence of macroscopic support, exceptional efforts are being reasonably made to develop new strategies for their synthesis.

3.2.1 Synthesis strategies

An effective route for the synthesis is a key point in the development of NMAs. The sol-gel method is the more suitable for the preparation, exploiting the mild reaction environment. Among all the phases that constitute it, the pivotal one is the formation of the hydrogel, which can determine the 3D network structure and, consequently, the properties of the resultant aerogel. The distinction between the two main methods of synthesis depends on whether, for the nanoparticles (NPs), a separated colloidal solution is required or not [147].

3.2.1.1 Two-Step method

The pioneering work by Bigall and co-authors [126] first opened the door for fabricating NMAs following this procedure. This method is mainly made of three steps NPs synthesis, purification, and concentration and finally, gelation. To summarize, the nanoparticles are synthesized in a prior step and only in a subsequent one the hydrogel is assembled. The as-prepared dilute NP solution is concentrated by ultracentrifugation in order to grow (up to 10 mM) its concentration. Then, a destabilization due to the addition of hydrogen peroxide (H_2O_2) or ethanol (C_2H_5OH) led to the hydrogel being formed in 1-4 weeks. In this way, the gels structured from NP-fuse branched nanowires are accomplished, although the process is lame in several respects: (1) expensive both economically and from the timing point of view, (2) monotonous ligaments sizes and microstructure, and (3) unclear gelation mechanisms. Anyway, to remove a limit to that wide application possibilities, various novel destabilization methods have been developed, like, for example, changing the synthesis parameters (temperature and disturbance) [148] or adding extra initiators (*e.g.*, salts and dopamine, among others) [149,150] and phase boundary gelation. For example, Wen *et al*. decreased the gelation time for Pd hydrogels to less than 5 min by crosslinking concentrated citrate-capped Pd NPs (>16 mM) with Ca^{2+}, which is 2–4 orders of magnitude faster than that of previous works. In short, the two-step method allows for better control over the formation of colloidal solutions and the destabilization process, making it easier to understand the mechanisms involved in the gel formation. However, this method is time-consuming and cumbersome, limiting its use in the field of NMAs. Additionally, some ligands may remain in the final NMAs and cannot be completely removed, which may affect their activity.

3.2.1.2 One-Step method

The one-step integrates NPs preparation and gel formation, which is more convenient than the previous one in terms of time and resources. The hydrogels are automatically generated through in situ reduction of noble metal salts with no addition of external stabilizers. A first attempt with this method was reported by Liu and co-workers [151] when they prepared α-, β-, or γ-cyclodextrin-modified Pd aerogels (Pd_{CD}) spontaneously, maintaining the room temperature (25 °C) and adding $NaBH_4$ as the reductant agent. Proper care was due to designing the feeding amount of the reductant, allowing the gelation to go directly from the salt solution to the final hydrogel. To solve this, Zhu group experienced the in situ reaction kinetically controlled by synthesizing M-Cu (M = Pd, Pt, Au) hydrogels within 6 hours, exploiting the enhancement of temperature [152]. An unconventional work reported by Ran and co-authors described a method for increasingly accelerating the gelling kinetics [148]. They carried out the appliance of an external force that was the stirring of the solution, and consequently, a series of monolithic gels were generated within only 10 minutes. This process relied on the self-healing ability of gel pieces in a one-step gelation route using $NaBH_4$. To conclude, the one-step method considerably simplifies the process of making a hydrogel in less time, even employing low-concentration solutions. Still, it also makes it difficult to understand the mechanisms involved and limits the ability to design the materials for specific purposes. The coupled process of nanoparticle creation and gel formation also makes it harder to control the reaction kinetics, especially when using high temperatures or concentrations, which brings out difficulties in finely engineering the microstructure for specific applications.

3.2.2 Gelation mechanism investigation

The NPs gelation process is complex and not fully understood. Although the sol-gel process has been studied extensively in many different materials, the gelation behaviour of noble metals is anomalous and complex. More research is needed to investigate the sol-gel process in NMAs systems. One notable aspect of this process is forming a thin gel film at the bottom of the container rather than a large gel of the same volume as the initial solution, resulting in a clear, colourless supernatant above the gel film. A thorough understanding of the gelation mechanisms is essential for synthesising NMAs. In general, gelation is a process in which individual building blocks self-assemble into a 3D porous gel. Many factors and processes are involved in this behaviour. In general, the gelation of noble metals is thought to involve the following stages: (1) formation of

individual nanoparticles, (2) formation of unfused aggregates, (3) formation of fused aggregates, and (4) formation of the final gel. The gel formation can be observed using real-time TEM and is assumed to involve an oriented-attachment mechanism [153]. The intense dipolar interaction between the building blocks leads to their attachment to the ends of other building blocks. The gelation process is regulated by thermodynamic laws, with the formation of covalent or noncovalent bonds resulting in a decrease in enthalpy, which speeds up the assembly process. However, this also leads to decreased degrees of freedom in the reaction system, which slows down the self-assembly process due to the reduced entropy change [137]. The change in Gibbs-free energy depends on the enthalpy and entropy effects. When the enthalpy effect is stronger than the entropy effect, the change in Gibbs-free energy is negative and leads to the formation of a branched network [154]. That indicates the formation of the network is thermodynamically favourable. In contrast to self-supported precipitates, the non-self-supported ones lack the attraction force needed to hold them together at larger scales. It becomes demanding to scale up them further, although displaying a monolithic feature at a smaller scale (*e.g.*, ≤ 0.1 mm). It is necessary to analyze the overall process and the molecular-level interactions involved to understand the gelation process. Theoretical calculations can also provide valuable insight into the underlying mechanisms. Therefore, a comprehensive study of the gelation process should involve a combination of experimental and theoretical approaches. Gelation kinetics, or the rate at which gelation occurs, can also be studied exploiting the dynamics principles. In fact, an increase in temperature or the creation of a disturbance in the environment can accelerate gelation. This is because both perturbations can promote Brownian motion, which is able to overcome the repulsive forces between the building blocks that make up the gel. The result is an enhancement in the diffusion rate and the formation of well-defined gel nanostructures. Vigorous disturbance can also alleviate diffusion barriers and enhance mass transfer and reaction speed. Zhu and his group described that boosting Cu concentration in a synthesis can expedite the gelation kinetics [152]. Such results enlighten that Cu atoms may play a crucial role such as a structure-directing. In the two-step method, the transition from building blocks to unfused aggregates is critical. This process, known as controlled destabilization, is driven by a driving force. Colloidal solutions are typically stabilized by ligands, which exert a weak interaction with building blocks. According to the DLVO theory, the stability of charged colloidal solution nanoparticles is primarily determined by van der Waals interaction, electrostatic repulsion, dipolar interaction, and charge-dipole interaction. The goal of the

assembly process is to remove surface ligands partially or completely. Then, mature destabilizing approaches can be classified into phase-separation gelation and phase-boundary gelation [155].

3.2.2.1 Phase-Separation Gelation Route

Phase-separation gelation, which results in the formation of a monolithic gel at the bottom of the container and a clear solution at the top, is typically preferred for synthesising gels with macroscopic dimensions and enhanced mechanical stability. It has been shown that temperature can be an effective method for dissociating or decomposing parts of the ligands, leading to a "metastable state". Additionally, oxidants such as H_2O_2 and $C(NO_2)_4$ can be used to etch the surface ligands, inducing fusion of the ligand-free nanoparticles [156]. The addition of certain solvents and electrolytes, such as C_2H_5OH and NaCl, has been observed to induce the assembly process effectively. That is accomplished by reducing the solubility of the building blocks and screening electrostatic repulsion through increasing ionic strength [157].

3.2.2.2 Phase-Boundary Gelation Route

A phase-boundary gelation route can create a large monolithic hydrogel from a colloidal solution. This process involves gelation occurring at the boundary between two phases. This method offers several advantages over other gelation methods, including creating gels with a wide range of sizes and shapes. Additionally, phase-boundary gelation allows for precise control over the gelation process, which can benefit applications requiring specific gel properties. For example, Fan and co-workers [158] fabricated Au hydrogels by a ligand-exchange process exploiting the proper polarity of the solvent. In preparing oleylamine (OAm) capped Au NPs, the NPs were initially synthesized in hexane and then transformed into a mixed polarity solvent containing water and N-methylformamide. The transformation was facilitated by the addition of $(NH_4)S_2$, which replaced the OAm ligands on the surface of the NPs due to their strong nucleophilic affinity. However, the shorter S^{2-} molecules could not completely cover the surface of the Au NPs, resulting in partially exposed surfaces with a specific orientation. This exposure led to reduced electrostatic repulsion between NPs in the mixed solution and increased surface energy on the exposed NPs, resulting in the anisotropic assembly of the NPs into nanowires. Additionally, using a freeze-thaw method allowed for the local concentration of solutes to increase sharply upon freezing, leading to the formation of small aggregates around adjacent ice crystals through the activation of the salt-outing effect [159].

The decreased reaction kinetics at low temperatures can be overcome by the van der Waals attractive interaction between the raised concentration of nanoparticles, allowing for the kinetically unfavourable gelation process to take place.

3.2.3 Characterization studies

The morphological characteristics of noble metal aerogels are usually studied using TEM and SEM. Three-dimensional network-like structures with extended nanochains characterize them interconnected with each other, and many open pores and tunnels. The appearance of the nanochains depends on the nature of the noble metal nanoparticles and could take the form of fused nanowire-like structures or necklace-like chains. The structure and elemental distribution of aerogels can be studied using techniques such as high-resolution transmission electron microscopy (HRTEM), XRD, and high-angle annular dark-field scanning transmission electron microscopy combined with energy-dispersive X-ray spectrometry (HAADF-STEM-EDX). Noble metal aerogels typically have a face-centred-cubic (fcc) polycrystalline structure. For bimetallic aerogels, it is important to understand the state of alloying, as it can affect the material's physical properties, chemical reactivity, and catalytic activity. In the case of bimetallic aerogels made using the method of two-step gelation, the initial gel structure consists of separate metal nanoparticles. That raises the question of whether interdiffusion and alloying occur under the given conditions or if the metals remain in separate phases within the structure. HRTEM and XRD can be used to confirm the alloying state of bimetallic aerogels made from metals with significantly different lattice parameters. For example, a Pt-Ag aerogel made by Bigall and colleagues [126], which evolved from preformed Pt and Ag NPs, showed the morphology of the as-synthesized nanocrystals without any further alloying or growth of secondary particles. The porosity and surface area of aerogels can be determined using nitrogen physisorption measurements. The isotherms for nitrogen adsorption and desorption of noble metal aerogels typically exhibit a combination of IUPAC type-II and type-IV characteristics. The surface areas of the aerogels are calculated using the BET method and are typically in the range of 32-168 $m^2\ g_{aerogel}^{-1}$. That is significantly higher than the surface areas of porous noble metals prepared using other methods, as reported in the literature (see Table S1 in the Supporting Information of Liu *et al*. [127]). The pore size distributions and cumulative pore volumes can be calculated from the desorption branch of the isotherms using the Barrett-Joyner-Halenda (BJH) theory or density functional theory, depending on the carbon content. The results and SEM and

TEM characterizations show that the aerogels have a wide range of pore sizes, from micropores to mesopores and macropores, with most of the pore volume coming from macropores. This hierarchical pore system is beneficial for minimizing diffusion barriers in sensor and catalytic applications. The diffusion rates through pores with diameters of 10-50 nm are similar to those of molecules in open media [160].

3.2.4 Applications

NMAs are known for their interconnected open nanostructures and unique physicochemical properties. These characteristics make them useful for various applications, including electrocatalysis, biosensors, and self-propulsion devices. These materials possess several advantageous characteristics that make them well-suited for these applications. Firstly, their hierarchical porous structures give them a very high specific surface area and allow for efficient mass transport through the pores, reducing diffusional resistance and providing easy access to active sites [161]. These features enhance the catalytic activity of the materials. Secondly, the aerogel networks are mostly composed of interconnected nanochains that are several nanometers in size, which is optimal for electrocatalytic processes such as oxygen reduction (ORR) [162]. Finally, the interconnected nanochains in these networks are mostly fused-nanowire-like structures with extended surfaces, which are expected to be highly durable during (electro)catalysis [163]. Additionally, the self-supporting nature of aerogels may prevent the durability issues commonly seen in conventional noble metal catalysts supported on carbon due to corrosion. Furthermore, the precise control over the molar ratio of the constituent elements in multimetallic aerogels allows for optimising factors such as composition, reactivity, durability, and cost. That enables the full exploitation of synergistic effects to enhance catalytic activity. Many noble metal foams (NMFs) applications, particularly NMAs, are focused on electrocatalysis, with a limited study of other important processes such as oxygen reduction, oxygen evolution, carbon dioxide reduction, and nitrogen reduction reactions.

3.3 State of the art on Pd and Cu based aerogels

Palladium and copper are both important metals that have been widely studied for their use in various electrochemical reactions, including the reduction of CO_2. These metals have unique electrocatalytic properties that make them suitable for use in various applications, including the production of fuels and chemicals. The aerogel form of these metals has gained significant attention in recent years

because of their high surface area and excellent thermal and electrical conductivity. Pd and Cu-based aerogels are effective catalysts for various reactions, including CO_2 reduction.

There are several approaches to CO_2 electrocatalytic reduction, using different electrocatalysts to facilitate the reduction reaction. Some common examples of electrocatalysts used in CO_2 reduction include metals such as copper, iron, and zinc, metal oxides and other inorganic materials. Nanostructured metal catalysts have been extensively studied for their potential in the electrocatalytic reduction of carbon dioxide. These catalysts' size, shape, and morphology have been shown to influence their performance in CO_2RR [165] significantly. However, new electrodes need to be developed to meet the criteria for practical applications in CO_2RR. Using Pd- and Cu-based aerogels in electrocatalysis has several advantages over traditional catalysts. Copper is an electrochemical catalyst widely studied for its ability to reduce CO_2 to a range of hydrocarbons, acids, and alcohols [41,164]. Nevertheless, Cu electrodes for CO_2 reduction have some limitations, including high overpotential, broad product distribution, and competition with hydrogen evolution. Researchers have attempted to address these issues by developing Cu complexes, nanoscale Cu, oxide-derived Cu, and alloys, in order to improve selectivity and current density for CO_2 reduction to specific products. In contrast, Palladium-based systems have low overpotential for CO_2 reduction but typically yield CO or HCOOH as major products, with low efficiency for producing alcohols. Recent developments in aerogel materials for electrocatalytic reduction of CO_2 have been demonstrated to yield promising results. The following paragraph aims to present the most effective materials and place our research within the current landscape of ongoing investigations.

Several works deal with Pd-based materials for their unique abovementioned properties. By taking advantage of the nanostructure engineering and new chemical reduction reaction, a novel, simple, eco-friendly, and surfactant-free procedure for fabricating self-assembled Pd aerogel was presented in the work of Hajnajafi and co-workers [165] using the spontaneous one-step gelation process for synthesis. In contrast with other methods, the advantages included being eco-friendly, simple, and having rapid synthesis. A palladium alcogel was prepared by reducing H_2PdCl_4 in ethanol utilizing C_2H_5OH/NaOH as a green reductant agent in a short time for the first time, and in the following step, the palladium aerogel was obtained by supercritical drying. An extraordinary 3D nanonetwork of the Pd aerogel with large porosity was then confirmed using several investigation methods. Due to the profuse open interconnected pores and large inner surface

areas, the Pd aerogel showed highly boosted electrocatalytic activity toward the ethanol oxidation reaction and depicted much higher stability, durability, and mass activity in alkaline electrolyte than Pd/C. In a separate study by Abdinejad and co-workers [166], Sn-Pd bimetallic aerogels supported by carbon nanotubes were found to selectively electro-reduce CO_2 to formate under ambient conditions. The introduction of amino substituents as an additional CO_2 capture site (Sn-Pd/CNT-NH_2) further enhanced the electrocatalytic activity, resulting in a current density of –39 mA cm^{-2} and 91% selectivity for formate at a potential of –0.4 V versus RHE. Moving from Pd to Cu-based materials, in 2021, Wang and co-workers [167] synthesized an Ag-Cu bimetallic aerogel by co-reducing Ag^+ and Cu^{2+} precursors and freeze-drying the resulting material. The optimal composition, obtained by controlling the equal molar ratio of Ag to Cu, was found to be $Ag_{88}Cu_{12}$. It demonstrated improved electrochemical stability, lower overpotential, higher selectivity, and current density compared to pure Ag aerogel. At a potential of –0.89 V versus RHE, the Faraday efficiency reached 89.40% and the CO partial current density was –5.86 mA cm^{-2}. The unique properties of the metal aerogel, including its hydrophobic nature, hierarchical porous structure, and conductivity, as well as the presence of rich grain boundaries and the introduction of Cu, contributed to the enhanced performance of the $Ag_{88}Cu_{12}$ aerogel. Another use of copper, here not combined with noble metals, concerns a material based on Bi. In this study, different bimetallic Cu_xBi aerogel electrocatalysts with adjustable compositions were designed, which showed tunable selectivity for CO_2 reduction. The maximum Faradaic efficiency for CO and formate over $Cu_{100}Bi$ and Cu_5Bi was 1.2 and 5.5 times higher than that of the pure Cu catalyst [168]. Analysis using X-ray photoelectron spectroscopy revealed that by varying the content of Bi in the catalysts, changes in the Cu(II)/Cu(I) ratios on the surface occur, which in turn regulated the hydrogenation capability of the reaction intermediates during CO_2 reduction. Finally, in a recent work [169], researchers developed a novel Pd_3Cu aerogel electrocatalyst through a mild reduction process using self-assembly and freeze-drying techniques. The resulting catalyst has a unique three-dimensional, “pearl-like” aerogel structure and exhibits exceptional performance due to its optimized chemical composition and structural features. Interestingly, Wu *et al*. utilized the same synthesis technique and selected the same metal catalysts as in this work, but for a different purpose - the search for an ORR catalyst. Finally, it is important to mention the work of Lu and co-workers [170] about a Pd-Cu bimetallic aerogel used to selectively transform CO_2 to methanol via electrocatalytic reduction, obtaining a faradaic efficiency of around 80% at a very low overpotential.

3.4 Pd-Cu xerogel synthesis methods

3.4.1 Reagents

$PdCl_2$ (purity > 99.9%), $CuCl_2$ (purity > 99.5%), Sodium tetrahydridoborate ($NaBH_4$ granular, > 98%), Nafion perfluorinated resin solution (5 wt.% in lower aliphatic alcohols and water contains 15-20% water), Isopropanol HPLC grade ($(CH_3)_2CHOH$, 99%) were purchased from Sigma-Aldrich. H_2PdCl_4 was prepared by dissolving $PdCl_2$ (44.5 mg) in HCl (20 mM, 25 ml) solution.

3.4.2 Synthesis procedure

The scheme of the reaction is shown in Figure 3.2a. To synthesize PdCu hydrogel, 35 mL of a solution containing 0.125 M H_2PdCl_4, and 41.6 mM $CuCl_2$ were mixed and stirred at 60 °C. Then, 2 mL of a 0.2 M $NaBH_4$ solution was added, causing the mixture to turn from light yellow to black. The resulting solution was stirred for one minute and allowed to sit at 60 °C for an additional six hours, forming a black PdCu hydrogel at the bottom of the flask (Figure 3.2b). The ratio of Pd to Cu in the hydrogel was adjusted by altering the ratio of H_2PdCl_4 and $CuCl_2$ used in the synthesis. In this work, a molar ratio between Pd and Cu of 3:1 was chosen. In particular, the significant increase in the concentration of the reactants, with respect to the conditions reported in the literature [170], and the possibility of working with multiple reaction vessels in parallel (Figure 3.2c) led to the production of a sufficient sample quantity to proceed with the drying phase, followed by characterizations and electrocatalytic testing.

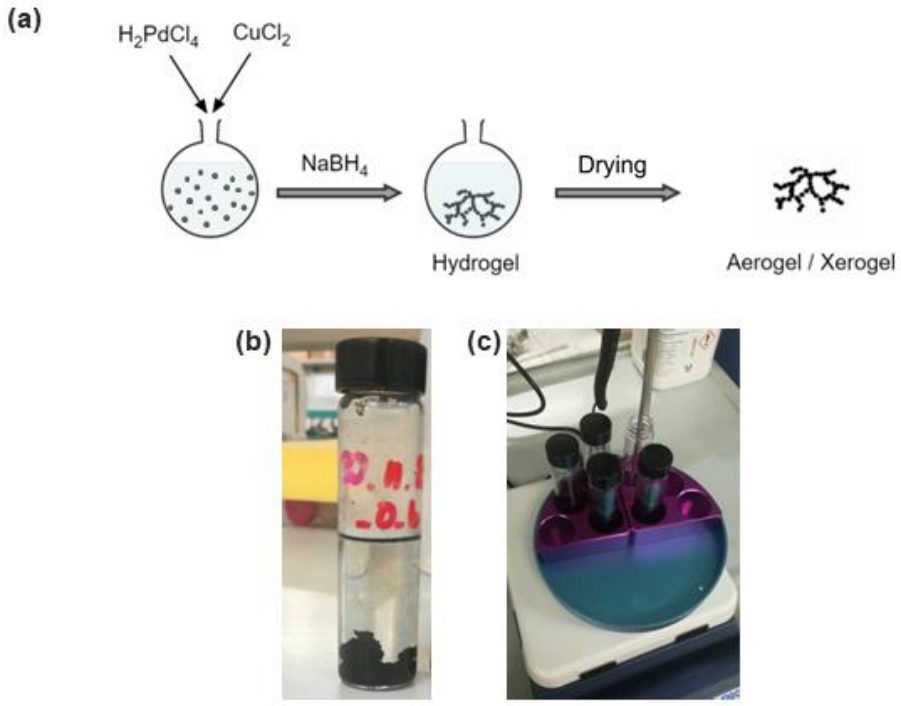
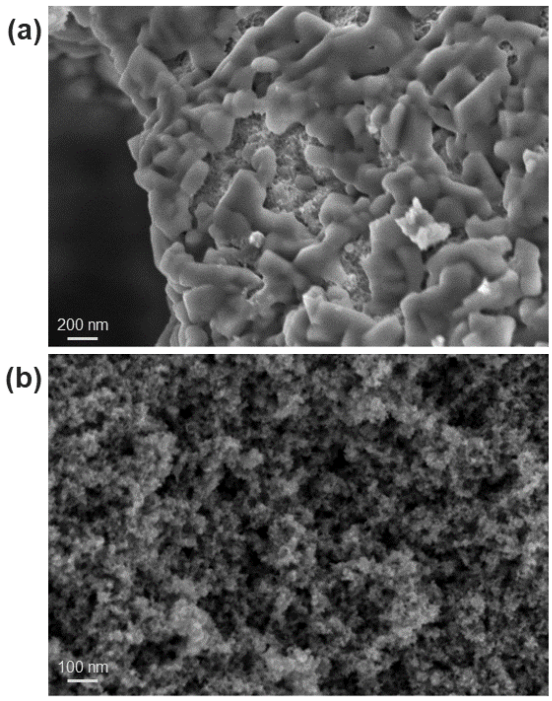


Figure 3.2 – (a) Scheme of the reaction for the formation of the PdCu aerogel; (b) Hydrogel sample (black) synthesized in laboratory deposited on the bottom of the tube; (c) Image of the set-up made for working in parallel on multiple tubes onto the heating plate for the reaction.

Special care was taken in defining a protocol for cleaning the product obtained at the end of the reduction reaction to avoid contaminants (*e.g.*, Na, Cl). Those were especially visible as coverage on the surface of the sample in the absence of washing, as reported in the Figure 3.3a, and potentially responsible for the decrease in the catalytic performance of the material. The absence of polluting elements was confirmed by FESEM and EDX analysis of the samples obtained (Figure 3.3b), thus validating the clean-up procedure, which consists of 5 successive exchanges of the reaction solvent with clean Milli-Q water, one every 30 minutes, that was replicated during the preparation of new samples.



Element	Atomic %
Pd	14.12 ± 1.67
Cu	1.40 ± 0.76
Na	48.00 ± 5.39
Cl	36.48 ± 4.09

Element	Atomic %
Pd	74.12 ± 11.34
Cu	25.88 ± 4.98
Na	n.d.
Cl	n.d.

Figure 3.3 – FESEM image and related EDX analysis of the atomic percentages of the elements of interest and contaminants for the catalyst sample (a) before and (b) after the clean-up procedure.

3.4.3 Comparison between different drying methods

The drying phase was carried out following two different procedures:

i. In a vacuum oven (Buchi High Vacuum Oven)
ii. In a reactor with supercritical CO_2 flow

In this phase, great importance was given to studying the effects of the two different procedures for obtaining the dried catalyst. In the following discussion, the samples obtained are indicated via acronyms associated with the instrument used for drying, HV (Buchi High Vacuum) and SC (Supercritical CO_2). Following the first method, the freshly prepared PdCu hydrogel was treated to replace water using ethanol as a solvent, introducing only the quantity necessary to cover the hydrogel formed on the bottom of the tube. Then it was placed in a vacuum drying oven at 50 °C for 4.5 hours to obtain the HV sample. Regarding the second drying method, the hydrogel was placed in a high-pressure stainless-steel container, and 10 mL of acetone was added to prevent the solvent from evaporating from the hydrogel before it came in contact with supercritical CO_2 and to avoid shrinkage

of the solid. CO_2 was then pumped into the vessel. The pressure of the CO_2 was set to 90 bar, at 30 °C, where acetone is miscible with liquid CO_2, and then it was settled 90' static mode and 30' dynamic mode. In particular, the static mode allowed the hydrogel to soak so that the CO_2 could penetrate the matrix and extract the solvent. Instead, during the dynamic interval, CO_2 carrying the solvent flowed out of the unit and into a pre-weighed collection flask, where the CO_2 was vented to a fume hood. In the following Section, the results of the characterization of the obtained catalysts using the two different drying methods are presented. These results and those of the electrocatalytic CO_2 reduction tests (Section 3.6) were used to make a balanced decision on the optimal catalyst for the development of the SATURNO project.

3.5 Catalyst characterization

The morphological, microstructural, and inner structure of the resulting PdCu catalyst were characterized by using the instruments and techniques described in Section 2.2. Only a few analyses were conducted on both the HV and SC samples, and the final catalyst was chosen to be HV, considering the electrocatalytic CO_2 reduction results and the availability and ease of use of the High Vacuum oven. From Section 3.5.2, the characterization was performed only on the PdCu_HV sample and its repetitions.

3.5.1 Comparison of drying methods: XRD and N_2 physisorption

The XRD analysis (Figure 3.4) revealed that the peaks in both the sample can be attributed to the (111), (200), (220), (311) and (222) planes of face-centred cubic Pd, consistent with the selected area electron diffraction pattern. The lack of a significant shift in peak position in the PdCu catalyst compared to pure Pd metal (JCPDS No. 65-6174) further supports the idea that the bimetallic nanostructures are composed of crystalline Pd and amorphous Cu, rather than a PdCu alloy. Moreover, no peaks due to Cu were found in the diffractograms. The behaviour of both samples is very similar to the one of the catalysts reported by Lu and co-workers [170], who first rejected the presence of a PdCu alloy. The surface areas estimated from BET plots and the pore size and volume, were reported in Table 3.2. The values obtained were fairly similar for the two catalysts, a slightly higher BET surface area was detected for the sample dried via the high-vacuum oven (44.18 vs. 40.76 m^2/g with respect to the PdCu_SC). Both results were lower than those reported by Lu *et al*. in their work on a similar bimetallic aerogel. Interestingly, the two catalysts obtained an equal pore volume value while the

PdCu_HV showed a slightly lower pore size. It was possible to directly correlate the higher surface area results obtained via BET with the increasing catalytic activity of the samples towards the CO_2RR products (which will be shown in Section 3.6.1).

Table 3.2 – Comparison of the results obtained from N_2 physisorption analysis of the two as-prepared samples.

Sample	PdCu_HV	PdCu_SC
BET surface area [m^2/g]	44.18 ± 0.122	40.76 ± 0.045
Pore volume [cm^2/g]	0.14	0.13
Pore size [nm]	12.7	13.5

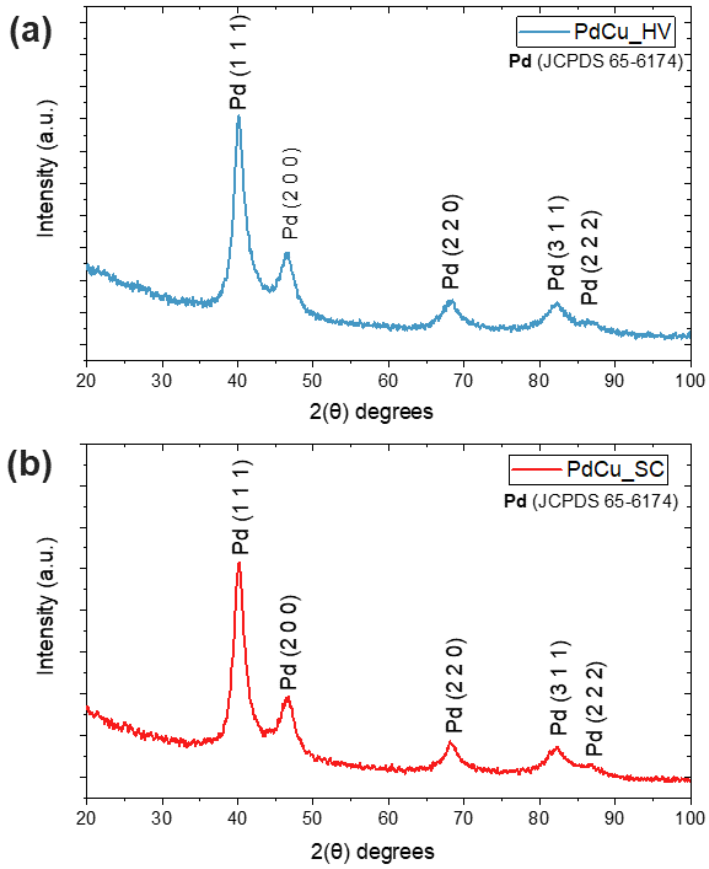


Figure 3.4 – XRD pattern of (a) HV sample and (b) SC sample.

3.5.2 XPS analysis

The PdCu_HV electrocatalyst was characterised via XPS to get information about possible relations between surface electronic states and catalytic activity. Firstly, from several repetitions of the superficial survey, it was possible to assess the relative abundance of the two main elements composing the material, such as Pd and Cu. Considering an average of 3 regions investigated, the final atomic percentage was 72% for Pd and 28% for Cu, associated with a standard deviation of ±1.80. The ratio between the two species was here on 2.5. Regarding the high-resolution spectra, the intense Pd $3d_{5/2}$ peaks of the sample at 335.4 eV correspond to the metallic Pd(0). The Cu2p spectra were fitted to understand the main components of oxidation states. It was performed a deconvolution procedure to evaluate the relative abundance of Cu(II) and Cu(0)+Cu(I) oxidation states. The abundance of the mixed Cu(I)+Cu(0) species was higher than the only Cu(II) one, reaching values of 58% and 42%, respectively. A signal due to Cl 2p was detected at around 198 eV, and deconvolution was applied to hint at the average oxidation state. The signal was too noisy for further evaluation. The presence of O species on the aerogel surface, for example, the copper-based ones, indicates that oxidation occurred when the aerogels were exposed to air. The bimetallic nanostructures consisted of crystallized Pd (fcc) and amorphous Cu. The amorphous Cu had a large amount of low-coordinated atoms, resulting in abundant defects and more catalytic centres being created to enhance CO_2 catalytic performance [171]. Additionally, the moderate O-modified PdCu surface can benefit the chemical adsorption of CO_2 and subsequent hydrogenation in CO_2RR [172,173]. The CO_{ads} and CHO_{ads} can also be efficiently adsorbed on Cu(I)+Cu(0) species, increasing CH_3OH yields [174].

3.5.3 Advanced characterization: TEM ex-situ and in-situ

After receiving the as-synthesized catalyst as an input, the IIT colleagues carried out TEM characterisation. Preliminary optimization tests were conducted for depositing the catalyst on the working electrode of the in situ electrochemical cell chip (the centre point of Figure 3.5a, the image of an electrochemical chip). This step is particularly critical as the deposited material must be well-distributed and very thin (thickness not exceeding 100 nm) in order to allow the electron beam to pass through the sample, ensuring electron transparency and reducing the amount of liquid in the cell. In fact, using a cell with a reduced liquid thickness ensures better resolution in the observation with a transmission electron microscope

during the electrochemical reaction. Optimizing the catalyst deposition on the working electrode is also quite important to leave the counter electrode and reference electrode clean. In Figure 3.5b-c, the FESEM images of a deposition test on test substrates before and after thickness optimization are shown, respectively. As can be seen in Figure 3.5c, the particle distribution on the surface and the dimensional scale is compatible with TEM observation. This characterization step was crucial and thus preceded any catalyst deposition, in order to avoid issues with the equipment during the experiment.

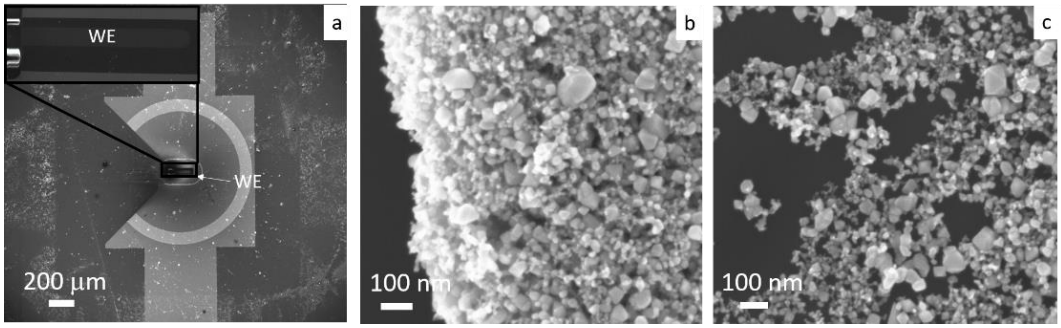


Figure 3.5 – FESEM images of catalyst deposited on: (a) chip, and on silicon substrate (b) before and (c) after thickness optimization.

A preliminary ex situ study was conducted using FESEM on PdCu-based sample to better prepare in situ experiments with the catalyst. The material was composed of particles that created a porous structure. The particle size was compatible with the correct thickness for TEM measurements. The most efficient developed catalytic systems were characterized by using advanced TEM techniques to identify the structure and active phase of the catalyst. To better approach to in-situ experiments, a TEM study (Figure 3.6a-d) was conducted on a new batch of PdCu catalyst. The Bright Field TEM image (BFTEM in Figure 3.6a) confirmed that the material had the desired characteristics for in-situ study, namely a maximum size compatible with electron transparency with an optimized liquid resolution as a result. It also confirmed that this material was composed of particles that create a porous structure (Figure 3.6a-b), while High-Resolution TEM images confirmed that the particles were crystalline (also in accordance with the Fast Fourier Transform in the insert of Figure 3.6c). SAED confirmed the presence of polycrystalline material characterized by ring patterns (Figure 3.6d), attributed to Pd (Palladium, JCPDS 00-065-2867). There was no evidence of the presence of crystalline Cu. However, this element was present in the material, as confirmed by EDX analyses (Figure 3.3a-b). EDX mapping was also performed, confirming that Cu was uniformly distributed and dispersed in the material (Figure 3.6f-h).

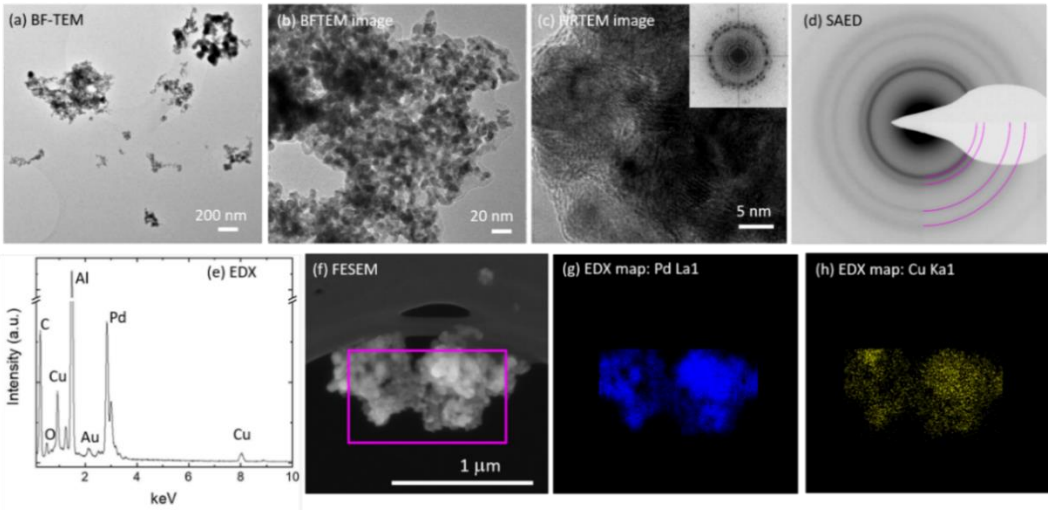


Figure 3.6 – TEM characterization of PdCu catalyst: (a,b): BFTEM, (c) High Resolution TEM, (d) SAED, (e) EDX spectrum, (f-h) FESEM image and EDX maps for Pd and Cu.

3.6 Electrocatalytic CO_2 reduction test

The tests discussed in this Section have been carried out in the RDE setup (more details are provided in Section 2.3.1). To briefly recap, electrochemical tests were performed in a H-cell, using a solution of $KHCO_3$ 0.1M as electrolyte (50mL in the catholyte chamber and 28mL into the anolyte one) and a three-electrode system consisting of Pt wire as counter electrode, Ag/AgCl as reference, and a working electrode composed of an RDE made of glassy carbon on which the ink containing the catalyst was deposited. The catalysts inks were prepared by ultrasonically dispersing the catalytic material particles with a Nafion solution (used as the binder) and Isopropanol (used as the carrier), with a mass ratio of active-phase/Nafion of 70:30 and an isopropanol/solids mass ratio of 97:3. A percentage of Vulcan XC 72R Carbon (VC, 9.5 wt.% of active-phase) was added to improve the conductivity of the catalyst dispersion. The mixture was sonicated for 10 min before drop-casting. The catalyst loading on the electrode was always kept at a value of 0.6 mg cm^{-2}. Electrochemical behaviour was evaluated by using Cyclic Voltammetry and Linear Sweep Voltammetry, both in N_2 and CO_2 saturated environment, and finally, by 2-hours electrochemical reduction of CO_2 using Chronoamperometry. The potentials are represented versus the RHE thanks to Equation 22 to make a reliable comparison of the results and to take into account the different pHs of the electrolyte in the different tests (*i.e.,* 8.4 in the solution saturated with N_2 and 6.8 in the presence of CO_2).

Equation 22 – Conversion $E_{Ag/AgCl}$ in E_{RHE}

$$E_{RHE} = E_{\frac{Ag}{AgCl}} + 0.21 + 0.059 \cdot pH$$

3.6.1 Comparison between PdCu_HV and PdCu_SC

Electrochemical tests of the PdCu_SC and PdCu_HV catalysts were carried out using the same set-up and protocol as described in previous Sections in order to enable a comparison of the performance of the two bimetallic catalysts obtained with the two different methods of drying. The outputs of the comparison were then considered for the choice of the final catalyst, so deciding in which way to perform the drying phase. The results of evaluating the electrochemical behaviour are reported in Figure 3.7. The Cyclic Voltammetry curves (Figure 3.7a) were obtained by scanning from 0.60 V vs. RHE to –1.38V vs. RHE. For both the samples, the onset potential value was found to be at around –0.55V vs. RHE, thus not showing significant differences in activity towards the reduction of CO_2. After that certain point, the behaviour of the two samples begins to differ: the PdCu_SC (red line) reached a current density (*J*) of around –15 mA cm^{-2}, sufficiently different from than HV sample which got to –23 mA cm^{-2}. Slightly higher activity is observed in the presence of this HV catalyst with respect to the SC one in terms of current densities measured at the same potential values (starting from ca. –0.5 V vs RHE). This improved result may be associated with a more efficient electrochemical CO_2 reduction. The same trend is shown in Figure 3.7b, where the linear polarization curves are shown, and the maximum current density of PdCu_HV catalyst arrived at a relevant value of –61 mA cm^{-2}, being around 20 mA cm^{-2} higher than SC sample, which reached –43 mA cm^{-2} at the potential value of –2.4 V vs. RHE. The proficiency of the bimetallic PdCu samples towards CO_2 electroreduction was evaluated under chronoamperometric conditions. The experiments were conducted at –0.9 V vs. RHE in 0.1 M $KHCO_3$ for 2 h under sealed conditions with vigorous magnetic stirring.

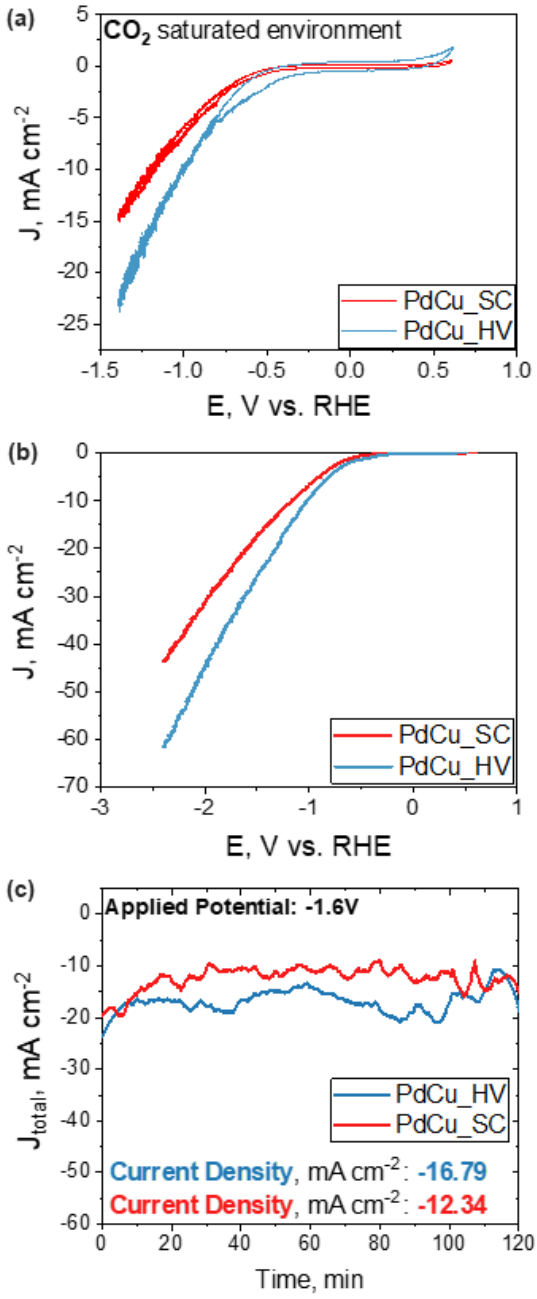


Figure 3.7 – RDE test of CO_2 reduction for the two catalysts: PdCu_HV blue line and PdCu_SC red line; (a) Cyclic Voltammetry performed in CO_2 ; (b) Linear Sweep Voltammetry performed in CO_2-environment; (c) Chronoamperometry test performed at –1.6V vs. Ag/AgCl.

As it can be observed in Figure 3.7c, both the samples presented a particularly unstable trend during the test, so the evaluation of the performance was done onto the average of the current density values. It resulted that PdCu_HV reached a mean value of around –17 mA cm^{-2}, which is higher than the PdCu_SC that slightly arrived to about –12 mA cm^{-2}. Despite these results were already enough to select the best catalyst between the two, the evaluation continued with the analysis of the products after the 2-hours chronoamperometry. In particular, Figure 3.8 showed a comparison of the results of the two catalysts in terms of FE associated with the various products revealed. In addition to the higher average current density (in absolute value) observed in the test with the HV catalyst, a higher FE was obtained for H_2 (39.1% vs. 33.6% for PdCu_SC) and a similar value to the SC catalyst for CO (46.4% for PdCu_HV vs. 47.4% for PdCu_SC). The Faradic Efficiency for formate was found to be double with the HV catalyst compared to that obtained in the SC test (13.3% vs. 6.3%). In terms of alcohols, the same value was observed in both tests for methanol (0.01%), ethanol had a 3-times higher efficiency in HV compared to SC (2.85% vs. 0.95%), while the opposite trend was evident for 2-propanol (1.9% for PdCu_HV vs. 5.4% for PdCu_SC).

Following the results of these electrocatalytic experiments for CO_2 reduction, it was decided to adopt the technique of drying with the Buchi high-vacuum oven to complete the synthesis and sample creation process. By definition, technically our samples consisted of palladium-copper based xerogels with a metal ratio of 3:1. The catalyst can now be referred to as Pd_3Cu_1. The synthesis was repeated to obtain a new catalyst powder, with exactly the same characteristics as the previous sample. Such powder was then subjected to further reduction tests, again in an *H-type* cell and finally scaling up to a larger cell as discussed in the following Sections.

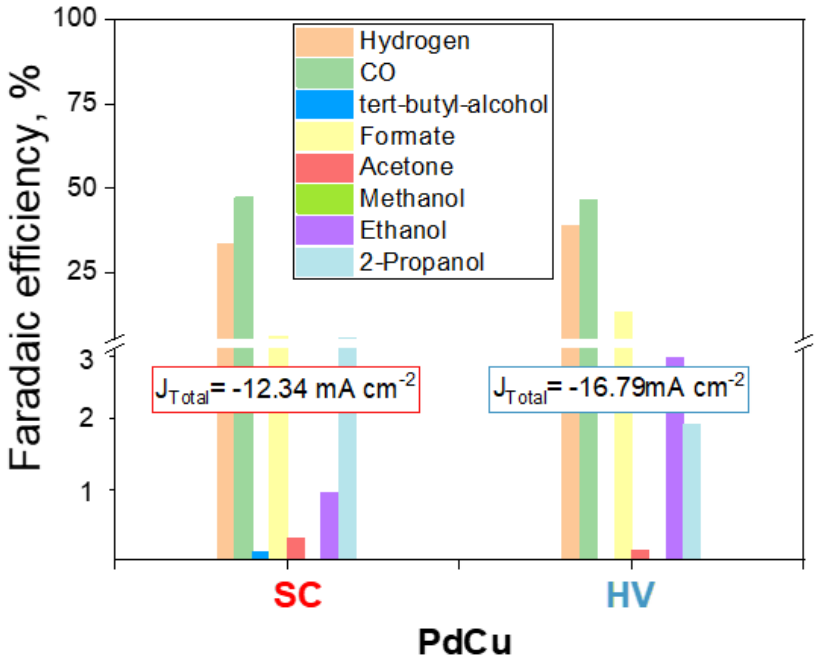


Figure 3.8 – Comparison of Faradaic Efficiencies for gaseous and liquid products detected after a two-hours chronoamperometry at an applied potential value of –0.9 V vs. RHE for both the catalysts (PdCu_SC in the left part of the graph and PdCu_HV in the right one).

3.6.2 Pd_3Cu_1 CO_2 reduction test

The electrochemical performance of the final Pd_3Cu_1 catalyst was evaluated by using the same experimental setup and protocol as described previously, in order to allow a comparison with previous results. Looking at Figure 3.7a and Figure 3.9a, it is evident that the PdCu_HV and the Pd_3Cu_1 curves were very similar, even if the latter one, the purple line, is slightly lower (–22.98 vs. –23.63 mA cm^{-2} referred to HV sample) in terms of maximum current density reached at the same potential (–1.4 V vs. RHE). The similarity was also appreciable in Linear Sweep Voltammetry curves (Figure 3.7b and Figure 3.9b), where there was almost complete overlap of the two lines, and it was also possible to reach a maximum value of $J \sim -65$ mA cm^{-2}, which was a significant increase compared to the lower value of the PdCu_SC (~ 40 mA cm^{-2}) mentioned in the Section 3.6.1. In Figure 3.9c is shown the average current density value of –15.39 mA cm^{-2}, which was obtained during the test (120 minutes, applied potential –0.9 V vs. RHE). It was slightly lower by 9% (in absolute value) than the one obtained by testing the first batch of the PdCu_HV (Figure 3.7c). Finally, comparing the results from Section 3.6.1 with those just presented, it can be said that the

agreement between the experiments is indeed good, and this proves that the synthesis was truly reproducible and that the samples obtained in this new synthesis batch had the same properties as the PdCu_HV sample.

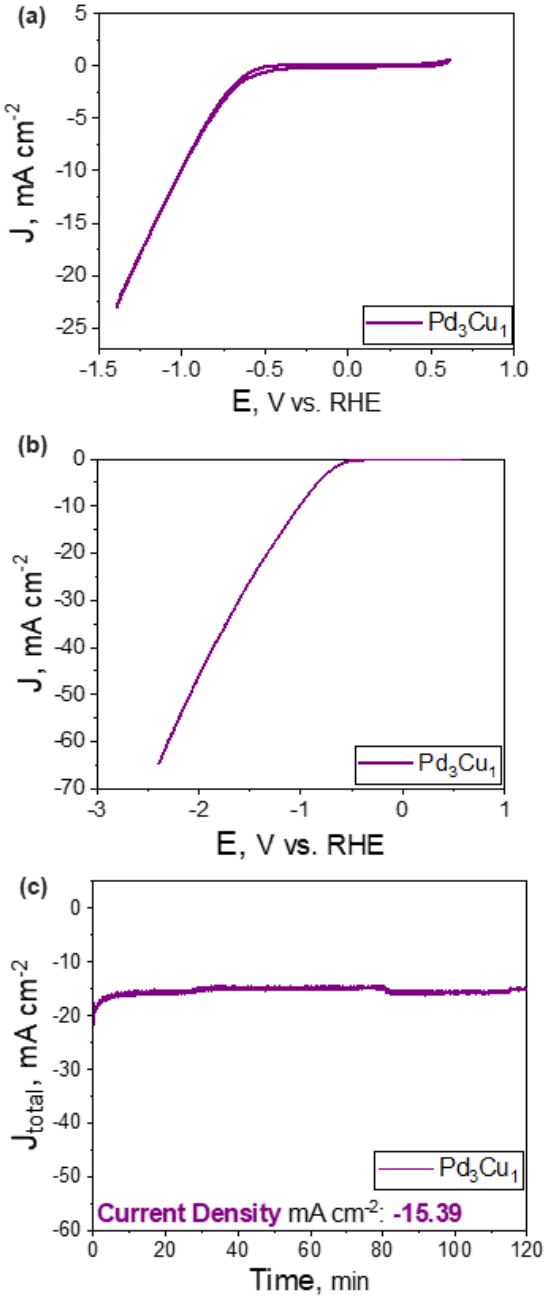


Figure 3.9 – RDE test of CO_2 reduction for the final Pd_3Cu_1 catalyst; (a) Cyclic Voltammetry performed in CO_2; (b) Linear Sweep Voltammetry performed in CO_2-environment; (c) Chronoamperometry test performed at –0.9V vs. RHE.

Finally, the values of the Faradic efficiencies for each product obtained were also compared with PdCu_HV catalyst, as shown in Figure 3.10. There was good agreement between the values of Faradic efficiency obtained in the two tests for H_2 and CO with the Pd_3Cu_1 catalyst, respectively 43.15% and 38.84% vs. 39.1% and 46.43% with PdCu_HV. There was also a decrease in formate selectivity with the Pd_3Cu_1 (8.7% vs. 13.29%), however balanced by an increase in the amount of ethanol (3.41% vs. 2.86%). The amounts of methanol produced in both cases was <0.05% (0.05% in the Pd_3Cu_1 catalyst vs. 0.01% in the PdCu_HV).

To conclude, some useful results in terms of concentrations of produced species and relative Faradic efficiency have emerged as ideas for future upgrades. With the collaboration of Hysytech, the development of a new electrochemical cell was studied to scale up the experimental setup at TRL4 for future developments.

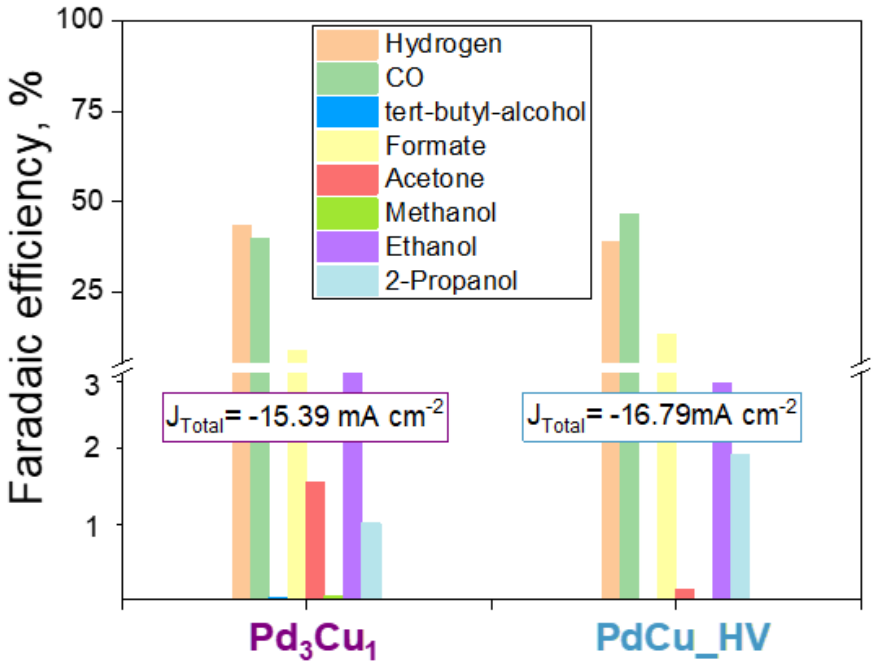


Figure 3.10 – Comparison of Faradaic Efficiencies for gaseous and liquid products detected after a two-hours chronoamperometry at an applied potential value of –0.9 V vs. RHE for the two the catalysts (Pd_3Cu_1 in the left part of the graph and PdCu_HV in the right one).

3.7 Scaling up: design of a GDE cell set-up

Based on the previous experience of our team, the technical specifications of an electrochemical cell suitable to for the electrocatalytic conversion of CO_2 to high-added value products were defined. The technical specifications of the cell are listed in Table 3.3. The mechanical design of the cell was carried out by Hysytech using these data. As shown in Figure 3.11a, the cell assembly consisted of (from left to right): the gas feed chamber, gas diffusion electrode (GDE), cathodic chamber, ion exchange membrane, anodic chamber, and counter-electrode. The cell was designed to be fed through the flow connections at the bottom, while the products are discharged through the connections at the top. The chambers were separated by using appropriate membranes and O-rings to seal and prevent the loss of fluids or gases between the chambers and to the outside. In addition, the inlet and outlet on the flow distributors were positioned at opposite corners to avoid the formation of stagnant zones of electrolyte and the formation of gas during operation. Flow distributors were also provided to improve fluid distribution and to protect the membrane. Concerning materials, the closing plates and current collectors were made of AISI316, while the frames in contact with the electrolyte and the insulating plates were made of PTFE. Figure 3.11b shows the cell built and assembled, ready for pressure tests to be carried out at the Hysytech facilities.

Table 3.3 – Technical specifications required for the design of the 100 cm^2 GDE electrochemical cell of the Saturno project.

Design temperature	120 °C
Design pressure	1.5 barg
Active area	100 cm^2
Gas feed	Ar-CO_2 mixture fed with MFC (mass flow controller) (3-150 Nml/min) and humidified with CEM (cation exchange membrane) (max 30 g/h of H_2O)
Catholyte	pH = 8-14 flow-rate = 15-30 g/h
Anolyte	pH = 8-14 flow-rate = 15-30 g/h
Component thicknesses	GDE = 155-225 micron cathodic flow distributor = 2 mm membrane = 183 micron anodic flow distributor = 2 mm counter-electrode = i) Ni mesh 1.7 mm

	ii) Carbon paper with Pt = 270 micron
Metal parts in contact with electrolyte	AISI 316
Other	reference electrode in the anodic chamber

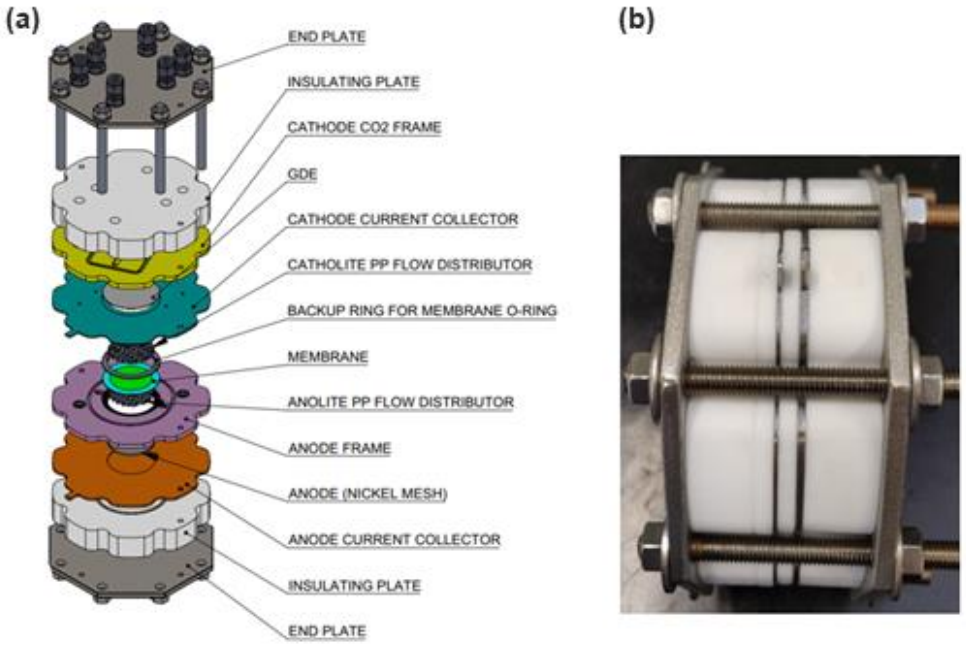


Figure 3.11 – Scaled-up 100 cm^2 GDE electrochemical cell of Saturno project: (a) Exploded view of the cell assembly; (b) side view of the constructed cell.

3.7.1 Electrocatalytic CO_2 reduction test in the new GDE set-up

The efficiency of Pd_3Cu_1 as an electrocatalyst for the reduction of CO_2 to high value-added products was investigated in the scale-up 100 cm^2 GDE cell of the Saturno project. The electrocatalytic activity of this material was evaluated in continuous flow with a GDE configuration. The catholyte (0.1 M $KHCO_3$) and anolyte (0.1 M KOH) chambers were separated by a PEEK-reinforced anion exchange membrane (FAA-3). The anode consisted of a rectangular plate made of iridium and metallic oxides (Ir-MMO) and the reference electrode was a leak-free Ag/AgCl (3.4 M KCl). In particular, to prevent vibrations that could interfere with measurements, the reference electrode was inserted in the anodic compartment. The flow of CO_2 was kept constant by using a Mass Flow Controller (EL-Flow

Select, PN64 from Bronkhorst High-Tech B.V., Ruurlo, Netherlands) at 20 NmL min^{-1}. The fabrication process of the working electrode was based on the preparation of a catalytic ink and its deposition on a conductive porous support (carbon paper Toray 060) by using the airbrushing technique. The catalytic ink was made as described in Section 3.6.

The GDE was prepared with a geometric area of 100 cm^2 and a catalyst loading of 0.6 mg cm^{-2}. The deposition process took place on a heating plate at 120 °C to ensure the complete evaporation of the solvent. The catalyst, composed of crystalline Pd and amorphous Cu, was able to generate high reduction current densities (~100 mA cm^{-2} at around –15 V vs. Ag/AgCl) in the presence of CO_2. This was observed in the linear polarization curves shown in Figure 3.12a. The applied potential was scanned between 0 V and –18 V (vs. Ag/AgCl) at a scanning rate of 30 mV s^{-1}. With the aim of studying the selectivity of the Pd_3Cu_1 electrode for the electrochemical reduction of CO_2, chronopotentiometry was carried out under CO_2 flow at three different constant current densities (10, 50, and 133 mA cm^{-2}), in the same reaction medium. Figure 3.12b showed that the total current density profiles over time were very stable, with no significant changes in current. As expected, the obtained cathodic potential increased with the applied current density. The photograph of the tested electrode (see Figure 3.12c), shown in the inset of Figure 3.12b, revealed that high current densities did not compromise the stability of the electrode as no detachment of the catalytic particles was observed during operation. Finally, Figure 3.12d showed the variation in the selectivity of the different CO_2 reduction products according to the applied current density. It is worth mentioning that in all cases, Faradic efficiencies towards C_1 products were below 40%. Hydrogen was detected as the main product of the CO_2 co-electrolysis reaction. In particular, the formation of CO and alcohols such as methanol, ethanol, and propanol increased with the applied current density. This behaviour indicates that the C-C coupling reaction is promoted at high overpotentials through the dimerization of *CO (*indicates species adsorbed on the surface) [175]. In fact, formate desorption was inhibited at the most negative applied current density, where the C-C coupling reaction was enhanced, reaching an approximate 22% selectivity towards alcohol production (ethanol, 1-propanol, 2-propanol). The activity and selectivity towards CO and C_{2+} products might be associated with the presence of different induced faces during the reaction. Typically, different reducing conditions give rise to different crystalline nanostructures. Probably, the angles, edges, and faces formed at the most negative applied current density favour an appropriate binding energy for the key intermediate for alcohol production [176]. The low productivity towards

liquid products can be attributed to the management of gaseous products transport (CO, H_2, and alcohols) from the surface to the reaction medium. In this sense, the enhanced production of H_2 and CO observed at lower overpotential (–0.9 V vs. RHE), with respect to the alcohols, is probably due to the higher diffusion coefficient of gaseous products. The generation and accumulation of gas bubbles could block active sites due to mass transfer limitations. The carbon support used here does not have the most suitable porosity to allow gas products to quickly exit the catalytic layer at high production rates. In this regard, the use of other types of supports, such as a PTFE membrane [177], could be considered in a future work.

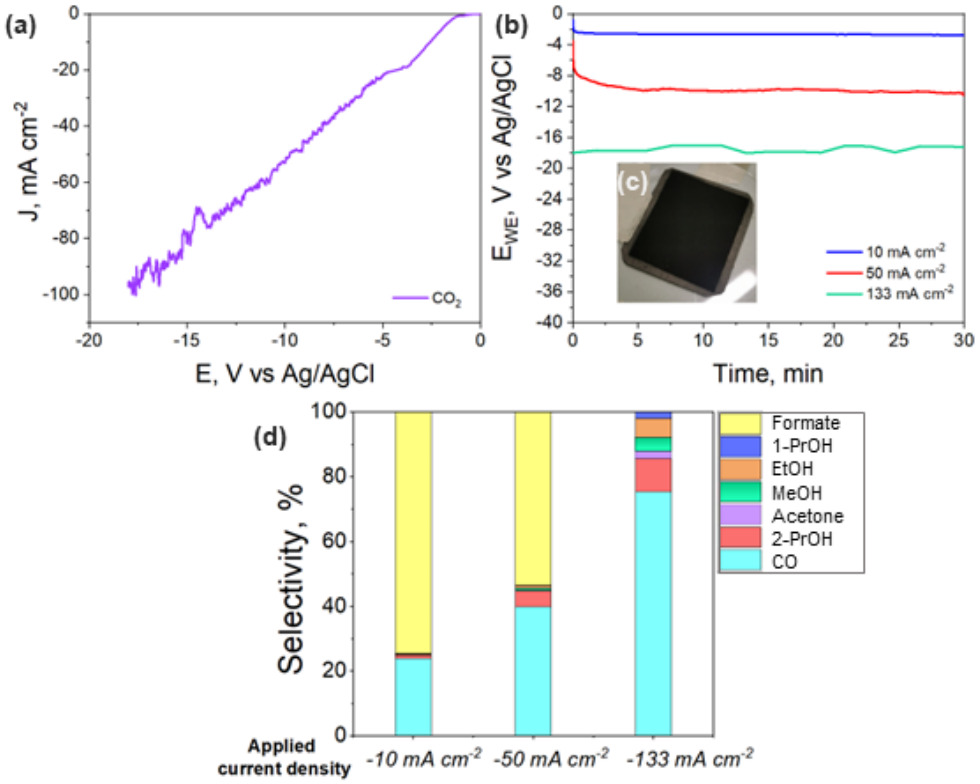


Figure 3.12 – Results of electrocatalytic CO_2 reduction test carried out in in a continuous flow electrochemical system: (a) Linear sweep voltammetry under CO_2 flow; (b) Chronopotentiometric curves; (c) Photo of the electrode after the test in the inset and (d) selectivity of CO_2 reduction products at different applied current densities (–10, –50, and –133 mA cm^{-2}) for the Pd_3Cu_1 catalyst-tested electrode.

3.8 Conclusions

In conclusion, the synthesis and reproducibility of the Pd_3Cu_1 catalyst has been successfully demonstrated through its use in CO_2 electrochemical reduction tests in an RDE system. The catalyst properties were investigated via different analytical techniques, such as XRD, XPS and N_2 physisorption, confirming the similarity of the catalyst with the others Pd-Cu based ones described in literature. In addition, advanced characterization through TEM and attempts of in-operando experiments were also performed. Initially, electrocatalytic CO_2 reduction tests were conducted in an RDE system using a *H-type* cell to gain a better understanding of the electrocatalytic properties of the new material. The tests, which involved a 2-hours chronoamperometry test at –1.6 V yielded good results in terms of the production of C-based compounds, including a CO faradaic efficiency of 38.84% and an ethanol yield of 3.41%. The tests to verify the possibility of reaching the project target (selectivity >70%, current density >100 mA cm^{-2}) were carried out in a scaled-up cell with 100 cm^2 electrodes. The developed catalyst demonstrated to be capable of generating high reduction current densities (–100 mA cm^{-2} at around –15 V vs. Ag/AgCl) as required for the SATURNO project. Selectivity of carbon compounds up to 40% was obtained (with values equal to or higher than 60% of green H_2 production) by testing the catalyst at different constant current densities, and possible theoretical and mechanistic explanations were identified through comparison with literature. Finally, it was proposed to consider the use of different supports for the catalyst to prevent the accumulation of gas bubbles near the catalytic layer in future tests.

Chapter 4

Co-precipitation synthesis of Cu_2O-SnO_2 catalyst for the photoelectrochemical CO_2 conversion

In Chapter 4, the interest in CO_2 conversion into high-value-added products is addressed to find substitutes for fossil-based ones and tackle the environmental crisis. Herein, a noble, simple, reproducible, and scalable Cu_2O-SnO_2 photo-electrocatalyst was synthesized and characterized. Coupling cuprous oxide with tin oxide allowed for protecting unstable Cu^+ species from photo-corrosion. Evidence of the SnO_2 stabilization role were found via chronoamperometry tests under chopped light and XPS analysis. An optimized catalytic ink was developed to prepare the photocathodes. The CO_2 photo-electroreduction tests demonstrated a prevalent production of CO and formate with Faradaic efficiencies of 35.47% and 19.58%, respectively, and a good system stability. Sunlight illumination demonstrated to play a major role to hinder H_2 evolution and promote $\geq C_{1Contri}$ products formation.

Contributions: This work has received funding from the European Union's Horizon 2020 Research and Innovation Action program under the Project

SunCoChem (Grant Agreement No 862192). In particular, the task involved was the one dealing with cathodic photo-electrocatalyst development and testing. The first attempts on the synthesis were carried out by the PhD student in collaboration with Daniela Roldan and Dr. Hilmar Guzman. Many of the analyses have been carried out in collaboration with partners from "Dipartimento di Scienza Applicata e Tecnologia" (DISAT) and "Istituto Italiano di Tecnologia" (IIT), in particular Dr. Angelica Chiodoni and Dr. Katarzyna Bejtka, for characterizing the prepared materials. They supported the PhD student in the FESEM, XRD, TEM data collection and curation. XPS analysis have been carried out by Dr. Micaela Castellino, a collaborator of the group, who took care of data collection and analysis. Maddalena Zoli performed the synthesis and the reproducibility assessment, also she managed to perform and present the results about the other characterization techniques, together with the data analysis and the *H-type* cell photo-electrocatalytic CO_2 reduction tests. The testing protocol was validated in collaboration with Dr. Hilmar Guzman and Prof. Simelys Hernandez. Dr. Adriano Sacco gave his assistance in understanding and evaluating the results of electrochemical impedance spectroscopy (EIS), as well as in improving the experimental methodology employed for data acquisition.

It is worth noting that the work elucidated in this Chapter represents a paper entitled "Facile and Scalable Synthesis of Cu_2O-SnO_2 Catalyst For The Photoelectrochemical CO_2 Conversion", by Maddalena Zoli, Daniela Roldán, Hilmar Guzmán, Micaela Castellino, Angelica Chiodoni, Katarzyna Bejtka, Nunzio Russo, Simelys Hernández, which was published on Catalysis Today [178].

4.1 Ultrasound-assisted co-precipitation synthesis

The chemical co-precipitation method is used to synthesize cathode materials through the kinetics of nucleation and involves the simultaneous occurrence of processes such as nucleation, growth, coarsening, and agglomeration in a homogeneous solution. The factors that influence the size, shape, and size distribution of the final nanostructures include temperature, pressure, concentration, pH, stirring speed, reaction time, the nature of the precursors, and the presence of surfactants or other growth inhibitors [179]. While it is a commonly used method, it can be challenging to produce controllable nanostructures using this method. These reactions typically produce insoluble products under conditions of high supersaturation, with nucleation being a key

step.
The supersaturation conditions necessary to induce precipitation are usually the result of a chemical reaction (Equation 23):

Equation 23 – Co-precipitation mechanism

$$XAy^{+}_{(aq)} + YBx^{-}_{(aq)} \rightarrow AxBy_{(s)}$$

Where A,B are the chemical elements while *XxYy* are the stochiometric parameters. Secondary processes, like Ostwald ripening and aggregation, can significantly affect the size, morphology, and properties of the products. The supersaturation necessary for precipitation is usually the result of a chemical reaction. Co-precipitation synthetic methods include the formation of metals from aqueous solutions, the reduction of metals from nonaqueous solutions, electrochemical reduction, and the decomposition of metallorganic precursors, as well as the formation of oxides and metal chalcogenides from aqueous and nonaqueous solutions, and microwave/sonication-assisted co-precipitation. Advantages of the co-precipitation method annoverate simplicity, rapid preparation, easy control of particle size and composition, the ability to modify the particle surface state, overall homogeneity, low temperature, energy efficiency, and the absence of organic solvent. Disadvantages encompass the inability to work with uncharged species, the potential for trace impurities to be precipitated along with the product, the time-consuming nature of the process, batch-to-batch reproducibility issues, and difficulty when the reactants have very different precipitation rates [180].

For the synthesis of a photoactive Cu-Sn-oxide-based catalyst for photo-electrocatalytic CO_2 reduction, the plan was to couple the co-precipitation method previously discussed with the ultrasonic contribution, following a method already known in the research group thanks to the work of Guzmán *et al*. [181]. A pioneering work, based on a similar catalyst and dealing with an ultrasound-assisted co-precipitation route, was reported by Allahyari *et al*. [182]. Their investigation aimed to understand how the power of ultrasound irradiation affect the properties of a co-precipitated CuO-ZnO-Al_2O_3/HZSM-5 catalyst, leading to favourable conditions for the nucleation and growth of the particles.

Sonochemistry is a chemical synthesis method that uses ultrasonic waves to generate chemical reactions. One advantage of this approach is that it is cost-effective, produces reactions quickly, allows for control over synthesis conditions, produces nanoparticles with a narrow size distribution, it is environmentally

friendly, and it can be easily scaled up [183]. The main physical process involved in sonochemistry is acoustic cavitation, which is the formation, growth, and collapse of bubbles in a solution. This process determines high temperatures and high pressures for short periods of time, creating conditions that are favourable for chemical reactions to occur by facilitating them and enhancing the nucleation rate and dispersion of fine active metal particles on a carrier [184]. Ultrasound irradiation can have an effect on crystallization by shortening the induction time between the establishment of supersaturation and the start of nucleation and crystallization, according to Luque de Castro and Priego-Capote [185]. They also note - and that was an aspect taken into account in the work accomplished in this Chapter - that ultrasound can increase the reproducibility of nucleation. Besides, they have a beneficial effect on preventing agglomeration, as the conditions created by the implosion of cavitation bubbles cause particles to have shorter contact times and reduced interactions with one another. Ultrasounds have been used for synthetising different kind of materials. Pinjari *et al*. [186] worked on nanostructured titanium dioxide using conventional and ultrasound-assisted sol-gel methods and found that the ultrasound-assisted process had a higher yield due to improved mass transfer and the development of an ordered surface morphology. Instead, Dasireddy and Likozar compared the use of co-precipitation, ultrasonic, sol-gel, and solid-state methods for the synthesis of Cu/Zn/Al catalysts for CO_2 hydrogenation to methanol and found that the ultrasonic method resulted in improved dispersion of copper particles, higher numbers of active sites, and significant selectivity towards methanol compared to other synthesis techniques. These findings motivated the use of ultrasound-assisted co-precipitation for the synthesis of new catalysts for the photo-electrocatalytic conversion of CO_2. This facile and scalable synthesis method allowed to obtain a stable photo-electrocatalyst with Cu^+ as main copper oxidation state, as confirmed by ex-situ characterizations before and after tests, which can be exploited as promising materials for the sun-driven CO_2 conversion.

4.2 Cu_2O-SnO_2 design of a novel catalyst

Cu_2O is a semiconductor that is naturally of p-type and serves as a photocathode. This is because its Fermi energy level, EF, is lower than that of the electrolytes, and the redox potential of the electrolyte, ER, can be considered as its Fermi level. As a result, electrons are transferred from the electrolyte to the catalyst. The interface between the Cu_2O and the electrolyte creates an electric field, causing the energy bands to bend. This is illustrated in Figure 4.1a. The

primary challenge with Cu_2O is its stability. When in the presence of an oxidizing atmosphere, Cu(I) tends to disproportionate to Cu(0) +Cu(II). Additionally, when undergoing photo-electrochemical testing, the electrodes change colour rapidly, indicating a change in energy band gap and oxidation state.

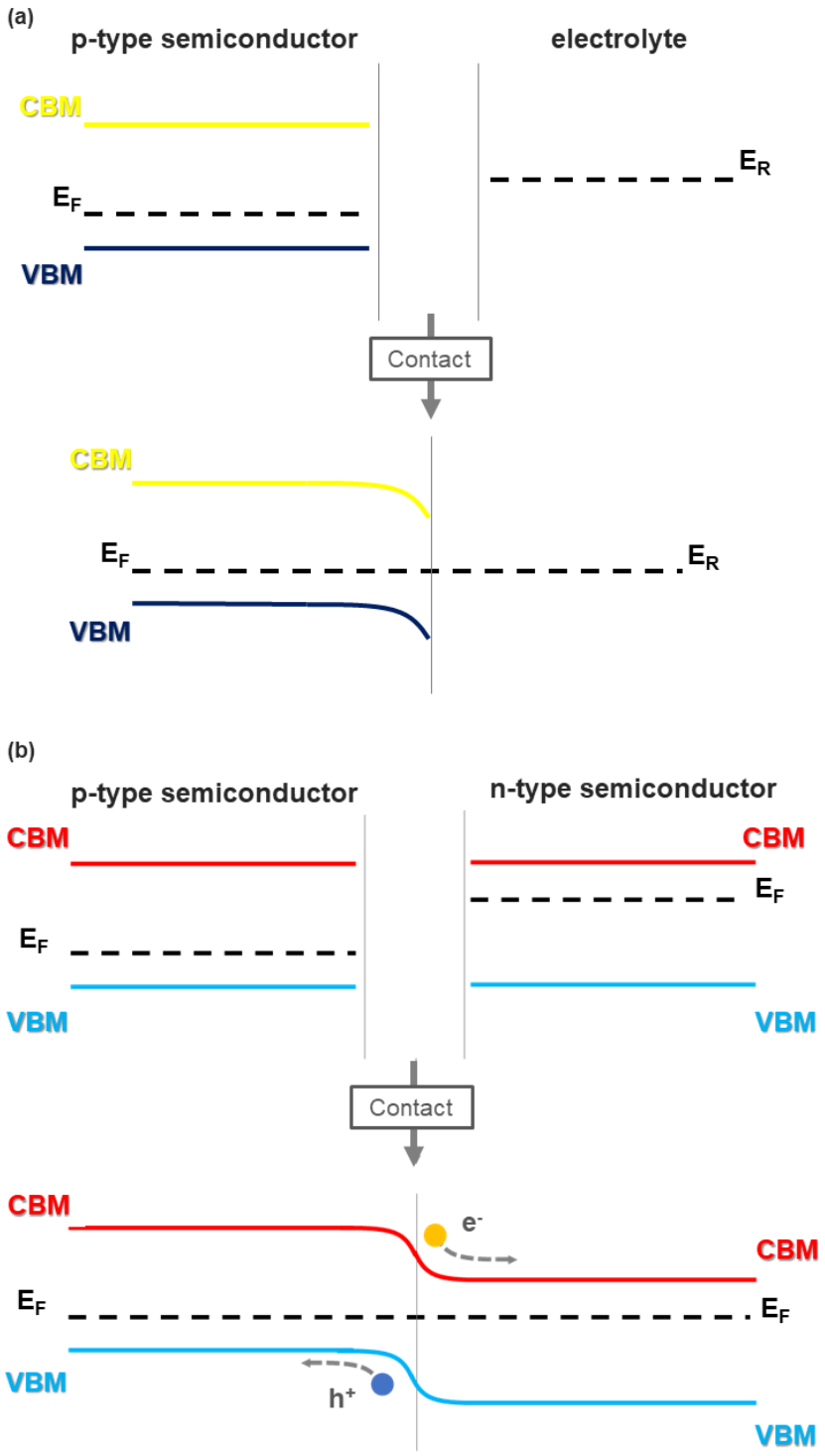


Figure 4.1 – (a) Energy band bending of a p-type semiconductor in contact with an electrolyte, and (b) staggered band heterojunction in a typical p-n junction.

The initial photoactivity of Cu_2O decreases quickly because the photo-generated charges are used for the material's self-decomposition instead of CO_2 reduction. However, efficient charge transfer can reduce self-photo-reduction and oxidation. One approach to protect the catalyst and improve charge transfer is to deposit an outer shell. It has been observed that a solid-state heterojunction based on copper oxide can efficiently separate photo-generated holes and electrons . By using an n-type semiconductor, it is possible to create a type II heterostructure with a staggered gap, forming a p-n junction that facilitates the transfer of photo-generated electrons from Cu_2O to the outer shell [187], as shown in Figure 4.1b. Studies [188–190] have shown that modifying oxide-derived copper with a precise amount of tin oxide can improve its faradaic efficiency for CO production. This approach has been applied to 0D-Cu (copper nanoparticles) to produce "earth-abundant" catalysts. The challenge lies in achieving uniform coverage and developing a synthesis method that is cost-effective and scalable. Tin oxide (SnO_2) is a suitable candidate for this purpose as it meets all the necessary requirements: it is a readily available metal-based oxide and an intrinsic n-type semiconductor.

4.3 Cu_2O-SnO_2 synthesis method

4.3.1 Reagents

Copper(II) nitrate trihydrate ($Cu(NO_3)_2 \cdot 3H_2O$, 99.5%) tin(IV) chloride pentahydrate ($SnCl_4 \cdot 5H_2O$, 98%), sodium carbonate (Na_2CO_3, 99.5%), and sodium borohydride ($NaBH_4$, 10-40 mesh, 98%) were used for catalyst preparation. Potassium bicarbonate ($KHCO_3$, 99.7%) and potassium hydroxide (KOH, 98%) were chosen as catholyte and anolyte, respectively. Nafion® 117 solution (5 wt.%) and ethanol were employed in the preparation of the catalytic ink. All the materials were purchased from Sigma-Aldrich (Milan, Italy), and they were used as received, unless otherwise specified. The support for the electrodes preparation is Toray carbon paper 060.

4.3.2 Synthesis procedure

In a typical synthesis, a Cu and Sn precursors solution (40 mL) was added to 200 mL of MilliQ water heated to 70 °C, in a completely automatized way via a peristaltic pump (5 mL min^{-1} rate). The solution was maintained under agitation. A solution of Na_2CO_3 was used as the precipitant agent, since such precursor was previously reported to provide slower growth kinetics than strong bases [191].

The addition occurs through a pump driven by a MC720 pH controller, sending the necessary amount of precipitating agent to maintain constant the pH at a value of 7. Finally, $NaBH_4$ was employed as reducing agent, as inspired from the work of Lu *et al*. [192], aiming to promote the Cu_2O formation, and added by a peristaltic pump at a flow rate of 4 mL min^{-1}. The ultrasonic processor (Frequency: 20 kHz, amplitude: 30%) was settled during the precipitation stage. The work-up, consisting of MilliQ water washings, was optimized to remove contaminants. After drying (60 °C), the catalyst was collected through in-vacuum filtration (with a nitrocellulose membrane filters, pore size 5 μm). Further details on the setup used for the synthesis can be found in Section 2.3.2.

4.3.3 Synthesis reproducibility

The reproducibility of the synthesis was assessed, since it is a key point for the validation of the new co-precipitation method. To confirm it, the synthesis was repeated for 5 times named S1-S5. Among all the characterization techniques, XRD and UV-Vis spectroscopy were chosen since they could provide quick characterization data, to check the physico-chemical properties of all the samples obtained from the repeated syntheses. The diffraction patterns and the Tauc's plot are shown in Figure 4.2. The crystallite size values and the energy band gap for each repeated sample are reported together with their standard deviation in Table 4.1. Their concordance allowed to determine the successful development of a facile co-precipitation method for the synthesis of a copper and tin-based photo-electrocatalyst for CO_2 reduction. Moreover, the Cu:Sn molar ratio was evaluated via ICP on each repeated sample, the results are reported in Table 4.1, further confirming the reproducibility of the synthesis process.

Table 4.1 – Crystallite sizes of the samples, calculated via Scherrer Equation, band gap, molar composition of the two metals of interest (Cu and Sn), and Cu:Sn ratio calculated via ICP analysis together with their standard deviation value.

	S1	**S2**	**S3**	**S4**	**S5**	**STD. Dev.**
Crystallites Size of Cu_2O (nm)	34.6	27.5	31.7	26.8	33.4	± 3.5
Band Gap (eV)	2.47	2.51	2.50	2.49	2.52	± 0.02
Cu Molar Composition (%)	67.7	69.5	63.4	65.4	68.2	± 2.46

Sn Molar Composition (%)	25.8	28.5	29.9	30.0	30.0	± 1.83
Cu:Sn ratio	2.62	2.44	2.12	2.17	2.27	± 0.21

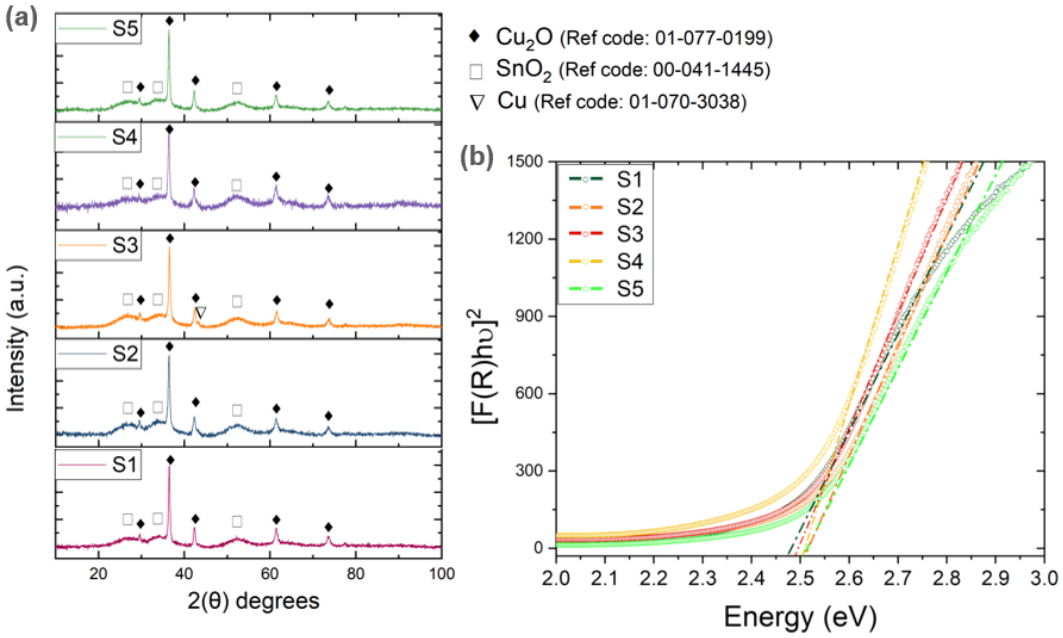


Figure 4.2 – (a) XRD pattern and (b) Tauc's Plots of the repeated samples (S1-5).

4.3.4 Electrodes preparation

The manufacturing process of the photo-electrodes was based on the preparation of a catalytic ink and its subsequent deposition on porous carbon support (Toray carbon paper 060) by airbrushing [64]. The ink consisted of three compounds: the Cu_2O-SnO_2 catalyst, Nafion as the particles binder, and ethanol as a carrier for improving the dispersion. The mixture was sonicated for 30 min until a uniform slurry was obtained. Each electrode was prepared with a catalyst loading of 1 mg cm^{-2} in 1 cm^2 of active area, which was completely illuminated with simulated sunlight during the test.

4.4 Catalyst characterization

4.4.1 Catalyst morphology

The catalyst was characterized on its physico-chemical properties, as synthesized and in the electrode after its testing, by different techniques. The XRD pattern of the synthesized Cu_2O-SnO_2 sample is shown in Figure 4.3. A cubic crystalline phase (cuprite) of Cu_2O (JCPDS 01-077-0199) is evident with the most intense peak (111) at 2θ value of 36.5°. No peaks related to CuO were observed in the diffraction pattern.

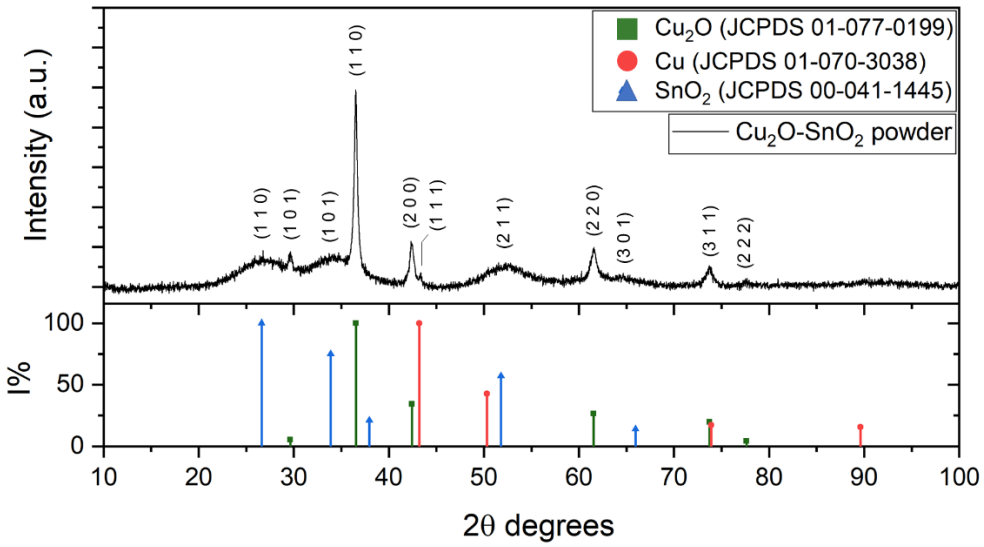


Figure 4.3 – XRD pattern of the Cu_2O-SnO_2 powder catalyst.

Metallic copper is also evident in a very small quantity, represented by the (111) peak at 43.3°, as a shoulder of the Cu_2O (200) peak at 42.3° (JCPDS 01-070-3039). Evidence of the SnO_2 presence (JCPDS 00-041-1445) was confirmed as well from its three most intense peaks at 2θ values of around 26.6° (110), 33.9° (200) and 51.8° (211), respectively. The presence of large bump distributed peaks, instead of a high intensity narrower shape, could lead to a double interpretation: (1) tin oxide could be in the sample with its amorphous phase, or (2) in so small sized crystallites that exhibits wide diffraction peaks because of their restricted number of reflection planes. TEM characterization was performed to better understand the morphological and structural properties of the catalyst in the bulk and at the Cu-Sn-oxides interfaces. The analysis of selected area diffraction patterns was carried out by means of the Circular Hough transform diffraction

analysis (A software tool for automated measurement of SAED patterns within Digital Micrograph) [193], and was superimposed on the SAED pattern, showing the position and size of the rings. They were compared to the reference patterns, and this confirmed the presence of polycrystalline Cu_2O, CuO and SnO_2 (JCPDS 00-005-0667, JCPDS 00-048-1548, JCPDS 00-041-1445 cards, respectively). BFTEM images shown in Figure 4.4a and Figure 4.4b evidence that various morphologies are present, namely large irregular particles and small particles, which is consistent with the FESEM observation. Large particles (100 nm) are decorated by smaller ones (1-10 nm). The large particles are not electronically transparent, therefore only limited signal can be detected from them both in TEM and in selected SAED analysis.

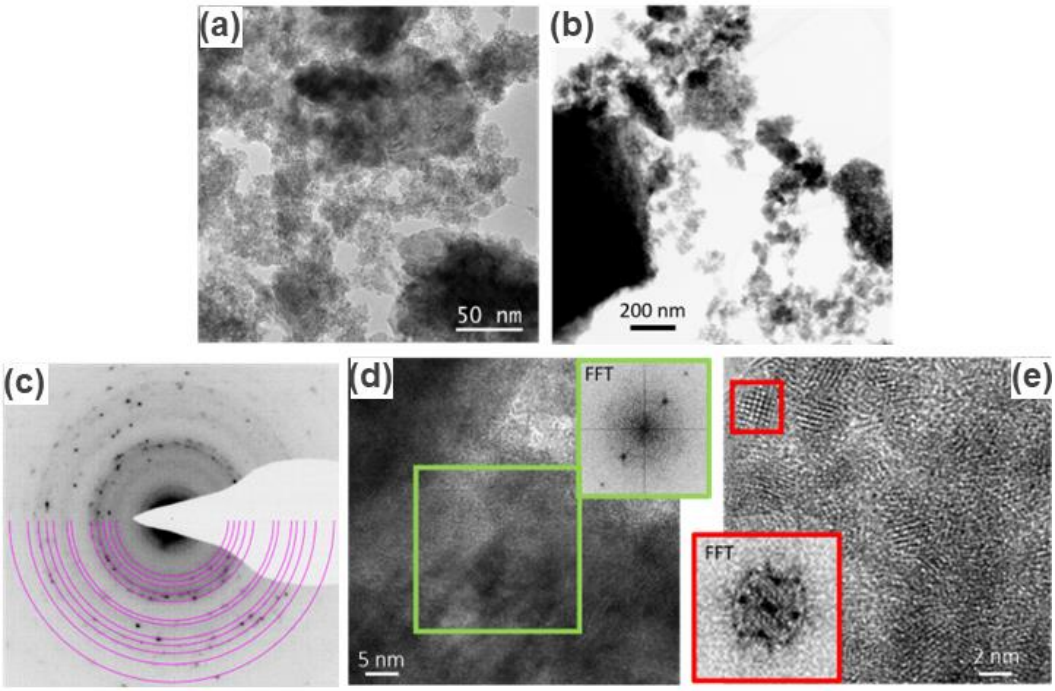


Figure 4.4 – (a) Bright-Field TEM low magnification image and (b) representative Bright-field TEM image; (c) the corresponding electron diffraction pattern and (d,e) High-Resolution TEM images with corresponding Fast Fourier Transform (FFT).

It was possible to determine the electron transparent regions that consist of edges of large particles and aggregates of nanoparticles, allowing for both the SAED analysis and HRTEM. The electron diffraction pattern in Figure 4.4c confirms the polycrystalline nature of the sample. Numerous reflections from various planes can be identified and ascribed to Cu_2O, CuO, and SnO_2 (JCPDS

00-005-0667, JCPDS 00-048-1548, JCPDS 00-041-1445 cards, respectively). The 1st most internal ring represents SnO_2 and it is diffused, so SnO_2 is present in amorphous phase with some very small crystallites. Cu_2O is represented by the 2nd ring with only several spots, relative to the largest particles. These are mostly not electron transparent and therefore do not contribute to SAED. The 3rd and more external rings are assigned to CuO. It disagrees with what was observed by XRD analysis. However, different results can arise from these two techniques since they investigate a different portion of the material and with a different sensitivity. XRD penetrates all the regions of the material under investigation, while SAED signal can be acquired from electronically transparent parts of the sample, therefore, the large particles are not investigated. Only their edges and small particles contribute to the SAED pattern. The HRTEM investigation was performed on large particles by studying their edges or corners (TEM visible parts of these) and on smaller separate particles. Figure 4.4d shows the HRTEM image of the edge of a large particle and the observed crystalline phase is confirmed by the Fast Fourier Transform (FFT shown in the inset) with interplanar spacing calculated from FFT of ~2.76 Å, which corresponds to (110) family of CuO structure planes. That agrees with SAED and suggest that a few amount of Cu^+ was oxidized to Cu^{2+}. Figure 4.4e shows HR-TEM image and corresponding FFT pattern of small crystallites, which can be found everywhere in the sample, and cover the large copper-based particles. This analysis confirms the presence of amorphous material and very small SnO_2 crystallites. It is in accordance with XRD, where a very broad peak for SnO_2 was observed, and SAED, where a high diffuse ring was detected. The morphology of the as-prepared Cu_2O-SnO_2 powder catalysts was studied by FESEM. As shown in Figure 4.5a,b,c the catalyst consists of an agglomerated and compact structure representing the bulk material, with surface decoration due to smaller particles (Figure 4.5b,c dimensions of around 20 nm). Within this peculiar structure it was possible to attribute to copper oxide the bulk section of the material and to tin oxide the outer components.

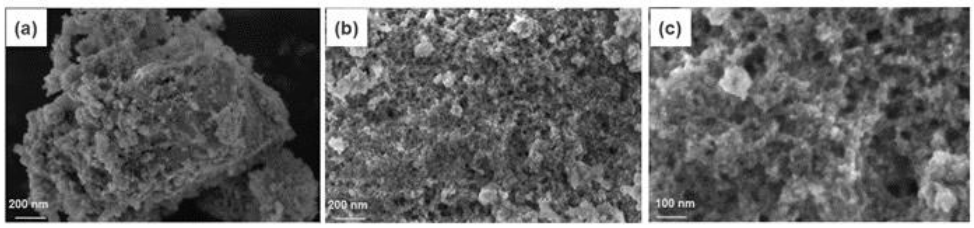


Figure 4.5 – FESEM images of the catalyst obtained at different magnification scale (a,b,c).

The morphologic hypothesis should be mirrored by comparing the results obtained with EDX and XPS techniques, performed to explore the elemental composition of the sample. Different regions of the sample were investigated to evaluate the average composition of the catalyst and the possible contaminants. Results are summarised in Table 4.2, in terms of atomic percentage of each element.

Table 4.2 – Comparison table of elements atomic percentage in EDX and XPS.

Element	EDX at.%	XPS at.%
Cu	27.9 ± 7.9	16.6 ± 0.6
Sn	13.5 ± 2.2	17.4 ± 0.5
O	57.6 ± 9.0	64.8 ± 1.1
Cl	1.0 ± 0.2	1.2 ± 0.8

From EDX, it appears that the initial ratio Cu:Sn = 2 was well maintained in the final product, while chlorine, a contaminant, was detected in very small quantities (less than 1.5%). The XPS survey spectrum of the final prepared catalyst was recorded, and the main peaks were observed at approximately 196.3, 485.1, and 931.6 eV, corresponding to Cl 2p, Sn 3d, and Cu 2p core levels. The Cu:Sn ratio detected by XPS settles on the value of 1, and chlorine species were found only in traces (1.2 ± 0.8%). The complementary information given by the two techniques allowed to better understand the composition of the material both in its bulk region (EDX) and on the surface (XPS). It appears that the stannous compound is mainly present onto the surface of the catalyst, constituting a protection layer to Cu_2O that can mitigate its reduction during the PEC CO_2 reduction test.

4.4.2 Copper oxidation state

Moreover, the optical band gap (E_g) of the samples was calculated by using the Tauc's method [194] from the F(R) spectra, obtained by using a spectrophotometer in the diffuse reflectance mode with an integrating sphere. The resulting plot can be observed in Figure 4.6. The obtained band gap value of 2.5 eV agrees with results found in literature on similar structures [195]. The increase in energy of the synthesized catalyst with respect to bare Cu_2O could be useful to

avoid photo-corrosion issues in aqueous solution during PEC CO_2 reduction tests, due to the redox reaction of Cu_2O itself [196,197]. Therefore, successfully ensuring a protective layer on the surface of Cu_2O could be the key factor for a long-timing life catalyst. Herein, the surface presence of SnO_2 led to an increase in the E_g value of the photo-electrocatalyst thanks to its higher band gap values (3.58-3.45 eV) [198]. The investigation on copper oxidation states at the catalyst surface was carried out by XPS analysis. The High-Resolution analysis of Cu species is shown in Figure 4.7a, and the doublet shape has been compared with values reported in the literature [199]. The presence of the well-known shake-up satellite found in Cu2p spectra is an indication of the presence of Cu^{2+} species.

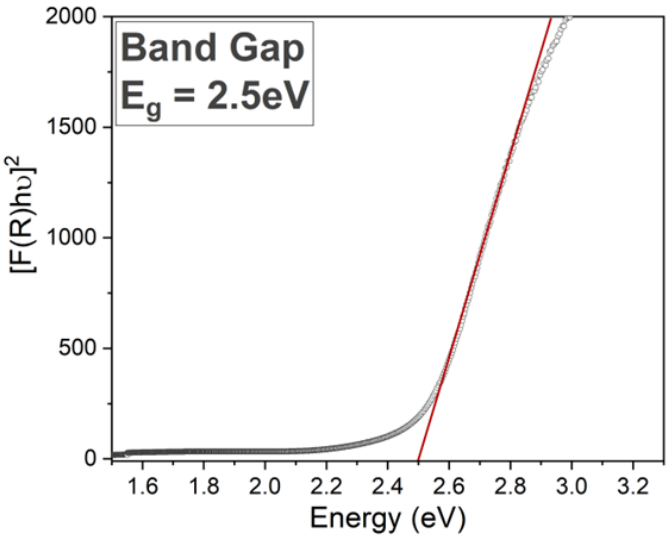


Figure 4.6 – Tauc's Plot for determining the material Band Gap.

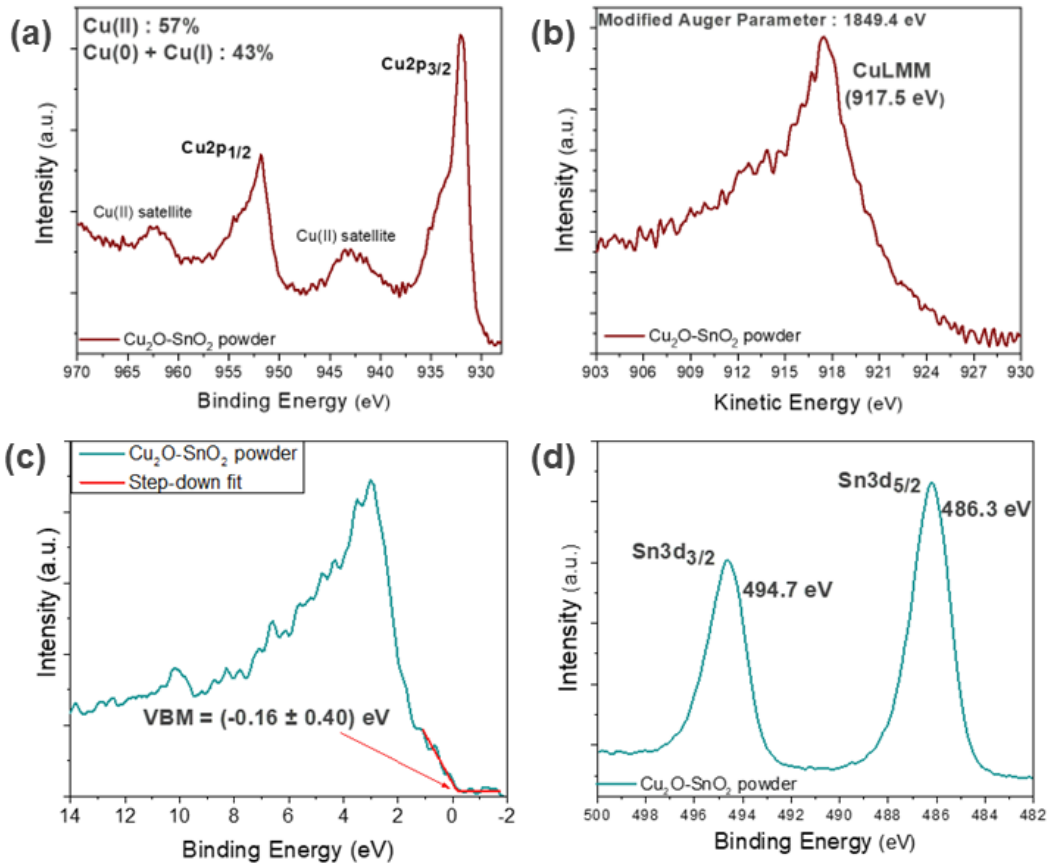


Figure 4.7 – XPS results of catalyst powder analysis: (a) high resolution $Cu2p_{1/2}$ and $Cu2p_{3/2}$ and abundance of copper oxidation states obtained from $Cu2p_{3/2}$ deconvolution procedure (not reported); (b) CuLMM spectra and Modified Auger Parameter value; (c) Cu_2O-SnO_2 Valence Band spectrum, linearly fitted in order to extrapolate the valence band maximum (VBM) position (red line), and (d) Sn3d doublet.

A deconvolution procedure [200], performed on $Cu2p_{3/2}$ peak and the related shake-up satellite to evaluate the relative abundance of Cu^{2+} and Cu^0 + Cu^+ oxidation states, led to the following results: 57% of Cu^{2+} and 43% of Cu^0 + Cu^+. In addition to the Auger parameter, the CuLMM peak shape (Figure 4.7b), can also be useful in revealing copper chemical states. It is particularly important when determining metallic Cu versus Cu^+. By using Equation 24:

Equation 24 – Auger Parameter

$$Auger\ parameter = hv - CuLMM + Cu2p_{3/2}$$

A value of 1849.4 eV was obtained. It was compared with the value of 1849.17 ± 0.03 eV referred to Cu_2O [201], thus enabling the average oxidation state of superficial copper in the whole sample to be assessed as Cu^+. Regarding the Sn oxide, the typical shape of XPS valence band spectra of SnO_2 (Figure 4.7c) with a maximum at ~2.5 eV is distinctive of Sn^{4+} and allow to distinguish it from Sn^{2+}, which has a similar binding energy position related to Sn3d doublet (Figure 4.7d). Based on the previous information, it can be affirmed that the desired Cu_2O-SnO_2 structure was obtained with the presence of some Cu^{2+} at the material surface, which could be due to the partial oxidation of the Cu^+ after the synthesis process. Finally, by means of XPS high resolution analysis in the valence band region, the valence band maximum position was extrapolated (Figure 4.7c), with a linear fit applied to the descending portion of the signal towards the 0 eV point, corresponding to the Fermi level. Due to the noisy signal of this region (which possesses a low emission cross section with X-ray source), the result obtained is affected by a huge standard deviation (–0.16 ± 0.40) eV. Thus, even if it was not possible to rely on this exact value, it can be stated that a change in the Cu_2O band structure was introduced, thanks to the outer SnO_2 modification, since a localised band bending was created, due to new available populated energy levels. The result of the p-n junction due to Cu_2O and SnO_2 interface, respectively, shows a new region which possesses an excess of electrons nearby the Fermi Energy level of the catalyst. Finally, the study of specific surface area and porosimetry of the material, calculated from N_2 adsorption/desorption isotherms, revealed a mesoporous structure, with a BET surface area value of 142 m^2/g, a pore volume of 0.12 cm^3/g and an average pore width of 5.9 nm, which were detected via BJH (Barrett-Joyner-Halenda Analysis) method. The high surface area and pore volume of the compound could be beneficial for the photocatalytic activity of the material.

4.4.2 Before PEC test electrodes characterization

The fresh Cu-Sn-based electrode was characterized on its superficial composition by XPS analysis before the tests, to ensure that the catalyst did not changed after the electrode preparation. Indeed, the deconvolution fit applied to the Cu2p spectrum, which allows to assess the relative abundance of Cu oxidation state, confirmed the previous results obtained in the powder, *i.e.,* 57% of Cu^{2+} and 43% of Cu^0 + Cu^+, as shown in Figure 4.7a. Also, from the HR CuLMM peak, the Auger parameter calculation (Equation 24) on the electrode confirmed that Cu^+ is the main average oxidation state of the fresh Cu-Sn-based electrode, with a value

of 1848.9 eV, perfectly in line with the one showed in Figure 4.7b for the catalyst powder. Therefore, it is possible to say that the procedure for preparation did not cause any changes in the oxidation state of copper. As a difference with respect to the powder sample, the presence of the Nafion fluorinated polymer, used as binder in the catalytic ink, was observed as C-F bonds that were visible in C1s spectrum (not reported).

4.5 PEC CO_2 reduction test

4.5.1 Setup and protocol

For the evaluation of the carbon paper (as the electrode support) contribution in the PEC test, the blank tests reported in Appendix A1 were taken into account. Then, the PEC behaviour of Cu_2O-SnO_2 catalyst was evaluated for the photo-electroreduction of CO_2 in an aqueous 0.1M $KHCO_3$ solution, while the whole setup was properly illuminated by a solar simulator. The setup used has already been described in Section 2.3.2. EIS tests were performed on the same setup as the PEC tests.

The measurement campaign comprises frequency sweeps from 10^6 Hz to 0.1 Hz of a 25 mV small sine signal superimposed over DC voltages from –800 mV vs. Ag/AgCl to –1500 mV vs. Ag/AgCl taking 100mV steps. Each campaign has been performed two times in a row on an unused sample to observe performance changes associated with catalyst reduction. Conditions have been varied between N2 and CO2 saturated electrolyte and keeping the sample under illumination or without it respectively, for a total of 4 measurement campaigns.

4.5.2 PEC results and discussion

The CV curves obtained by saturating the cell in N_2 or in CO_2 are shown in Figure 4.8a. The onset potential is the lowest potential value at which a reaction product is formed (a Faradaic current is measured) with a given electrode under defined conditions. The onset potential diminished by changing from the inert environment to the CO_2 saturated solution. In fact, there is a difference of around 0.2 V vs. RHE passing from N_2 (–0.67 V vs. RHE) to CO_2 (–0.46 V vs. RHE).

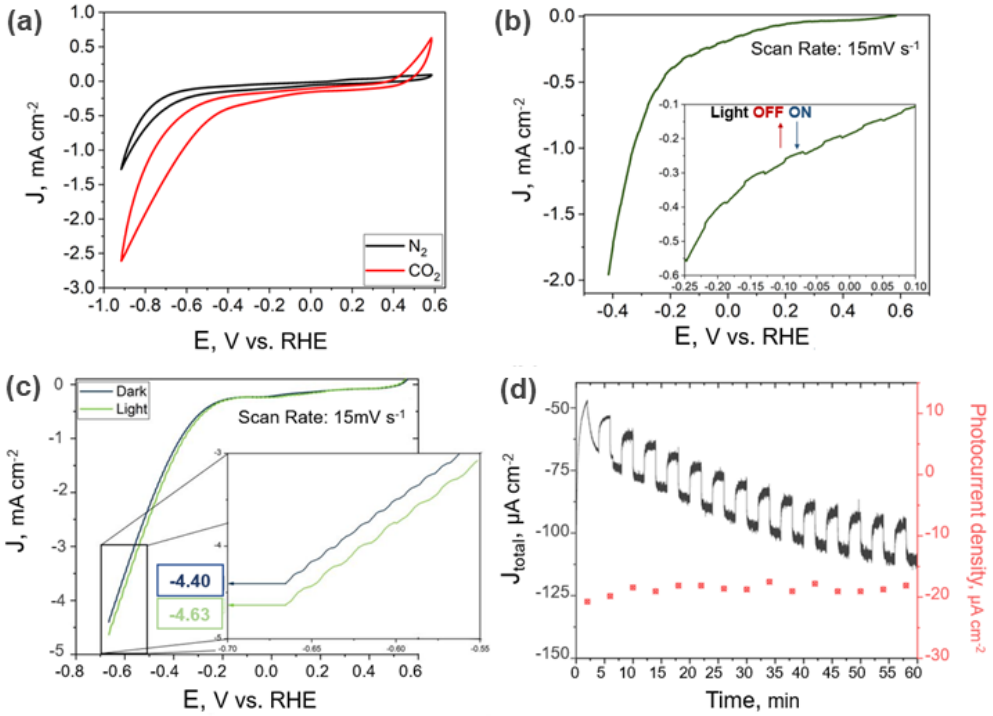


Figure 4.8 – PEC test of CO_2 reduction; (a) Cyclic Voltammetry performed in N_2 and CO_2 ; (b) Linear Sweep Voltammetry performed in CO_2-environment with chopped light; (c) Linear Sweep Voltammetry curves carried out in dark (blue line) and in light (green line) pointing out the different final *J* value due to light influence. (d) Chronoamperometry test performed at –250mV, pointing out the stability of the photocurrent density (red dots).

The reduced CO_2RR onset potential indicates a higher catalytic activity in CO_2 than in N_2 and the first H^+/e^- transfer to C-based intermediate species at the electrode surface [202]. Figure 4.8b shows the LSV pattern recorded with a scan rate of 15 mV s^{-1} under chopped illumination (Δt = 2s). The inset demonstrates the behaviour of the cathodic current under the effect of light at low potential values. It increases when light is on (blue arrow), conversely, it diminishes in dark conditions (red arrow). A sudden increase in the absolute photocurrent value was

observed during the enlightenment since a part of the energy required for the CO_2 reduction is currently provided by the internal photovoltage generated by the photocatalyst material under simulated sunlight illumination. This increment reached a maximum (0.02 mA) at about 0.1 V vs RHE. The onset potential was identified at –0.1 V vs. RHE at a current density value of about –0.3 mA cm^{-2}, and the photocurrent started decreasing at –0.2 V vs RHE, because the onset of the dark Faradaic current exceeds the photoactivity gain. A representative plot of photocurrent vs. potential is shown in Figure 4.8c. In this case, tests were carried out in totally dark conditions (blue line) and in totally light ones (green line) to assess the photocurrent contribution. The trends of both curves are very similar, especially until the onset potential point (around –0.25 V vs. RHE), which is slightly lower for the green line, indicating a higher activity towards CO_2 reduction in case of lighting. From that point up to around –0.65 V vs. RHE there is a moderate difference among them, finally showing the contribution due to light presence in the green one at the end of the plot. In Figure 4.8c inset, a magnification of that region is reported, clearly showing the corresponding current density values for both curves with the help of the two arrows. Here the contribution due to light counts for 23 µA cm^{-2}, so the current density value of the dark test is –4.40 mA cm^{-2} at –0.66 V (vs. RHE), while the one attributed to the light one is –4.63 mA cm^{-2} at the same potential. Chronoamperometry tests were led under the alternance of dark and light conditions by applying a fixed potential of –250 mV to show the catalyst photoactivity. As reported in Figure 4.8d, the photocurrent density was maintained stable for 1 h (red dots), as evidence of the whole system stability, even when the total current density trend seems to decrease (grey line). The net photocurrent density value stands to –18 µA cm^{-2}. As reported in previous works [203], the presence of SnO_2 coupled to Cu_2O showed improved performances with respect to the bare Cu_2O (Appendix A2), as another proof of the protection role proposed for tin oxide towards Cu_2O stability. It is possible to find an optimum between the external bias voltage or the applied current density and the photo-electrocatalytic CO_2 reduction conversion rate. The intent would be to perform the test so that, under the optimal bias voltage condition, separation efficiency of photogenerated electron-hole pairs reaches the maximum. It was demonstrated that, even if the external bias voltage continues to increase, the photo-electrocatalytic CO_2 reduction efficiency could no longer increase [204]. In our experience, by applying an excessive bias voltage a lower selectivity to the desired products was obtained, as well as an energy loss of the whole PEC CO_2 system. Thus, the effect of different values of applied current density was herein investigated (6 values were chosen ranging from –0.25 to –10

mA cm^{-2}) to find the best one for the photo-activated CO_2 conversion process. Figure 4.9 illustrates how the applied current density can affect the photo-electrochemical CO_2 reduction with the Cu-Sn-based electrode, in 0.1M $KHCO_3$ buffer solution, with CO_2 bubbling inside the cell and under simulated solar radiation.

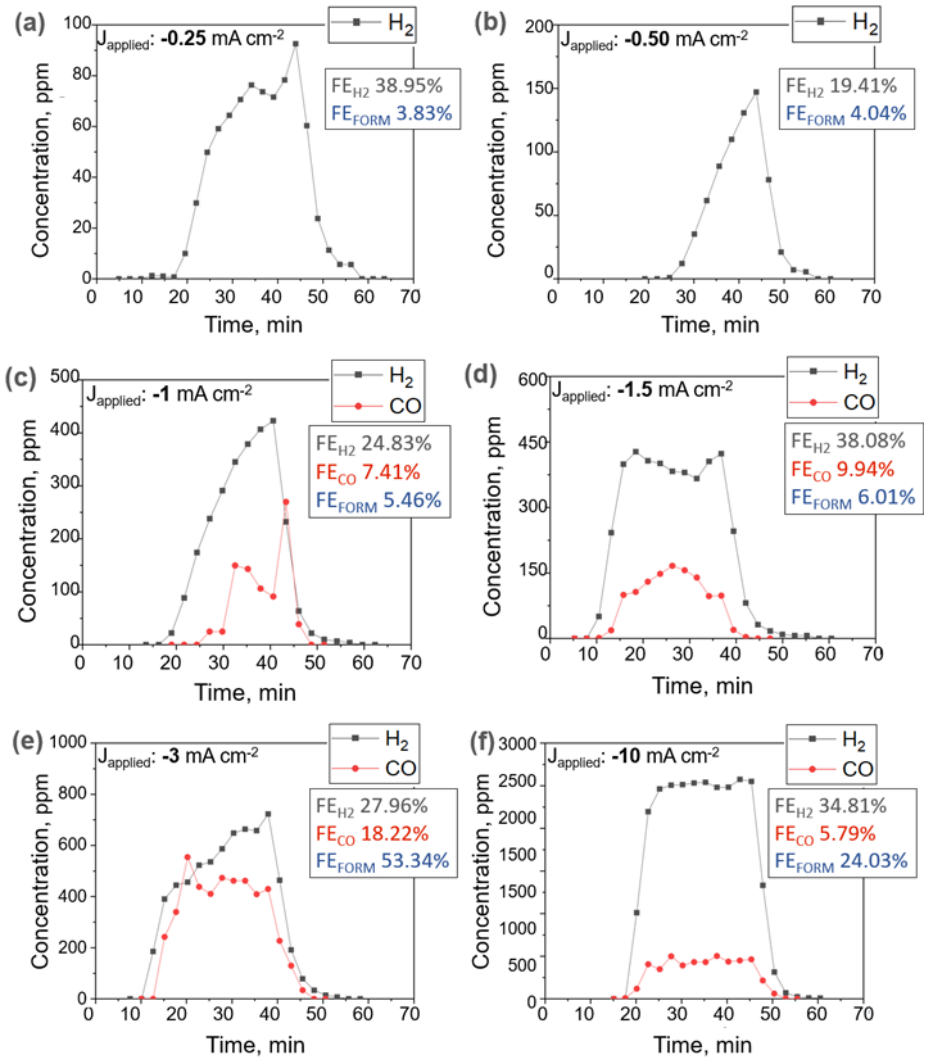


Figure 4.9 – Gaseous product evolution and summary of faradaic efficiencies for main products; values have been obtained in aqueous based electrolyte (0.1M $KHCO_3$) after 30 minutes long chronopotentiometries at different applied values of current density *J*, in particular: (a) –0.25 mA cm^{-2} , (b) –0.50 mA cm^{-2} , (c) –1 mA cm^{-2} , (d) –1.5 mA cm^{-2} , (e) –3 mA cm^{-2} , (f) –10 mA cm^{-2}.

The curves reporting the gaseous products evolution do not show CO formation by applying the first two current density values (–0.25 and –0.50 mA cm^{-2}), since it was within the sensitivity range of the technique. Only H_2 was

detected as product by the μ-GC, with Faradaic efficiencies values of 38.95% and 19.41%, respectively (Figure 4.9a,b). Formate was also revealed by HPLC with a Faradaic efficiency value of around 4% in both tests. Hydrogen production increased in a monotonous way while the current density was applied, and then it fastly decreased to zero. The CO was detected for an applied current density of –1 mA cm^{-2}, as shown in Figure 4.9c (red line), with a non-stable trend and a low Faradaic efficiency (*i.e.,* 7.41%). By increasing the applied current density, also the CO evolution curves become more balanced and stable during time, with no significant peaks or drastic diminishing during the 30-minutes lasting chronopotentiometries. We observed a steady behaviour also for H_2 during the tests carried out at –1.5 and –10 mA cm^{-2} (Figure 4.9d,f). In the first, the H_2 concentration exceeded the CO one of 3 times (450 vs. 150 ppm), in the latter of 5 times (2500 vs. 500 ppm). A different behaviour is reported at –3 mA cm^{-2} test (Figure 4.9e), during which the gaseous species present a parallel rise for the first half of the test, then H_2 intensifies its presence, up to 750 ppm, while CO remained stable until the end of the CP. In this test the calculated Faradaic efficiencies are about 28% for H_2 and 18% for CO. Besides, the presence of Formate (FE = 53%) is remarkable, the highest observed by scanning among the six current density values. Additionally, excessive bias voltage reduce the selectivity to C-based products and also increase the energy losses of the whole photo-electrocatalytic CO_2 reduction system. At high overpotentials, as for Figure 4.9f, the rate of CO evolution becomes lower than the H_2 one, probably due to the limited mass transport of CO_2 in the H-cell system. Therefore, the comparison of dark vs. light activity was made until –3 mA cm^{-2} of applied current density.

Figure 4.10a and Figure 4.10b exhibit the FEs achieved for the test carried out in dark and light conditions. The values were obtained by applying Equation 20 after a chronopotentiometry test of 2 h at two different current densities of –1 mA cm^{-2} and –3 mA cm^{-2}. In both cases, the CO_2 reduction products (mainly CO and formate) increased in lighting conditions. In fact, at –1 mA cm^{-2}, the FE toward H_2 decreased by 30% under illumination with respect to the dark test, while the total FE of C-based products doubled, reaching around 13%. A similar behaviour was also identified in the two tests at –3 mA cm^{-2}. The reduction of the FE_{H2} was observed under light conditions, but at such current density in a more limited way (decreasing from 23.5% to 20.7%). Respect to the previous case, a smaller increase (~ 18%) in the CO production was noticed under illumination at –3 mA cm^{-2}, reaching a FE_{CO} of 35.5%. The main differences are related to the other C-based products. Indeed, the FE towards formate increased by about four times (5.7% in dark vs. 19.6% in light) and ethanol, which was no detected among the

liquid products during the dark test, was produced with a FE of 9.3% under light irradiation.

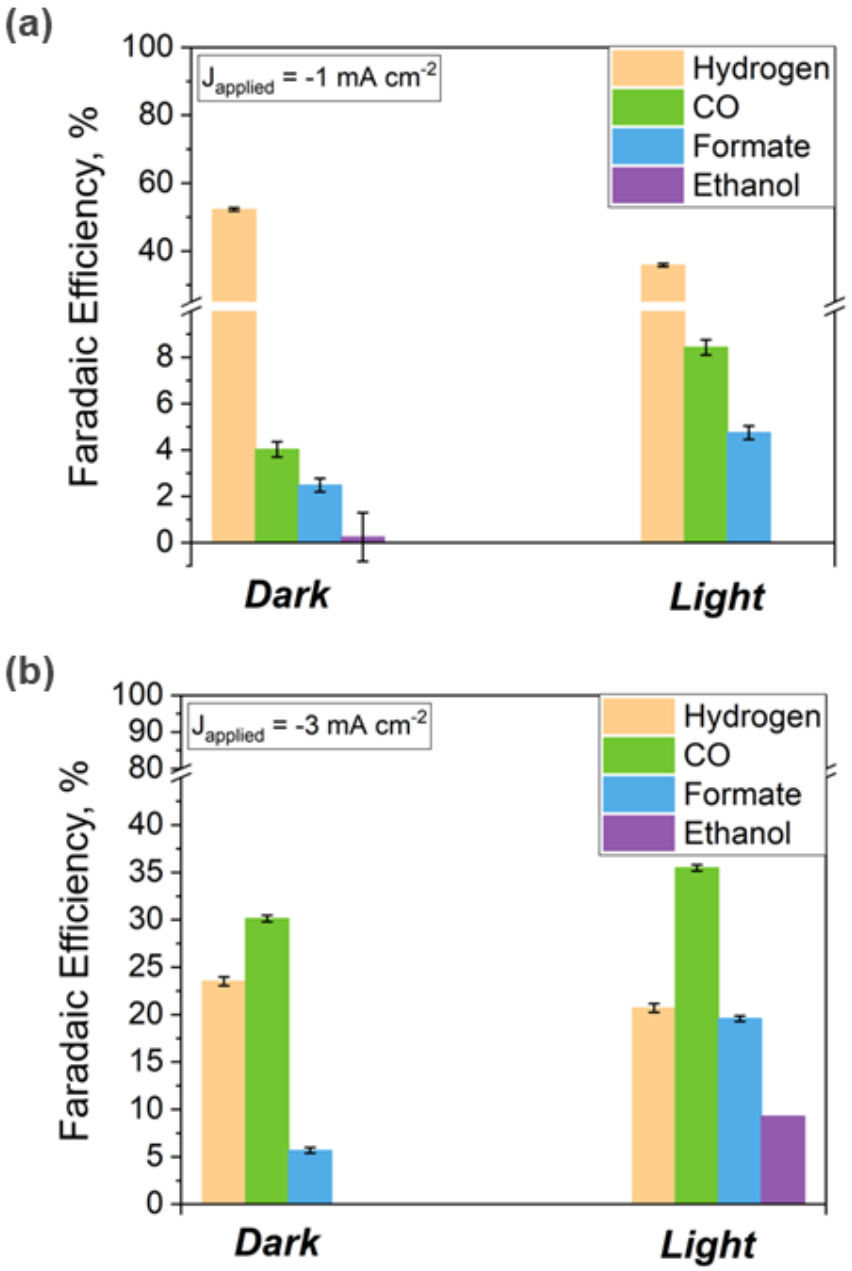


Figure 4.10 – FEs of gas and liquid products detected after a 2-hours Chronopotentiometry in 0.1M $KHCO_3$ aqueous electrolyte at (d) –1 mA cm^{-2} and (e) –3 mA cm^{-2}. For each current density value, the products are reported both for the test without and under illumination.

The rising value of FE_{CO} at expense of H_2 is reported also by Zeng *et al*. [95] during the electrocatalytic CO_2RR via a Cu-Sn-based foam. Moving from –0.5 to –0.6 V vs. RHE, they observed a FE_{CO} gain to ~15% while the FE_{H2} was more than halved. A similar trend was found by Zhang *et al*., [205] by using Cu_2O-nanowires as the bare catalyst and decorated with SnO_x particles, for syngas production. Herein, this phenomenon is also present for both bare Cu_2O (Appendix A2) and Cu_2O-SnO_2-based electrodes. In fact, more negative potentials led to a higher amount of CO with respect to H_2, since higher current density values lead to higher negative potentials (driving force) onto the electrode, which then favour CO_2 reduction over H_2 evolution. Finally, by comparing previous electrocatalytic versus PEC CO_2RR results, Zhang *et al*., [205] data showed higher FE values for CO under illumination with their Cu_2O nanowires, at every applied potential, confirming that the increase in the CO_2RR activity and selectivity are strongly influenced by the illumination, like in our experiments. On the other hand, their CO:H_2 ratio is higher than our results. They reached the maximum of ~4.5 by applying –0.35 V vs. RHE while herein a CO/H_2 ratio of 1.7 was obtained in the test at –3 mA cm^{-2}. This could be a starting point to further investigate the role of different applied potentials and current density values. Nonetheless, with the here reported synthetic approach, the here prepared Cu_2O-SnO_2 catalyst was selective for ethanol production at –3 mA cm^{-2}, which implies the more difficult C-C coupling, and more than doubled the FE to formate, if compared to Zhang and co-workers test. Therefore, we believed that the prepared Cu_2O-SnO_2 catalyst could be used not only in PEC CO_2RR processes to produce syngas but also for formate and other high value-added molecules production. In another work, Chen and co-workers [206] modelled the dependence of current densities of some CO_2 reduction products (H_2, CO, Formate) as a function of illumination intensity. They obtained that the current density for all the products increased as the illumination intensity increased. Moreover, the product distribution varied as a function of applied potential. That behaviour is because, with respect to dark conditions, the simulated sunlight provides an extra energy source that generates separated photocarriers and excite electrons that are then able to participate in the CO_2R reaction with lower external energy consumption, leading to easier production of C_1 compounds [204]. In addition, the use of visible light seems to be highly appealing for the photo-excitation of the CO_2 radical anion, known as the first activated intermediate specie of CO_2, before its reduction in a multi-step mechanism to produce either formate, CO, or C_{2+} products [207]. Indeed, C_2 products are expected to be favoured in the presence of Cu^+ and Cu^0 interfaces at the catalyst surface, which could promote dimerization of *CO or

*CH_x adsorbed intermediates [208]. On the other hand, the reason behind the not null dark currents is because CO_2 is converted even in dark conditions on Cu-based catalysts, whose performance is among the best that has ever been achieved for CO_2 electroreduction to > C_1 and multicarbon products [209,210]. However, herein, the CO_2 reduction is noticeably enhanced under light irradiation, thanks to the overpotential generated at the irradiated semiconductor/solution junction, which photo-generated electrons with the energy required for the CO_2 reduction into valuable products. Moreover, the SnO_2 presence on Cu_2O particles could provide extra states where photogenerated carriers could separate, instead of directly recombining and the photoelectrons can take part in the reduction reaction. Indeed, the stability reached in the 1-hour-long test could be proof of the inhibition of photo-corrosion of Cu_2O due to the transfer of photogenerated carriers.

4.5.3 After PEC test electrodes characterization

Ex-situ XRD and XPS characterisations were performed on the tested electrodes to investigate the modification of the copper oxidation state that occurred under the PEC CO_2R conditions. Both analyses demonstrated that the crystalline phase composition partially changed during the test. XRD analysis, shown in Figure 4.11a, is dominated by the contribution from the support, therefore, we focus on the part of the spectrum in the inset. The XRD characterization indicates that only two peaks attributed to Cu_2O remained visible in the diffractogram (36.5° and 42.4°) collected from the tested electrode. The remaining diffraction peaks refer to metallic copper (JCPDS 01-070-3039), such as (200), (220) and (311) placed at 50.3°, 73.9° and 89.9°, respectively. Moreover, XPS analysis on the tested electrodes in dark and light conditions are shown in Figure 4.11b. As a further confirmation of the change in oxidation state, XPS analysis of tested electrodes revealed a remarkable reduction of the Cu^{2+} and an increase in the Cu^{+}+Cu^{0} percentage, with respect to results obtained by analyzing the electrodes before the test. The presence of about 30% of Cu^{2+} and 70% of Cu^{+}+Cu^{0} was observed on both dark and light electrodes from the Cu2p HR spectra. Indeed, in most cases, the overall FE value is less than 100% and the partial reduction of the copper species could have partially contributed to the consumption of electrons. As it is well-known, previous Cu_2O-based photo-electrocatalysts for CO_2RR still suffer from poor stability due to the reduction of Cu^{1} to Cu^{0}. Further efforts are needed to enhance and maintain their current densities to significant values without losses in catalytic structure or changing of

morphology and oxidation states. However, Auger's parameters calculation (Equation 24) applied to CuLMM spectra of our tested samples (values of 1849.2 eV and 1849.1 for the electrode tested in dark and in light conditions, respectively) confirmed the Cu^{+} as the average oxidation state of Cu at the catalyst surface.

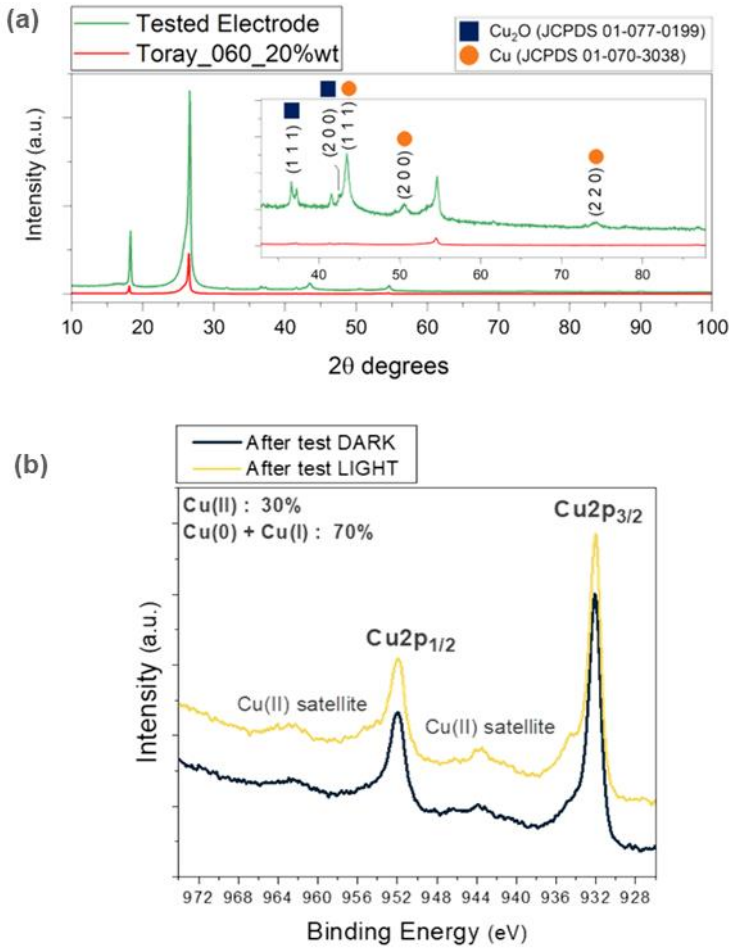


Figure 4.11 – (a) XRD pattern of Carbon Paper (electrodes support) (red line) and the electrode with the Cu_2O-SnO_2 catalyst after the test under light conditions (green line). In the inset the peaks attributed to the catalyst are reported and labelled; (b) XPS High-Resolution spectra of two electrodes one after a test in dark (blue line) the other after a test in light (yellow line), focusing on the copper peaks.

Hence, although in the catalyst bulk, the Cu_2O was reduced to Cu^0 (as shown from the XRD data), the XPS results demonstrate how valuable the here reported synthesis method is to incorporate SnO_2 as a protector of the Cu^{+} superficial states.

4.5.4 EIS analysis

The EIS analysis was carried out, based on the circuit model described in Figure 2.4, in Section 2.2.3.3. In this specific case, the R1 resistance modelled the electrodes contacts, the R2/CPE2 parallel circuit accounted for the charge transport while the R3/CPE3 parallel modelled charge transfer at the interface. The parameters of each part of the circuit were adjusted to make the circuit best match the real system. The R1 part of the circuit did not change across different conditions tested, while the two other parts showed a more complex behaviour. The R3/CPE3 part of the circuit was the most important in determining the overall shape of the electrical measurements, while the R2/CPE2 part was important in making sure the shape was symmetrical.

Results from the EIS analysis confirmed some insights and provided new topics. R3 and T3 values (Figure 4.12a and Figure 4.12b, respectively) showed an order of magnitude difference between N_2 and CO_2 saturations, confirming that the catalyst has an overall current gain due to CO_2R. Both trends decreased across many orders of magnitude as potentials get more negative in a logarithmic scale. This behaviour was associated with charge transfers limitations related to reaction mechanisms [211] and thus it confirmed the choice of R3/CPE3 as the rate-determining component. Interestingly, repeating the measurement provided two distinct trends. The first part of the campaign had lower resistance/time constant values than the "*post*" one at the start of the campaign. The two trends then reached similar values only at the last 2/3 DC potential values. The behaviour was interpreted as a confirmation that the Cu_2O catalyst reduced to Cu^0 during the first part of the measurement, and it became fully reduced when the second part began, which would also explain why the "*post*" measurements had a more stable trend and followed a clear exponential trend. Constant phase β values were found to be very stable across every potential, saturation and illumination condition. β3 values, associated with the electrode electrolyte interface, ranged between 0.7 and 0.85, confirming that the R3/CPE3 parallel behaved similarly to an ideal RC circuit. On the other hand, β2 values ranged between 0.45 and 0.30, indicating that the conduction inside the bulk of the catalyst resembled that of a common resistor. R2 values further confirm that the R2/CPE2 parallel was related to conduction processes, as resistance values were stable across every potential value and illumination condition.

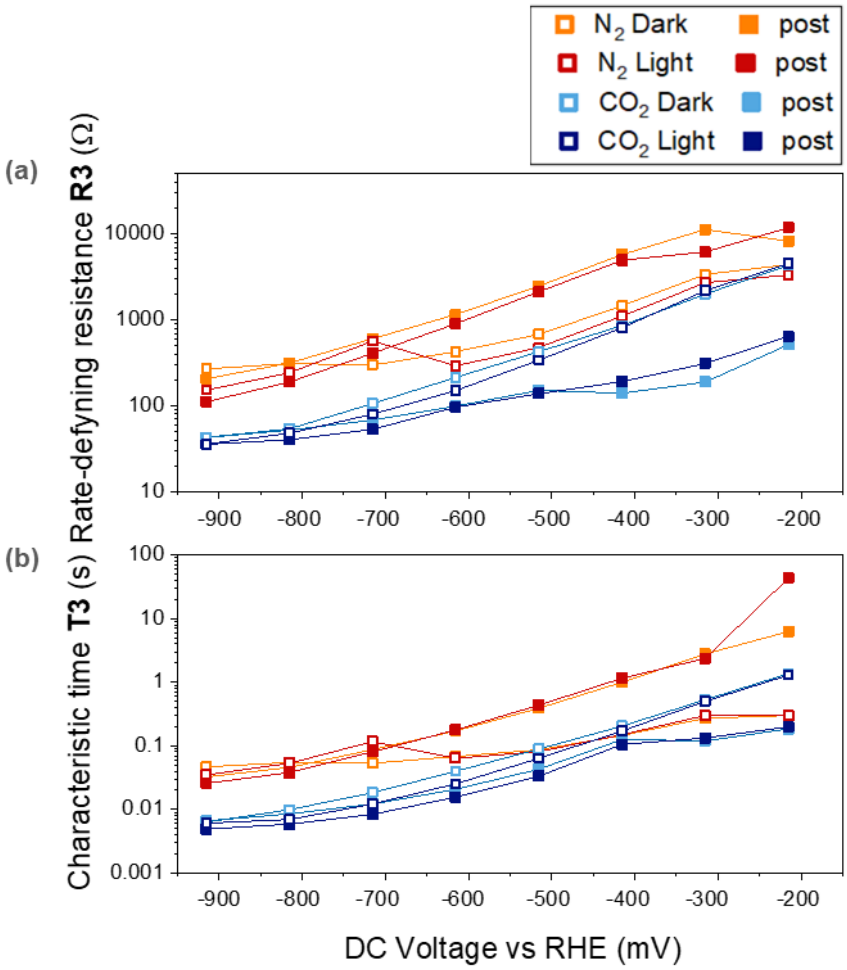


Figure 4.12 – EIS analysis results: (a) values of rate-defining resistance R3, (b) characteristic time T3 obtained via fitting operations.

4.6 Conclusions

In this study, a facile, scalable, and reproducible method for the synthesis of a Cu_2O-SnO_2 catalyst was developed. The samples were characterized and analyzed using various techniques, and it was discovered that Cu^+ was the main copper oxidation state, with no notable traces of contaminants in either the bulk or surface of the catalyst. To understand the impact of light on product formation, PEC CO_2 reduction tests were performed both in dark and light conditions, resulting in an improvement of C-based compound production under illumination. To the best of our knowledge, this study is among the first to investigate the trend of gaseous and liquid C-based products with Cu_2O-SnO_2 nanoparticle-based catalysts, demonstrating the role of light in promoting C_1 (CO and formate) and

C_2 products like ethanol at low potential values. This result is significant for tuning the catalyst selectivity towards desired CO_2 reduction products. The catalyst restructuring was also examined, with a focus on the changes in copper oxidation state. It was found that Cu^+ was the average oxidation state on the surface of the tested electrodes, confirming the effectiveness of the synthesis approach in stabilizing Cu_2O by SnO_2 nanoparticles. However, the future tuning of the synthesis process parameters to modify particle size may be necessary to enhance the number of superficial sites and limit bulk Cu formation. Additionally, long-term stability at high current densities remains a challenge. Nevertheless, due to the high abundance of their precursors, Cu and Sn, and the unique photo-catalytic properties, the developed catalyst holds promise as a platform for utilizing solar energy and converting CO_2 into useful products.

Chapter 5

Core-shell Cu_2O-SnO_2 photo-electrocatalyst for the CO_2RR: comparison with co-precipitation and new features

The Chapter 5 presents a novel synthetic approach for the production of a Cu_2O-SnO_2 catalyst that is suitable for use in PEC CO_2 reduction. The core-shell approach was selected based on previous successful studies. The core was made of Cu_2O, which is abundant, cheap, and photoactive, while the shell was composed of SnO_2. The authors compare the morphology and PEC performance of the new catalyst with a previously developed one that employed co-precipitation. They found that the photoactivity of the Cu_2O-SnO_2 catalyst was improved by 30% compared to the previous catalyst, and its activity was also greater. Additionally, the new approach allowed for a finer tuning of the ratio of metallic precursors. Overall, the Cu_2O-SnO_2 core-shell catalyst offers a versatile platform for CO_2 reduction, providing improved selectivity, activity, stability, and control over the reaction environment, while also reducing costs.

Contributions: This work has received funding from the European Union's Horizon 2020 Research and Innovation Action program under the Project SunCoChem (Grant Agreement No 862192). In particular, the task involved was

the one dealing with cathodic photo-electrocatalyst development and testing. The new synthetic route was developed by the PhD student in collaboration with two Master students, Antonio Bucci and Giacomo Alloatti. Their thesis were entitled:

"Development of Cu-Sn-based photo-electrocatalysts for the CO_2 valorization" by A. Bucci, supervised by S. Hernández, N. Russo, Politecnico di Torino, academic year: 2020/2021

"Design and testing of a Cu-based photocathode for CO_2 reduction in aqueous electrolyte" by G. Alloatti, supervised by E. Vittone, S. Hernández, Università degli Studi di Torino, academic year: 2020/2021

Many of the physico-chemical characterizations were carried out in collaboration with partners from "Dipartimento di Scienza Applicata e Tecnologia" (DISAT) and "Istituto Italiano di Tecnologia" (IIT), in particular Dr. Angelica Chiodoni and Dr. Katarzyna Bejtka supported the PhD student in the FESEM, XRD, data collection and curation. The ICP-OES facility was owned by Dr. Peter Bogdanoff, from Helmholtz-Zentrum Berlin. The methodology and the experimental procedure was discussed together with Ursula Michalczik, then the calibration lines were obtained by the PhD student. The PhD student performed the synthesis and the reproducibility assessment, presented and critically analyzed the results of the characterization techniques and their correlation with the data analysis of photo-electrocatalytic CO_2 reduction tests on *H-type* cell, equally carried out by the student. The photo-electrochemical testing protocol was validated in collaboration with Dr. Hilmar Guzmán and Prof. Simelys Hernández. The assictance provided by Dr. Adriano Sacco (IIT) was critical in comprehending and assessing the electrochemical impedance spectroscopy (EIS) outcomes, as well as in refining the experimental technique employed to gather the data.

It is worth noting that part of the work elucidated in this and the previous Chapter, represents a paper entitled "Cu_2O/SnO_2 heterostructures: role of the synthesis procedure on the PEC CO_2 conversion", by Maddalena Zoli, Hilmar Guzmán, Adriano Sacco, Nunzio Russo, Simelys Hernández, which was accepted on Materials.

5.1 Core-shell nanoparticles (CSNs)

The field of nanotechnology has seen significant progresses in recent years, leading to a new understanding of conventional heterogeneous catalysts [212,213]. Through the use of nanotechnology-enabled processes, catalytic materials can now be prepared with great precision, including the synthesis of nanoparticles containing noble metals as active catalytic components with well-defined sizes, shapes, crystal facets, structure, and composition. This level of control over materials structures has the potential to lead to the development of new technologies for applications in green, sustainable, and economically-viable chemical processes [214]. Core-shell nanostructures, also known as CSNs, have traditionally been defined as composite nanomaterials consisting of cores (inner material) and shells (outer layer material) at the nano-scale [215]. With the growing interest in task-specific nanomaterials with multifunctional capabilities and enhanced properties, CSNs are increasingly gaining attention for their versatile compositions and structures that make them suitable for these various purposes. Furthermore, the unique properties of CSNs can be synergistic between the cores and shells and/or offer new properties depending on the interactions between them. These useful and tailorable properties have made CSNs an emerging class of nanomaterials for a wide range of applications like fuel cell, dye sensitized solar cells, and many important catalytic processes. The development of highly active and selective, robust, low-cost and environmental-friendly catalytic systems is a significant challenge faced in the field of catalysis. The advantages offered by core-shell nanostructures include [216]:

i. using the core as a support to create specific nanoarchitecture on the surface of the shell, leading to superior catalytic performance;
ii. the potential for synergy between the shell and core to increase efficiency, yield, and selectivity in catalytic applications;
iii. the ability to combine the properties of the core and shell for improved or combined applications (*e.g.,* magnetically separable nanocatalysts that can be reused without loss of efficiency).

The (photo)-electrocatalytic activity of these materials relies on the synergistic interactions between the core and shell. Three major effects can play a role in determining the activity of these materials [216]: (a) ligand effect, which involves the interaction between the core and shell due to their proximity, affecting charge transfer and altering band structures; (b) ensemble effects, which are influenced

by the material's adsorption on the surface due to the presence of distinct atomic groups; and (c) geometric effects, resulting from the differing reactivity of surface atoms based on their three-dimensional structural constraints. The characteristics resulting from the core or shell materials can be very dissimilar. Either the constituent materials or the core to shell ratio can be changed to alter the characteristics [217]. The attributes of the core particle, such as reactivity or thermal stability, can be altered by the shell material coating, increasing the core particle's stability and dispersibility. The work presented in this Chapter and in the following ones originates from these assumptions.

A general classification of these materials was provided by Chaudhuri and Paria [218], dividing them into two main categories: organics and inorganics. The "organic" class refers to carbon-based materials, mostly polymers, while the "inorganic" class includes metal, metalloid, and metal salt NPs. Into the class of metals-based CSNs, regarding the synthesis process, the bottom-up approach is more suitable because it allows for better control over uniform coating of the shell materials during particle formation. A combination of both approaches can also be used, such as core particles synthesized by the top-down approach and then coated by a bottom-up approach to ensure uniformity and control over the final product.

5.2 Core-shell synthesis method

The idea behind this particle design was to create Cu_2O particles in the form of cubic nanoparticles, and then add a thin layer of SnO_2 on top of them. The SnO_2 layer should protect the Cu_2O particles from reduction, allowing them to perform CO_2 reduction for a longer period of time. The novelty of this process is the use of a synthesis method called "coordinated etching", which was first introduced by Wang *et al.* [219] as a low-cost method to create hollow micro/nano structures. This method uses Cu_2O nanocubes as a template to grow the SnO_2 layer, by dissolving the tin oxide precursor $SnCl_4$ in an aqueous solution containing the Cu_2O nanoparticles. Such solution contains CuCl, formed as intermediate by adding the Cu_2O NPs in a NaCl aqueous solution by coordinating Cu^+ with Cl^-. Zhang *et al.* [220] later modified the synthesis method and presented it as a versatile way to synthesize materials for CO_2 reduction as a catalyst. They modified a well-established method for synthesizing Cu_2O nanoparticles by wet precipitation and adjusted the coordinated etching process to allow for growth of tin oxide without fully dissolving the Cu_2O particles.

5.2.1 Reagents

Copper(II) chloride ($CuCl_2$, 99%), sodium hydroxide (NaOH, ≥98%), L-ascorbic acid ($C_6H_8O_6$, ≥98%) were used in the Cu_2O nanocubes synthesis. To perform the second step of the synthesis, the previously obtained Cu_2O nanocrystals were dispersed in ethanol (C_2H_6O, ≥99.8%), they were mixed with tin(IV) chloride pentahydrate ($SnCl_4 \cdot 5H_2O$, 98%) as tin oxide precursor, and a sodium chloride (NaCl, ≥99.5%) solution to favour ion exchange. All the reagents were purchased from Sigma-Aldrich (Milan, Italy), and they were used as received, unless otherwise specified. Cellulose nitrate membrane filters (purchased from WhatmanTM), with a pore diameter of 0.2 μm, were used for the vacuum filtration step. Ultrapure type 1 water (MilliQ) was utilized to prepare all the aqueous solutions and for cleaning of dedicated glassware and instruments. A silicone oil (purchased from Sigma Aldrich) bath was used to keep the temperature constant. Potassium bicarbonate ($KHCO_3$, 99.7%) and potassium hydroxide (KOH, 98%) were chosen to prepare the catholyte and anolyte, respectively. Nafion® 117 solution (5 wt.%) and ethanol were employed in the preparation of the catalytic ink. The support for the electrodes preparation was Toray carbon paper 060.

5.2.2 Synthesis method

In this study, the Cu_2O-SnO_2 core-shell nanocrystals were produced through a simple and affordable two-step synthesis method consisting of wet precipitation followed by a modified coordinating etching process. This method can be done in a laboratory beaker under atmospheric conditions, making it ideal for scaling up.

5.2.2.1 Cu_2O nanocubes

The synthesis started by making 500 mL aqueous solution of copper(II) chloride 0.02 M. The solution was placed in a beaker, stirred with a magnetic stirrer ARGOlab M3-D. 50 mL of a 6 M NaOH solution were added dropwise as precipitation agent, causing a rapid change from light blue to a dark blue colour. The solution was kept under stirring for 30 minutes at room temperature, resulting in the formation of blue particle agglomerates. Then, the reducing agent was added, 50 mL of 1.8 M ascorbic acid solution, and the solution slowly transition to a bright orange colour. The reactor was left to age for 3 hours under continuous stirring. The orange precipitate was collected by vacuum filtration onto cellulose nitrate membrane filters, and MilliQ water was added in increasing amounts

during the process to avoid contaminants. The precipitate was dried at 60 °C for 12 hours into a Buchi in-vacuum oven, to remove residual water without affecting the Cu oxidation state. The resulting Cu_2O powder was involved in the second step of the procedure. The reported synthesis method for the Cu_2O nanocubes creation was chosen after a study on the molarity and volume of the reagents solutions. Further details can be found in Appendix A2.

5.2.2.2 SnO_2 shell

The Cu_2O powder from the first stage was dispersed in a 150 mL ethanol solution. 4.5 mL of a 0.2 M NaCl solution were added with a quantity of tin oxide precursor ($SnCl_4 \cdot 5H_2O$) that was determined based on the desired ratio with respect to Cu_2O. In order to understand the role of SnO_2 shell within the PEC CO_2 reduction, the synthetic strategy involved the change of the Cu_2O to $SnCl_4$ precursor ratios during the second synthesis step. The ratios varied from 200:1 to 3:1, and five different samples were created. These catalysts were labelled as CS*x* depending on the molar ratio between the two precursors (the sample with the Cu:Sn ratio equal to 200:1 was named CS200). The Cu to Sn molar ratios of the synthesized catalysts were determined by using ICP-OES. Results are listed in Table 5.1 in next Section. The theoretical ratio was optimized through experimentation during the work. Once the ratio was fixed, the previously obtained precursors solutions (Cu_2O in ethanol and SnO_2 added by NaCl in ethanol) were slowly mixed while stirring. The process was completed in 10 minutes, after which the synthesized particles were separated from the solution by centrifugation and vacuum drying, resulting in a bright orange powder.

5.3 Catalyst characterization

In this Section, firstly some analysis onto Cu_2O nanocubes are provided. Then, the main aim of the preliminary characterization of the 5 different Cu-Sn-based catalytic samples was to assess:

i. the real amount of Sn (%) into the samples,
ii. the effective presence of a coverage made of SnO_2,
iii. the crystalline phases constituting the samples.

5.3.1 Cu_2O Nanocubes characterization

To determine the crystal phase of the as-synthetised Cu_2O nanocubes, the sample was characterized before undergoing the second synthesis step. The results

of X-ray diffraction analysis are shown in Figure 5.1a. The diffractogram showed a perfect fit with the Cu_2O pattern (JCPDS 01-077-0199). The most intense peaks corresponded to the (111), (200) and (220) orientations, corresponding to the angles at about 36.5°, 42.5°, and 52.6° respectively. Although the sample is polycrystalline, an analysis of the (111) peak/(200) peak intensities has been done, obtaining a value of 3.35 and indicating the preferential growing of the crystals towards the (111) orientation. Moreover, unlike what was observed for the co-precipitation sample, some usually less intense peaks, like the (211) and (222) planes, were here clearly recognisable. No traces of peaks attributed to the other copper phases are present, meaning that the synthesis method is completely suitable for obtaining the desired Cu_2O crystalline phase.

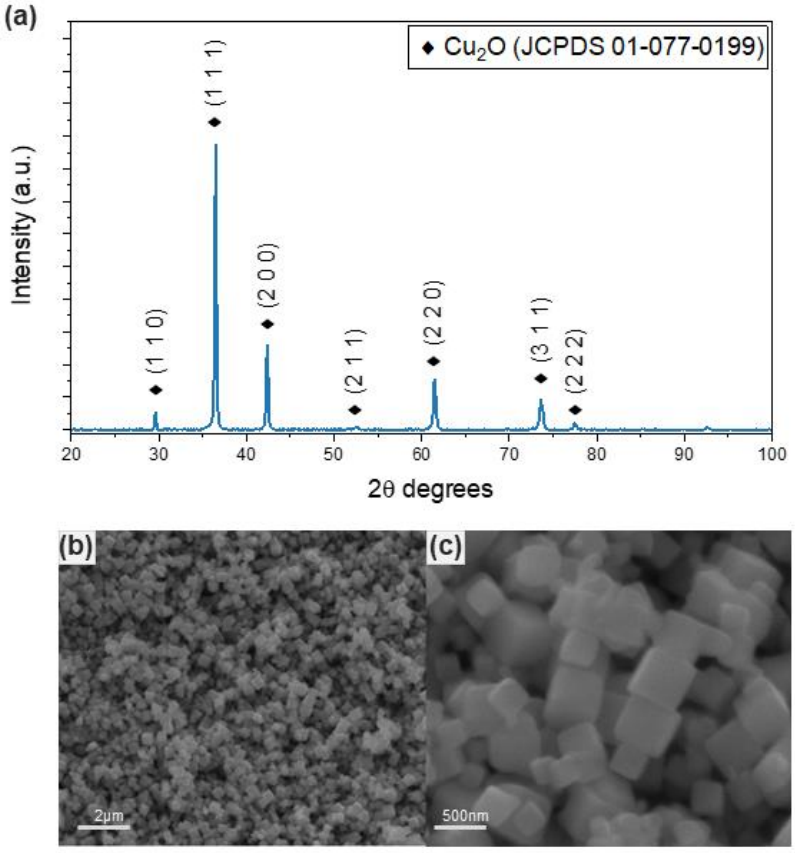


Figure 5.1 – Characterization of Cu_2O nanocubes; in particular: (a) XRD pattern, and (b) (c) SEM images at two different magnification.

The morphology of the nanocubes was obtained by a FEI Inspect SEM and the micrographies are reported in Figure 5.1b,c. From both the pictures it was possible to appreciate the smoothness of the nanocubes surface, according with

what reported by Zhang and co-workers [220]. Cubes dimensions vary (Figure 5.1c) from hundreds to less than 100 nm. Also EDX was performed onto the sample, by investigating different regions of the sample. The only two elements detected, as expected, were Cu, with an atomic percentage of 66 ± 2, and O, resulting in a value of 33 ± 2%. From the value of specific surface area measured by N_2 physisorption analysis and calculated by the BET method it was noticed that the bare Cu_2O samples prepared by the here employed technique did not show mesoporous behaviour. For this reason, only the adsorption curve was analyzed in order to obtain the value of 4.29 ± 0.03 m^2/g as BET area. Lastly, the optical band gap of the bare sample was determined with the Tauc's method, by analyzing the F(R) spectra acquired from the spectrophotometer in diffuse reflectance mode with an integrating sphere. The obtained Energy Band Gap value, as reported in Figure 5.2, is E_g = 2.43 eV. The value is slightly higher than literature value of ~ 2.17 [221,222], but such difference may be due to the nanometric dimension of the particles. As reported by Huang [223], the properties of materials change depending on the size, leading to the value of ~2.2 eV for the Cu_2O bulk, and ~2.5 eV for the cubes.

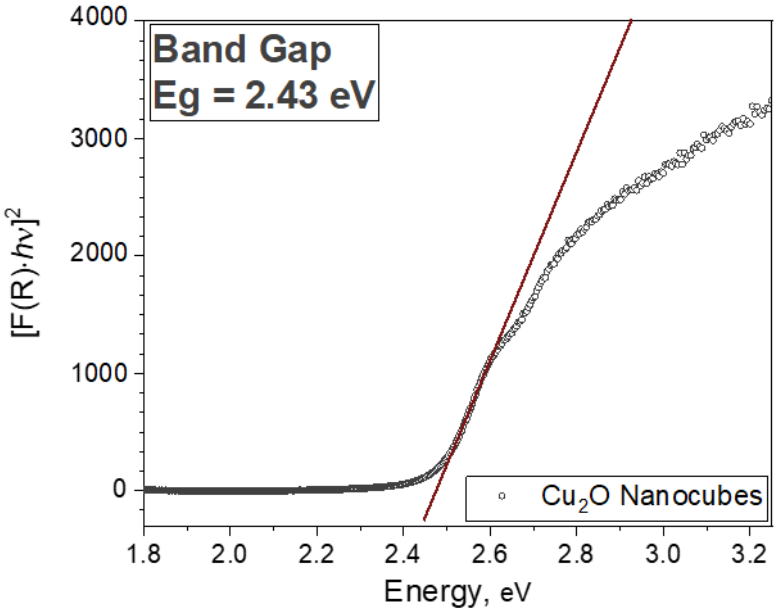


Figure 5.2 – Tauc Plot for the Cu_2O nanocubes band gap energy determination.

5.3.2 Cu_2O-SnO_2 characterization

The molar ratios of bulk copper and tin in the as-synthesized catalysts were determined by using inductively-coupled plasma optical emission spectrometry (ICP-OES). The instrument worked with a ThermoFisher system (ICAP 7000) using QTEGRA software, for which use Dr. P. Bogdanoff and U. Michalczik, from Helmholtz-Zentrum Berlin are acknowledged. The chemical attack was carried out onto a heating plate placed into a chemical hood. The treatment consisted of solubilising about 100 mg of each sample in a mixture of 60% HCl, 20% HNO_3 and 20% HF and maintain it under stirring for 1 hour at 100 °C. After the cooling down of the solution, the solution was diluted with MilliQ water in order to obtain a concentration of 1-5 ppm of each analyte. Then the samples were inserted into the instrument. A calibration line for each analyte was prepared and standard samples were made to run into the instrument. The prepared calibration lines were reported in Figure 5.3a and Figure 5.3b, respectively, for the Cu and the Sn detection. Also the blanks were evaluated, in particular one sample contained only MilliQ water, one the acidic mixture with no metallic samples addition, having undergone the same heating treatment of the real samples. The results provided a clear and concise picture of the Cu to Sn molar ratios in the catalysts, which are crucial for evaluating their performance and determining their suitability for CO_2RR. In Table 5.1, the atomic percentage of the two metals (Cu and Sn) detected into each sample were reported. The samples were named as in the first column of the Table, on the basis of the Cu:Sn ratio detected within each of them (last column).

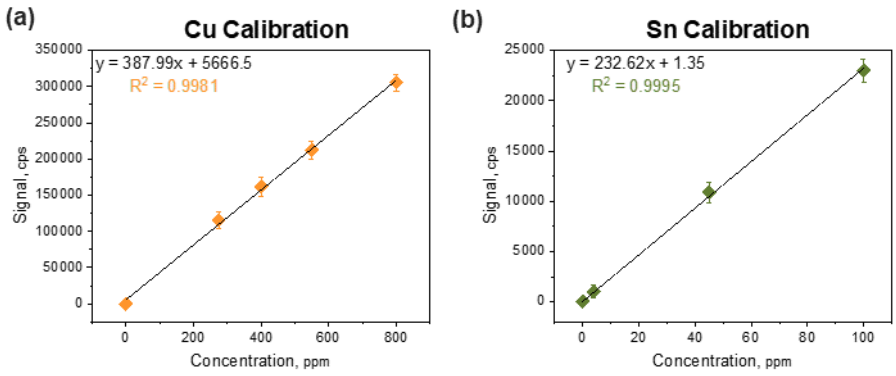


Figure 5.3 – Calibration lines of: (a) Cu and (b) Sn for the ICP-OES detection of metal amounts into catalytic samples.

Table 5.1 – Measured Cu and Sn bulk concentrations in Cu_2-SnO_2 catalysts. In the sample name CS*X*, *X* stands for the molar ratio between Cu and Sn, as reported in the last column.

Sample Name	at.% Sn (detected)	Cu:Sn Ratio
CS200	0.45	200:1
CS65	1.43	65:1
CS12	8.01	12:1
CS5	16.44	5:1
CS3	23.43	3:1

After assessing the Sn amount into the samples, the investigation proceeded towards understanding the morphological and structural modifications of the sample after the addition of the external shell. From the comparison between XRD analysis of all the samples (see Figure 5.4) and the Cu_2O and SnO_2 peaks intensities, it can be observed a different behaviour than the one observed in the co-precipitation sample. In this case it was not possible to detect the peaks related to SnO_2, not even wide and largely distributed as in Figure 4.3 in the co-precipitation sample diffractogram. For all the five samples the Cu_2O main peaks, (111), (200), and (220) are the most intense ones, and they are placed at 2θ of 36.5, 42.3, and 61.5 degrees, respectively. No evidence of SnO_2 was found in any of the samples. A notable difference was observed in the diffractogram of sample CS65. In this case, the presence of additional peaks in comparison the other samples was detected. By studying the diffractogram, such peaks were attributed to Cl_2, (JCPDS 01-073-2104, as reported in the picture). The black circle indicates the (112) peak of Cl_2, positioned at 2θ of 32.7 degrees. It was hypothesized that the presence of Cl_2 was due to an error occurred during the second synthesis step, where the tin chloride precursor was used to create the outer shell. Instead a contamination during the first step (formation of nanocubes) can be ruled out since the Cu_2O particles from the same synthesis batch were then subsequently used for the formation of CS65 and CS200, and the latter does not present similar peaks related to chlorinated species.

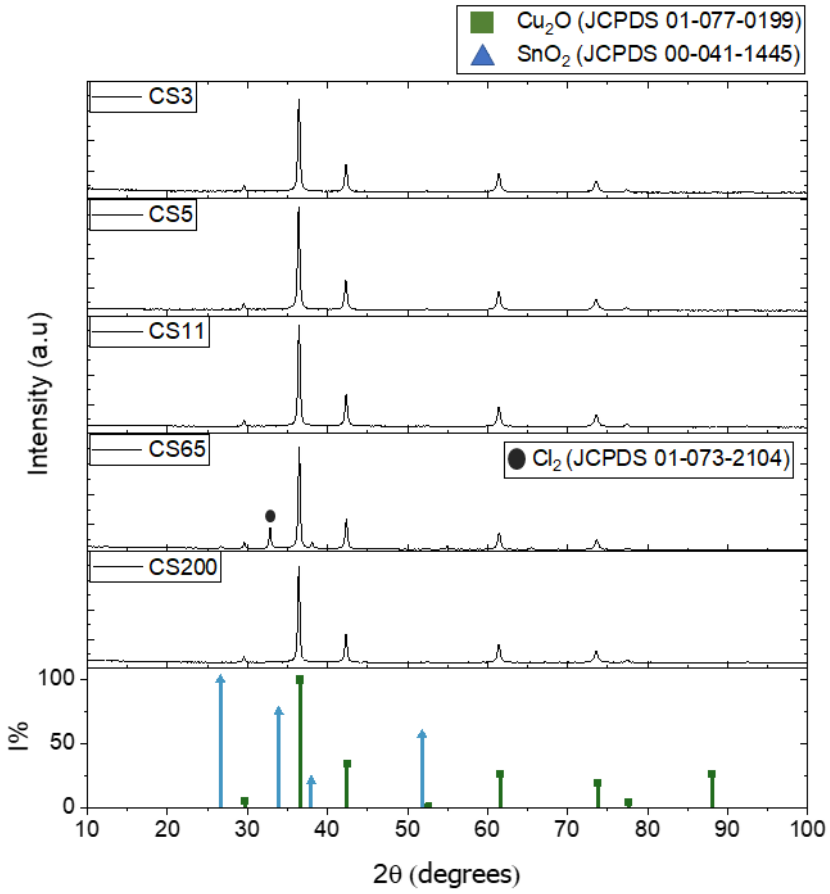


Figure 5.4 – XRD of core-shell samples; from the top: CS3, CS5, CS11, CS65, CS200. The graph placed lower down the figure reports the relative intensities of the Cu_2O and SnO_2 peaks (green and blue lines, respectively).

Focusing on the noticeable changes, in terms of morphology and structure of the catalyst after the creation of the outer shell, it is worth to examinate the morphology of the coated nanocubes. In particular, the sample CS11 was characterized as it was considered more promising to investigate a higher amount of Sn in the catalyst. Results in terms of FESEM analysis and Band Gap Energy calculations are reported in Figure 5.5. It is straightfoward to observe the difference between the Figure 5.5a, representing the core-shell structure, and the Figure 5.1b,c, which reports the bare nanocubes. Indeed, from the core-shell FESEM micrography, an increase in the thickness of the cubes, the disappearance of the smoothness from the nanocubes precursors, and the formation of roughness and generally a less ordered coverage of the material is visible. This was consistent with the hypothesis that the tin oxide surface layer was amorphous, as suggested by XRD results. Along with this, the BET surface area also confirmed

that the particles surface increased its roughness because of the addition of SnO_2. It was observed that the very low surface area stated in the previous paragraph increases to around 61 m^2/g.

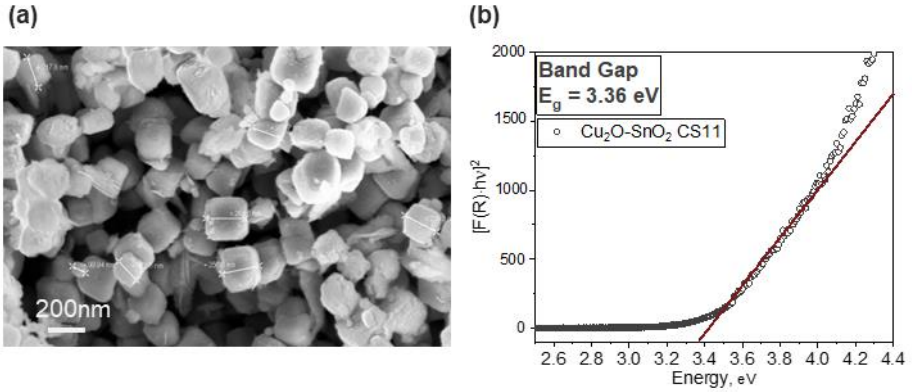


Figure 5.5 – Morphology (a) image obtained by FESEM and Tauc method calculations (b) for E_g determination, for the sample CS65.

In addition to the morphological changes described, it was possible to assess the structural change of the catalyst. The band gap energy determined via Tauc's method accounted for 3.36 eV, about 1 eV higher with respect to the bare nanocubes (2.43 eV). In this case, the influence of SnO_2 on Cu_2O was predominant. In fact, the band gap energy of SnO_2 is reported to be approximately 3.60 eV [187]. Although the catalyst evolved towards a structure with a higher band gap, thus characterized by decreasing ability to absorb solar radiation, this change in synthesis strategy and catalyst structure was applied to ensure greater protection to Cu_2O. In principle, longer stability should allow to maintain the photoactivity, even during longer tests.

In the next Sections, such hypothetical improvement in protection is assessed, confirming if this design choice had a positive impact, and whether the synergy of the two semiconductor materials effectively enhanced the performance for CO_2RR.

5.4 PEC CO_2 reduction test

The manufacture of photo-electrodes followed the same procedure as described in Section 4.2.4, *i.e.,* deposition on a porous carbon support by airbrushing of the catalytic ink. The tests were performed in the same setup described in Section 2.3.2. The test protocol, as stated in Section 4.4.1, was

designed to characterize the photoactivity of the different catalysts, aiming at maintaining their stability over time and avoiding damage due to currents or potentials applied. The results are discussed below, both in terms of the photoelectrochemical characterization of the various synthesized core-shell samples and of the comparison of the two synthetic routes employed for producing Cu_2O-SnO_2.

5.4.1 Core-shell Cu_2O-SnO_2 PEC results

In this Section, the results of the preparatory tests performed on the Cu_2O-SnO_2 catalyst synthesized through the core-shell synthesis are reported and commented. The cyclic voltammetry and linear sweep voltammetry tests are showed, and foremost the focus was on comparing the catalyst activity between a N_2-saturated environment, therefore in an inert atmosphere, and a CO_2-saturated one. The plots reported in Figure 5.6a,c were the result of a bare Cu_2O catalyst tests, while the ones in Figure 5.6b,d referred to a sample with a Cu:Sn ratio of about 3.

The results of cyclic voltammetry scans, performed at a rate of 30 mV s^{-1} from 0 to –1.5 V vs. Ag/AgCl, were depicted in Figure 5.6a,b. Comparable results were achieved, suggesting a correlation between the onset potential and the increased catalytic activity towards CO_2RR in a CO_2-saturated environment, as opposed to water splitting. In Figure 5.6a, investigating the bare Cu_2O by setting at the J value of –0.5 mA cm^{-2}, the onset potential for the N_2-saturated experiment lied at around –1.15 V vs. Ag/AgCl, while it decreased to –1.05 V vs. Ag/AgCl in presence of CO_2. Also the maximum current density value reached followed the same trend, increasing in the CO_2 saturated electrolyte (–6.3 vs. –4.5 mA cm^{-2}) due to CO_2 reduction. The presence of a small peak placed at around –1 V vs. Ag/AgCl in the red curve was reported also in similar tests carried out by Roy *et al*. [224] on mixed Cu-phases (Cu^{2+} and Cu^{+} oxides) supported on Ni electrodes. They found, in absence of CO_2, two reduction peaks at −0.6 V and −1.0 V, which were attributed to the transition of CuO to Cu_2O and Cu_2O to Cu, respectively. Instead, when the electrolyte was saturated with CO_2, the only reduction peak was at −1.0 V vs. Ag/AgCl, which they ascribed to the CO_2 reduction [225]. The same behaviour was observed during our test of Cu_2O-SnO_2 catalyst, as reported in Figure 5.6b. By placing at J = –0.5 mA cm^{-2}, the onset potential slightly moved to –0.75 V, and to –1.25 V vs. Ag/AgCl respectively for CO_2 and N_2-saturated test.

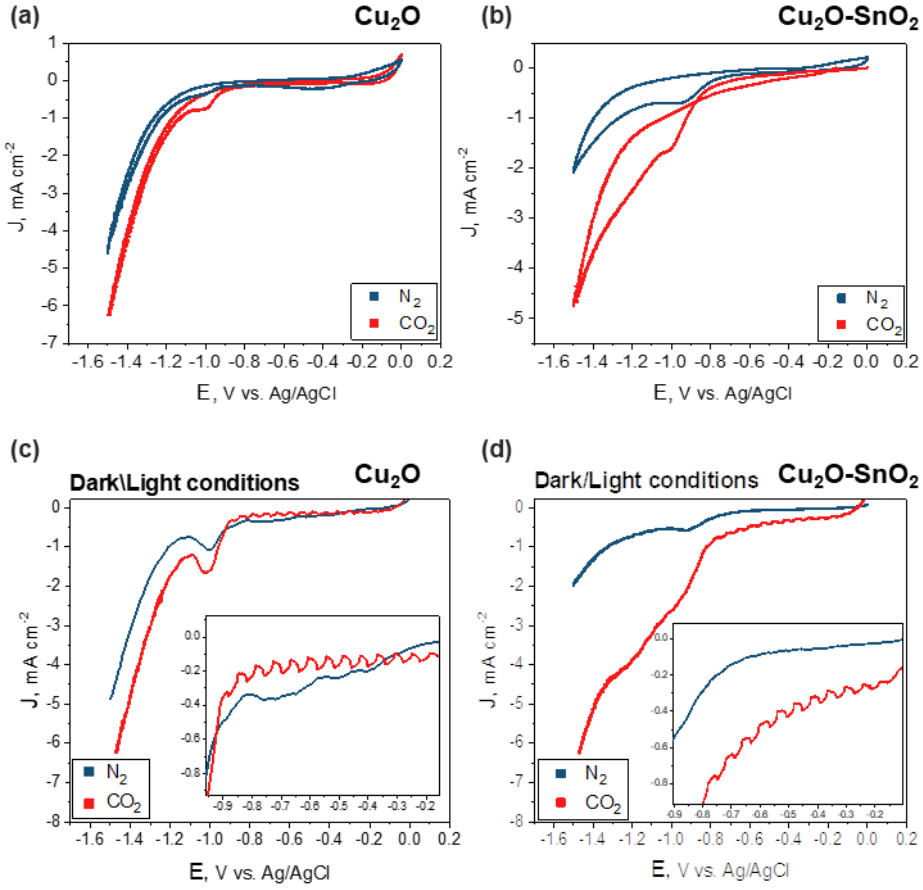


Figure 5.6 – Photo-electrocatalytic tests carried out in N_2-saturated environment (blue lines) and CO_2-saturated one (red lines). In particular (a) CV of a bare Cu_2O catalyst, (b) CV of the core-shell Cu_2O-SnO_2 one at the same conditions. (c) LSV of the bare Cu_2O catalyst and (d) LSV of the core-shell Cu_2O-SnO_2 at the same conditions.

Finally, the maximum of current density in CO_2-saturated electrolyte reached a value of around –5 mA cm^{-2} at –1.5 V vs Ag/AgCl, significantly higher than the value in N_2 environment (around –2 mA cm^{-2}). Our results lied within the same range of values as that obtained by Chang *et al.*, [226] who tested Cu_2O-catalysed carbon cloth in an electrolyte slightly more basic than 0.1M $KHCO_3$ assessed in this work. Instead, the current density was considerably lower than the one reported by Roy and co-workers [224]. We attributed such difference to their mix of Cu oxidation states, obtained from heterostructure of Cu^+ and Cu^{2+} with different synergistic relations, thus improving the functional characteristics of the material. When a SnO_2-shell of protection for the Cu^+ is absent, copper can undergo some phase change due to the testing protocol or the atmospheric

oxidation, leading to higher overall current density value, as observed by Roy *et al*. Instead, when the Cu^+ phase is well stabilised and protected by the outer shell, as in our case, the global *J* value remains lower, as observed in Figure 5.6b, but the stability of the material is guaranteed to be longer.

Moving to LSV results, the tests carried out on bare Cu_2O and Cu_2O-SnO_2 were compared in Figure 5.6c and in Figure 5.6d respectively. The photoactivity was evident in both tests carried out in CO_2 saturation. Slightly higher photoactivity values were ascribed to the bare Cu_2O because of the enhanced photoactive properties of the material without the SnO_2 coverage. In both tests it could be noted that the photoreactive behaviour persisted only up to around –1 V vs. Ag/AgCl, where the peak due to the CO_2 adsorption was detected. The two N_2 tests led to rather different results in terms of maximum current density reached. In fact such value decreased from about –5 mA cm^{-2} for bare Cu_2O to –2 mA cm^{-2} for the complete core-shell. This could be an indication that Cu_2O alone behaves as a photoelectrocatalyst even in water splitting reactions, as confirmed in the pioneering work by Hara *et al.* [227].

5.4.2 Comparison: Cu_2O-SnO_2 co-precipitation vs. core-shell

The catalysts compared in this Section were generally named "co-precipitation" and "core-shell". More specifically, they are: a new synthetic batch of the "co-precipitation" catalyst described in Chapter 4, and the core-shell one previously named CS3, which in this paragraph will be generically referred to as core-shell. Such study aimed at comparing catalysts characterized by comparable quantities of Cu and Sn (the ratio Cu:Sn was 2 in co-precipitation and 3 in core-shell samples). The idea behind the comparison was to validate if it could be preferred to shift to this novel synthetic design.

In particular, the focus was on the photoactivity of the two materials, especially evaluated via LSV (Figure 5.7a) and Chronoamperometry tests (Figure 5.7b) The parameters for the LSV were set from 0 to –1.5 V vs. Ag/AgCl, and the cell was saturated with CO_2 for around 30 mins. The solar simulator was pointed on the photo-electrode and light/dark conditions were alternated every 2 seconds. By observing the *J* value of –0.5 mA cm^{-2}, the co-precipitation sample (CP, green line) was characterized by an higher onset potential around –1.0 V vs. Ag/AgCl, than the core-shell one (CS, orange line) which was exhibiting a lower value (–0.6 V vs. Ag/AgCl). Thus, the CS sample enabled CO_2 reduction at lower potentials with respect to the CP one. As a consequence, current density values were overall

lower in the CS sample. A *J* value of around –4 mA cm^{-2} was reached in the CS sample at –1.5 V vs. Ag/AgCl, while –6.5 mA cm^{-2} was observed on the CP one by applying the same potential. The LSV curves showed the typical wavy pattern (increase/decrease) due to the dark/light alternance. It can be observed in the inset of the figure that the CS sample exhibited more defined steps due to a bigger gain in photocurrent. Moreover, even after the onset potential, the CS sample showed a wavy pattern, differentiating from the CP sample, for which the increasing of dark Faradaic current exceeded the photoactivity gain. To determine the stability and the effective photocurrent contribution due to the material, the chronoamperometry tests were performed.

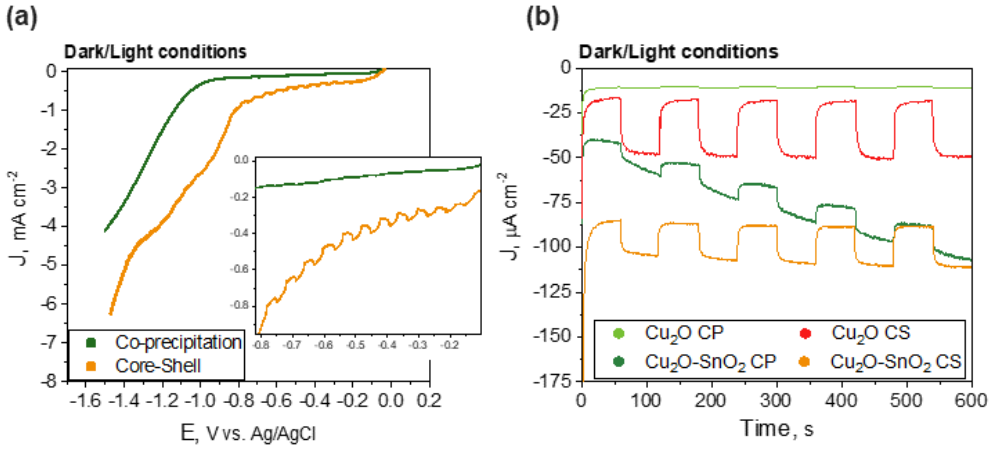


Figure 5.7 – Comparison of co-precipitation and core-shell Cu_2O-SnO_2 results; in particular: (a) LSV curves and (b) CA curves of the CP (green) and CS (orange) samples, together with Cu_2O samples obtained via co-precipitation (light green) and core-shell synthesis (red).

Instead of evaluating the stability of the material with a 1-hour lasting test (as performed in Section 4.4.2, Figure 4.8c), the catalysts performance was examined with a shorter test, as shown in Figure 5.7b. The chronoamperometry tests were set at a applied potential of –0.2 V vs. RHE, with a duration of 10 minutes for each test. Four different samples were compared, including the bare Cu_2O obtained with the two syntheses (light green line for co-precipitation and red one for core-shell) in addition to the Cu_2O-SnO_2 samples (dark green and orange line for co-precipitation and core-shell, respectively). Investigating the two samples obtained via the co-precipitation synthesis, the results generally agree with those of Chapter 4 and Appendix A2. The bare Cu_2O CP revealed a photocurrent gain value of 6 µA cm^{-2}, which could be ascribed to the progressive reduction of the Cu_2O species to Cu^0, and the consequent loss of photoactive properties (Appendix

A2). Instead, the SnO_2-modified catalyst presented the same photocurrent value obtained in Figure 4.8c, *i.e.,* 18 μA cm^{-2} and the decreasing trend of its curve (dark green) was in line with the findings of the previous Chapter. This result indicated the progressive reduction of the photoactive species during the chronoamperometry test, also confirmed by the enhancement of the dark Faradaic current in comparison to the constant photocurrent gain. Focusing now on the catalysts synthesized by the core-shell method, both curves were more stable over time, unlike what was observed for Cu_2O-SnO_2 CP. This could indicate the ability of the core-shell synthesis to provide a more stable and functional SnO_2 protection layer if compared to the co precipitation method. The fact that the photocurrent gain observed on Cu_2O was greater than the one of the Cu_2O-SnO_2 catalyst (~31 μA cm^{-2} vs. 24 μA cm^{-2}) was motivated by the respective band gap (smaller for Cu_2O than Cu_2O-SnO_2) as observed the Tauc plots of Section 5.3 (Figure 5.2 and Figure 5.5b). In fact, a larger band gap implied that more energy was required to excite an electron from the valance band to the conduction band and hence light of a higher frequency and lower wavelength was required [228]. If the band gap is too high, most photons will not cause photovoltaic effect, causing worse performance in the CO_2RR.

To sum up, by analyzing the materials developed in these works from a photoactivity perspective, it can be concluded that performance improvement as achieved with a rational synthesis design, moving from co-precipitation to core-shell route. Inside this latter case, although the photoactive performance slightly decreased due to the creation of the outer shell, the stability of the material over time was gained. This capability interestingly made the catalyst a candidate for further technological developments. Also, the overall current density values reached (dark + light) were higher (in absolute value) for the CuSn-based catalyst, confirming a boost in efficiency compared to those previously tested in CO_2RR.

5.4.3 Screening of 5 core-shell samples

After the first optimization of the core-shell synthesis and the first characterization steps, a large effort was made to understand the dependence of the catalytic performances on the Cu_2O-SnO_2 precursor ratio.

The tests carried out, whose results are reported in Figure 5.8, were: (i) LSV with light/dark alternation scanning from 0 to –1.5 V vs. Ag/AgCl, to understand the presence of photoactivity; (ii) then a subsequent CA, –0.2 V applied vs. OCP during 10 minutes in light/dark alternation, to quantify the photocurrent gain and

evaluate the trends; (iii) finally a CP for two hours by applying –3 mA cm^{-2} and completely exposing the catalyst to light. Following this last, the Faradic efficiencies of gaseous and liquid products were calculated by using Equation 20 as reported in Section 2.4. All the test above-described were carried out in CO_2-saturated environment. The bare Cu_2O coming from another synthesis batch was also considered in the creation of these plots.

Linear sweep voltammetry curves of each sample in Figure 5.8a showed the evidence of photoactivity, reporting the typical wavy pattern. Interestingly, the maximum value of current density achieved was due to the bare Cu_2O, because of its intrinsic enhanced behaviour in CO_2 reduction even under dark conditions, with a value of around 4.5 mA cm^{-2}. After that, the trend was not univocally linear. The second highest value was referred to the CS3 sample, characterized by the biggest amount of Sn, followed by the CS200, the most similar to bare Cu_2O because of its low Sn percentage. Probably, the effects of SnO_2 stabilization of Cu_2O (due to the tin amount in CS3 sample) competed with the catalytic activity of Cu_2O or analogous phases with similar CO_2 reduction properties. The result was in line with previous ones obtained by Brito *et al*. [229], where Cu/Cu_2O mixed film reached comparable current density values after a LSV test in a 0.1 M sodium sulfate electrolyte under illumination. The CS200 (pink line) evidence a broad reductive peak at around –1.1 V vs. Ag/AgCl, and a similar but less evident behaviour for the CS65 (green line). S. Nakayama [230] reported a very similar peak in a system made of mixed copper oxidation species ($CuO/Cu_2O/Cu$) as a working electrode, the Ag/AgCl as the reference one, and an electrolyte solution of KCl 0.1 M. The parallelism with CS200 and CS65o samples could be due to the fact that they presented a very thin SnO_2 protection layer. They may have undergone a reduction or change of the crystalline phase present on the electrode surface during the previous PEC tests, then presenting themselves as Cu species with different oxidation states during LSV.

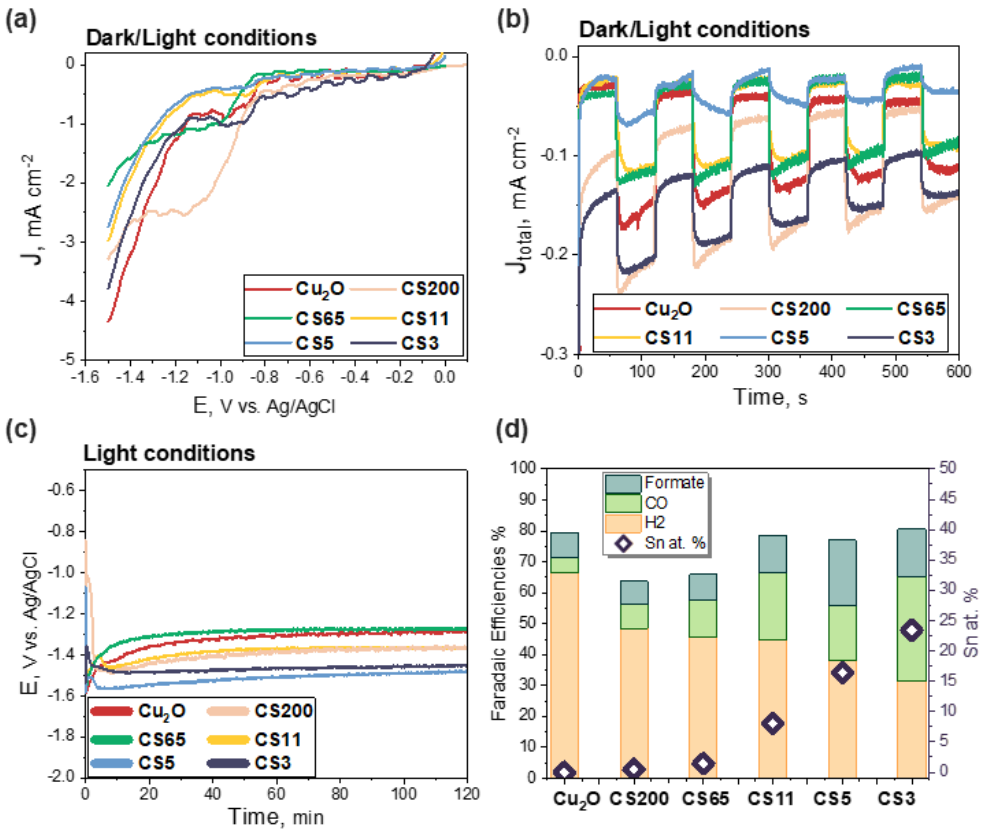


Figure 5.8 – Results of PEC tests on the 5 different core-shell samples; in particular: (a) LSV curves, (b) chronoamperometry test, both in light/dark chopped conditions, (c) chronopotentiometry curves lasting 2-hours, obtained at an applied current density of –3 mA cm^{-2}, (d) Faradaic efficiency results of the 6 samples after the chronopotentiometry test, related to the Sn atomic percentage within each sample (purple rhombus).

The chrono-amperometric behaviour of the catalysts is shown in Figure 5.8b, while the photocurrent gain values are reported in Table 5.2 for an easier consultation. In this kind of experiment, the alternation light/dark was due every 60 seconds. It was not possible to individuate a clear trend among the data, in particular with respect to the photocurrent gain. It was observed that as the amount of tin increases, generally the photocurrent gain decreases, albeit not linearly, if compared to samples with Cu^{+} as the only (or most abundant) species. That behaviour was not true only for the CS65 sample, which reached the average photocurrent gain of 105 µA cm^{-2} during the chronoamperometry test. It can be also noticed that the uncertainty on the values decreases slightly as the tin percentage increases. This could be a proof of a greater sample stability during the test, ensured by the outer shell. It must be considered that the values are generally

lower than some remarkable literature ones [205,220], although in those cases the electrode supports were different (*e.g.,* Cu foam or Fluorine Doped Tin Oxide (FTO)). An agreement was noticed with the results obtained by Liu *et al.*, [231] in their investigation on the photocorrosion of the bare Cu_2O catalyst in aqueous electrolytes. They reported a chronoamperometry with an applied potential of –0.4 vs. RHE, and observed a photocurrent gain of around 0.1 mA cm^{-2} for the bare Cu_2O on FTO and around 0.05 mA cm^{-2} for the Cu_2O/FTO with Ag nanoparticles electrodeposited to partially avoid the Cu_2O photoreduction.

Table 5.2 – Photocurrent gain of the 6 samples analyzed via chronoamperometry test at –200 mV vs. OCP in chopped light mode and CO_2-saturated environment.

Sample	Cu_2O	CS200	CS65	CS11	CS5	CS3
Photocurrent gain [µA cm^{-2}]	91±10	77±5	104±5	76±5	28±3	55±3

The chronopotentiometry test were reported in Figure 5.8c. The decision of applying a current density value of –3 mA cm^{-2} was taken based on the results of gaseous products evolution and of the comparison of dark/light currents obtained in preliminary tests (see Chapter 4). The potential obtained lay from –1.6 V to –1.35 V vs. Ag/AgCl, and no clear trend was recognizable. The plot showed that each sample curve evolved slowly during the first 40 minutes and remain relatively stable during the rest of the test. Interestingly, the two samples with highest Sn content showed an univoque behaviour reported also by de Brito and co-workers [209]. In their work, they performed a current vs time plot recorded during the photo-electrocatalytic reduction of CO_2 at Cu/Cu_2O electrode. In line with their study, the reductive photocurrent was seen to increase in the first minutes of electrolysis and decreases thereafter, reaching lower, but stable in our case, values after 120 minutes. This was explained by assuming the formation of intermediate $CO_2^{\bullet-}$ in the beginning of the electrolysis followed by its further reduction to generate of C-compounds derivatives. Potential values do not show a uniform trend if related to the precursor ratio, but product quantity does.

Total Faradaic efficiency trend are reported in Figure 5.8d. The tests have been executed totally in light conditions. It resulted that increasing the tin precursor quantity strongly dampens HER, while it promotes CO_2 reduction toward CO and formate production. The linear trend between formate production and Sn amount was expected from literature results [116,232,233]. In fact, the

increasing amount of Sn inside the catalyst is one of the parameters that greatly affects the selectivity of CO_2 reduction products. As observed in the previous Chapter, the light role together with the tin presence can tune the selectivity of the catalyst towards the CO_2RR. In the plot it was clearly observable the shift from a H_2 Faradaic efficiency higher than 65% attributed to the bare Cu_2O to its halving in the test carried out with CS3 (FE = 30%). The increase of CO production was also noticeable, moving from less than 5% of efficiency in the Cu_2O test, to around 35% with CS3 sample, potentially be due to a synergy between the core and shell materials.

The gaseous products in this final test presented the remarkable CO:H_2 ratio ~ 1, pretty interesting from industrial utilization of syngas in hydroformylation processes [234]. Even if H_2:CO ratio should be 2 or 3 for methanol synthesis and 2 for Fisher-Tropsch process [235], here the CS3 sample became the more suitable candidate for further characterizations, possible modifications, and stability tests.

5.4.4 EIS analysis

An electrochemical impedance spectroscopy measurement campaign was carried out on the batch of core-shell catalysts with different tin precursor ratios, similar to the one analyzed in the previous Chapter. The tests were conducted with an analogous set up as for the co-precipitation samples, ranging the frequencies from 10^6 Hz to 0.1 Hz and DC electric potentials varying from –800 mV vs. Ag/AgCl to –1500 mV vs. Ag/AgCl. The electric potential values were converted in V vs. RHE by using the Equation 22 in order to be comparable with the ones reported previously. The measurement campaign was repeated twice, before and after a 10 minutes lasting chronoamperometry test, carried out at the same applied potential, to observe the catalysts evolution. The results are labelled as "*post*" when they refer to the second part of the measurement.

Figure 5.9 presented the Nyquist plots of one of the core-shell samples (CS3) measured at different potentials in the CO_2-saturated electrolyte during the solar simulator enlightenment. The inset in figure showed the pattern recorded at the lowest applied potential, enlarged to be better understood. As the applied potential became more negative, the impedance magnitude decreased, indicating higher Faradaic reaction rates on the electrode surface.

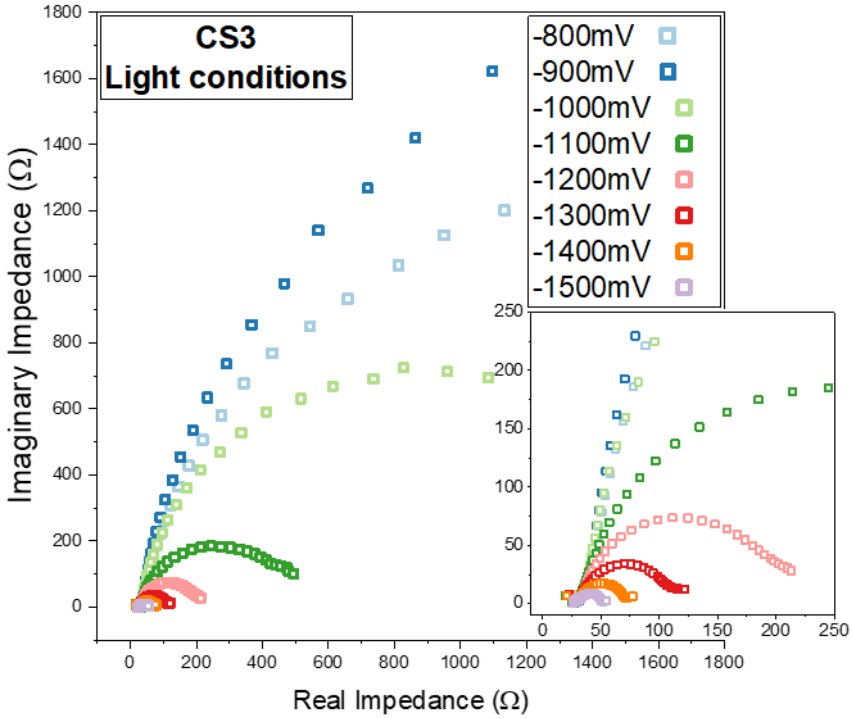


Figure 5.9 – Nyquist plots related to one of the core-shell samples sample measured at different potentials vs. Ag/AgCl in CO_2-saturated electrolyte in tests enlightened by the solar radiation (the points are experimental data).

That was not true in the two lowest potential values applied –800 and –900 mV vs. Ag/AgCl, where the former line presented an impedance magnitude lower than the one registered for the latter. The LSV test (Figure 5.8a) registered for CS3 sample (purple line) a reduction peak pointed at –900 mV vs. Ag/AgCl, attributed to the Cu2O reduction. The phenomenon originated an increase of *J* value (in terms of absolute value), associated to a lower impedance. The current density continuously increased from -1000 mV vs. Ag/AgCl onward, so the decreasing trend was linear passing from –1000 to –1500 mV vs. Ag/AgCl. The global behaviour was the same as for the co-precipitation samples anaysed in Chapter 4, moreover this was true for the whole series of core-shell catalysts analyzed. In general, the electrical behaviour of an electrochemical system can change as a function of potential. Whether the semicircle is closed or open in the Nyquist plot obtained from the EIS measurement depends on the resistivity of the system. In fact, a less resistive system will present a closing semicircle, differently than a more resistive one. At low electric potentials (*i.e.,* before the onset potential) the CO_2RR processes in the system may not be active and the semicircle remains open. At higher potentials (*i.e.,* after the onset potential), the semicircle could close because phenomena of exchange of charges (reaction

occurring at the electrode/electrolyte interface) are taken into account. These processes may become more prominent and influence the impedance behaviour [236]. So, the fact that a Nyquist plot obtained from an EIS test registered at lower potentials did not close while at higher potentials the semicircle closed, can indicate a change in the electrochemical behaviour of the system as a function of potential. The hypothesis that a change in electrochemical behaviour happened and it was related to the applied potential value was supported by an analysis of the LSV curves of the catalysts (Figure 5.8a), which indeed showed the overcome of the Faradaic current onto the photoinduced one starting at around –1.2 V vs. Ag/AgCl, with the *J* decisively increasing up to –1.5 V vs. Ag/AgCl. Thus, before that specific potential value, no actually photo-electrocatalytic reduction activity of CO_2 was actually pesent. Such observation differs from the behaviour in the range of values from 0 to –0.8 V vs. Ag/AgCl, where signs of photoactivity were confirmed by the typical undulating trend, but also the actual current density value did not deviate significantly from zero.

Therefore, focusing on the region with the lowest impedance value, and taking into account that, as shown in Figure 5.8c, the average potential recorded during the 2-hours chronopotentiometry was –1.5 V vs. Ag/AgCl, it was decided to investigate the behaviour recorded for some catalysts at that specific applied potential. It was chosen to consider not only the set of tests performed in light but also those carried out in the dark and for each one the "*pre*" and "*post*" data were analyzed. The results are reported in Figure 5.10 for three catalysts, selected to investigate an eventual trend. Thus, it was decided to observe potential differences moving from a molar percentage of Sn equal to zero (Cu_2O, Figure 5.10a) to higher Sn amount (CS5 and CS3, Figure 5.10b,c respectively). For an easier consultation, the impedance values determined from the curves in the three Nyquist plots are listed in

. The resistance values that were here taken into account are the one labelled as "R3" in the equivalent circuit reported in Figure 2.4.

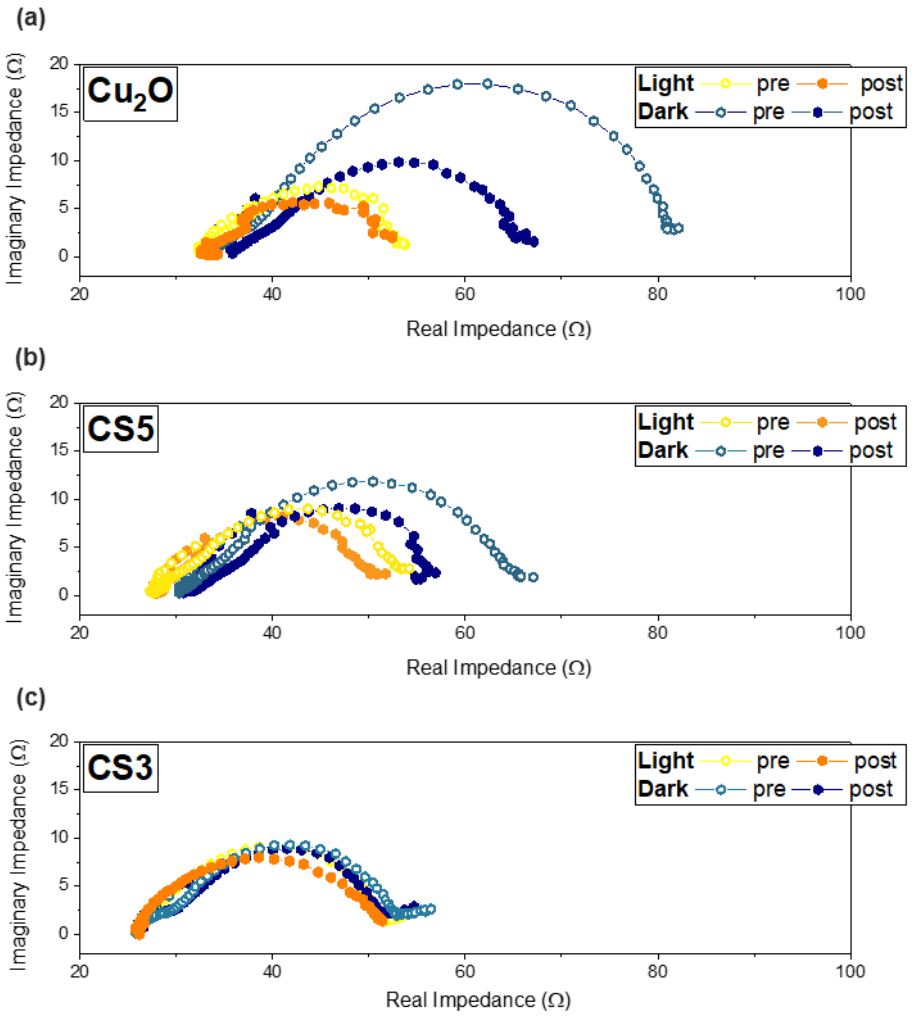


Figure 5.10 – Nyquist plot of three different catalyst, (a) Cu_2O, (b) CS5, and (c) CS3, obtained during the "*pre*" and "*post*" campaign of measurement carried out at –1.5 V vs. Ag/AgCl in CO_2-saturated environment both in dark and light conditions.

The results of the tests on the Cu_2O and CS5 catalysts showed that the resistance in dark conditions was higher, with a trend towards a decreasing impedance value from "*pre*" to "*post*" measurements. The impact of this behaviour was more pronounced for Cu_2O reported in Figure 5.10a, where the R_{Dpre} (where D is for dark conditions and "*pre*" means that the test was carried out before a chronoamperometry) value was 47.13 Ω compared to R_{Dpost}, which measured 31.20 Ω. Instead, the difference between R_{Dpre} and R_{Dpost} for the CS5 catalyst (Figure 5.10b) was lower, at around 10 Ω (36.76 vs 26.14 Ω, respectively). The absence of an external shell to protect the Cu^+ phase in the Cu_2O catalyst was deemed responsible to changes of phases during the CO_2R

tests, with Cu_2O gradually transforming it into its metallic phase (Cu). Such hypothesis would explain the lower impedance value due to the intrinsic properties of metals and their activity in reducing CO_2. As a further proof of such insight, as the SnO_2-based shell became thicker (at higher amount of Sn, CS3 sample in Figure 5.10c), the impedance difference between "*pre*" and "*post*" tended to significantly decrease. This can be observed in the CS3 catalyst plot, where the value change between R_{Dpre} and R_{Dpost} was less than 1 Ω, and in general the values were smaller than those observed for the other two catalysts. This behaviour was also observed in the light-influenced test of the CS3 catalyst, and indeed, the

showed that the R_{Lpre} and R_{Lpost} values (where L stands for the light test) were substantially equal. Solar radiation had a positive influence on the results of the other two catalysts as well. The orange and yellow points shown in the graphs depicted a situation of substantial similarity between the "*pre*" and the "*post*"-chronoamperometry test at –1.5 V vs. Ag/AgCl. It was still observed that the "*post*" test had a lower impedance value, although, unlike the dark tests, the values here were rather similar between "*pre*" and "*post*". This could be a confirmation of the fact that light led to a higher internal photovoltage within the catalyst, which was not used to reduce the Cu_2O to the corresponding metallic species. By using these EIS tests as a "state-of-health" check of the catalyst during the test, it can be stated that the light tests imply lower level of modification of the catalyst and its oxidation state, and such result is further confirmed as the presence of SnO_2 as an external shell increased.

Table 5.3 – Values of impedance (R) obtained from the plots reported in Figure 5.10 for three different catalysts.

Samples	**Dark** R_{Dpre} [Ω]	R_{Dpost} [Ω]	**Light** R_{Lpre} [Ω]	R_{Lpost} [Ω]
Cu_2O	47.13	31.20	19.86	19.84
CS5	36.76	26.14	26.53	24.03
CS3	26.66	27.59	25.53	25.29

Even without the fit, two distinct behaviours were observable. The addition of tin oxide in the synthesis process seemed to protect the catalyst from degradation (Figure 5.10b and Figure 5.10c), making the "*pre*" and "*post*" measurements similar. On the other hand, an increase in the overall radius of the imperfect semicircle was observed comparing the sample with no Sn added in the synthetic process with the catalysts with increasing presence of SnO_2 in the external layer. This last phenomenon could theoretically indicate the suppression of catalytic performances.

To gain insights into the behaviour observed, EIS data was analyzed by fitting it to an equivalent circuit model as depicted in Figure 2.4. The model comprised of a resistance R1, representing electrolyte resistance, and a parallel combination of resistance R2 and constant phase element Q2, which characterize transport properties within the catalyst. In addition, the model also included another parallel R3//Q3 that accounts for reduction reactions [237]. The trends of equivalent resistance R3, calculated for all the core-shell samples, are depicted in Figure 5.11a. The empty squared symbols represented the impedance values obtained during the "*pre*" measurement, while the filled ones represented the values obtained during the "*post*" measurement. Each value correspond to the potential applied during the 10-minutes EIS and chronoamperometry test. For the purpose of comparison, the trends observed for the co-precipitation catalyst, which were discussed in Chapter 4, were included in the same plot.

As the applied potential become more negative, the resistance values were observed to decrease exponentially over several orders of magnitude, in agreement with the results from the co-precipitation sample tests. This behaviour has been associated with charge transfer limitations and reaction mechanisms by Zeng *et al.* [95], and confirms R3/CPE3 to be the rate-determining component. The trends of each individual catalyst, both core-shell and co-precipitation, are presented in Figure 5.11b-h. By focusing on the R3 values at –1.5 V vs. Ag/AgCl (the leftmost value), all the catalysts showed values in the same order of magnitude (10^1 Ω), with CP and CS11, CS5, and CS3 having higher values compared to Cu_2O, CS200, and CS65. For example, R3 values of CP and CS11 values found by fitting the data were around 36 and 26 Ω respectively, while CS200 and CS65 were both found to be around 10 Ω. The hypothesis is that the impedance value related to CO_2RR increases as the Sn content increases, compared to samples with low or no Sn content (bare Cu_2O). The Sn content also impacted the curve behaviour in other ways, with a smaller Sn content (Figure 5.11c,d,e) resulting in a larger difference between the "*pre*" and "*post*" values,

suggesting that the application of a potential may modify the catalyst during the test. This confirms the protective role of SnO_2 in mitigating the reduction of Cu_2O during the test. Additionally, for the co-precipitation sample, the spread between the "*pre*" and "*post*" curves increased as the applied potential decreased, with the two trends becoming similar only at lower potential values. However, this was not observed for the other catalysts, where the difference between the "*pre*" and "*post*" values was not as pronounced at higher applied potentials. In particular, the CS5 and CS3 catalysts (Figure 5.11g,h) showed almost complete overlap between the "*pre*" and "*post*" curves, indicating that the modification of the catalyst during the test was negligible and possibly suppressed by the presence of a thicker SnO_2 outer shell. These observations, along with the lower R3 value, suggested that the stability issues associated with the co-precipitation sample may be improved or resolved by changing the catalyst design and synthetic approach to the core-shell structure.

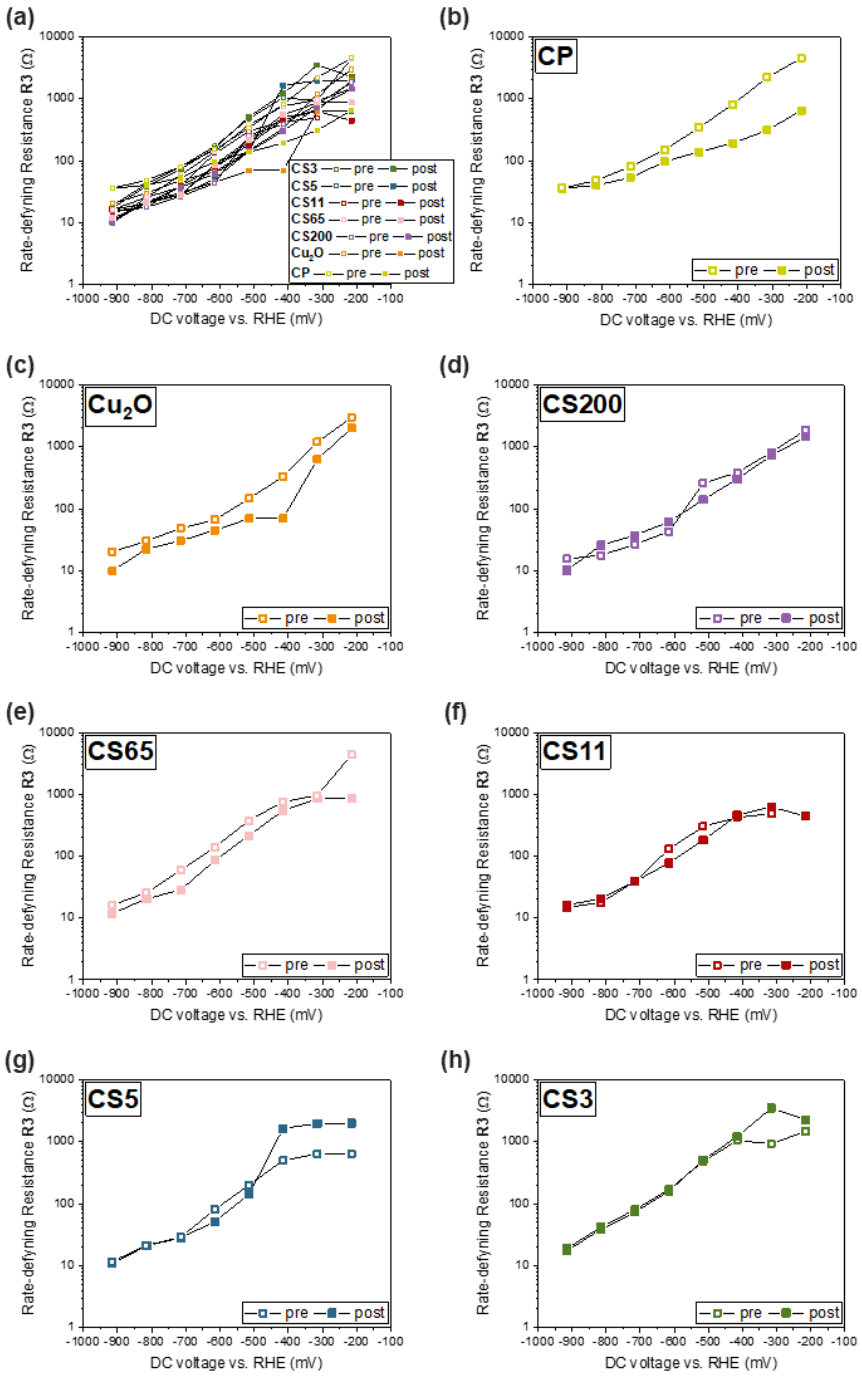


Figure 5.11 – Equivalent resistance R3 trends of (a) all the samples, (b) co-precipitation sample, (c) Cu_2O, (d) CS200, (e) CS65, (f) CS11, (g) CS5, and (h) CS3; open symbols represent the "*pre*" measurements while solid ones, that are labelled "*post*", represent the one executed after the chronoamperometry. R3 values were calculated through a fitting procedure using the equivalent electrical circuit shown in Figure 2.4

5.5 Conclusions

The work was based on the development of a new synthetic approach for the attainment of a Cu_2O-SnO_2 catalyst useful for the PEC CO_2 reduction. The choice of employing the core-shell route for the catalyst synthesis was driven by some relevant recent results found in literature on similar structures. Overall, the core-shell catalyst provides a versatile platform for CO_2 reduction, offering improved selectivity, activity, stability, control over the reaction environment, and reduced cost. The core was chosen to be the promising, abundant, cheap and photoactive Cu_2O and the external shell was made of SnO_2. The creation of a catalyst that possessed the same catalytic species as the one previously studied and developed in the previous Chapter allowed for a comparison in terms of both morphology and PEC performance.

It was observed that the photoactivity of a generic Cu_2O-SnO_2 core-shell based catalyst was increased by 30% compared to the previous co-precipitation obtained catalyst (18 vs. 24 μA cm^{-2} increase in photocurrent obtained in a chronoamperometry performed applying –0.2 V vs. OCP), and also that the activity of the former was greater than the latter, assessing this parameter from the shift to values closer to zero of the onset potential. In addition, from a comparison with the previously developed catalyst, the introduction of the new core-shell synthetic approach enabled a finer tuning of the ratio of metallic precursors within the final catalyst. Different samples of the same Cu_2O-SnO_2 catalyst were synthesized with an increasing molar percentage of Sn relative to the Cu_2O core. The effective amount of Sn in the final catalyst was also evaluated using ICP-OES, which was the only way to accurately assess the true value of Sn in the sample since only Cu_2O peaks were obtained in the diffractograms of all samples.

After morphological characterization of the 5 different catalysts prepared (CS200, CS65, CS11, CS5, CS3), their PEC characteristics for CO_2 reduction were compared with each other. It was immediately clear that in the samples with higher Sn content, photocurrent decreased in accordance with an increase in selectivity towards C-products after 2 hours of chronopotentiometry testing. The photocurrent gain of CS5 and CS3 was equal to 28 and 55 μA cm^{-2}, respectively, while it was more than double for CS200 and CS65 with values of 77 and 104 μA cm^{-2}, respectively. Besides, CS5 showed an interesting formate FE value of 20% while in the CS3 test a CO:H_2 ratio was obtained that was approximately equal to 1. Given that the main focus of these studies was on the stability and selectivity of

the catalyst, the results of the catalysts with high Sn % were considered promising.

As a further confirmation, the results of the EIS tests were observed, and in particular, some interesting information was obtained by plotting the trend of the R3 value for each sample at different investigated voltages. The outcomes of this investigation provided evidence that the stability of the core-shell catalysts was in general higher than the one of co-precipitation sample, and that the CO_2R tests carried out on the catalyst did not result in significant degradation. A detailed analysis of the catalyst before and after the test can help understand the material's stability potential. In situ characterization of photo-electrodes during CO_2R tests can provide additional insight. This study is a starting point for investigating Cu_2O-SnO_2-based core-shell catalysts and determining the amount of Sn within them. EIS can be used as a useful and versatile tool for monitoring the catalysts' health during tests.

Chapter 6

Advanced characterization of core-shell samples via TRMC and IMVS

The study of charge carriers and their time constants is fundamental for understanding the behaviour and properties of materials. In Chapter 6, the carrier dynamics of Cu_2O-SnO_2 core-shell catalysts were investigated through Time-Resolved Microwave Conductivity (TRMC) and Impedance Modulated Photovoltage Spectroscopy (IMVS) analysis to understand their correlation with the results of photo-electrocatalytic reduction of CO_2. The selectivity for C-compounds increased with increasing amounts of Sn in the catalysts, and TRMC analysis showed that the mobility of charge carriers also increased proportionally to the amount of Sn. IMVS analysis was adapted to study the catalyst during CO_2 reduction, and it was observed that the electron lifetime in the core-shell samples decreased with increasing amounts of Sn. Correlations were inferred between the results obtained from the two techniques and the PEC test results previously obtained. The study provided a detailed analysis of the carriers mobility within these types of CO_2RR catalysts, which is lacking in the literature.

Contributions: This work has received funding from the European Union's Horizon 2020 Research and Innovation Action program under the Project SunCoChem (Grant Agreement No 862192). During the PhD student's period abroad at Helmholtz-Zentrum Berlin (from February to June 2022), Dr. Fatwa Abdi hosted the student and supervised the work presented in this Chapter. The PhD student was initially taught the TRMC setup and analysis protocol by Dr.

Dennis Friedrich, and was able to perform the analysis independently after receiving the necessary training. The results were discussed by the PhD student in collaboration with Dr. Dennis Friedrich and Dr. Fatwa Abdi. Erwin Fernandez was involved in the UV-Vis analysis, which was performed jointly. Dr. Fatwa Abdi guided the PhD student in the use of the IMPS setup and analysis protocol, and together they approached the theoretical aspects of the results and discussed them.

6.1 Carriers mobility

The design of chemical processes is commonly based on the concept of unit operations, which are defined by the principles of transport phenomena. A unit operation is a fundamental process phase. Separation, crystallization, evaporation, filtration, polymerization, isomerization, and other reactions are examples of unit processes that entail a physical change or chemical transformation. These principles include the three fundamental transfer processes of momentum, heat, and mass transfer, which can account for all unit operations used in traditional chemical industries [238]. However, dealing with nanostructures, another essential transfer process must be added to the list: charge-carrier transfer [239,240]. The movement of charge carriers can be categorized in the same way. In this scenario, the density of electric current, also known as charge carrier flux, is directly proportional to the voltage drop or driving force, as per Ohm's law. This can be expressed mathematically as Equation 25:

Equation 25 – Density of electric current

$$J_x = -\sigma \frac{dU_x}{dx}$$

Here, J_x represents the component of the electric current density in the *x*-direction, and σ represents the electrical conductivity. The term $\frac{dU_x}{dx}$ refers to the voltage gradient in the *x*-direction, and it can also be expressed as in Equation 26:

Equation 26 – Voltage Gradient

$$F_x = -\frac{dU_x}{dx}$$

Where F_x represents the component of the electric field strength along the *x*-direction. The electrical conductivity, measured in S m^{-1}, is a function of both the

electric field strength and temperature. In summary, if the electric current density is measured in A m^{-2} and the electric field strength is measured in V m^{-1}, the electrical conductivity is calculated using the formula $\sigma = \frac{J_x}{F_x}$. Therefore, careful consideration of charge-carrier transfer processes is crucial for developing solutions to many problems in this field.

In physics, a charge carrier refers to a particle that is free to move and carries an electric charge, especially in electrical conductors. Common examples of charge carriers include electrons and ions. When an electric field is present in a conducting medium, it exerts force on these free particles, leading to a net motion of the particles and resulting in an electric current. In semiconductors, both electrons and holes serve as charge carriers. With the application of the electric field, the electrons gain a net velocity in the direction of the field called the drift velocity, defined as in the Equation 27:

Equation 27 – Drift velocity Equation

$$v_d = \pm \frac{q\tau_c}{2m_{n,p}} E$$

where τ_c is the mean free time, q is the charge, $m_{n,p}$ is the effective mass of an electron or hole and E is the intensity of the electric field applied to a material. In parallel, the carrier mobility [$cm^2\ V^{-1}\ s^{-1}$] is defined as in Equation 28:

Equation 28 – Carrier Mobility

$$\mu_{n,p} = \frac{q\tau_c}{2m_{n,p}}$$

that is true for both electrons (μ_n) and holes (μ_p). Holes, which are the traveling vacancies in the valence-band electron population, are treated as mobile positive charges. It is important to note that electrons and holes are both considered charge carriers in semiconductors. Carrier mobility is a crucial factor in evaluating the performance of semiconductor materials. It refers to the speed at which charge carriers, such as electrons or holes, can move within the material in response to an applied electric field. This parameter has a significant impact on the suitability of a semiconductor for various electronic applications. Understanding the mobility determined by a specific characterization method and its limitations is important as it can vary based on the measurement technique

used. The carrier mobility affects the device behaviour by influencing its frequency and time response.

Electric conduction, or the transfer of charge carriers, in all materials is made up of two fundamental processes: the generation of charge carriers and the transportation of the generated carriers. These processes can be described by Equation 29:

Equation 29 – Generation and transportation of carriers

$$\sigma = en\mu$$

in which, e represents the elementary charge, n represents the density of carriers, and μ represents the carrier mobility. The number of carriers is connected to generation processes, whereas the mobility is related to transport processes. A material with high mobility generally results in a high frequency response due to faster carrier velocity and high device current, allowing capacitances to be charged more rapidly [241]. It is important to note that the number of charge carriers in solids or the process of charge-carrier transfer is closely tied to the generation mechanisms, while the mobility of these carriers is related to transport mechanisms. In a photocatalytic reaction, for example, charge carriers are produced through the illumination of a semiconductor material, and can either be trapped or recombine or participate in multiple redox reactions [242]. These processes occur on extremely short timescales, ranging from femtoseconds to nanoseconds, and are currently being investigated through various time-resolved techniques, including absorption spectroscopy, diffuse reflectance, electron spin resonance, and microwave conductivity, among others [243–245]. In next Section, TRMC will be introduced and discussed.

6.2 Time-Resolved Microwave Conductivity

The term “Time-Resolved Microwave Conductivity” (TRMC) was adopted from the work of Warman and his colleagues [246], who conducted during 80s detailed quantitative studies on charge carrier kinetics in low-conductivity systems over the last decade. They used microwave methods to study excess charge carriers in photosensitive powders and published their research. Kunst and Beck then extended Warman’s studies to systems with arbitrary dark conductivity [247], aiming at measuring excess conductivity induced by pulsed excitation in semiconductors using microwave power.

6.2.1 Fundamentals

Providing a solution to Maxwell's equations, or an approximation thereof, allows to quantitatively create a connection between microwave propagation measurements and the properties of the sample being measured. Traditionally, this calculations have been done analytically, although there are currently some numerical methods developed at TU Delft which are a notable exception [248]. The basic principle of TRMC involves measuring the change in microwave power reflected by a sample induced by laser pulsed illumination. The relative change of the reflected microwave power is caused by a variation of the sample conductivity induced by the laser. In a TRMC experiment, it is not possible to measure the contributions of electrons and holes to conductivity separately [248]. This is because, as in Equation 30, the change in conductivity ($\Delta\sigma$) is given by the sum of the photo-induced change in concentration (Δn_i) of each carrier type and the corresponding mobility (μ_i) of that carrier type, multiplied by the electronic charge (e):

Equation 30 – Conductivity change

$$\Delta\sigma = e\sum n_i\mu_i$$

It is clear from Equation 30 that the most mobile carriers make the largest contribution to conductivity, so light-induced carriers in regions with high mobility dominate the TRMC signal. Microwave measurements can be conducted in reflection using different microwave cells. An open cell is used in normal reflection mode, while a microwave cavity is used to measure under resonant microwave conditions.

In the work here described, we mainly used a cavity, which provided higher sensitivity (>10 times) to the technique even if this increased the instrument response time. For small perturbations of conductivity, the normalized change in microwave power reflected by the cavity ($\Delta P/P$) is related to the change in conductance ΔG. A proportionality between the change in microwave power and the change in sample conductivity is given by Equation 31:

Equation 31 – Change in microwave power reflected

$$\frac{\Delta P(t)}{P} = -\mathrm{K}\Delta G(t)$$

where $\Delta P(t)$ is the change in microwave power at time t, P is the initial microwave power level, $\Delta G(t)$ is the change in microwave power reflected at time t induced by the laser. The proportionality constant K, known as the sensitivity factor, depends on several factors such as the dimensions of the cavity, the quality of its inner walls, and the dielectric properties of the sample under investigation. The change in conductance (ΔG) is defined as the product of the change in conductivity ($\Delta\sigma$) and the ratio between the area of the sample (A) perpendicular to the electric field vector of the microwaves, E_{mic}, and the length d of the sample in the direction of E_{mic}, as given by Equation 32.

Equation 32 – Conductance change

$$\Delta G = \Delta\sigma \frac{A}{b}$$

A is defined as $a \cdot l$, where l is the thickness and a is the width of the sample, and b corresponds to the length of the sample. From Equation 32, Equation 33 can be derived:

Equation 33 – Derivation of conductance change

$$\Delta G = \Delta\sigma \frac{a}{b} l = \Delta\sigma\beta l$$

where β is the ratio between a and b, respectively the width and length of the sample placed into the cavity. By utilizing a known value of K to measure the absolute change in conductance, it becomes possible to infer the yield of charge carrier generation and the mobility of the resultant carrier.

Assuming that each photon generates a single positive and negative charge carrier, Equation 29 can be expressed as in Equation 34:

Equation 34 – Conductivity change expressed in terms of carriers mobility

$$\Delta\sigma = en \sum_i \mu_i = en(\mu_e + \mu_h)$$

where n denotes the concentration, μ_e and μ_h represent respectively the electrons and holes mobility. If no charge carrier recombination has occurred during the response time of the set-up, the yield (ϕ) can be defined as in Equation 35:

Equation 35 – Yield

$$\phi = \frac{n\lambda}{I_0 F_A}$$

where I_0 is the intensity of the laser in photons/pulse/unit area, and F_A represents the optical attenuation or the fraction of light absorbed at the specific excitation wavelength. Equation 36 is derived by using the maximum value of the change in conductance (ΔG_{MAX}) over time and combining Equation 33, Equation 34 and Equation 35. It can be expressed as

Equation 36 – Maximum of mobility

$$\phi \sum_i \mu_i = \frac{\Delta G_{MAX}}{\beta e I_0 F_A}$$

This equation is commonly utilized to compare microwave signals from different samples since the product $\phi\Sigma\mu_i$ is normalized to the amount of absorbed photons. One significant aspect of Equation 36 is that it does not take the materials thickness into account. This is pertinent as, in strongly absorbing media, like most solar cell materials, the charge carrier concentration is not uniform across the film.

The TRMC so-obtained signal is called (microwave) photoconductivity, and it allows direct measurement of the decay of the number of electrons and holes after the laser pulse by recombination or trapping of the charge carriers.

6.2.2 Experimental apparatus

The set-up for microwave photoconductance involves four main components:

i. a stable microwave source;
ii. a pulsed and adjustable photo-excitation source;
iii. a microwave cell containing the sample being studied;
iv. a sensitive detection and data acquisition system.

A schematic representation of the set-up is reported in Figure 6.1. All experiments were conducted in reflection mode, which requires a microwave circulator to separate the incident and reflected microwaves even if measurements of TRMC can be also performed in transmission mode. To induce a change in conductance, visible light is used to excite the sample through 3-5 nanosecond

wide pulses from an optical parametric oscillator (OPO), which is powered by the third harmonic of an Nd:YAG laser. The output of the OPO can also be switched to the idler, which enables the excitation of the sample in the near-infrared (NIR) region. The photoconductance can be measured over a wide range of incident light intensity, utilizing metal-coated neutral density filters to control the photons flu. This is expressed in terms of fluence, that is the measure of energy delivered per unit area and typically falls in the range of 10^{11} to 10^{15} photons per pulse per square centimetre. To generate microwaves within the X-band region (8-12 GHz), a voltage-controlled oscillator was employed. The detection of microwaves was performed using a Schottky barrier diode, which converts the microwave power into a DC output. When the voltage passes across a 50 Ω resistor, a voltage response between 0.5 and 1 V is generated. The DC level is then subtracted using an offset regulator, and the remaining AC signal is amplified by a broadband amplifier. The time-resolved signal is then routed into a digital oscilloscope, which has a sampling rate that exceeds 1 GHz. Typically, the acquisition is triggered by a fast photodiode that is directly illuminated by the laser pulse. To obtain a high-quality signal, the microwave conductance signals are usually taken by recording various values (10-1000) and making an average, resulting in signals on the order of 1 mV after 100 times of amplification. The total set-up provides a signal-to-noise ratio larger than 10^5. A cavity operating in the TE102 mode for X-band waveguides was constructed using a piece of gold-plated copper or brass with internal dimensions of a = 22.8 mm, b = 10.1 mm, and $l \approx 48$ mm.

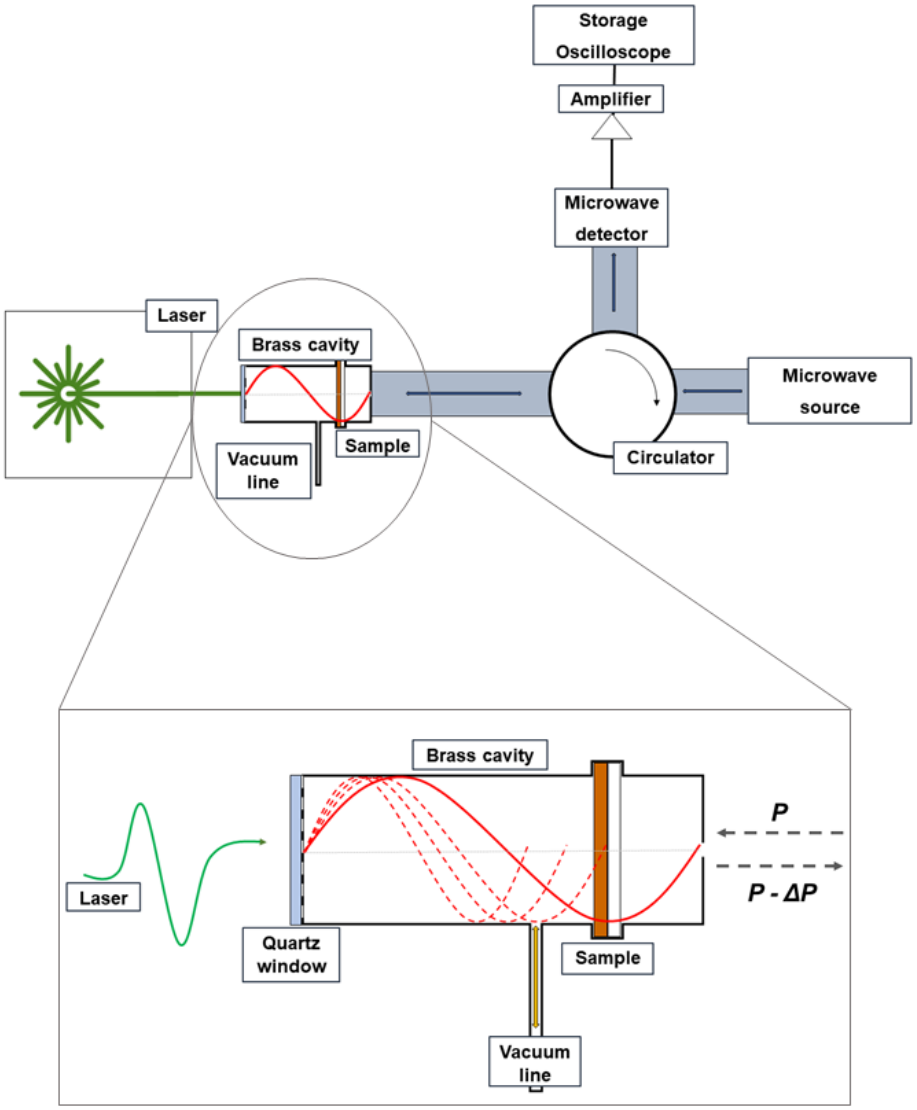


Figure 6.1 – Scheme of the experimental setup and illustration of the measurement principle of cavity-based TRMC.

The electric field vector of the microwaves in the rectangular cavity is directed along the *y*-axis, and the field strength is constant along the short *y*-axis while following a sine function along the *x*-axis. The sample is placed at a distance of ¾ × *l* from the entrance window, coinciding with one of the two positions with the maximum electric field strength. The light is introduced through a horizontal grating in the brass end plate of the cell, which is sealed with a UV grade quartz window. An iris made of a 0.5 mm copper plate with a 9-10 mm diameter hole is used. Figure 6.1, in its inset, provides a schematic

representation of a cross-section of the cell, where the dimension *a* is along the *x*-axis, *b* is along the *y*-axis, and *L* is along the *z*-axis.

6.2.3 Experimental procedures

The objective of this measurement was to gain a thorough understanding of the carrier dynamics in the 5 core-shell samples, as well as in the bare Cu_2O. Subsequently, the estimated mobility and time were compared with the results obtained in PEC CO_2RR tests with the aim of establishing a correlation.

As a preparatory measurement, UV-Vis spectra of each samples were recorded to estimate the F_A parameter, required as in Equation 35 for the mobility determination. UV-Visible spectra were obtained using a PerkinElmer Lambda 950 spectrophotometer equipped with an integrating sphere. The films were positioned in the integrating sphere using a centre mount sample holder, and they were placed at an angle of approximately 7.5° away from the incoming light. The samples were air-brushed onto a quartz, non-conductive, support and then placed into the instrument for the measurements. It is worth to note that the creation of the catalytic ink followed the procedure previously explained in Section 4.2.4, by scaling the quantities with respect to an higher active area to be covered.

The resulting spectra for all the samples are reported in Figure 6.2, with the transflectance value reported on *y*-axis. Transflectance in UV-Vis spectroscopy is a technique used to measure the reflectance and transmittance of a sample simultaneously [249]. It involves shining light onto the sample and measuring the amount of light that is reflected and transmitted through the sample at different wavelengths. In transflectance mode, a sample is placed on a substrate that is partially transparent and partially reflective. The substrate reflects some of the light back into the sample, which is then re-reflected and transmitted through the substrate. By measuring the intensity of both the reflected and transmitted light, the absorption spectrum of the sample can be obtained.

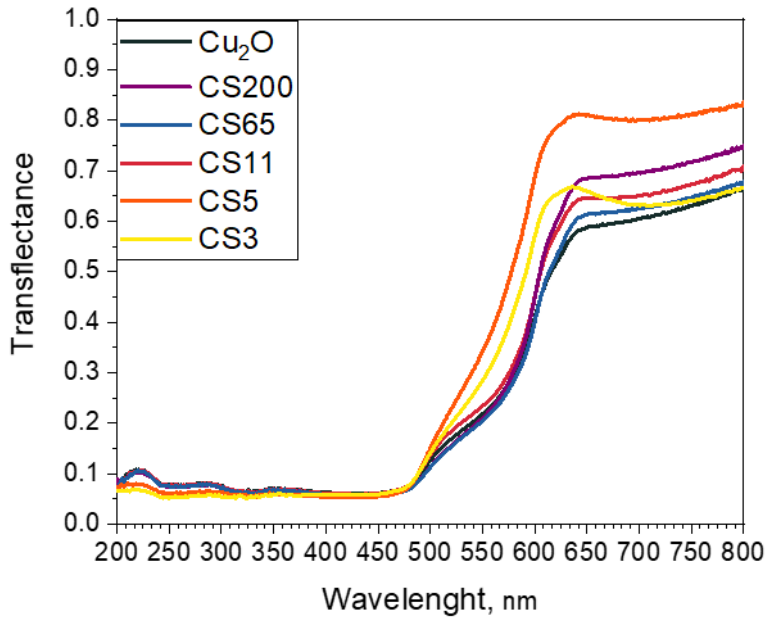


Figure 6.2 – UV-Visible spectra of core-shell and bare Cu_2O samples air-brushed onto a quartz substrate.

To establish a 100% transflectance baseline for the Cu-Sn-based films, the transflectance of the quartz substrate was utilized. Based on the transflectance data, the absorptance and absorption coefficient of the films were then calculated as in Equation 37, using the transflectance value F_{tr} at a certain wavelength.

Equation 37 – Absorptance value from Transflectance data

$$F_{\mathrm{A}} = 1 - F_{\mathrm{tr}}$$

Time-resolved microwave conductivity measurements were then conducted using a frequency-doubled Q-switched Nd:YAG laser. Nine different wavelengths were investigated (410-450-460-470-480-500-540-560-570 nm) at all the intensities of laser (Neutral Density = ND = 0.0-2.5). Some noteworthy graphs and discussion of the main results are reported in the following Section.

6.2.4 Results and discussion

At the lower wavelength investigated (410 nm), there were not significant signals of photoinduced conductivity into the sample. Instead, all the others investigated λ reported a signal discernible from the noise. In this Section, some of the mobility values vs. time are reported for each sample. In particular, trend of

the maximum of mobility vs. time are reported for λ = 450 nm (Figure 6.3), λ = 500 nm (Figure 6.4), and λ = 560 nm (Figure 6.5).

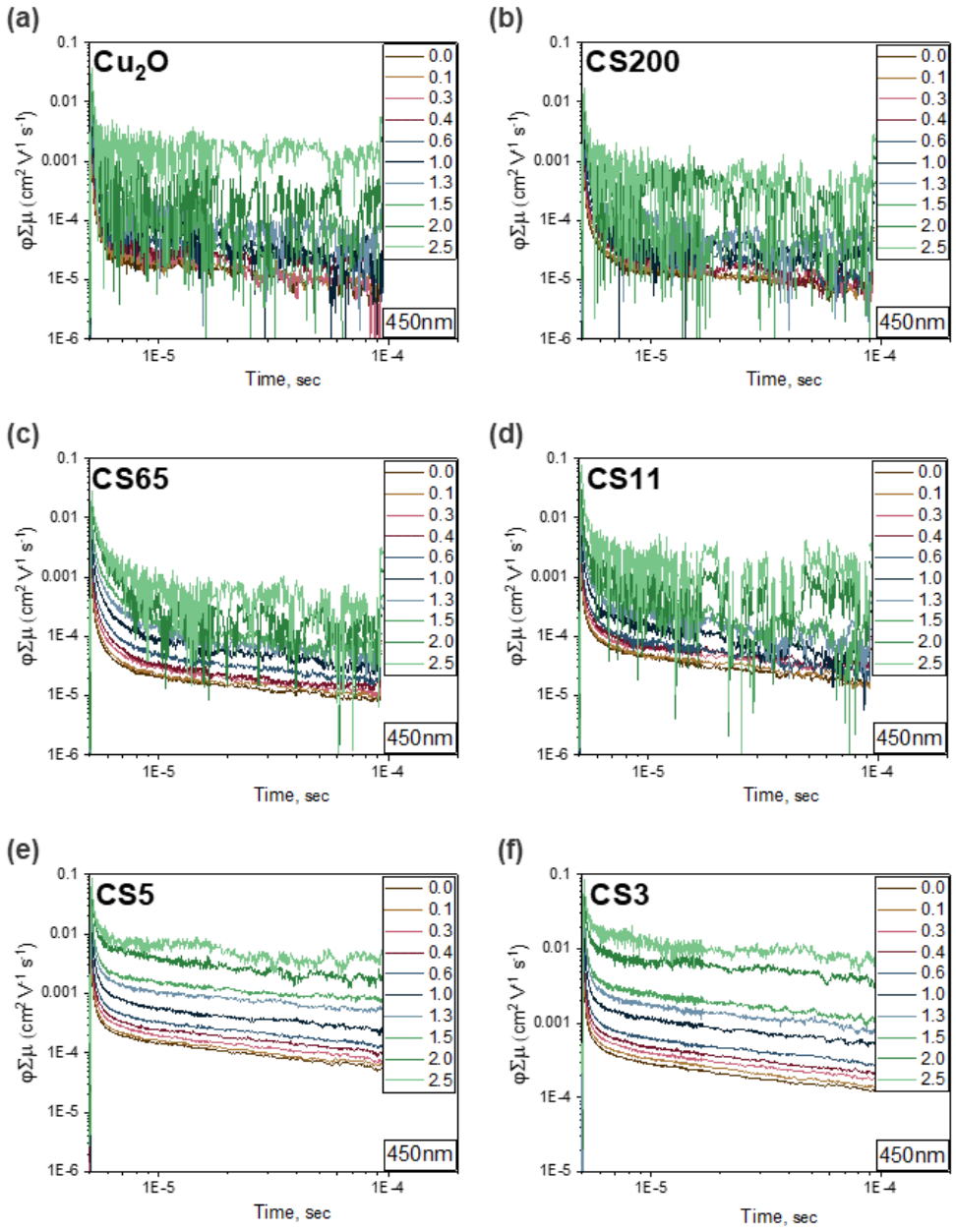


Figure 6.3 – Plots of maximum of carriers mobility vs. time for each analyzed sample at 450 nm; in particular: (a) Cu_2O, (b) CS200, (c) CS65, (d) CS11, (e) CS5, and (f) CS3. Both the axes are given in a logarithmic scale.

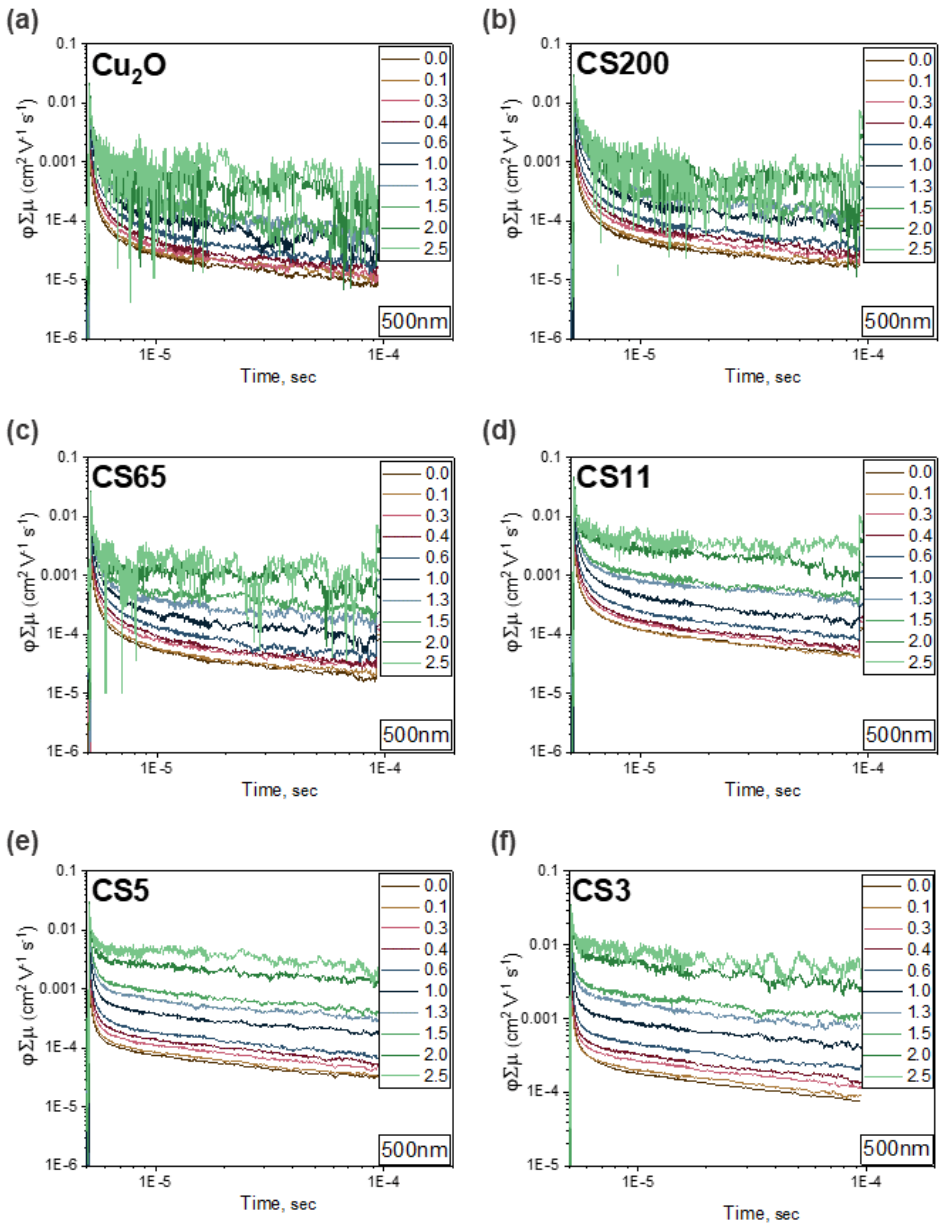


Figure 6.4 – Plots of maximum of carriers mobility vs. time for each analyzed sample at 500 nm; in particular: (a) Cu_2O, (b) CS200, (c) CS65, (d) CS11, (e) CS5, and (f) CS3. Both the axes are given a logarithmic scale.

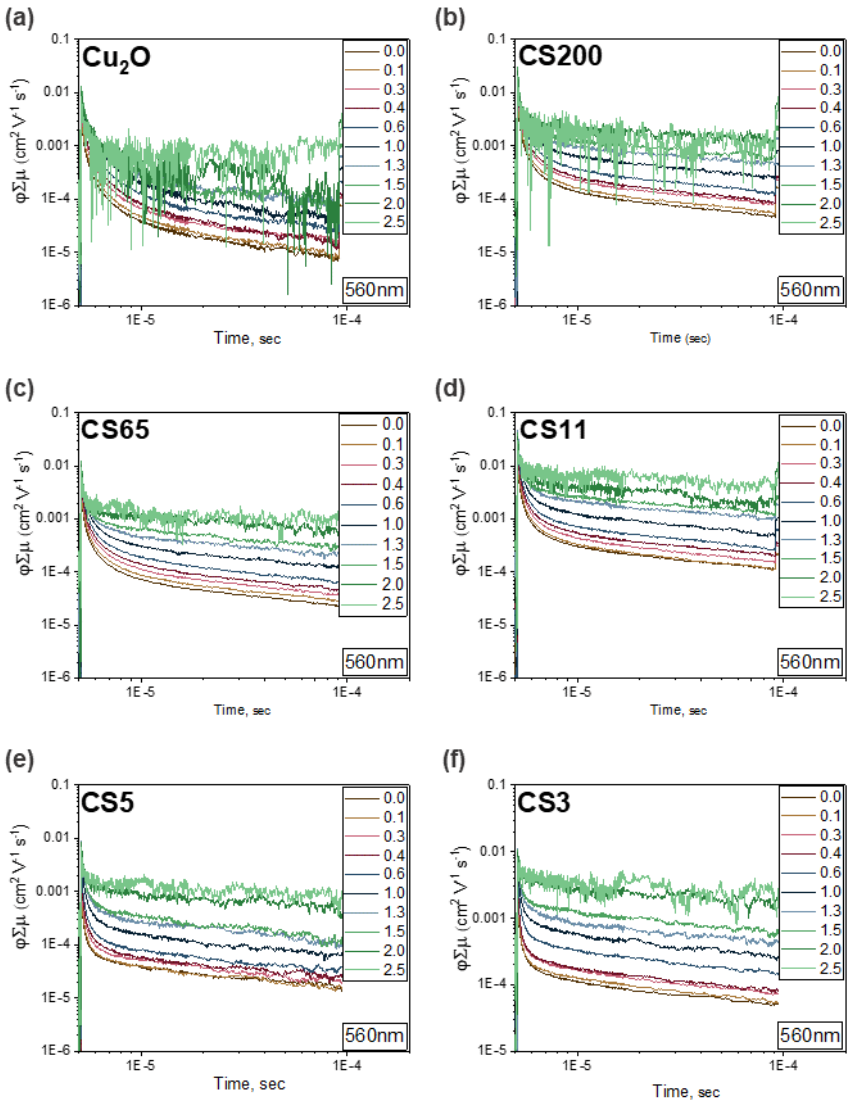


Figure 6.5 – Plots of maximum of carriers mobility vs. time for each analyzed sample at 560 nm; in particular: (a) Cu_2O, (b) CS200, (c) CS65, (d) CS11, (e) CS5, and (f) CS3. Both the axes report a logarithmic scale.

In general, the behaviour of samples with a lower Sn percentage was noisier and more unstable (see Cu_2O and CS200 samples in Figure 6.3a,b and Figure 6.4a,b). At 450 nm, the samples with more Sn (CS5 and CS3, Figure 6.3e,f) exhibited a maximum mobility that was approximately one order of magnitude greater than the other samples. The gap gradually decreased at 500 nm, where it appeared that the highest maximum mobility value was recorded for the CS11 sample (Figure 6.4). Generally, lower values were recorded in the data collected at 560 nm. However, it is important to decouple the maximum mobility from

lambda and the amount of incident photons, which is a specific value of the laser at a certain wavelength and with a certain neutral density filter applied. For this reason, the graphs in Figure 6.6 were created.

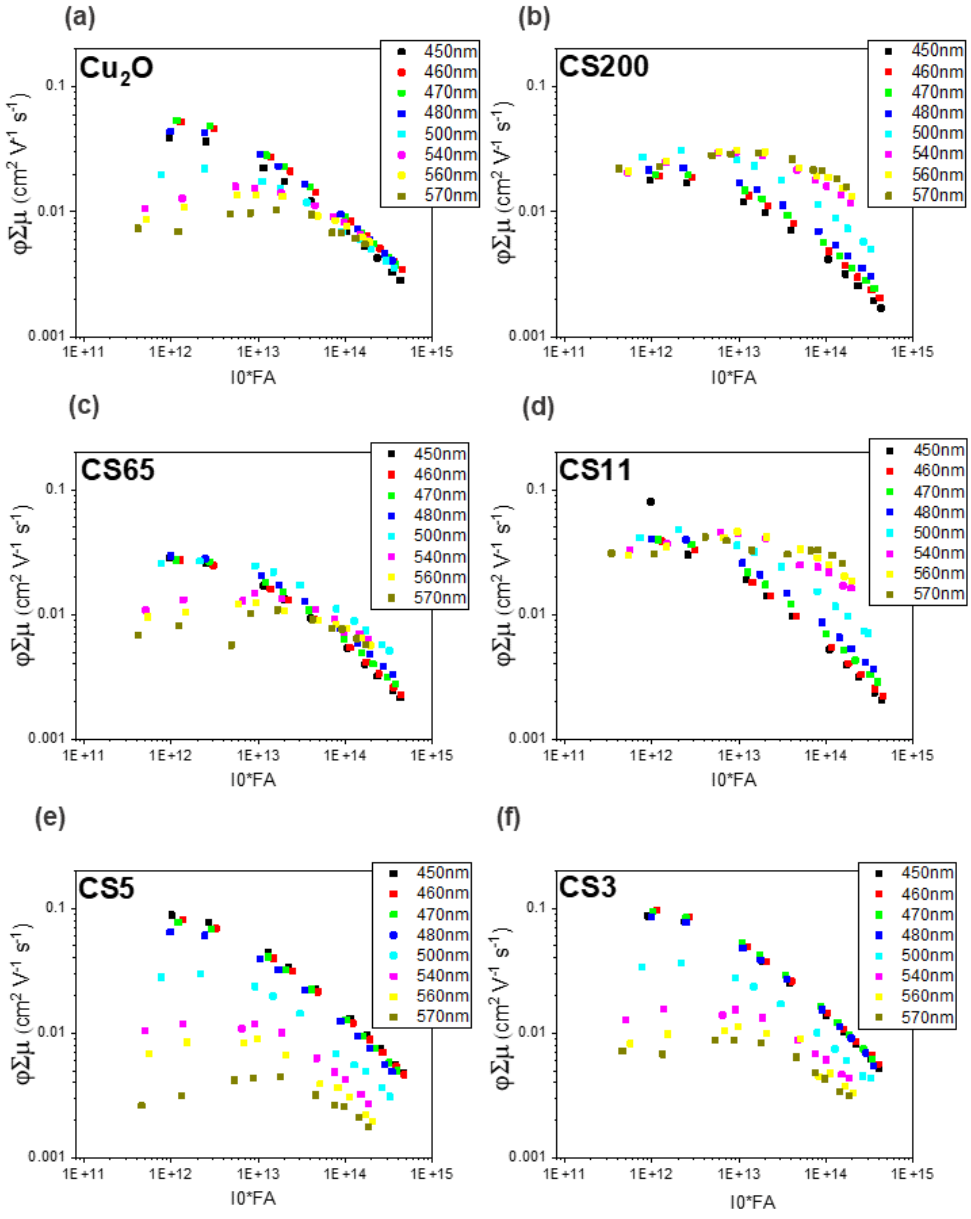


Figure 6.6 – Maximum TRMC signal $(\phi\Sigma\mu)_{max}$ vs. incident laser pulse intensity for core-shell samples and bare Cu_2O one in all the different excitation wavelengths.

Figure 6.6 shows the maximum values of the TRMC signals, $(\phi\Sigma\mu)_{max}$, versus incident laser pulse intensity. The $(\phi\Sigma\mu)_{max}$ signal gradually decreased with

increasing intensity of the excitation light among the wavelengths investigated. The phenomenon in literature is typically observed and well-described, and several works have attributed it to nongeminate higher-order electron-hole recombination [250–252]. This refers to a process in which multiple carriers (electrons and holes in this case) are involved in the recombination event. When there is an excess of photogenerated carriers, the probability of nongeminate higher-order recombination increases because there are more carriers available to participate in the recombination process [253]. To further proof such explanation, at lower light intensities recombination was reduced, which contributed to the creation of a plateau with a factor $\phi\Sigma\mu$ independent from the intensity. This phenomenon was observed in CS200, CS65, and CS11 at low laser pulse intensities (10^{11} – 10^{13} photons per pulse), as depicted in Figure 6.6b-d. The maximum $\phi\Sigma\mu$ could be considered a representative value for the effective carrier mobility in a semiconductor. Thus, a summary graphic displaying the maximum mobility value for all six samples at the three wavelengths mentioned above was created and is presented in Figure 6.7. To evaluate the $(\phi\Sigma\mu)_{max}$ and make a comparison among the samples, the laser intensity of 10^{12} photons per pulse was chosen. The Sn amount percentage was reported in the right-Y axis.

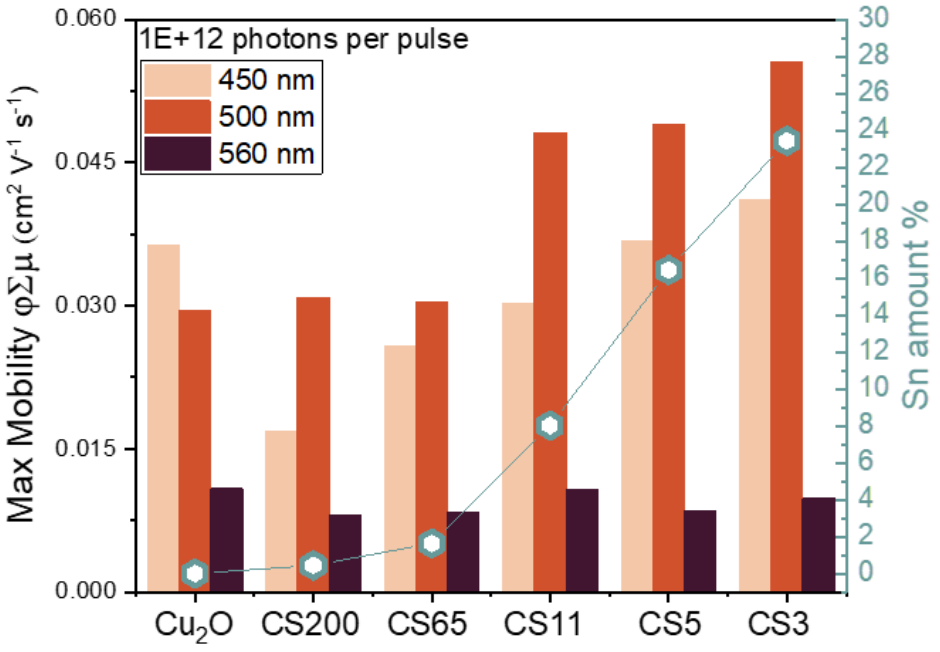


Figure 6.7 – Trends of maximum mobility values $(\phi\Sigma\mu)_{max}$ detected at λ = 450 nm (pink bars), 500 nm (orange bars), and 560 nm (purple bars) for all the core-shell and the bare Cu_2O samples. The laser light intensity was chosen to be 10^{12} photons per pulse. The Sn amount within each sample is showed in the right-Y axis.

The Cu_2O sample had a different behaviour from all the other samples. In fact, its peak of maximum mobility was observed at a wavelength of 450 nm, whereas for all the other samples, the highest value was recorded at 500 nm. This could be taken as further confirmation that the presence of SnO_2 modifies the position and state of the valence and conduction bands of the material, even in samples with low Sn content. The value obtained for the Cu_2O sample, equal to 0.039 $cm^2\ V^{-1}\ s^{-1}$, can be compared with some results found in the literature. The same experiment on Cu_2O cubic particles was recently performed by Toe *et al*. [252] at a wavelength of 355 nm laser pulse of $7.0 \cdot 10^{12}$ photons $pulse^{-1}$ cm^2. The maximum mobility estimated for cubic Cu_2O was 0.006 $cm^2\ V^{-1}\ s^{-1}$, while the signal from the rhombododecahedral crystalline phase was almost two orders of magnitude higher. In another work, a $Cu_2V_2O_7$ film synthesized by spray pyrolysis by Song *et al.* [251] was tested, using an excitation wavelength of 450 nm. Carrier mobilities were measured for various incident laser pulse intensities. The results showed that for laser pulse intensities between $5.4 \cdot 10^{14}$ and $9.5 \cdot 10^{14}$ photons cm^{-2}, the obtained carrier mobilities range from $3.4 \cdot 10^{-3}$ to $4.1 \cdot 10^{-3}$ $cm^2\ V^{-1}\ s^{-1}$.

Regarding the values obtained with an excitation wavelength of 450 nm as well as 500 nm, the trend is immediately recognizable in samples containing Sn. At both wavelengths, there is a marked increase in the maximum mobility value, proportional to the amount of Sn present in the sample. In fact, the values increase from around 0.015 and 0.030 $cm^2\ V^{-1}\ s^{-1}$ for the CS200 sample (at 450 and 500 nm respectively), to approximately doubled values of 0.040 and 0.057 $cm^2\ V^{-1}\ s^{-1}$ for the CS3 sample at the same wavelengths. The values at 450 nm show a linear increase across the samples, while those at 500 nm are very similar for both the CS200 and CS65 samples (about 0.030 $cm^2\ V^{-1}\ s^{-1}$) and for the pair of CS11 and CS5 samples (about 0.048 $cm^2\ V^{-1}\ s^{-1}$). To conclude the analysis, for all samples, it was found that the maximum mobility value reached at 560 nm was consistent and lower than the others (averaging around 0.011 $cm^2\ V^{-1}\ s^{-1}$), and did not follow a unique trend (in fact, a slightly higher value than the others was reached by CS65).

Combining the information contained in the plots in Figure 6.4 and Figure 6.5, we hypothesized that the presence of SnO_2 actually led to the inhibition of electron-hole recombinations, especially at lower laser energies, resulting in those samples showing significantly higher maximum mobility. However, the same impact of the *n*-type semiconductor (SnO_2) could not be maintained at too high

energy values (10^{14}-10^{15} photons pulse^{-1}), where the decrease in maximum mobility affected all samples regardless of the amount of Sn present.

The effective carrier lifetimes of the samples were determined from the decay of their TRMC signals. The fit of the decays curves for each sample at each wavelength was obtained by applying two linear fits in the first and in the second part of the curve, respectively. The first linear fit provided information on the short decay, and the slope of the line, that was called β, was taken as an indication on the lifetime. The same procedure was applied to the second region of the curve, in which the slope values were called γ, referring to the long decay. Results are reported in Figure 6.8. Looking at the plots of the different samples (Figure 6.8a-e), it can be noted that for almost all 5 samples, there is a rather stable behaviour for γ, with values aligning around –0.25. Instead, the behaviour of β was more interesting, as it could be seen that at lower wavelengths, the reported values for all the samples were higher in absolute value (on the left side of the graphs), and then get closer to the values of gamma at higher wavelengths. By looking at the comparison between the average values of β and γ for each sample (Figure 6.8f), it is worth to notice that they were obtained by averaging all the points obtained at different wavelengths. These mean values were correlated with the percentage of Sn present in each sample (circles with grey borders). It was observed that the value of beta and the percentage of Sn are directly proportional in their growth. The value of γ remains rather stable for all samples around -0.25. Instead, a trend could be observed for β, which was in absolute value higher than γ. This was in line with the fact that the higher (in absolute value) the value of β or γ, the faster the decay will be. Given the low value of γ, this indicates a slower and longer decay. Instead, the factor β, associated with the first part of the decay, provided confirmation that the thicker the SnO_2 layer covering the Cu_2O core becomes, the easier it will be for a carrier to move up to that region. Once there, the charge carrier can remain there for a long time and be available for the CO_2RR reaction. This was again an indication that the presence of larger amounts of SnO_2 affects the properties of the materials and that this is subsequently linked to selectivity, as reported in Figure 6.8g.

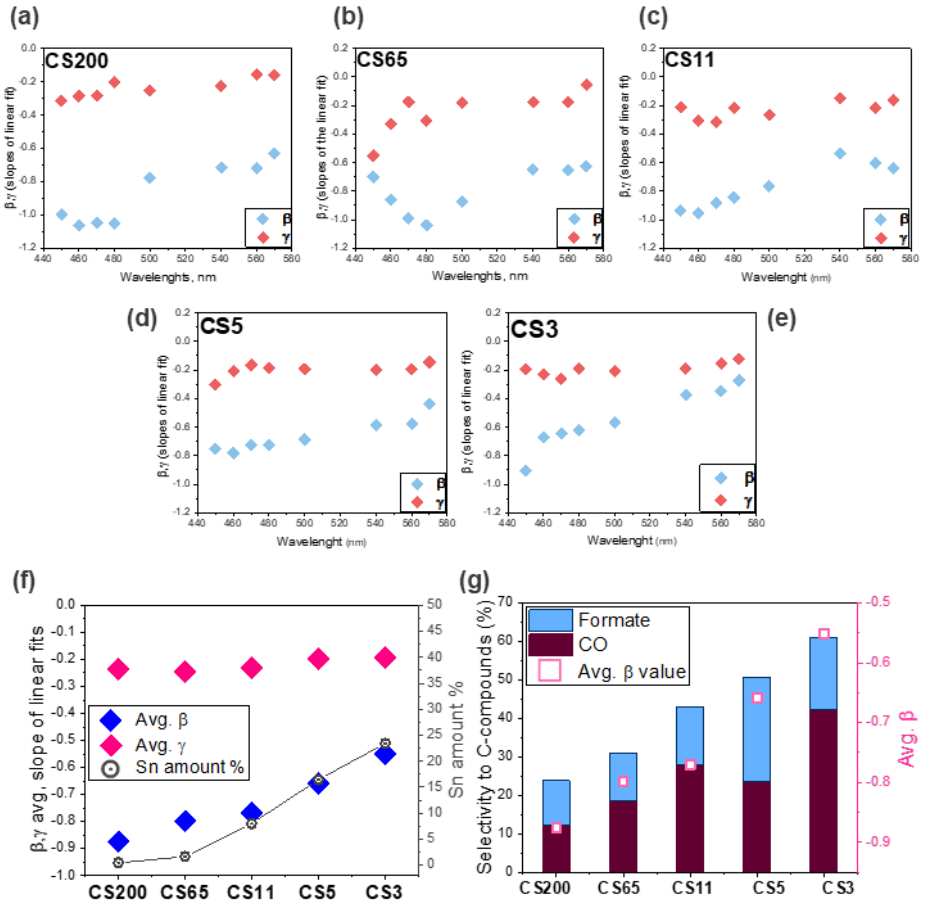


Figure 6.8 – *β* and *γ* values for each samples obtained as the slopes of the linear fit applied to the decay curves obtained at each wavelength; in particular: (a) CS200, (b) CS65, (c) CS11, (d) CS5, (e) CS3, (f) the average values of *β* and *γ* for each sample related to the Sn amount (%) within each sample, and (g) the correlation between the average *β* with the C-compounds selectivity as showed in Chapter 5.

6.3 Light Intensity Modulated Impedance Spectroscopy

Potentiostatic impedance spectroscopy is a well-established technique for analyzing the electrical properties of materials and solar cells, including their resistance, capacitance, and inductance [254]. In the field of photovoltaics, a common characterization method is to measure the open-circuit condition under steady-state illumination and to apply a small voltage perturbation at different light intensities to measure and analyze the IS spectra. This enables the determination of important parameters such as the recombination resistance (R_{rec}), chemical capacitance (C_{μ}), and characteristic lifetimes (τ) [255]. An alternative

approach involves separately characterizing photo-sensitive samples using intensity modulated photocurrent spectroscopy (IMPS) and intensity modulated photovoltage spectroscopy (IMVS).

6.3.1 Intensity modulated photocurrent spectroscopy

Frequency-resolved techniques can be used to study the charge carrier dynamics at the interface between a semiconductor and an electrolyte [256]. One such technique is intensity modulated photocurrent spectroscopy (IMPS), where the sample is subjected to a small-amplitude modulated illumination using an LED. The incident illumination used in IMPS is time-dependent and can be represented by the Equation 38:

Equation 38 – Time-dependent incident illumination

$$I(t) = I_0(1 + \delta \sin(\omega t))$$

where δ is the depth of modulation and I_0 is the mean intensity [257]. The resulting modulated photocurrent has the same frequency as the illumination, but with a different magnitude and phase. By scanning the frequency during the measurements, a Nyquist plot can be constructed to show the real and imaginary parts of the photocurrent. The plot consists of a lower quadrant semicircle and an upper quadrant semicircle, representing the total cell series resistance and capacitance, and charge transfer and recombination at the interface, respectively. By analyzing the modulated photocurrent response, which consists of the hole current and the electron current, IMPS can unravel the competition between hole transfer and surface recombination. When studying the photocurrent response in a material, it is important to understand how the frequency of the incident light affects the system. The imaginary photocurrent, which represents the current component out of phase with the voltage, reaches its maximum when the frequency matches the characteristic relaxation constant of the system. This frequency can be calculated using Equation 39:

Equation 39 – Maximum of frequency

$$\boldsymbol{\omega_{max} = k_{inj} + k_{rec}}$$

which takes into account the first order charge transfer and recombination rate constants (k_{inj} and k_{rec}, respectively) [258]. The intercepts of the *x*-axis, where the imaginary current equals zero, correspond to the spike and steady state photocurrents in a transient photocurrent experiment. The high frequency

intercept, where recombination is blocked due to fast modulation, represents the hole current, while the low frequency intercept represents the charge transfer efficiency. Equation 40 reports the charge transfer efficiency, which is the fraction of transferred holes that contribute to the overall surface processes, including both hole transfer and recombination.

Equation 40 – Charge transfer efficiency

$$\eta_{\mathrm{CT}} = \frac{k_{\mathrm{inj}}}{k_{\mathrm{inj}} + k_{\mathrm{rec}}}$$

It can be expressed as a function of the first order charge transfer and recombination rate constants. From Equation 39 and Equation 40, it is possible to calculate the individual reaction rates [258].

6.3.2. Intensity modulated photovoltage spectroscopy

IMVS, as its name implies, investigates the correlation between photovoltage and light intensity while maintaining constant current under open-circuit conditions [259]. The IMVS technique employs the same intensity modulation as IMPS, but instead measures the periodic modulation of the photovoltage. This modulation is influenced by the difference between the Fermi level in the dark and the quasi Fermi level under illumination. While IMPS offers insights into the dynamics of charge transport and back reaction under short-circuit conditions, IMVS measurements are influenced by the electron lifetime under open-circuit conditions [260]. The op-n circuit potential is the potential difference between the two electrodes of an electrochemical cell when there is no current flowing between them. It is defined as the potential difference between the anode and cathode when they are not connected by an external circuit. Referring to a solar cell, that is a system more likely the one in use in this Section, the open-circuit potential is the maximum potential of the cell before power is dissipated instead of being generated. The band gap between valence band and conduction band is small at this potential. Hence reactions on the back layer of the electrode are less likely. Most generated photoelectrons are injected into the semiconductor conduction band. In addition, cell reaches steady-state at the open-circuit potential. This means that the rate of electron injection into the conduction band is equal to the electron recombination rate. In general, the IMVS technique yields a semicircular response with a maximum radial frequency that corresponds to the

inverse of the photovoltage decay time constant, τ_{rec}. The Equation 41 describes this phenomenon.

Equation 41 – Recombination time constant

$$\tau_{rec} = \frac{1}{2\pi \cdot f_{\mathrm{IMVS}}}$$

When the impact of geometric or junction capacitance is negligible, τ_{rec} is calculated as the product of the recombination resistance and the chemical capacitance, which represents the ambipolar carrier lifetime.

Despite the fact that the fundamental principles behind IMVS are similar to those of IMPS (Section 6.3.1), it is not as commonly utilized as a measurement technique. In general, IMVS has mainly been used in DSSC (Dye-Sensitized Solar Cell) measurements [261,262] and its application for PEC water splitting is limited [263]. As far as current knowledge is concerned, there have been no studies reported on IMVS investigations of CO_2RR catalysts.

6.3.3 Experimental apparatus and procedures

A frequency range of 1 Hz to 100 kHz was applied. Measurements were performed with modulated illumination provided by a light-emitting diode with a wavelength of 455 nm (Thorlabs M455L3) driven by an LED driver (Thorlabs DC2100). Using a beam splitter, the light was split into two beams: one onto the PEC cell, and the other onto a high-speed Si photodiode (Thorlabs PDA10A-EC). The signal output of a frequency response analyzer (FRA, Solartron 1250, Schlumberger) was used to modulate the light intensity sinusoidally. An EG&G PAR 283 potentiostat was used to control the potential. The active area of the catalyst was 0.283 cm^2. The reference electrode was an Ag/AgCl saturated in 3 M KCl, while the counter was a Pt wire. The experimental apparatus was schematically reported in Figure 6.9.

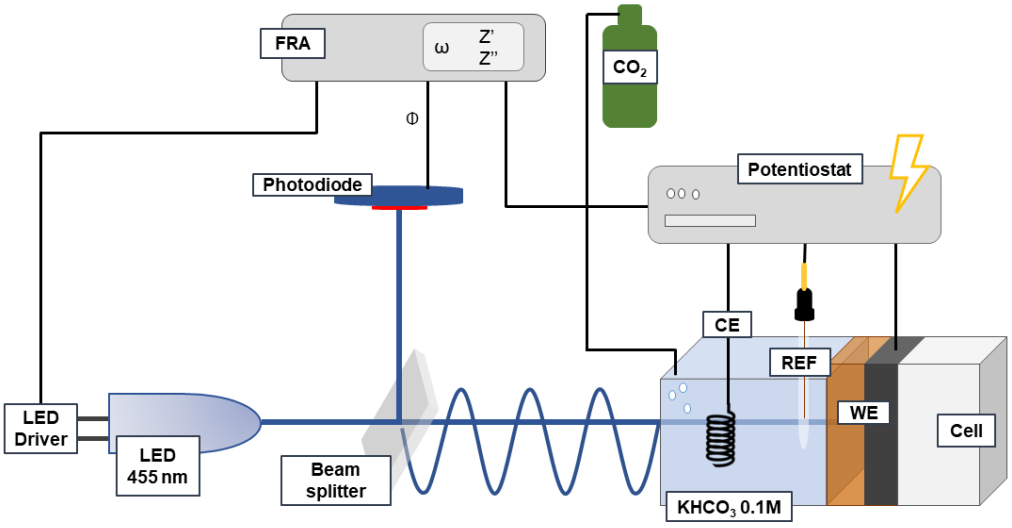


Figure 6.9 – Schematic diagram of the setup for intensity modulated photovoltage/photocurrent spectroscopy (IMVS/IMPS).

IMVS measurements were carried out in an aqueous solution of 0.1 M $KHCO_3$. The measurements were performed on the bare Cu_2O and on the 5 core-shell samples supported on Carbon Paper electrodes (deposited previously via air-brushing). The lack of literature studies on the use of this technique with catalysts for CO_2 reduction has led to the adoption of different and less conventional methodologies to complete the test. Two distinct methods were used:

1. The exploitation of the chemical equilibrium present in the electrolyte solution
$$H_2O + CO_2 \leftrightarrows H_2CO_3 \leftrightarrows H^+ + CO_3^{2-}$$
as the primary source of CO_2 to the catalyst;
2. The utilization of a CO_2 cylinder which directly bubbles gaseous CO_2 into the cell.

For each sample, the bias applied was 1 V. Three values of amplitude were also recorded: 100 – 200 – 300 mV. IMVS results and a brief discussion are reported in next Section.

6.3.4 Results and discussion

In all the plots reporting the semicircles V_{real} vs. $V_{imaginary}$, the observed trend was the same of the one reported by Son and co-workers [262]: the higher the voltage applied (in the case of this work the amplitude chosen), the smaller the

semicircle radius. The plots were reported in Appendix A4 in Figure A.5 and Figure A.6. The only exception to the above-described behaviour was the sample CS11, Figure A.5c, in the test without the direct CO_2 bubbling from the cylinder.

By obtaining from each of the IMVS plots the f_{IMVS} value, *i.e.,* the minimum point in which the semicircle arrives, it was possible to observe a frequency trend, reported in Figure 6.10.

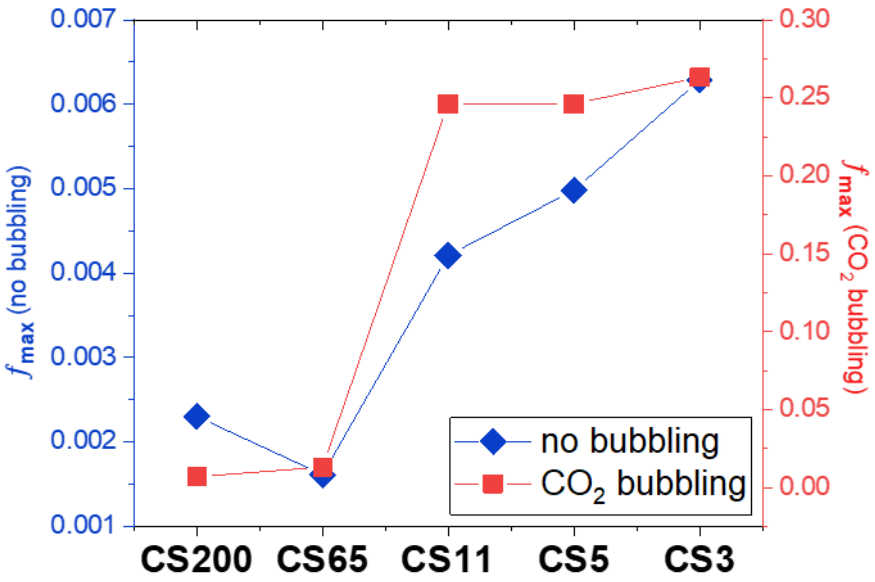


Figure 6.10 – The effects of different Sn amount into the 5 core-shell samples on f_{IMVS} values; results of both the experiment types were showed in the plot: blue points are referred to the test with no bubbling while the red ones are proper of the CO_2 bubbling experiment.

As deduced by Equation 40, there is an inverse proportionality between frequency and the time constant indicating electron-hole recombination at the electrode/electrolyte interface. In this case, since an increasing trend of frequency can be observed with increasing amounts of Sn, the lifetime will behave oppositely, progressively decreasing with increasing amounts of Sn. The same analysis was reported in the work carried out by Yang and co-workers [264], in which they related the decreasing recombination time, and so an indication of the electron lifetime, with the increasing size of TiO_2 nanoparticles. Typically, a longer lifetime of an excited electron suggests a slower rate of recombination and a higher density of conduction band electrons, which can be associated with an increased V_{OC} value [265]. There may be many factors that influence the relationship between the amount of Sn and the electron lifetime, such as

temperature, pressure, and electrolyte properties, but the investigation of these parameters were the subject of research in this work up to this point.

6.4 Conclusions

The investigation of the carrier dynamics of the Cu_2O-SnO_2 core-shell samples, whose synthesis and characterization were described in the previous Chapter, was carried out via TRMC and IMVS analysis. The purpose of this characterization was to obtain information that could be correlated with the results of the photo-electrocatalytic reduction of CO_2 using the catalysts in question. A significant increase in the selectivity for C-compounds was observed with increasing amounts of Sn in the catalysts (particularly for the catalyst named CS3). Investigation through TRMC of the same samples revealed that the mobility of charge carriers increases proportionally to the amount of Sn at both 450 nm (slightly less prominently) and 500 nm (in a more definite shape). Another important finding is that the outer SnO_2 shell may somehow help to prevent electron-hole recombination when present in a thicker layer, but the non-geminate recombination prevailed when the energy of the radiation applied was too high to concur with. By comparing this result with other literature reports on copper-based catalysts, it was found to be sometimes consistent with values reported by other groups, and in some cases, better in terms of maximum mobility by at least an order of magnitude.

Subsequently, efforts were carried on in developing a different analysis technique to study more carefully the catalyst during the CO_2 reduction reaction. To achieve this, an attempt was made to adapt the IMPS and IMVS setup to the necessary environment for the catalyst to carry out CO_2RR, since in the literature these methodologies are much more common for solar cells or catalysts used for water splitting. Thus, we defined two protocols for conducting IMVS tests on the core-shell catalysts, either by exploiting the equilibrium generated in the electrolyte solution ($KHCO_3$ 0.1M) or by directly connecting CO_2 bubbling from a cylinder to the setup. The IMVS tests resulted in the estimation of the minimum value of the frequency reached by the semicircles in the tests, which can be correlated to the electron lifetime at the electrode/electrolyte interface. It was observed that the electron lifetime in the core-shell samples decreases with increasing amounts of Sn in the materials. Based on the results described, correlations can be inferred between these and the previously obtained PEC test results. Specifically, each of the two techniques used in this Chapter can provide

an explanation for the observed phenomenon of selectivity shifting with increasing Sn content.

i. As the Sn content increases, the maximum mobility of the charge carriers increases, resulting in more available electron density for CO_2R reaction in materials with higher Sn content. Indeed, it can be experimentally observed that the faradaic efficiencies for C-compounds are significantly higher in catalysts with more Sn than those with lower Sn content.
ii. The electron lifetime decreases with increasing Sn content, which may explain why, despite higher efficiencies, only C_1 compounds such as CO and Formate are produced, and selectivity towards longer chain compounds is not achieved.

These hypotheses can be combined with the ones from previous Chapters and further explain the behaviour of charge carrier dynamics within the analyzed samples. Finally, it is necessary to note that, to the best of our knowledge, there are no literature works regarding such a detailed description of this type of CO_2RR catalysts.

Chapter 7

Functionalization of Cu_2O-SnO_2 catalyst with Ru-Re based hybrid supramolecular complexes

The Chapter 7 discusses the standardization of the Cu_2O wet precipitation synthesis and the reproducibility of Cu_2O samples, based on the results from the previous Chapters. The study also assesses the tunability of some characteristics of the materials based on the flow rate of the reagents into the reactor. The Cu_2O-SnO_2 samples were synthesized and then functionalized by electropolymerization to deposit Ru/Re-based cocatalyst on their surface. Three different kinds of Ru/Re-based complexes were anchored onto the photoelectrode surface. The modified catalysts were tested, and promising results were obtained in terms of the catalyst's activity towards CO_2 reduction and the possibility of using such a catalyst and the generated gaseous products for hydroformylation reactions.

Contributions: This work has received funding from the European Union's Horizon 2020 Research and Innovation Action program under the Project SunCoChem (Grant Agreement No 862192). The standardization of the synthetic route developed in Chapter 5 was mainly studied by Giulia Cuatto, Mario Gallone, and Dr. Hilmar Guzmán, especially referring to the Cu_2O synthetic approach. The impregnation phase was developed by Giulia Cuatto, Mario Gallone, Dr. Hilmar Guzmán together with the PhD student. The resulting Master thesis written by Giulia Cuatto was entitled:

"Cu_2O-SnO_2 core-shell nanocatalysts for the photo/electrochemical CO_2 conversion: synthesis standardization" by G. Cuatto, supervised by S. Hernández, M. Castellino, Politecnico di Torino, academic year: 2021/2022.

The XRD measurements were accomplished by Camilla Galletti, Prof. Fabio Deorsola and Dr. Giuseppe Pipitone, while the analysis was completed by Giulia Cuatto and Mario Gallone together with the PhD student. The UV-Vis measurements and analysis were made by Giulia Cuatto. The XPS measurements and analysis were conducted by Dr. Micaela Castellino and Giulia Cuatto. The ECSA evaluation was accomplished by Giulia Cuatto under the supervision of Dr. Hilmar Guzmán. The FESEM images were obtained by Dr. Federico Dattila. The functionalization of the metallic catalyst was performed by Dr. Roger Miró Serra, from Eurecat Centre Tecnològic, as a partner within the SunCoChem European Project, following the work published by him and co-workers, entitled: "Solar-driven CO_2 reduction catalysed by Hybrid Supramolecular Photocathodes and enhanced by Ionic Liquids" [266]. The PEC results were obtained by the PhD student and Giulia Cuatto.

7.1 Ru-Re supramolecular complexes

Photo-electrochemical CO_2 reduction using hybrid photocathodes composed of *p*-type semiconductors, visible light-absorbing chromophores, and molecular catalysts has been deeply explored [267–270]. As key factors in achieving high catalytic efficiencies and a complete artificial photosynthesis, four primary processes are necessary [271]:

i. light absorption by light absorbers,
ii. charge separation in the light absorbers,
iii. charge transfer from the light absorbers to the catalysts,
iv. catalytic reactions.

Therefore, two crucial components are required for developing photo-electrocatalytic devices:

i. efficient catalysts with a high intrinsic activity and stability,
ii. ideal light absorbers that possess a broad absorption in the solar spectrum, stable excited states, and high charge carrier mobility.

In order to absorb light and generate charges carriers, photosensitizers like molecular dyes [272], semiconductors, and quantum dots [273] are necessary. Moreover, since these reactions involve multiple electron and proton transfers, efficient catalysts are needed to overcome high reaction barriers, lower the overpotential, and accelerate the reaction rate. The development of molecular catalysts is the most promising approach to achieve catalysts with high intrinsic activity, low overpotential, and a high catalytic rate. Molecular metal complexes are compounds that contain a metal centre surrounded by ligands, which can be organic or inorganic molecules that coordinate to the metal through their atoms or functional groups. These complexes can exhibit a wide range of physical and chemical properties depending on the nature of the metal centre and the ligands. As a result of this configuration, molecular catalysts have numerous advantages. Molecular catalysts offer tunability, whereby the steric configuration and electronic structure can be precisely adjusted through ligands design in the specific coordination environment. Thanks to that, molecular complexes can be fine-tuned after extensive research to produce efficient catalysts for various reactions. Besides, selectivity could be critical factor, and molecular catalysts could overcome the product selectivity issue. With their single, easily identifiable, and adjustable active sites, molecular catalysts offer ample opportunities to regulate the selectivity of CO_2 reduction catalysis, as demonstrated in previous studies [274,275]. It is also worth to mention that in the context of artificial photosynthesis, the most significant advantage of molecular catalysts is their metal-atom economy. Efficient utilization of metal atoms is crucial for the practical application of catalysts, especially those based on rare metals such as Pd, Rh, Pt, Ir, and Ru. Nano-structures in inorganic material-based catalysts are composed of aggregates of hundreds or thousands of metal atoms, with only a small number of atoms acting as active sites at surfaces, edges, corners, and heterojunctions [276].

Although the nano-structured materials have their strengths and weaknesses, their main limitations such as low oxidation ability, low selectivity for reduction reactions, and stability issues can be overcome by developing appropriate molecule/semiconductor hybrid materials. The success of this approach relies on the efficient electron transfer from a semiconductor to an immobilized molecular catalyst, as well as the suppression of back electron transfer [277]. Therefore, it is important to carefully design both the conduction band potential of the semiconductor and the reduction potential of the molecular unit to achieve optimal reduction of CO_2 on the molecule/semiconductor hybrid material.

Molecular metal complexes coupled with several semiconductors are promising photocatalysts for reducing CO_2 to hydrocarbons such as CO, formic acid, and formaldehyde [271]. In particular, the interest is here focused on: Ru^{2+} and Re^{+} (ruthenium and rhenium)-based molecular complexes. They are a class of molecules that have been investigated and then developed for various applications, including photocatalysis, photovoltaics, and photo-electrochemical conversion [277–279]. These complexes consist of a Ru and Re metal centre, linked by a bridging ligand. The combination of these two metals provides a unique electronic structure and a high level of stability, which makes them excellent candidates for catalytic applications. Li *et al*., [280] recently developed an integrated photo-electrode capable of reducing CO_2 to CO in neutral aqueous solutions for over 10 hours with sustained photo-electrocatalytic efficiency ($F.E._{CO}$ ~68%) using a two-step electropolymerization procedure. The assembly comprised a molecular chromophore (Ru-based) and a CO_2R co-catalyst (Re-based), and it was constructed on electrode surfaces through the silanization of the semiconductor catalyst (NiO in that case). Based on the successful outcomes obtained from different semiconductor and immobilization techniques, in this Chapter the synthesis of diverse hybrid assemblies is reported together with the promising results obtained.

7.2 Cu_2O-SnO_2 Synthesis standardization

Standardization of the synthesis process is essential when developing a new catalyst to ensure the reproducibility of the catalyst's properties and performance. Without standardization, variations in the synthesis method could result in significant differences in the catalyst's morphology, composition, and surface area, which could affect its catalytic activity. Standardizing the synthesis process allows researchers to control the critical parameters, such as temperature, pressure, and reactant ratios, leading to consistent and predictable catalyst properties. Standardization also simplifies the process of scaling up the catalyst production, making it more feasible for industrial applications. To advance beyond TRL 4 (*i.e.,* the last laboratory-scale Technology Readiness Level), the synthesis environment must become as close to industrial as possible, as TRL 5 represents the beginning of the testing in a relevant environment. Therefore, standardizing the synthesis process is critical for achieving TRL 5 and beyond, allowing the development of new catalysts with reliable and reproducible catalytic performance in real-world conditions. The aim of the work is to establish a consistent method for producing Cu_2O–SnO_2 core-shell catalysts. This is achieved

by utilizing peristaltic pumps to feed NaOH and L-ascorbic acid during the initial stage and NaCl and $SnCl_4 \cdot 5H_2O$ during the impregnation phase of the synthesis process. Firstly, the Cu_2O synthesis were completely standardized, and the optimal sample conditions were employed for the core synthesis, followed by the deposition of SnO_2.

7.2.1 Reagents and instruments

Copper(II) chloride ($CuCl_2$, 99%), sodium hydroxide (NaOH, ≥98%), L-ascorbic acid ($C_6H_8O_6$, ≥98%) were used in the Cu_2O nanocubes synthesis. To perform the second step of the synthesis, the previously obtained Cu_2O nanocrystals were dispersed in ethanol (C_2H_6O, ≥99.8%) and added to tin(IV) chloride pentahydrate ($SnCl_4 \cdot 5H_2O$, 98%) as tin oxide precursor and sodium chloride (NaCl, ≥99.5%) to favour ion exchange. All the reagents were purchased from Sigma-Aldrich (Milan, Italy), and they were used as received, unless otherwise specified. Cellulose nitrate membrane filters (purchased from WhatmanTM), with a pore diameter of 0.2 μm, were used for the vacuum filtration step. Ultrapure type 1 water (MilliQ) was utilized to prepare all the aqueous solutions and for cleaning dedicated glassware and instruments. A silicone oil (purchased from Sigma Aldrich) bath was used to keep the temperature constant. Potassium bicarbonate ($KHCO_3$, 99.7%) and potassium hydroxide (KOH, 98%) were chosen as catholyte and anolyte, respectively. Nafion® 117 solution (5 wt.%) and ethanol were employed in the preparation of the catalytic ink. The support for the electrodes preparation was Toray carbon paper 060.

Here, a list of instruments utilized during the synthesis process is provided. A thermal magnetic plate provided by ARGO LAB with a thermocouple was used to mix the solution and control temperature. The pH during Cu_2O synthesis was monitored using a Milwaukee pH meter, which was linked to a peristaltic pump used for delivering NaOH and NaCl. Three peristaltic pumps from Gilson®, Ismatec®, and Montepaone S.R.L were used to distribute L-ascorbic acid and $SnCl_4 \cdot 5H_2O$ at different delivery velocities. For vacuum filtration, a pump provided by Steroglass was implemented, and a Thermo Fisher Scientific centrifuge was required to separate the Cu_2O-SnO_2 powder from the ethanol suspension. Finally, a vacuum oven from Büchi Labortechnik AG was used for drying the samples.

7.2.2 Synthesis method

The method created by Zhang *et al.* [220] served as an inspiration for the reference synthesis technique. The insights gained on the volume and concentration of the different precursors from the core-shell synthesis described within the Chapter 5 were also considered. The process was formally separated into two steps. First, wet precipitation was used to create Cu_2O nanocubes, and then impregnation served to create the SnO_2 outer shell. The schematic representation of the synthetic method followed within this work is provided in Figure 7.1. The steps needed for the formation of Cu_2O core nanoparticles is represented in Figure 7.1a, while the ones due to the SnO_2 coverage process are reported in Figure 7.1b. Each stage was carried out using magnetic stirring at ambient temperature.

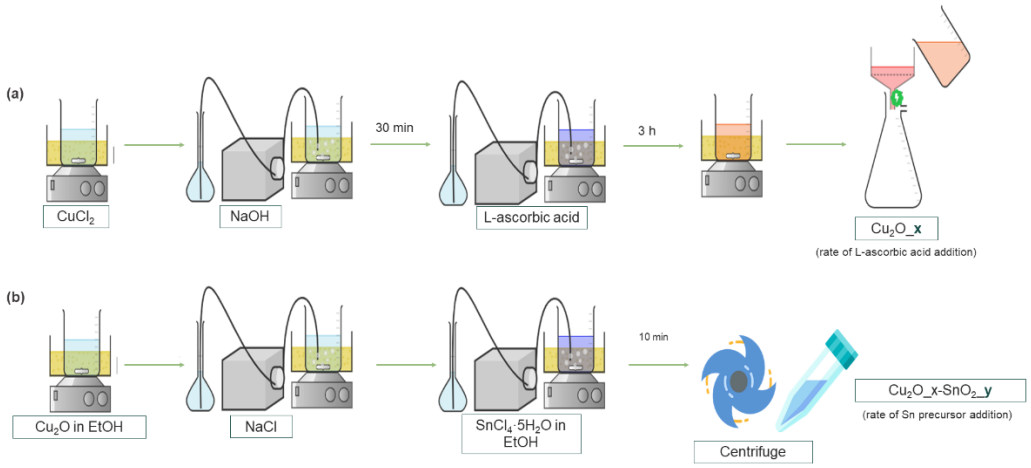


Figure 7.1 – Schematic representation of the instruments and reagents involved in the (a) first part of the synthesis and (b) its second part.

7.2.2.1 Cu_2O core synthesis

As already stated, starting from the synthetic method described in Chapter 5, following the work of Zhang *et al.* [220], the reagents concentrations and volumes reported in Table 7.1 were implemented to increase the yield of the Cu_2O synthesis.

Table 7.1 – Volumes and concentrations of the reagents solutions.

Reagent	$CuCl_2$	NaOH	$C_6H_8O_6$

Volume (mL)	250	25	25
Concentration (M)	0.02	6.00	1.80

The solution of $Cu(OH)_2$ precipitates turned from light blue to bright blue when the NaOH aqueous solution 6.00 M was added through the pump in the $CuCl_2$ aqueous solution 0.02 M. (Figure 7.2a,b). L-ascorbic acid was supplied with a regulated flow rate after 30 minutes. Intense blue became green, then mustard yellow, and finally orange as the suspension of Cu_2O stabilized (Figure 7.2c-i).

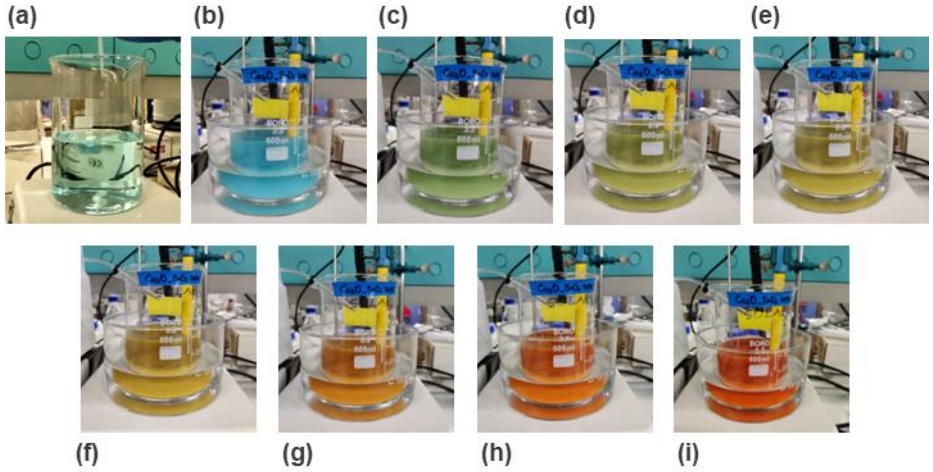


Figure 7.2 – Colour changes: (a) $CuCl_2$ solution, (b) NaOH addition, (c) L-ascorbic acid addition – green, (d,e,f,g) L-ascorbic acid addition – mustard yellow, (h,i) L-ascorbic acid addition – orange.

The suspension was stirred for three hours at 25 °C before being vacuum filtered and washed with MilliQ. The resulting Cu_2O powder was then dried in a vacuum oven at 60 °C for about 12 hours. In the Cu_2O synthesis, NaOH solution was delivered at a rate of 25 L min^{-1} while L-ascorbic acid (the reducing agent) was delivered at rates of 5, 10, 20, 60, 100, and 200 mL min^{-1}. Only the flow rate of L-ascorbic acid was varied since its flow rate affected the nucleation and growth of Cu_2O. In contrast, the addition of NaOH led to precipitation of copper hydroxide. Monitoring the pH level during the synthesis process provided the first insight to ensure synthesis repeatability. Four different stages of the reaction allowed for the recording of pH. The obtained values did not change significantly during the different syntheses. The various materials obtained from this synthesis step will henceforth be called Cu_2O_x with x = the flow rate of L-ascorbic acid used to obtain that specific material (expressed in mL min^{-1}).

7.2.2.2 SnO_2 shell synthesis

The impregnation stage started by suspending 350 mg of the Cu_2O nanoparticles previously produced in 150 mL of ethanol. Then 4.5 mL of a 0.2 M NaCl aqueous solution were first added and consequently 150 mL of a solution of $SnCl_4 \cdot 5H_2O$ in ethanol were additionally inserted. The Cu_2O nanocubes and $SnCl_4 \cdot 5H_2O$ reagent had a molar ratio of 3, which was assumed from the work described in Chapters 5 and 6. For each synthesis repetition, the NaCl solution was fed at a rate of 25 mL min^{-1}, while the $SnCl_4 \cdot 5H_2O$ in ethanol was injected a different rates of 60, 100, and 200 mL min^{-1}, in both cases by using a peristaltic pump. The addition of the Sn precursor through a EtOH solution formed the oxide following an ion exchange reaction, and it is thus linked to the most crucial process in this stage, *i.e.,* the precipitation of tin oxide. The flow rate of the NaCl solution had very little effect on the final product because it was solely utilized as promoter of the ion exchange. The suspension was stirred for 10 minutes and then the Cu_2O-SnO_2 powder was separated from the ethanol suspension by centrifugation. The resulting powder was cleaned twice with ethanol and three times with MilliQ water. The powder was dried at 60 °C in a vacuum oven for around 12 hours. The powder was then gathered and weighed. After this second synthetic step, the samples will maintain the first part of their name as described in the previous Section (*i.e.*, Cu_2O_60), followed by the SnO_2_*y*, with y = the $SnCl_4 \cdot 5H_2O$ flow rate (in mL min^{-1}). As an example, the sample obtained by setting the L-ascorbic acid pump at 60 mL min^{-1} and the $SnCl_4 \cdot 5H_2O$ flow rate at 60 mL min^{-1} will be labelled: Cu_2O_60_SnO_2_60.

7.3 Characterization and reproducibility

Testing samples and demonstrating good reproducibility under defined conditions is essential to achieve a standard process. As such, the characterization of each sample is indispensable in determining the reproducibility of the synthesis method. During the study, the reproducibility of the synthesis was evaluated by using various techniques, including X-Ray diffraction, X-Ray photoelectron spectroscopy, scanning electron microscopy, direct reflectance UV-vis, and ECSA. Once the synthesis repeatability for Cu_2O cores was verified, certain conditions, such as the flow rate of the L-ascorbic acid, were deliberately altered in order to investigate the dependence of the material characteristics and catalytic activity on the perturbed parameter.

7.3.1 Reproducibility and dependence with flow rate

Two techniques allowed to assess the reproducibility of the synthetic method of Cu_2O nanocubes. In particular, in this paragraph XRD and ECSA were reported together with the correlation of the results with the parameters of the synthesis such as flow rate. Starting from the former, Figure 7.3a displays the X-ray diffraction spectra of the Cu_2O powders, which exhibited identical patterns representing the Cu_2O (JCPDS 01-077-0199). All the spectra presented the same intense peaks, corresponding to the (111), (200), and (220) directions and had an approximate angle of 36.5°, 42.5°, and 52.6°, respectively. The intensity ratio of the (111) peak to the (200) peak was analyzed, and the results are reported in Figure 7.3b. All the samples were characterized by a mean value of such ratio of 3.21 ± 0.13, regardless of the rate at which L-ascorbic acid was delivered. This indicated that the crystals preferential growth directions were almost unaffected by the L-ascorbic acid flow rate.

Based on these results, the synthesis could be considered highly reproducible, as the obtained phase and preferential growth direction did not depend on the analyzed synthesis conditions. Instead, the Scherrer analysis showed differences in crystallite dimension, indicating that the nucleation and growth process of Cu_2O was influenced by the L-ascorbic acid flow rate. The crystallite size D was calculated for each sample in the (111), (200), and (220) directions, and the values were reported in Figure 7.3c. The values obtained for all crystalline directions were similar, with a standard deviation of approximately 12% for all samples. The mean value was then calculated for each sample, and the mean crystallite size was determined for each L-ascorbic acid flow rate. As expected, the crystallite size was found to be dependent on the synthesis conditions, with values showing a decreasing trend as the L-ascorbic acid flow rate increased (Figure 7.3c).

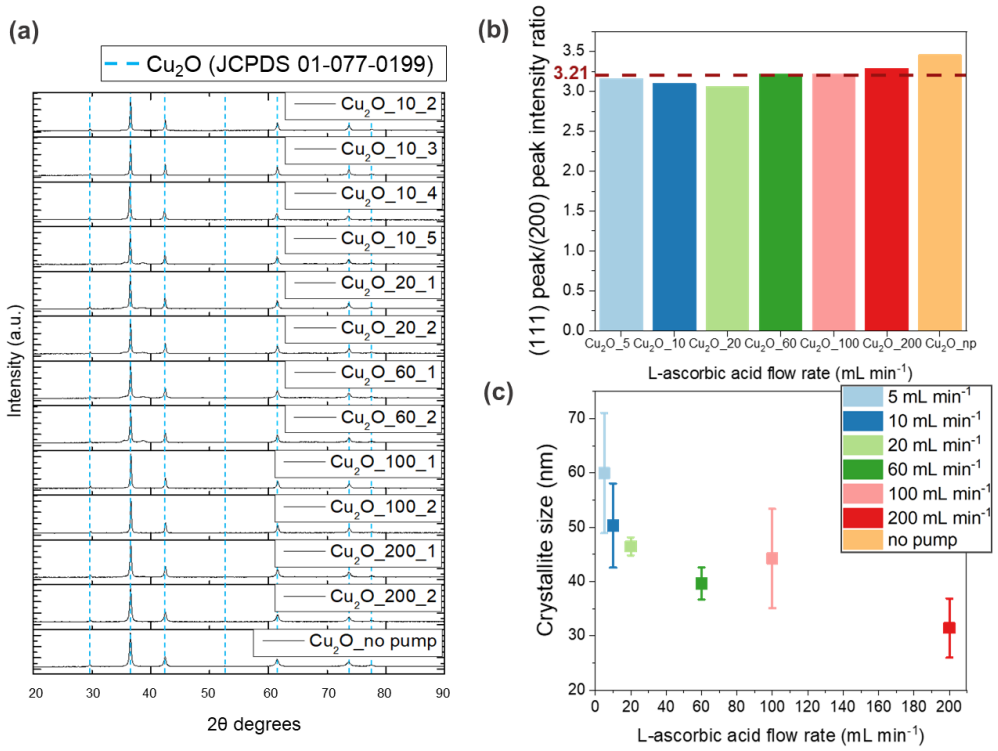


Figure 7.3 – XRD characterization of the Cu_2O samples; (a) spectra of the Cu_2O samples, (b) (100) peak/(200) peak ratio, and (c) mean crystallite size per flow rate.

For performing ECSA measurements, the powders were used to prepare an ink by using an ultrasound-assisted procedure. Then, 10 µL of the suspension was weighed three times to obtain an average density value. The volume needed for a catalyst loading of 1.4 1 mg cm^{-2} was calculated using the percentage of powder in the ink. This volume was deposited over the glassy carbon electrode of a rotating disc electrode (RDE) system and left to dry in air. Meanwhile, a solution containing 65 mL of $KHCO_3$ 0.1 M was saturated in N_2. When the electrode was dried, it was inserted into the cell with the platinum wire counter electrode and the Ag/AgCl KCl 3M reference electrode. Cyclic Voltammetries at the different scan rate were recorded (Appendix A4, Figure A.7a). Using the current density values obtained at the OCV (Equation 13), it was feasible to create a plot of the average current density at each scan rate against the scan rate. Additionally, performing a linear regression on this data enabled the calculation of ECSA values, which are presented in Figure 7.4. An illustration of the linear regression is provided in Appendix A4, Figure A.7b.

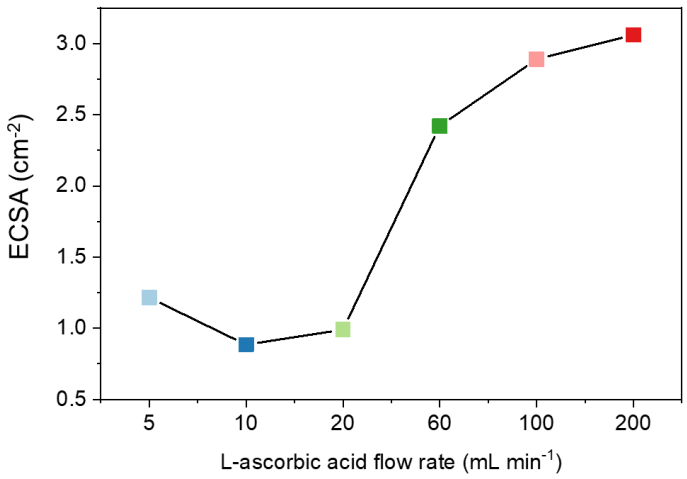


Figure 7.4 – ECSA values of Cu_2O sample obtained with different L-ascorbic acid flow rates.

For low L-ascorbic acid delivery velocities the ECSA did not change significantly, but it increased considerably for velocities above 60 mL min^{-1}. Within the range of 20 mL min^{-1} to 60 mL min^{-1}, the ECSA increased from 0.99 cm^2 to 2.42 cm^2. For higher velocities, the ECSA did not noticeably change, but a discernible trend was observed. Cu_2O_60, Cu_2O_100, and Cu_2O_200 exhibited the largest electrochemical surface areas. So, the increase of the L-ascorbic acid flow rate was related to the higher electrochemical surface area of the Cu_2O nanocubes. Based on these results, Cu_2O_60, Cu_2O_100, and Cu_2O_200 were selected as the core materials for the Cu_2O-SnO_2 core-shell structure.

7.3.2 Core-shell catalysts characterization

In this paragraph, only some of the characterizations are reported to focus on the key aspects. The techniques used are described in the characterization Section (XRD, XPS, UV-VIS, FESEM, EDX, ECSA) and we have here decided to discuss only the results from FESEM, which allows the comparison of particle morphology before and after the SnO_2 impregnation step, UV-Vis, which enables the estimation of the band structure of the final Cu_2O-SnO_2 catalyst, and XPS, to evaluate the amount of Sn present in the catalyst and to compare it with the ICP-OES results obtained in the previous Chapters. The main aim, at this stage of the research, was the identification of the specific and necessary characteristics of the catalyst as it was conceived and developed, rather than the actual reproducibility of the synthesis step to obtain impregnation with SnO_2. The choice of the final

catalyst, which is discussed in Section 7.5, was mainly made by observing the PEC stability results of some of the tested samples, as reported in Section 7.4.

FESEM images were obtained both for Cu_2O_100 and Cu_2O_100_SnO_2_100, and the comparison was reported in Figure 7.5a,b. In the core-shell sample, the Cu_2O cubic nanoparticles were not visible in their original and sharp shape, as all the particles were covered by an external layer of tin oxide. The average particles dimensions were equal to 90 nm regarding bare Cu_2O, while it increased approximately 230 nm after the impregnation step. The Cu_2O surface was homogeneously covered by the SnO_2 shell. The behaviour of thick coverage due to the SnO_2 presence was in common among the different samples, sometimes also small agglomerates with a size of about 30 nm were visible.

From the DR-UV-vis spectra of samples, by utilizing the Kubelka-Munk function, it was possible to convert diffuse reflectance to absorbance. Using the fitted linear portion of the Tauc plot, with absorbance versus energy in eV (Tauc Equation, Equation 12 in Chapter 2), energy gap was estimated. The energy gap values were acquired from the intersection of the linear fit and the *x*-axis. The errors were computed from the standard error for the slope and the intercept of the linear fitting. The values were very similar among the bare Cu_2O samples, as the standard deviation was only 0.02 eV. The mean energy gap value was 2.49 ± 0.02 eV. The same procedure was employed for all the Cu_2O-SnO_2 samples. The mean value calculated for all the samples was 3.46 eV, associated to a standard deviation of 0.04 eV. This small standard deviation indicated that the impregnation process was reliable for the Cu_2O-SnO_2 samples. This value was close to the energy band gap value of tin oxide found in the literature, which is 3.60 eV [187], and confirms the coverage of the Cu_2O with the shell of SnO_2.

From XPS analysis, the survey spectra (Figure 7.5c for the one of Cu_2O_100_SnO_2_100 and Figure A.8b Appendix A4 for the others) revealed the presence of several elements, including Cu, O, Sn, C, and Cl (atomic percentages can be found in Table A.2, Appendix A4). The mean atomic ratio between copper and tin on the surface was approximately 2.5. This is an indication that, compared to the desired Cu:Sn ratio of 3 pursued in Chapter 6, the catalyst had a very similar composition to the one previously discussed. Therefore, the work carried out and discussed in this Chapter can be considered as a continuation of the previously conducted work in the field of advanced characterization. High-resolution spectra of Cu2p, Cu LMM, valence band, Sn3d5/2, and Cl2p were obtained. The information extracted from the Cu2p peaks were the same as that

from the bare Cu_2O samples. In all the Cu_2O-SnO_2 samples, Cu(0) + Cu(I) were the main oxidation states. The Sn3d5/2 peak could differentiate between Sn(0) and Sn(II) and Sn(IV) because the peaks shapes were different. The peak exhibited an asymmetric shape for metallic tin, where the higher binding energy tail was due to the interaction between the photo-emitted electrons and the free electrons present in the metal. The Sn(II) and Sn(IV) could be distinguished from the valence band peak, but due to the elevated cross-section of the copper, such band was covered. From the Sn3d peak, it was possible to distinguish the metallic tin from the oxide form. The tin oxide had a peak at higher binding energy (around 486.0 eV for the SnO and 486.6 eV for the SnO_2 oxide), while the metallic tin had a peak centred at 485.0 eV. All the samples had this peak at a binding energy higher than 486.0 (Figure 7.5d), indicating that the tin was mainly traceable to the oxide form. It was also possible to observe the symmetry of the principal peak (the one at lower binding energies). A symmetric peak indicated tin presented as oxide, while an asymmetric peak on the right side indicated metallic tin. Since the Cl peak had a flat background (Figure A.8c, in Appendix A4), before and after its region, Cl was assumed to be located on the samples' surface because the non-stepped background due to multilayer structured material could be clearly observed at higher binding energy [281].

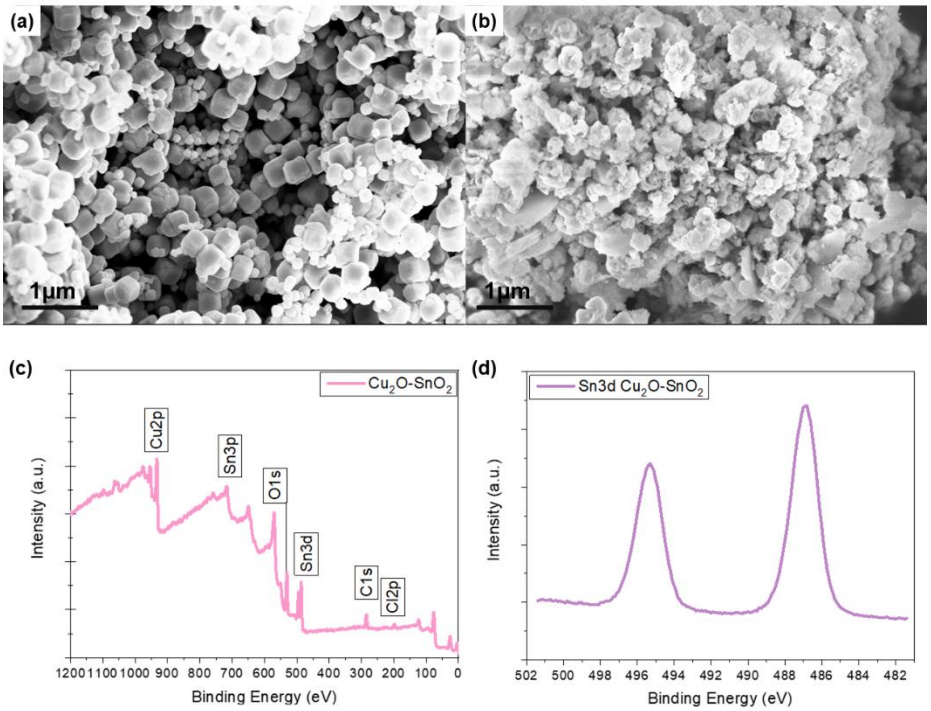


Figure 7.5 – Characterization of the Cu_2O_100_SnO_2_100, in particular: (a) FESEM images of Cu_2O_100, and (b) of Cu_2O_100_SnO_2_100, performed at the same magnification to observe the differences due to the external shell, (c) XPS survey spectrum and, (d) Sn3d region of the XPS spectrum of Cu_2O_100_SnO_2_100.

The energy band structure obtained from the fitting of the valence band and the energy gap value from DR-UV-vis for the Cu_2O-SnO_2 sample is reported in Figure 7.6.

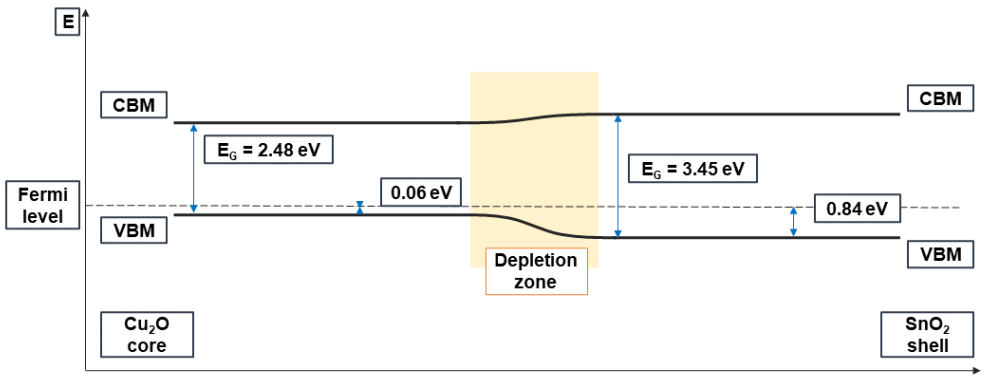


Figure 7.6 – Band structure for the Cu_2O-SnO_2 core-shell samples.

7.4 Preliminary PEC results

The three samples, Cu_2O_60_SnO_2_60, Cu_2O_100_SnO_2_100, and Cu_2O_200_SnO_2_200, were subjected to identical photoelectrochemical tests protocol with respect to the protocol used in Chapter 5. This analysis does not aim at providing the understanding of the performance of each $SnCl_4 \cdot 5H_2O$ delivery rate, instead the ultimate goal was only to identify the most stable among the various synthesized catalysts, in order to subsequently undergo the functionalization discussed in paragraph 7.5. Thus, we here report only some relevant tests of the already discussed protocol. Focusing on the trend of the gaseous products formed during the chronopotentiometry tests rather than the final quantification, the continuous response of the μ-GC was used to monitor the real-time production of H_2 and CO. Among the photo-electrocatalytic CO_2 reduction test, the linear sweep voltammetries going from 0 to –1.5 V vs. Ag/AgCl with a scan rate of 10 mV s^{-1} of the three samples are reported in Figure 7.7. The aim was to evaluate the photoactivity of each sample, especially in the first region of the curve, which ranged from about 0.1 V vs. Ag/AgCl to the value of –1.0 V vs. Ag/AgCl for all three samples). The wavy trend of the curves can be better appreciated by observing the inset of the figure. There is no significant photocurrent gain for the Cu_2O-SnO_2 100-100 sample compared to the one associated with the 60-60 and 200-200 samples. It is worth to add that, as the results of chronoamperometry tests performed at –0.5 V vs. Ag/AgCl for 10 minutes of alternated illumination, it was detected a photocurrent gain of around 70, 16.5 and 7.5 μA cm^{-2} for the Cu_2O-SnO_2 60-60, 100-100, and 200-200, respectively.

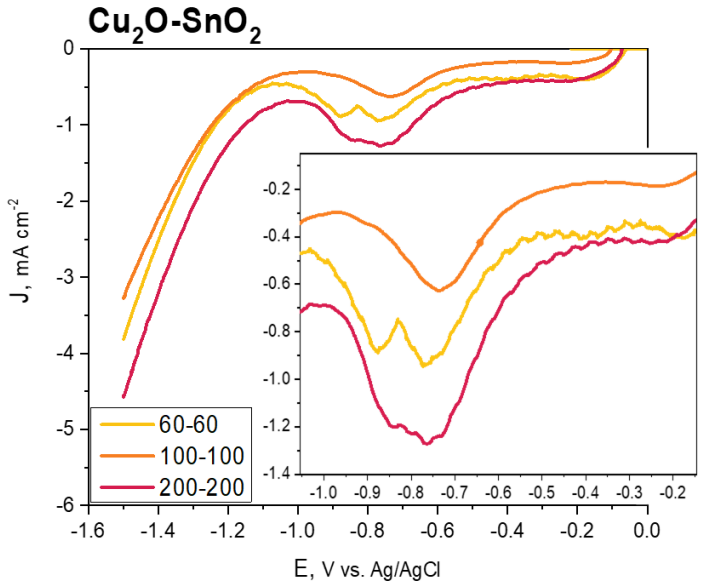


Figure 7.7 – LSV curves of the three different Cu_2O-SnO_2 samples, with a zoomed region of the plot present in the inset.

It was also noted that the current density value reached by the three samples at −1.5 V vs. Ag/AgCl differs the one to each others about 1 mA cm^{-2}. In fact, the value went from about –3.3 mA cm^{-2} for the sample labelled 100-100, to values of about –4 and –4.5 mA cm^{-2} associated with Cu_2O-SnO_2 60-60 and 200-200, respectively. In the inset of Figure 7.7, a reduction peak was present at around −0.75 V vs. Ag/AgCl and it was observable in each samples curve. Literature studies on cuprous oxide confirmed that a similar peak could be attributed to the electrosorption of oxygen species [282,283]. 2-hours chronopotentiometry tests were performed at a current density of –3 mA cm^{-2} on the three samples. The curves are reported in Figure 7.8a. For each curve, a stable behaviour was observed during the whole measurement, even with a slightly different mean voltage value. In fact, Cu_2O-SnO_2 60-60 and 200-200 showed around –1.5 V vs. Ag/AgCl for the whole test, while Cu_2O_100_SnO_2_100, it settled at –1.65 V vs Ag/AgCl after approximately ten minutes of increase. In parallel, the real-time quantification of the gaseous products (H_2 and CO) made by the μGC was accomplished. The results are showed in Figure 7.8b-d for Cu_2O-SnO_2 60-60, 100-100, and 200-200 respectively.

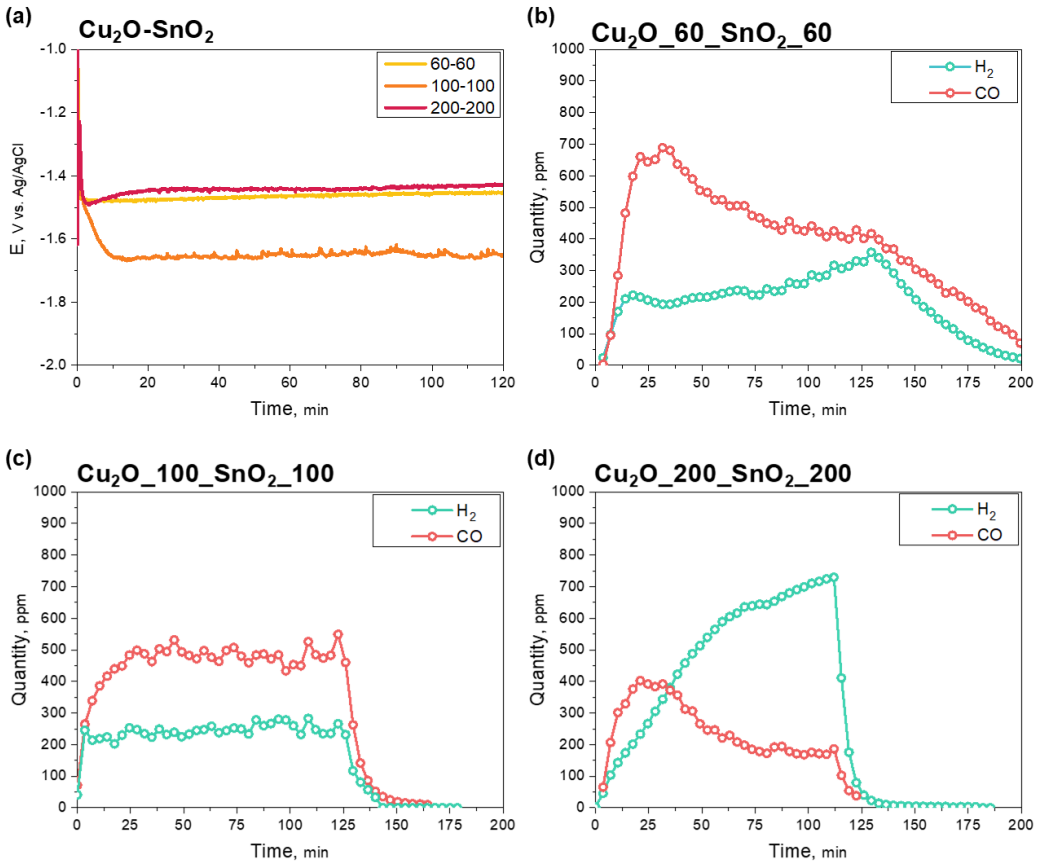


Figure 7.8 – Results of chronopotentiometry test on the three $Cu_2O_SnO_2$ samples: (a) chronopotentiometry curves registered at $J_{applied}$ = –3 mA cm^{-2}, and gaseous products evolution of (b) $Cu_2O_60_SnO_2_60$, (c) $Cu_2O_100_SnO_2_100$, and (d) $Cu_2O_60_SnO_2_60$, detected by a µGC.

While Cu_2O-SnO_2 60-60 (Figure 7.8b) showed a higher actual production of CO compared to H_2, reaching a quantity of 700 ppm of CO in the initial minutes, Cu_2O-SnO_2 200-200 (Figure 7.8d) showed a clear and constant increase in the formation of H_2 over time, reaching a production of about 800 ppm at the end of the 2-hour test. The most interesting behaviour was observed with the $Cu_2O_100_SnO_2_100$ sample, which, unlike the two previously described samples, showed stability in the production of the two products of interest throughout the entire 120-minute test, with a ratio of about 2:1 between CO and H_2 in terms of ppm formed. It was possible to observe a nearly constant production of H_2 at around 200 ppm, while CO remained between 400 and 500 ppm during the test. For this reason, it was decided to investigate the same sample by manufacturing new electrodes from the same batch of the synthesized powder

as described before and testing different applied current densities and test durations. The results are shown in the Figure 7.9.

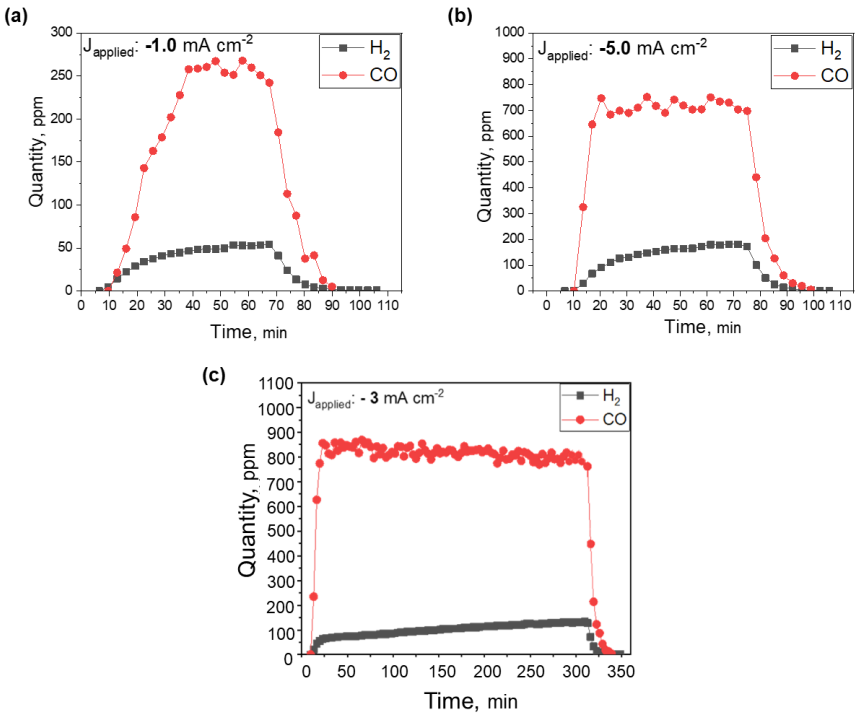


Figure 7.9 – Gaseous products evolution during three different chronopotentiometry tests on Cu_2O_100_SnO_2_100, in particular reported at: (a) $J_{applied}$ = –1 mA cm^{-2} for 1 hour, (b) $J_{applied}$ = –5 mA cm^{-2} for 1 hour, and (c) $J_{applied}$ = –3 mA cm^{-2} for 5 hours.

The plots in Figure 7.9a,b confirmed an expected trend. The test carried out at a higher current density resulted in a greater quantity of gaseous products, *i.e.,* about double for H_2 and more than double for CO when going from –1 to –5 mA cm^{-2}). Interestingly, even when higher current densities were applied, the stability of production was not affected (Figure 7.9b), confirming the stability of the catalyst during the test. From these first two tests, the ratios obtained between CO and H_2 were approximately of 4 for the chronopotentiometry performed at –1 mA cm^{-2} and approximately 5 for that at –5 mA cm^{-2}. Since the test at –3 mA cm^{-2} had already been performed for a duration of 2 hours, we increased the duration to effectively evaluate stability over time. A 5-hour test is reported as the results of gas products in Figure 7.9c. In this case, in addition to the confirmed stability in CO production throughout the whole test duration, it was possible to appreciate that the quantity of the product formed was slightly higher than that obtained in

the test at –5 mA cm^{-2}, averaging about 800 ppm throughout the test duration. H_2 never exceeded 150 ppm during the test and also remained stable. Finally, the CO:H_2 ratio was calculated to be approximately 7. Once these promising results were obtained, it was decided to functionalize the metallic catalyst using a methodology previously studied and recently published by Miró *et al.* [266] on a very similar metallic catalyst.

7.5 Catalyst functionalization

The synthesis of the organo-metallic molecules needed for the catalyst functionalization was performed by Roger Miró Serra. The production of a visible light absorber and a CO_2 reduction co-catalyst followed some state-of-the-art techniques. Two configurations were synthesized, respectively a tandem system with two separate catalysts or a supramolecular catalyst containing both coupled catalysts, to investigate the impact of the different structure. The resulting catalysts, with which the Cu_2O-SnO_2 was functionalised, were RuRe1, RuRe2, and Ru+Re (the separated Ru_{VLA} and Re_{CAT} both deposited onto a unique electrode). The molecular formula of the metallic complexes is provided in Figure 7.10. Vinyltriethoxysilane (VTES) was employed as the alkyl-siloxane anchoring group for the molecular immobilization of the Ru-Re-based complexes employed as visible light absorbing and co-catalysts. Functionalization with VTES was performed by adapting the procedure reported by Hijazi *et al.* [284]. The Cu_2O-SnO_2 was first dispersed in isopropanol, then the vinyltriethoxysilane was added. A schematic representation of the attachment of the anchoring group onto the semiconductor catalyst is reported in Figure 7.11. The preparation of the photocathodes involved first the Cu_2O-SnO_2-VTES electrode. The catalytic ink was prepared and then air-brushed onto a porous carbon support (Toray Carbon Paper 060). Then, the electrodes went through electropolimerization in a solution containing the proper molecular complex (as previously reported by Miró *et al*., [285]).

To summarize, the three different photo-electrodes prepared were:

1. Cu_2O-SnO_2-Ru+Re (co-immobilization of Ru_{VLA} and Re_{CAT})
2. Cu_2O-SnO_2-RuRe1 (Supramolecular Ru-Re complex)
3. Cu_2O-SnO_2-RuRe2 (binuclear Ru-Re complex)

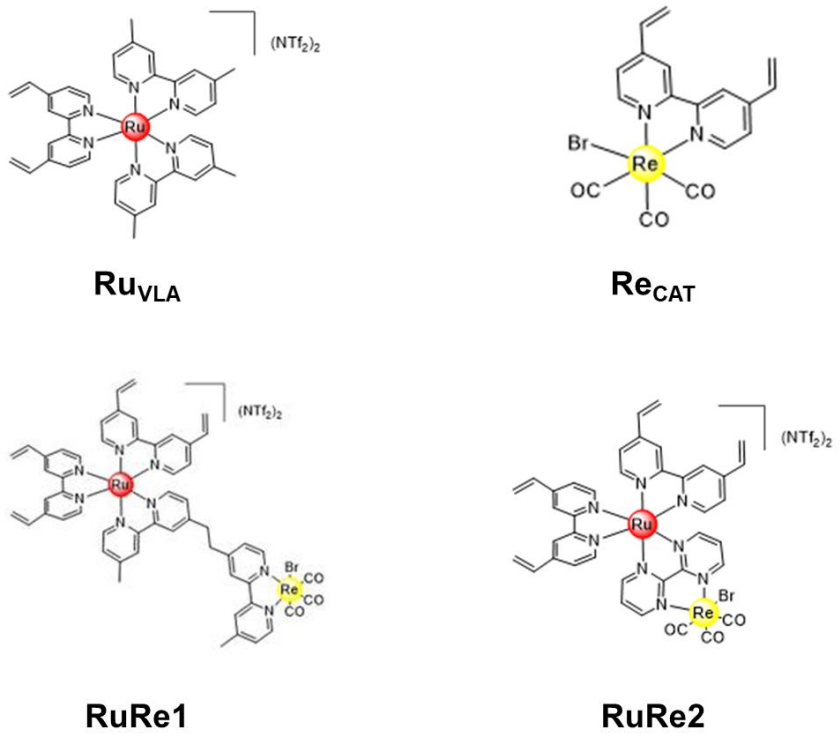


Figure 7.10 – Schematic representation of the Ru and Re complexes used in this work.

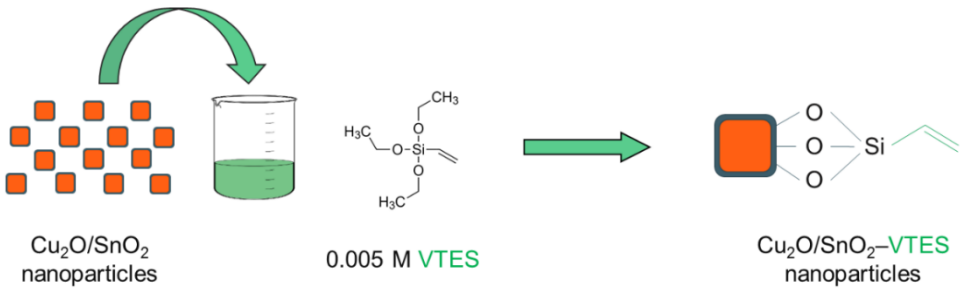


Figure 7.11 – Functionalization of the Cu_2O-SnO_2 nanoparticles with VTES schematic representation.

The photoelectrodes were created through electropolymerization of synthesized homogeneous complexes, as shown in Figure 7.12. Such method was indicated as the most suitable for the metallic-complexes based photoelectrodes in the original study [266], since the effectiveness of the process was confirmed by the progressively increasing current densities with each scan, indicating the formation of polymeric layers on the electrode surface. The presence of numerous

vinyl groups in the various Ru and Re complexes resulted in a layer-by-layer polymer assembly, determining diverse combinations of interconnected complexes toward a high molecular loading on the electrode surface [280]. This complexes assembly was observed by Miró and co-workers [266] through the formation of multiple polymers, visible by FESEM investigation.

In our study, the electropolimerization process involved 60 scans of cyclic voltammetry tests for each photoelectrode. The CV were performed from 0 to –1.9 V vs $Ag/AgNO_3$ in acetonitrile solution containing 0.1 M $TBAPF_6$ and 0.5 mM of the corresponding complex. The procedure is reported in Figure 7.12.

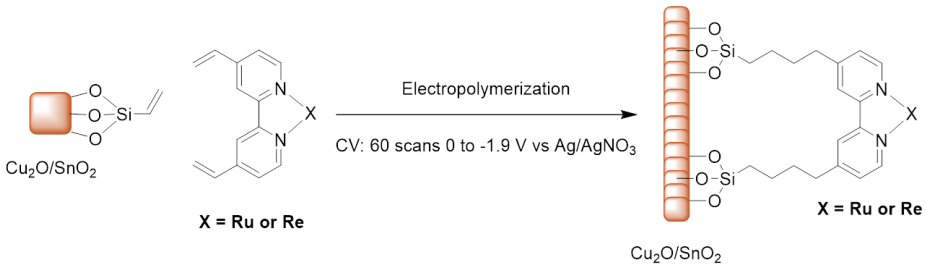


Figure 7.12 – Electropolymerization of the molecular complexes scheme.

The FESEM-EDX analysis confirmed the fixation of Re and Ru onto the semiconductor catalyst. The results are reported in Table 7.2 in terms of the ratios between Ru and Re, expressed as atomic percentages from EDX analysis. Contrary to the insight from Miró's work, the Ru:Re ratio remained shifted towards Ru. However, this results may be spuriously affected by the difference in energy of the EDX signal of the individual elements. In fact, Lα emissions of Rhenium, located around 8.65 eV, may overlap with the Kα emissions of copper, which fall at 8.04 eV. Other Re signals, for instance the Mα around 1.84 eV, could again overlap with copper's Lα at 0.92 eV, that is extremely intense. Indeed, by analyzing a series of three regions via EDX, copper was always the most present element in atomic percentage. It was also observed, as in Miró's work, that Cu was much more abundant in the Re+Ru and RuRe2 samples compared to the RuRe1 sample. On the other hand, no agglomerates were perceived in the RuRe1 sample attached to the electrode, unlike the literature report on $CuGaO_2$ (Figure 7.13). Finally, the 1:1 ratio between Ru and Re is maintained only on the electrode functionalized with RuRe1, while the RuRe2 electrode showed a ratio of about 2:1 Ruthenium vs. Rhenium. It is noteworthy that, in the Re+Ru sample, the presence of Re could be barely observed, although

three areas were investigated. Other types of characterization could be carried out to better assess the presence of Ru-Re based complexes on the electrodes, for example, UV-visible spectroscopy as suggested in Miró's work [266].

Table 7.2 – Average of approximated amounts of Ru and Re onto the electrodes surface, analyzed by EDX and correlated by atomic percentages.

Sample (Cu_2O-SnO_2)	Cu:Ru	Cu:Re	Ru:Re
Ru+Re	35:1	350:1	10:1
RuRe1	7:1	7:1	1:1
RuRe2	25:1	50:1	2:1

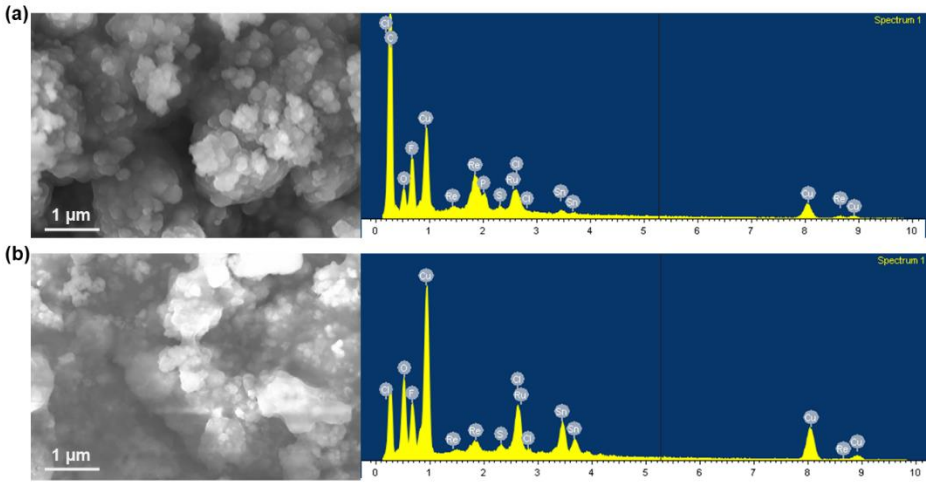


Figure 7.13 – FESEM images and EDX analysis of: (a) Cu_2O-SnO_2-RuRe1, and (b) Cu_2O-SnO_2-RuRe2.

7.6 Stability test of modified catalysts

The photo-electrocatalytic properties of the modified Cu_2O-SnO_2 samples were assessed by undergoing a shorter protocol of testing. The experiments were conducted in a $KHCO_3$ 0.1 M electrolyte, saturated with a continuous CO_2 flux from the cylinder, using a solar simulator to enlighten the catalyst deposited onto

the photoelectrode during the test. In the framework of this work, $KHCO_3$ 0.1 M was employed as a representative example of an aqueous electrolyte [286], thus no other electrolytes were tested. Such choice allowed the comparison with the previous works performed by our team, about the Cu-Sn-based catalyst for the PEC CO_2 reduction. Instead, the work done by Miró and co-workers [285], reported the use of ionic liquid (acetonitrile 0.3 M BMIM·TfO solution) as the electrolyte. Firstly, LSV curves were obtained, under the chopped illumination from the Xe lamp, going from 0 to –1.5 V vs. Ag/AgCl with a scan rate of 10 mV sec^{-1}. The current-potential curves are reported in Figure 7.14a. It is evident that the RuRe1 modified sample performed better than the others, by reaching the current density value of around –6.5 mA cm^{-2} at –1.5 V vs. Ag/AgCl, while the *J* for the other two samples settled around –4 mA cm^{-2}. The onset potential point settled at J = –0.5 mA cm^{-2} was also slightly lower for the RuRe1 catalyst than for the others. It was located at –1.1 V vs. Ag/AgCl for the RuRe1 electrode while for the other two catalysts it is at about –1.2 V vs. Ag/AgCl. Few traces of photocurrent contribution were observable during these tests. The only recognizable evidence of the typical wavy behaviour of the curves was detected in the region closer to the 0 voltage value for the RuRe2 catalyst. Future studies are necessary to deepen this aspect toward a full understanding of the behaviour of the samples.

Chronopotentiometry experiments of 5 hours duration were accomplished in order to compare the performance with the bare catalyst described in Section 7.4. Tests were carried out under light irradiation by applying a current density value of –3 mA cm^{-2} as resulting from the previous results. It is worth to notice that some other studies on the stability of similar catalytic systems are already present in literature, such as the work of Schreier and co-workers [269], however the experiments here reported are rather longer (5 vs. 1.5 hours). The stability plots are reported in Figure 7.14b. As observed in the previous PEC test, the two Ru+Re and RuRe2 catalysts performed similarly with a rather stable performance, while the RuRe1 showed a slightly different behaviour. The two former catalysts settled immediately at a potential value of –1.6 V vs. Ag/AgCl, which was stable for the whole duration of the experiment. Instead for the RuRe1 (light blue line) there was a slower increase of the reported potential value for the first 100 minutes and then a stabilization of the curve at around –1.62 V vs. Ag/AgCl. Such increment coincided with the maximum of CO production (red dots) that after about 100 min decreased, as observed from the tracking of gaseous product evolution reported in Figure 7.14d. It probably indicates the catalyst modification

during the early stages of the test until stabilization was reached. Also the hydrogen evolution (grey dots) in Figure 7.14d showed a slower increase in the first part of the experiment, where instead mainly CO evolution occurred. The gaseous products formation trends follow the previously observed behaviour: RuRe1 plots was different and more stable after 100 min of a provably catalyst restructuration, in comparison to Ru+Re and RuRe2, which instead showed similar formation rates.

The Ru+Re and the RuRe2 catalyst (see Figure 7.14c and Figure 7.14e, respectively) showed a sort of a peak of CO production after around 1 hour of experiment, and then a slow but constant decrease in CO selectivity until the end of the test. The quantities reached were remarkably different. The maximum value, in ppm, for the Ru+Re was higher than 900 ppm, while the one of RuRe2 got only up to 700 ppm. A different behaviour was detected for H_2, which in both experiments tended to grow even more slowly but steadily throughout the duration of the test. The only difference was detected in the first minutes of the test, when a peak exceeding 1000 ppm of H_2 was observed with RuRe2 catalyst. The RuRe1 samples showed the highest concentration of CO, reaching a maximum peak of about 1400 ppm, while H_2 maximum value was reported at the end of the experiment up to around 900 ppm. In general, for all the three catalysts, the H_2 curves were significantly more stable than the CO ones.

An effective quantification of the products was provided by Faradaic efficiencies calculations. The resulting values are showed in Figure 7.14f. As expected, the highest production rates are observed for RuRe1. That sample showed a higher Faradaic efficiency toward CO in comparison with H_2, *i.e.,* 54.82% and 32.63% respectively. The formate was the less abundant product in this test, having an efficiency of 10.78%. Formate selectivity remained more or less constant in all the three tests, reaching the values of 7.57% for Ru+Re catalyst and 6.76% for the RuRe2. This is attributable to the analogous SnO_2 content present in all the three samples. Such semiconductor is typically selective toward formate and was employed as the shell of the bare catalyst during the synthesis of the samples. The CO:H_2 ratio was equal to 1.7 for RuRe1, while it was always lower that 1 for the other two catalysts tested. For Ru+Re, the Faradaic efficiencies were 50.42% for H_2 and 27.63 for CO, obtaining a CO:H_2 ratio of around 1:2. The last catalyst, RuRe2, obtained the lowest general FE percentage, with 50.13% for H_2 and 6.76 for CO.

From a partial screening of these hybrid materials carried out in specific conditions (*i.e.,* electrolyte, current density applied, simulated solar irradiation), Cu_2O-SnO_2-RuRe1 showed the best performance.

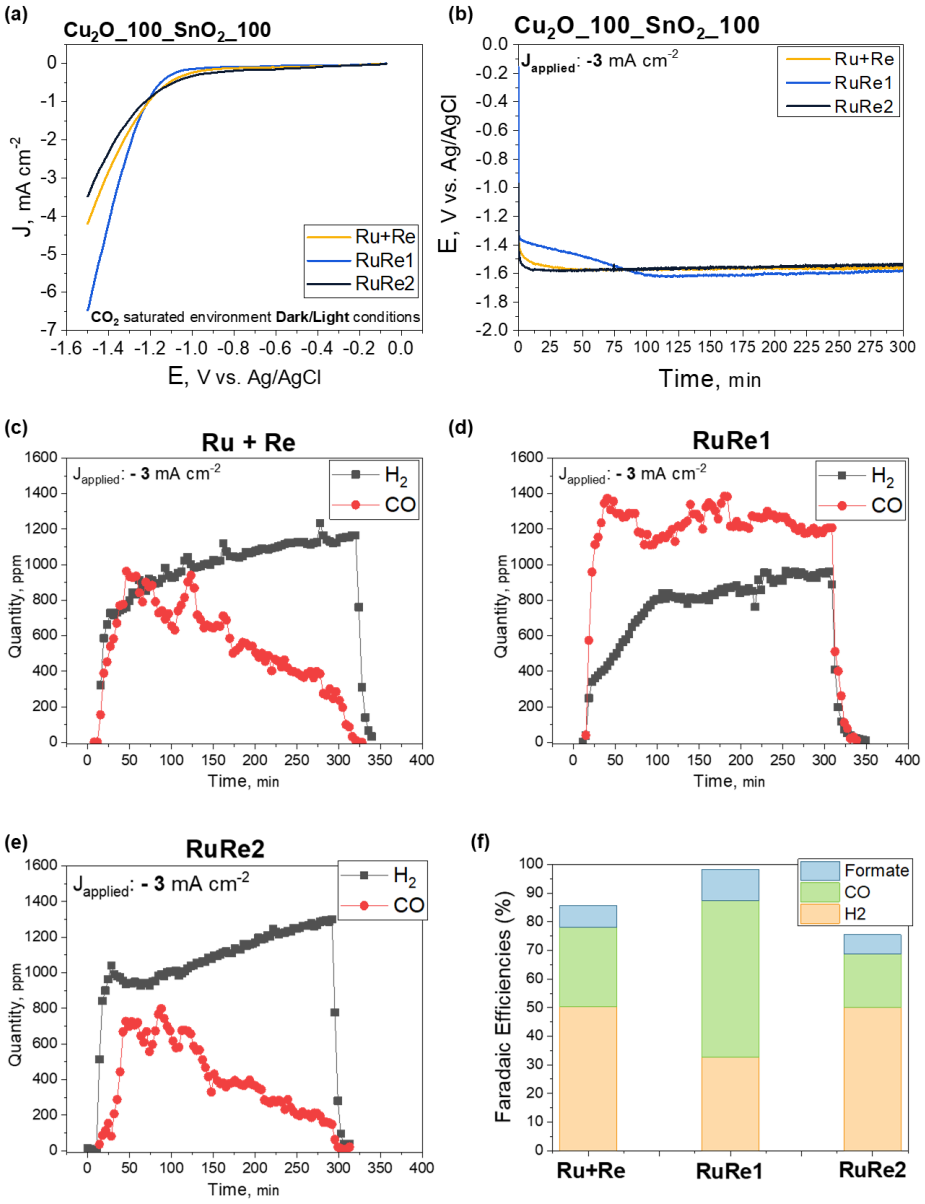


Figure 7.14 – Results of the photo-electrocatalytic tests on the three modified Cu_2O_100_SnO_2_100 samples; (a) LSV curves, (b) 300 minutes chronopotentiometry curves, applying –3 mA cm^{-2} as the current density under simulated sunlight, and the gaseous products behaviour during the test of (c) Ru+Re sample, (d) RuRe1, and (e) RuRe2 ones, and (f) Faradaic efficiency values of the three samples obtained after the tests.

7.7 Conclusions

The standardization of the Cu_2O wet precipitation synthesis was achieved by employing peristaltic pumps to maintain consistent synthesis conditions and reduce human errors. Reproducibility of the synthetic procedure to prepare Cu_2O nanocubes was demonstrated through XRD over repeated samples. The tunability of some characteristics of the as-synthetised materials depending on the flow rate of the reagents into the reactor was assessed. In particular, the ECSA of the samples increased sharply at high flow rates of the L-ascorbic acid. The step of SnO_2 impregnation needed further analysis to ensure its reproducibility, while in some chosen samples the presence of Sn was clearly recognizable from several aspects, such as the change in the morphology of the material observed by FESEM before and after the impregnation (from defined Cu_2O nanocubes to a very thick layer of SnO_2 on the nanoparticles). The final energy band gap was estimated to be 3.46 eV, in line with literature data, and noticeably different from the one obtained from the cubic Cu_2O nanoparticles, which demonstrate their coverage. Finally, the amount of Sn was evaluated via XPS calculations of the atomic percentage of the surface elements in the core-shell samples, and the Cu:Sn ratio obtained was around 2.5, in agreement with the samples synthetized and analyzed in the previous Sections.

The photo-electrocatalytic performance of three samples synthesized at different delivery velocities of the precursors was tested with the same protocol used in previous Sections. A 5 hours chronopotentiometry test demonstrated the outstanding stability of the Cu_2O_100_SnO_2_100 sample during the evolution of the gaseous products and led to a promising CO:H_2 ratio of around 7. The functionalization of this bare semiconductor catalyst was performed by adopting an immobilization technique that already worked with a semiconductor catalyst made of $CuGaO_2$. The modified VTES Cu_2O-SnO_2 was subjected to electropolimerization. In that way, three different kind of Ru/Re based complexes were attached onto the photoelectrodes surface. The FESEM/EDX analysis confirmed the successful anchoring by detecting the Ru and Re atoms within the observed fresh photoelectrodes. Higher photovoltage generation was observed with photocathodes bearing the RuRe1 with respect to the ones with RuRe2 or Ru_{VLA} + Re_{CAT}. Longer stability tests were repeated with the modified catalysts in an aqueous electrolyte environment under simulated solar irradiation. Generally, high total Faradaic efficiency values were obtained by applying –3 mA cm^{-2} as the current density. Very similar behaviours were registered for RuRe2 and

Ru+Re modified catalyst, with an overall higher amount of H_2 with respect to CO, while a remarkable increase in CO production was observed in the RuRe1 experiment. A ratio of around 1.7 between CO and H_2 was registered, with FE values of 54.82% and 32.63%, respectively, being formate produced in a lower amount.

As a last remark, we demonstrated a method to protect Cu_2O semiconductor photocatalyst with SnO_2 and stabilize its photocatalytic activity during the CO_2 reduction by an enhancement of carriers transport with respect to the bare material. These promising results suggest the possibility of using such a catalyst to produce syngas that can be employed as a starting point for hydroformylation or carbonylation reactions, *i.e.,* reaction of the produced syngas with olefins to form aldehydes (higher value products).

Chapter 8

Summary and Conclusions

The main objective of this thesis was to study the electro and photo-electrochemical conversion of CO_2 into valuable chemicals as a means of reducing the increasing amount of CO_2 in the atmosphere. The research focused on designing and developing Cu-based materials for CO_2 conversion, with the aim of making a positive contribution to the current climate challenge.

The work started in Chapter 1 by framing the global warming causes and some possible solutions, by identifying the CO_2 as the most abundant species among the GHGs. Regarding the technologies for CO_2 conversion, the electro and photo-electrocatalytic processes were presented as advantageous, cheap, and easy.

The Chapter 2 presented the materials employed and the characterization and testing methods applied in the experimental work.

The Chapter 3 dealt with the studies on Pd/Cu-based catalyst applicable in electrocatalytic systems for CO_2RR. The process went through a scale-up by increasing the electrode area and the cell dimensions, enhancing the catalyst performance. The objective was to produce a scalable, repeatable catalyst material made of Pd and Cu that would be useful for an electro-catalytic process for the conversion of CO_2 into alcohols and other high-value products. In Chapter 3, Pd/Cu-based catalysts were synthesized and the reproducibility of the synthetic method was assessed. Their performance was tested in CO_2 electrochemical reduction experiments in an RDE system. In a *H-type* cell set-up, the FE towards C-compounds were 40% higher than on the RDE, with around 39% of CO and

more than 3% of ethanol. By scaling up the set-up, besides confirming the ability to generate high reduction current densities (–100 mA cm^{-2} at around –15 V vs. Ag/AgCl, fulfilling Saturno Project requirements), it was observed that the selectivity to CO and alcohols increased following the increase in current density. Such change was attributed to change in morphologies, which should be further assessed through further characterization, such as by *TEM-in operando* studies.

Designing, synthesizing, and testing a scalable and reproducible catalyst material made of Cu and Sn, evaluating its electrocatalytic activity to produce C_{1+} products from the photo-electrocatalytic CO_2 conversion, and determining the impact of light on selectivity were the second and third objectives of the thesis work.

Starting in in Chapter 4, a novel Cu_2O-SnO_2 catalyst obtained via co-precipitation method was prepared, characterized, and tested for the PEC CO_2 reduction. The role of the light in affecting the selectivity was also investigated. As an additional step toward the design of the Cu-Sn-based catalysts, in Chapter 5 the core-shell synthesis was described together with the analysis of the amount of Sn used for the shell creation, and the effects on the activity of the photo-electrocatalyst.

In Chapter 4, a first attempt for the synthesis, characterization, and testing of a Cu_2O-SnO_2 catalyst for the PEC CO_2RR was developed, following the co-precipitation route. Much attention was devoted to assess the presence of Cu^+ as the main copper oxidation state in the material, because of its photoactivity. The analysis of the evolution trends of gaseous and liquid products of CO_2RR allowed to select the best applied current density values to test the reaction with and without the solar simulated enlightenment. This let us investigate the impact of light on product formation. The observed improvement of C-based compound production under illumination demonstrated the role of light in promoting C_1 (CO and formate) and C_2 products like ethanol at low potential values.

Once we understood the role of light, the focus of Chapter 5 was to unveil the SnO_2 protection role of the instable Cu_2O. For that reason, an alternative synthetic route, the core-shell one, was considered, because of the advantages offered by this versatile platform for CO_2 reduction (*i.e.,* selectivity, activity, stability). A general Cu_2O-SnO_2 core-shell based catalyst's photoactivity was found to be 30% higher than that of the co-precipitation catalyst developed before (18 vs. 24 A cm^{-2} increase in photocurrent during chronoamperometry at –0.2 V vs. OCP). The

novel catalyst structure made it possible to study the impact of SnO_2 content on the PEC CO_2RR. Five different samples of the Cu_2O-SnO_2 catalyst were created with increasing molar percentage of Sn in comparison to the Cu_2O core. From PEC and EIS results, it was clear that the samples with higher Sn content were characterized by a syngas ratio similar to 1, while the formate production was higher. Moreover the stability of the core-shell structure was enhanced with respect to the co-precipitation ones, leading to a non-significant degradation during the CO_2R test.

In Chapter 6, the goal was to assess the carriers dynamics inside the synthesized core-shell materials both during exposure to light radiation and during the CO_2 reduction reaction for the assessment of the carriers mobility into the samples and the phenomena happening at the electrode/electrolyte interface. According to the findings, the mobility of charge carriers rose in direct proportion to the amount of tin. Additionally, the outer SnO_2 shell may aid in some way to reduce electron-hole recombination when present in a thicker layer, which could partially explain the higher faradaic efficiencies for C-compounds reported for catalysts with higher Sn content. Besides, the exclusive selectivity toward C_1, compounds like CO and formate and the absence of longer chain compounds may be due to the fact that the electron lifetime at the interface electrode/electrolyte reduces with increasing Sn concentration making harder the possibility of, for example, *CO dimerization.

The best-performing catalyst was revealed and in Chapter 7 its synthesis was standardised. Then, its surface was functionalised with Ru/Re-based supramolecular complexes in order to enhance the selectivity towards syngas (1:1 CO:H_2) and its stability during time. In Chapter 7 we aimed at standardizing the synthesis method to recreate the best core-shell Cu_2O-SnO_2 identified, with the selected Cu:Sn ratio of 3:1 (CS3). Then, the functionalization of the bare semiconductor catalyst was performed by adopting electropolimerization as the immobilization technique of 3 different types of Ru/Re-based supramolecular complexes. The success of the anchoring operation was evaluated via FESEM and EDX. Overall, better results in terms of stability of PEC CO_2 reduction tests during time were obtained, however the best performance was observed for the so-called RuRe1-modified catalyst. A ratio of around 1.7 between CO and H_2 was registered, with FE values of 54.82% and 32.63% respectively after a 5-hours experiment.

To summarize, the thesis focused on Cu-based materials for CO_2 (photo)-electroreduction to high-added value products. The switch from Pd to Sn coupled with Cu was crucial in order to diminish the costs and address the selectivity towards formate/formic acid. The size of the global formic acid market is estimated at USD 1.6 billion in 2021, and it is anticipated to have a compound annual growth rate (CAGR) of USD 3.85 billion by 2030 [287]. Along with selectivity tuning, the presence of SnO_2 allowed to protect the photoactive as unstable Cu_2O from degradation due to light and voltage applied during CO_2 photo-electroreduction tests. The search for the best Cu-Sn-based catalyst was carried out not only by testing different synthesis methods (*i.e.,* co-precipitation and core-shell) but also by investigating the best relationship between metal precursors and deeply studying the dynamics of charge carriers within catalysts, in relation to the tests carried out in the set-up of photo-electro CO_2 reduction. Finally, the best semiconductor catalyst was modified by attaching onto it a Ru/Re-based organo-metallic compound, to enhance the catalyst protection, *i.e.,* to say the stability during time, and to address the selectivity thanks to the visible-light absorber properties of the compound. The potential for using such a catalyst to generate precursors for hydroformylation reactions (mixing the syngas with olefins to form aldehydes) is suggested by the promising results in terms of FEs, of the syngas mixture produced from the CO_2 reduction. The final developed catalyst can be further employed as a platform for using solar energy and turning CO_2 into valuable products due to the great abundance of its metallic precursors, the reproducibility of the catalytic synthesis, and distinctive photo-catalytic capabilities.

References

[1] P. Forster, K. Alterskjaer, C. Smith, R. Colman, H. Damon Matthews, V. Ramaswamy, T. Storelvmo, K. Armour, W. Collins, J. Dufresne, D. Frame, D. Lunt, T. Mauritsen, M. Watanabe, M. Wild, H. Zhang, V. Masson-Delmotte, P. Zhai, A. Pirani, S. Connors, C. Péan, S. Berger, N. Caud, Y. Chen, L. Goldfarb, M. Gomis, M. Huang, K. Leitzell, E. Lonnoy, J. Matthews, T. Maycock, T. Waterfield, O. Yelekçi, R. Yu, B. Zhou, The Earth's Energy Budget, Climate Feedbacks, and Climate Sensitivity. In Climate Change 2021: The Physical Science Basis. Contribution of Working Group I to the Sixth Assessment Report of the Intergovernmental Panel on Climate Change, 2021. https://doi.org/10.1017/9781009157896.009.923.

[2] M. Wild, D. Folini, M.Z. Hakuba, C. Schär, S.I. Seneviratne, S. Kato, D. Rutan, C. Ammann, E.F. Wood, G. König-Langlo, The energy balance over land and oceans: an assessment based on direct observations and CMIP5 climate models, Clim. Dyn. 44 (2015) 3393–3429. https://doi.org/10.1007/s00382-014-2430-z.

[3] Attribution 4.0 International, CC Creat. Commons. (n.d.). https://creativecommons.org/licenses/by/4.0/legalcode (accessed January 13, 2023).

[4] IPCC, Climate change 2007: Appendix to synthesis report. Climate change 2007: Synthesis report. Contribution of working groups I, II and III to the fourth assessment report of the intergovernmental panel on climate change., Core Writ. Team, Pachauri, R.K Reisinger, A. (2007) 75–104. https://www.ipcc.ch/pdf/assessment-report/ar4/syr/ar4_syr_appendix.pdf.

[5] IPCC, Climate Change 2007: The Mitigation of Climate Change Contribution tof Working Group III to the Fourth Assessment Report of the IPCC, Cambridge University Press, Cambridge, United Kingdom and New York, NY, USA, 2007. https://doi.org/10.4324/9781351297967-12.

[6] C. Korner, Biosphere Responses to CO2 Enrichment, Ecol. Appl. 10 (2000) 1590. https://doi.org/10.2307/2641226.

[7] D.S. Arndt, J. Blunden, R.J.H. Dunn, State of the Climate in 2019, Bull. Am. Meteorol. Soc. 101 (2020) SI-S8. https://doi.org/10.1175/2020BAMSSTATEOFTHECLIMATE.1.

[8] IPCC, Summary for Policymakers: Climate Change 2022_ Impacts, Adaptation and Vulnerability_Working Group II contribution to the Sixth Assessment Report of the Intergovernamental Panel on Climate Change, 2022. https://doi.org/10.1017/9781009325844.Front.

[9] Our World in Data, Annual share of global CO_2 emissions, Our World Data Based Glob. Carbon Proj. (2022). OurWorldInData.org/co2-and-other-greenhouse-gas-em.

[10] C.A. and N. Institute, Climate Action Tracker. 2100 Warming Projections: Emissions and expected warming based on pledges and current policies., 2022. https://climateactiontracker.org/global/temperatures/.

[11] Our World in Data, Share of primary energy from fossil fuels, Our World Data Based BP Stat. Rev. World Energy. (2022).

[12] F. Karimi, R. Khalilpour, Evolution of carbon capture and storage research: Trends of international collaborations and knowledge maps, Int. J. Greenh. Gas Control. 37 (2015) 362–376. https://doi.org/10.1016/j.ijggc.2015.04.002.

[13] G. Dicks, World Energy Outlook, Econ. Outlook. 11 (2016) 1–8. https://doi.org/10.1111/j.1468-0319.1987.tb00425.x.

[14] P. De Luna, C. Hahn, D. Higgins, S.A. Jaffer, T.F. Jaramillo, E.H. Sargent, What would it take for renewably powered electrosynthesis to displace petrochemical processes?, Science (80-.). 364 (2019). https://doi.org/10.1126/science.aav3506.

[15] K. Gao, Y. Zheng, Combined effects of ocean acidification and solar UV radiation on photosynthesis, growth, pigmentation and calcification of the coralline alga Corallina sessilis (Rhodophyta), Glob. Chang. Biol. 16 (2010) 2388–2398. https://doi.org/10.1111/j.1365-2486.2009.02113.x.

[16] S. Bachu, Sequestration of CO2 in geological media: Criteria and approach for site selection in response to climate change, Energy Convers. Manag. 41 (2000) 953–970. https://doi.org/10.1016/S0196-8904(99)00149-1.

[17] Z. Zhang, S.Y. Pan, H. Li, J. Cai, A.G. Olabi, E.J. Anthony, V. Manovic, Recent advances in carbon dioxide utilization, Renew. Sustain. Energy Rev. 125 (2020) 109799. https://doi.org/10.1016/j.rser.2020.109799.

[18] W. Zhang, A.R. Mohamed, W.J. Ong, Z-Scheme Photocatalytic Systems for Carbon Dioxide Reduction: Where Are We Now?, Angew. Chemie - Int. Ed. 59 (2020) 22894–22915. https://doi.org/10.1002/anie.201914925.

[19] K.D. Ramachandriya, D.K. Kundiyana, M.R. Wilkins, J.B. Terrill, H.K. Atiyeh, R.L. Huhnke, Carbon dioxide conversion to fuels and chemicals using a hybrid green process, Appl. Energy. 112 (2013) 289–299. https://doi.org/10.1016/j.apenergy.2013.06.017.

[20] C. Song, Global challenges and strategies for control, conversion and utilization of CO2 for sustainable development involving energy, catalysis, adsorption and chemical processing, Catal. Today. 115 (2006) 2–32. https://doi.org/10.1016/j.cattod.2006.02.029.

[21] M. Aresta, A. Dibenedetto, Utilisation of CO2 as a chemical feedstock: Opportunities and challenges, J. Chem. Soc. Dalt. Trans. (2007) 2975–2992. https://doi.org/10.1039/b700658f.

[22] M. North, What is CO2? Thermodynamics, Basic Reactions and Physical Chemistry, Elsevier B.V., 2015. https://doi.org/10.1016/B978-0-444-62746-9.00001-3.

[23] I. Ganesh, Conversion of carbon dioxide into methanol - A potential liquid fuel: Fundamental challenges and opportunities (a review), Renew. Sustain. Energy Rev. 31 (2014) 221–257. https://doi.org/10.1016/j.rser.2013.11.045.

[24] C.H. Huang, C.S. Tan, A review: CO2 utilization, Aerosol Air Qual. Res. 14 (2014) 480–499. https://doi.org/10.4209/aaqr.2013.10.0326.

[25] C.H. Vo, C. Mondelli, H. Hamedi, J. Pérez-Ramírez, S. Farooq, I.A. Karimi, Sustainability Assessment of Thermocatalytic Conversion of CO2to Transportation Fuels, Methanol, and 1-Propanol, ACS Sustain. Chem. Eng. 9 (2021) 10591–10600. https://doi.org/10.1021/acssuschemeng.1c02805.

[26] A. Corma, H. Garcia, Photocatalytic reduction of CO2 for fuel production: Possibilities and challenges, J. Catal. 308 (2013) 168–175. https://doi.org/10.1016/j.jcat.2013.06.008.

[27] H. Guzmán, N. Russo, S. Hernández, CO2 valorisation towards alcohols by Cu-based electrocatalysts: challenges and perspectives, Green Chem. 23 (2021) 1896–1920. https://doi.org/10.1039/d0gc03334k.

[28] P. Chen, Y. Zhang, Y. Zhou, F. Dong, Photoelectrocatalytic carbon dioxide reduction: Fundamental, advances and challenges, Nano Mater. Sci. 3 (2021) 344–367. https://doi.org/10.1016/j.nanoms.2021.05.003.

[29] D.S.A. Simakov, Thermocatalytic Conversion of CO2, (2017) 1–25. https://doi.org/10.1007/978-3-319-61112-9_1.

[30] D.S.A. Simakov, Y. Román-Leshkov, Highly efficient methane reforming over a low-loading Ru/Γ-Al2O3 catalyst in a Pd-Ag membrane reactor, AIChE J. 64 (2018) 3101–3108. https://doi.org/10.1002/aic.16094.

[31] A. Wolf, A. Jess, C. Kern, Syngas Production via Reverse Water-Gas Shift Reaction over a Ni-Al2O3 Catalyst: Catalyst Stability, Reaction Kinetics, and Modeling, Chem. Eng. Technol. 39 (2016) 1040–1048. https://doi.org/10.1002/ceat.201500548.

[32] J.J. Concepcion, R.L. House, J.M. Papanikolas, T.J. Meyer, Chemical approaches to artificial photosynthesis, Proc. Natl. Acad. Sci. U. S. A. 109 (2012) 15560–15564. https://doi.org/10.1073/pnas.1212254109.

[33] M. Khalil, J. Gunlazuardi, T.A. Ivandini, A. Umar, Photocatalytic conversion of CO2 using earth-abundant catalysts: A review on mechanism and catalytic performance, Renew. Sustain. Energy Rev. 113 (2019) 109246. https://doi.org/10.1016/j.rser.2019.109246.

[34] K. Li, X. An, K.H. Park, M. Khraisheh, J. Tang, A critical review of CO2 photoconversion: Catalysts and reactors, Catal. Today. 224 (2014) 3–12. https://doi.org/10.1016/j.cattod.2013.12.006.

[35] H. Zhou, J. Guo, P. Li, T. Fan, D. Zhang, J. Ye, Leaf-architectured 3D hierarchical artificial photosynthetic system of perovskite titanates towards CO2 photoreduction into hydrocarbon fuels, Sci. Rep. 3 (2013) 1–9. https://doi.org/10.1038/srep01667.

[36] Y. Izumi, Recent advances in the photocatalytic conversion of carbon dioxide to fuels with water and/or hydrogen using solar energy and beyond, Coord. Chem. Rev. 257 (2013) 171–186. https://doi.org/10.1016/j.ccr.2012.04.018.

[37] D. Johnson, Z. Qiao, A. Djire, Progress and Challenges of Carbon Dioxide Reduction Reaction on Transition Metal Based Electrocatalysts, ACS Appl. Energy Mater. 4 (2021) 8661–8684. https://doi.org/10.1021/acsaem.1c01624.

[38] R.M. Arán-Ais, D. Gao, B. Roldan Cuenya, Structure- and Electrolyte-Sensitivity in CO2 Electroreduction, Acc. Chem. Res. 51 (2018) 2906–2917. https://doi.org/10.1021/acs.accounts.8b00360.

[39] K.S. Adarsh, N. Chandrasekaran, V. Chakrapani, In-situ Spectroscopic Techniques as Critical Evaluation Tools for Electrochemical Carbon dioxide Reduction: A Mini Review, Front. Chem. 8 (2020) 1–9. https://doi.org/10.3389/fchem.2020.00137.

[40] A. Goyal, G. Marcandalli, V.A. Mints, M.T.M. Koper, Competition between CO2Reduction and Hydrogen Evolution on a Gold Electrode under Well-Defined Mass Transport Conditions, J. Am. Chem. Soc. 142 (2020) 4154–4161. https://doi.org/10.1021/jacs.9b10061.

[41] S. Nitopi, E. Bertheussen, S.B. Scott, X. Liu, A.K. Engstfeld, S. Horch, B. Seger, I.E.L. Stephens, K. Chan, C. Hahn, J.K. Nørskov, T.F. Jaramillo, I. Chorkendorff, Progress and Perspectives of Electrochemical CO2 Reduction on Copper in Aqueous Electrolyte, Chem. Rev. 119 (2019) 7610–7672. https://doi.org/10.1021/acs.chemrev.8b00705.

[42] A. Álvarez, M. Borges, J.J. Corral-Pérez, J.G. Olcina, L. Hu, D. Cornu, R. Huang, D. Stoian, A. Urakawa, CO2 Activation over Catalytic Surfaces, ChemPhysChem. 18 (2017) 3135–3141. https://doi.org/10.1002/cphc.201700782.

[43] H. Guzmán, F. Salomone, E. Batuecas, T. Tommasi, N. Russo, S. Bensaid, S. Hernández, How to make sustainable CO2 conversion to Methanol: Thermocatalytic versus electrocatalytic technology, Chem. Eng. J. 417 (2021). https://doi.org/10.1016/j.cej.2020.127973.

[44] X. Nie, M.R. Esopi, M.J. Janik, A. Asthagiri, Selectivity of CO2 reduction on copper electrodes: The role of the kinetics of elementary steps, Angew. Chemie - Int. Ed. 52 (2013) 2459–2462. https://doi.org/10.1002/anie.201208320.

[45] L. Zhang, Z.J. Zhao, J. Gong, Nanostructured Materials for Heterogeneous Electrocatalytic CO2 Reduction and their Related Reaction Mechanisms, Angew. Chemie - Int. Ed. 56 (2017) 11326–11353. https://doi.org/10.1002/anie.201612214.

[46] W.H. Koppenol, J.D. Rush, Reduction potential of the CO2/CO2•- couple. A comparison with other C1 radicals, J. Phys. Chem. 91 (1987) 4429–4430. https://doi.org/10.1021/j100300a045.

[47] H. Ooka, M.C. Figueiredo, M.T.M. Koper, Competition between Hydrogen Evolution and Carbon Dioxide Reduction on Copper Electrodes in Mildly Acidic Media, Langmuir. 33 (2017) 9307–9313. https://doi.org/10.1021/acs.langmuir.7b00696.

[48] T. Cheng, H. Xiao, W.A. Goddard, Reaction Mechanisms for the Electrochemical Reduction of CO2 to CO and Formate on the Cu(100) Surface at 298 K from Quantum Mechanics Free Energy Calculations with Explicit Water, J. Am. Chem. Soc. 138 (2016) 13802–13805. https://doi.org/10.1021/jacs.6b08534.

[49] T.T. Zhuang, Z.Q. Liang, A. Seifitokaldani, Y. Li, P. De Luna, T. Burdyny, F. Che, F. Meng, Y. Min, R. Quintero-Bermudez, C.T. Dinh, Y. Pang, M. Zhong, B. Zhang, J. Li, P.N. Chen, X.L. Zheng, H. Liang, W.N. Ge, B.J. Ye, D. Sinton, S.H. Yu, E.H. Sargent, Steering post-C-C coupling selectivity enables high efficiency electroreduction of carbon dioxide to multi-carbon alcohols, Nat. Catal. 1 (2018) 421–428. https://doi.org/10.1038/s41929-018-0084-7.

[50] Z. Tian, C. Priest, L. Chen, Recent Progress in the Theoretical Investigation of Electrocatalytic Reduction of CO2, Adv. Theory Simulations. 1 (2018) 1–23. https://doi.org/10.1002/adts.201800004.

[51] H. Xiao, T. Cheng, W.A. Goddard, Atomistic Mechanisms Underlying Selectivities in C 1 and C 2 Products from Electrochemical Reduction of CO on Cu(111), J. Am. Chem. Soc. 139 (2017) 130–136. https://doi.org/10.1021/jacs.6b06846.

[52] G.L. De Gregorio, T. Burdyny, A. Loiudice, P. Iyengar, W.A. Smith, R. Buonsanti, Facet-Dependent Selectivity of Cu Catalysts in Electrochemical CO2 Reduction at Commercially Viable Current Densities, ACS Catal. 10 (2020) 4854–4862. https://doi.org/10.1021/acscatal.0c00297.

[53] Z.W. She, J. Kibsgaard, C.F. Dickens, I. Chorkendorff, J.K. Nørskov, T.F. Jaramillo, Combining theory and experiment in electrocatalysis: Insights into materials design, Science (80-.). 355 (2017). https://doi.org/10.1126/science.aad4998.

[54] C. Yang, Y. Wang, L. Qian, A.M. Al-Enizi, L. Zhang, G. Zheng, Heterogeneous Electrocatalysts for CO2Reduction, ACS Appl. Energy Mater. 4 (2021) 1034–1044. https://doi.org/10.1021/acsaem.0c02648.

[55] P. Akhter, M.A. Farkhondehfal, S. Hernández, M. Hussain, A. Fina, G. Saracco, A.U. Khan, N. Russo, Environmental issues regarding CO2 and recent strategies for alternative fuels through photocatalytic reduction with titania-based materials, J. Environ. Chem. Eng. 4 (2016) 3934–3953. https://doi.org/10.1016/j.jece.2016.09.004.

[56] S. Zhang, Q. Fan, R. Xia, T.J. Meyer, CO2 Reduction: From Homogeneous to Heterogeneous Electrocatalysis, Acc. Chem. Res. 53 (2020) 255–264. https://doi.org/10.1021/acs.accounts.9b00496.

[57] X. Feng, K. Jiang, S. Fan, M.W. Kanan, Grain-Boundary-Dependent CO2 Electroreduction Activity, J. Am. Chem. Soc. 137 (2015) 4606–4609. https://doi.org/10.1021/ja5130513.

[58] N. Zhang, R. Long, C. Gao, Y. Xiong, Recent progress on advanced design for photoelectrochemical reduction of CO2 to fuels, Sci. China Mater. 61 (2018) 771–805. https://doi.org/10.1007/s40843-017-9151-y.

[59] J. Hu, C. Zhai, M. Zhu, Photo-responsive metal/semiconductor hybrid nanostructure: A promising electrocatalyst for solar light enhanced fuel cell reaction, Chinese Chem. Lett. 32 (2021) 1348–1358. https://doi.org/10.1016/j.cclet.2020.09.049.

[60] J. Yu, J. Wang, Y. Ma, J. Zhou, Y. Wang, P. Lu, J. Yin, R. Ye, Z. Zhu, Z. Fan, Recent Progresses in Electrochemical Carbon Dioxide Reduction on Copper-Based Catalysts toward Multicarbon Products, Adv. Funct. Mater. 31 (2021). https://doi.org/10.1002/adfm.202102151.

[61] S. Xu, E.A. Carter, Theoretical Insights into Heterogeneous (Photo)electrochemical CO2 Reduction, Chem. Rev. 119 (2019) 6631–6669. https://doi.org/10.1021/acs.chemrev.8b00481.

[62] Y. Qu, X. Duan, Progress, challenge and perspective of heterogeneous photocatalysts, Chem. Soc. Rev. 42 (2013) 2568–2580. https://doi.org/10.1039/c2cs35355e.

[63] B. Kumar, M. Llorente, J. Froehlich, T. Dang, A. Sathrum, C.P. Kubiak, Photochemical and photoelectrochemical reduction of CO2, Annu. Rev. Phys. Chem. 63 (2012) 541–569. https://doi.org/10.1146/annurev-physchem-032511-143759.

[64] H. Guzmán, F. Zammillo, D. Roldán, C. Galletti, N. Russo, S. Hernández, Investigation of gas diffusion electrode systems for the electrochemical CO2 conversion, Catalysts. 11 (2021). https://doi.org/10.3390/catal11040482.

[65] H. Dau, E. Fujita, L. Sun, Artificial Photosynthesis: Beyond Mimicking Nature, ChemSusChem. 10 (2017) 4228–4235. https://doi.org/10.1002/cssc.201702106.

[66] Y. Hori, K. Kikuchi, S. Shin, Production of CO and CH4 in electrochemical reduction of co2 at metal electrodes in aqueous hydrogencarbonate solution, Cemistry Lett. 20 (1985) 1695–1698. https://doi.org/10.1016/S0075-7535(08)70092-5.

[67] H. Guzmán, N. Russo, S. Hernández, CO2 valorization towards alcohols by Cu-based electrocatalysts: challenges and perspectives, Green Chem. 23 (2021) 1896–1920. https://doi.org/10.1039/d0gc03334k.

[68] R.M. Arán-Ais, F. Scholten, S. Kunze, R. Rizo, B. Roldan Cuenya, The role of in situ generated morphological motifs and Cu(i) species in C2+ product selectivity during CO2 pulsed electroreduction, Nat. Energy. 5 (2020) 317–325. https://doi.org/10.1038/s41560-020-0594-9.

[69] K.P. Kuhl, E.R. Cave, D.N. Abram, T.F. Jaramillo, New insights into the electrochemical reduction of carbon dioxide on metallic copper surfaces, Energy Environ. Sci. 5 (2012) 7050. https://doi.org/10.1039/c2ee21234j.

[70] S.H. Lee, K.Y. Kim, Y. Shin, Effective feature selection method for deep learning-based automatic modulation classification scheme using higher-order statistics, Appl. Sci. 10 (2020). https://doi.org/10.3390/app10020588.

[71] C.C. Chang, E.Y. Li, M.K. Tsai, A computational exploration of CO2 reduction: Via CO dimerization on mixed-valence copper oxide surface, Phys. Chem. Chem. Phys. 20 (2018) 16906–16909. https://doi.org/10.1039/c8cp00592c.

[72] W. Ye, X. Guo, T. Ma, A review on electrochemical synthesized copper-based catalysts for electrochemical reduction of CO2 to C2+ products, Chem. Eng. J. 414 (2021) 128825. https://doi.org/10.1016/j.cej.2021.128825.

[73] Z. Yin, C. Yu, Z. Zhao, X. Guo, M. Shen, N. Li, M. Muzzio, J. Li, H. Liu, H. Lin, J. Yin, G. Lu, D. Su, S. Sun, Cu3n nanocubes for selective electrochemical reduction of co2 to ethylene, Nano Lett. (2019) 8658–8663. https://doi.org/10.1021/acs.nanolett.9b03324.

[74] H.M. Jeong, Y. Kwon, J.H. Won, Y. Lum, M.J. Cheng, K.H. Kim, M. Head-Gordon, J.K. Kang, Atomic-Scale Spacing between Copper Facets for the Electrochemical Reduction of Carbon Dioxide, Adv. Energy Mater. 10 (2020) 1–12. https://doi.org/10.1002/aenm.201903423.

[75] I. Merino-Garcia, J. Albo, J. Solla-Gullón, V. Montiel, A. Irabien, Cu oxide/ZnO-based surfaces for a selective ethylene production from gas-phase CO2 electroconversion, J. CO2 Util. 31 (2019) 135–142. https://doi.org/10.1016/j.jcou.2019.03.002.

[76] A.D. Handoko, J. Tang, Controllable proton and CO2 photoreduction over Cu2O with various morphologies, in: Int. J. Hydrogen Energy, 2013: pp. 13017–13022. https://doi.org/10.1016/j.ijhydene.2013.03.128.

[77] J.C. Wang, L. Zhang, W.X. Fang, J. Ren, Y.Y. Li, H.C. Yao, J.S. Wang, Z.J. Li, Enhanced photoreduction CO2 activity over direct Z-Scheme α-Fe2O3/Cu2O heterostructures under visible light irradiation, ACS Appl.

Mater. Interfaces. 7 (2015) 8631–8639. https://doi.org/10.1021/acsami.5b00822.

[78] S. Sun, X. Zhang, Q. Yang, S. Liang, X. Zhang, Z. Yang, Cuprous oxide (Cu2O) crystals with tailored architectures: A comprehensive review on synthesis, fundamental properties, functional modifications and applications, Prog. Mater. Sci. 96 (2018) 111–173. https://doi.org/10.1016/j.pmatsci.2018.03.006.

[79] H. Guzmán, M.A. Farkhondehfal, K.R. Tolod, S. Hernández, N. Russo, Photo/electrocatalytic hydrogen exploitation for CO2 reduction toward solar fuels production, in: Sol. Hydrog. Prod. Process. Syst. Technol., Elsevier, 2019: pp. 365–418. https://doi.org/10.1016/B978-0-12-814853-2.00011-4.

[80] A. Paracchino, V. Laporte, K. Sivula, M. Grätzel, E. Thimsen, Highly active oxide photocathode for photoelectrochemical water reduction, Nat. Mater. 10 (2011) 456–461. https://doi.org/10.1038/nmat3017.

[81] D. Gao, H. Zhou, J. Wang, S. Miao, F. Yang, G. Wang, J. Wang, X. Bao, Size-Dependent Electrocatalytic Reduction of CO2 over Pd Nanoparticles, J. Am. Chem. Soc. 137 (2015) 4288–4291. https://doi.org/10.1021/jacs.5b00046.

[82] K. Ohkawa, K. Hashimoto, A. Fujishima, Y. Noguchi, S. Nakayama, Electrochemical reduction of carbon dioxide on hydrogenstoring materials. Part 1. The effect of hydrogen absorption on the electrochemical behavior on palladium electrodes, J. Electroanal. Chem. 345 (1993) 445–456. https://doi.org/10.1016/0022-0728(93)80495-4.

[83] B.M. Tackett, J.H. Lee, J.G. Chen, Electrochemical Conversion of CO2to Syngas with Palladium-Based Electrocatalysts, Acc. Chem. Res. 53 (2020) 1535–1544. https://doi.org/10.1021/acs.accounts.0c00277.

[84] X. Nie, X. Jiang, H. Wang, W. Luo, M.J. Janik, Y. Chen, X. Guo, C. Song, Mechanistic Understanding of Alloy Effect and Water Promotion for Pd-Cu Bimetallic Catalysts in CO2 Hydrogenation to Methanol, ACS Catal. 8 (2018) 4873–4892. https://doi.org/10.1021/acscatal.7b04150.

[85] Y. Mun, S. Lee, A. Cho, S. Kim, J.W. Han, J. Lee, Cu-Pd alloy nanoparticles as highly selective catalysts for efficient electrochemical reduction of CO2 to CO, Appl. Catal. B Environ. 246 (2019) 82–88. https://doi.org/10.1016/j.apcatb.2019.01.021.

[86] W. Luc, C. Collins, S. Wang, H. Xin, K. He, Y. Kang, F. Jiao, Ag-sn

bimetallic catalyst with a core-shell structure for CO2 reduction, J. Am. Chem. Soc. 139 (2017) 1885–1893. https://doi.org/10.1021/jacs.6b10435.

[87] X. Bai, W. Chen, C. Zhao, S. Li, Y. Song, R. Ge, W. Wei, Y. Sun, Exclusive Formation of Formic Acid from CO 2 Electroreduction by a Tunable Pd-Sn Alloy , Angew. Chemie. 129 (2017) 12387–12391. https://doi.org/10.1002/ange.201707098.

[88] J.T. Feaster, C. Shi, E.R. Cave, T. Hatsukade, D.N. Abram, K.P. Kuhl, C. Hahn, J.K. Nørskov, T.F. Jaramillo, Understanding Selectivity for the Electrochemical Reduction of Carbon Dioxide to Formic Acid and Carbon Monoxide on Metal Electrodes, ACS Catal. 7 (2017) 4822–4827. https://doi.org/10.1021/acscatal.7b00687.

[89] H. Mun, H. Yang, J. Park, C. Ju, K. Char, High electron mobility in epitaxial SnO2-x in semiconducting regime, APL Mater. 3 (2015). https://doi.org/10.1063/1.4927470.

[90] M. Li, X. Tian, S. Garg, T.E. Rufford, P. Zhao, Y. Wu, A.J. Yago, L. Ge, V. Rudolph, G. Wang, Modulated Sn Oxidation States over a Cu2O-Derived Substrate for Selective Electrochemical CO2 Reduction, ACS Appl. Mater. Interfaces. 12 (2020) 22760–22770. https://doi.org/10.1021/acsami.0c00412.

[91] S. Zhao, S. Li, T. Guo, S. Zhang, J. Wang, Y. Wu, Y. Chen, Advances in Sn-Based Catalysts for Electrochemical CO2 Reduction, Nano-Micro Lett. 11 (2019). https://doi.org/10.1007/s40820-019-0293-x.

[92] A. Dutta, A. Kuzume, M. Rahaman, S. Vesztergom, P. Broekmann, Monitoring the Chemical State of Catalysts for CO2 Electroreduction: An In Operando Study, ACS Catal. 5 (2015) 7498–7502. https://doi.org/10.1021/acscatal.5b02322.

[93] Y. Chen, M.W. Kanan, Tin oxide dependence of the CO 2 reduction efficiency on tin electrodes and enhanced activity for tin/tin oxide thin-film catalysts, J. Am. Chem. Soc. 134 (2012) 1986–1989. https://doi.org/10.1021/ja2108799.

[94] M.F. Baruch, J.E. Pander, J.L. White, A.B. Bocarsly, Mechanistic Insights into the Reduction of CO2 on Tin Electrodes using in Situ ATR-IR Spectroscopy, ACS Catal. 5 (2015) 3148–3156. https://doi.org/10.1021/acscatal.5b00402.

[95] J. Zeng, K. Bejtka, W. Ju, M. Castellino, A. Chiodoni, A. Sacco, M.A. Farkhondehfal, S. Hernández, D. Rentsch, C. Battaglia, C.F. Pirri,

Advanced Cu-Sn foam for selectively converting CO2 to CO in aqueous solution, Appl. Catal. B Environ. 236 (2018) 475–482. https://doi.org/10.1016/j.apcatb.2018.05.056.

[96] R. Chen, Z. Wang, Q. Zhou, J. Lu, M. Zheng, A Template-Free Microwave Synthesis of One-Dimensional Cu2O Nanowires with Desired Photocatalytic Property, Materials (Basel). 11 (2018) 1843. https://doi.org/10.3390/ma11101843.

[97] Y. Du, N. Zhang, C. Wang, Photo-catalytic degradation of trifluralin by SnO2-doped Cu2O crystals, Catal. Commun. 11 (2010) 670–674. https://doi.org/10.1016/j.catcom.2010.01.021.

[98] S. Bonnamy, A. Oberlin, Transmission Electron Microscopy, Elsevier Ltd, 2016. https://doi.org/10.1016/B978-0-12-805256-3.00004-0.

[99] Z.L. Wang, Transmission electron microscopy of shape-controlled nanocrystals and their assemblies, J. Phys. Chem. B. 104 (2000) 1153–1175. https://doi.org/10.1021/jp993593c.

[100] M. Naderi, Surface Area: Brunauer-Emmett-Teller (BET), Prog. Filtr. Sep. (2015) 585–608. https://doi.org/10.1016/B978-0-12-384746-1.00014-8.

[101] M. Abd Mutalib, M.A. Rahman, M.H.D. Othman, A.F. Ismail, J. Jaafar, Scanning Electron Microscopy (SEM) and Energy-Dispersive X-Ray (EDX) Spectroscopy, Elsevier B.V., 2017. https://doi.org/10.1016/B978-0-444-63776-5.00009-7.

[102] A.A. Bunaciu, E. gabriela Udriştioiu, H.Y. Aboul-Enein, X-Ray Diffraction: Instrumentation and Applications, Crit. Rev. Anal. Chem. 45 (2015) 289–299. https://doi.org/10.1080/10408347.2014.949616.

[103] J.W. Lee, W.B. Park, J.H. Lee, S.P. Singh, K.S. Sohn, A deep-learning technique for phase identification in multiphase inorganic compounds using synthetic XRD powder patterns, Nat. Commun. 11 (2020) 1–11. https://doi.org/10.1038/s41467-019-13749-3.

[104] M. Scimeca, S. Bischetti, H.K. Lamsira, R. Bonfiglio, E. Bonanno, Energy dispersive X-ray (EDX) microanalysis: A powerful tool in biomedical research and diagnosis, Eur. J. Histochem. 62 (2018) 89–99. https://doi.org/10.4081/ejh.2018.2841.

[105] V.D. Hodoroaba, S. Rades, W.E.S. Unger, Inspection of morphology and elemental imaging of single nanoparticles by highresolution SEM/EDX in transmission mode, Surf. Interface Anal. 46 (2014) 945–948.

https://doi.org/10.1002/sia.5426.

[106] J.K. Patra, K.H. Baek, Green Nanobiotechnology: Factors Affecting Synthesis and Characterization Techniques, J. Nanomater. 2014 (2014). https://doi.org/10.1155/2014/417305.

[107] G. Tyler, ICP-OES , ICP-MS and AAS Techniques Compared, Tech. Note 05 ICP Opt. Spectrosc. (2001) 1–11.

[108] S. Trasatti, O.A. Petrii, International Union of Pure and Applied Chemistry Physical Chemistry Division Commission on Electrochemistry: Real Surface Area Measurements in Electrochemistry, Pure Appl. Chem. 63 (1991) 711–734. https://doi.org/10.1351/pac199163050711.

[109] M. Lukaszewski, M. Soszko, A. Czerwiński, Electrochemical methods of real surface area determination of noble metal electrodes - an overview, Int. J. Electrochem. Sci. 11 (2016) 4442–4469. https://doi.org/10.20964/2016.06.71.

[110] F.E. Osterloh, Inorganic materials as catalysts for photochemical splitting of water, Chem. Mater. 20 (2008) 35–54. https://doi.org/10.1021/cm7024203.

[111] P. V. Sarma, C.S. Tiwary, S. Radhakrishnan, P.M. Ajayan, M.M. Shaijumon, Oxygen incorporated WS2 nanoclusters with superior electrocatalytic properties for hydrogen evolution reaction, Nanoscale. 10 (2018) 9516–9524. https://doi.org/10.1039/c8nr00253c.

[112] K. Ngamchuea, S. Eloul, K. Tschulik, R.G. Compton, Planar diffusion to macro disc electrodes—what electrode size is required for the Cottrell and Randles-Sevcik equations to apply quantitatively?, J. Solid State Electrochem. 18 (2014) 3251–3257. https://doi.org/10.1007/s10008-014-2664-z.

[113] D.M. Morales, M. Risch, Seven steps to reliable cyclic voltammetry measurements for the determination of double layer capacitance, JPhys Energy. 3 (2021). https://doi.org/10.1088/2515-7655/abee33.

[114] E.L. Clark, J. Resasco, A. Landers, J. Lin, L.T. Chung, A. Walton, C. Hahn, T.F. Jaramillo, A.T. Bell, Standards and Protocols for Data Acquisition and Reporting for Studies of the Electrochemical Reduction of Carbon Dioxide, ACS Catal. 8 (2018) 6560–6570. https://doi.org/10.1021/acscatal.8b01340.

[115] M.R. Shoar Abouzari, F. Berkemeier, G. Schmitz, D. Wilmer, On the

physical interpretation of constant phase elements, Solid State Ionics. 180 (2009) 922–927. https://doi.org/10.1016/j.ssi.2009.04.002.

[116] W. Lv, J. Zhou, F. Kong, H. Fang, W. Wang, Porous tin-based film deposited on copper foil for electrochemical reduction of carbon dioxide to formate, Int. J. Hydrogen Energy. 41 (2016) 1585–1591. https://doi.org/10.1016/j.ijhydene.2015.11.100.

[117] N. Hüsing, U. Schubert, Aerogels - Airy Materials: Chemistry, Structure, and Properties, Angew. Chemie - Int. Ed. 37 (1998) 22–45. https://doi.org/10.1002/(sici)1521-3773(19980202)37:1/2<22::aid-anie22>3.0.co;2-i.

[118] H.D. Gesser, P.C. Goswami, Aerogels and Related Porous Materials, Chem. Rev. 89 (1989) 765–788. https://doi.org/10.1021/cr00094a003.

[119] A. Bisson, A. Rigacci, D. Lecomte, E. Rodier, P. Achard, Drying of Silica Gels to Obtain Aerogels:Phenomenology and Basic Techniques, Dry. Technol. 21 (2003) 593–628. https://doi.org/10.1081/drt-120019055.

[120] S.S. Kistler, Coherent Expanded Aerogels and Jellies., Nature. 127 (1931) 741.

[121] M. Cantin, M. Casse, L. Koch, R. Jouan, P. Mestreau, D. Roussel, F. Bonnin, J. Moutel, S.J. Teichner, Silica aerogels used as Cherenkov radiators, Nucl. Instruments Methods. 118 (1974) 177–182. https://doi.org/10.1016/0029-554X(74)90700-9.

[122] C. Moreno-Castilla, F.J. Maldonado-Hódar, Carbon aerogels for catalysis applications: An overview, Carbon N. Y. 43 (2005) 455–465. https://doi.org/10.1016/j.carbon.2004.10.022.

[123] N. Leventis, Three-dimensional core-shell superstructures: Mechanically strong aerogels, Acc. Chem. Res. 40 (2007) 874–884. https://doi.org/10.1021/ar600033s.

[124] S. Ghosal, J.C. Hemminger, H. Bluhm, B.S. Mun, E.L.D. Hebenstreit, G. Ketteler, D.F. Ogletree, F.G. Requejo, M. Salmeron, Electron spectroscopy of aqueous solution interfaces reveals surface enhancement of halides, Science (80-.). 307 (2005) 563–566. https://doi.org/10.1126/science.1106525.

[125] C.A. Morris, M.L. Anderson, R.M. Stroud, C.I. Merzbacher, D.R. Rolison, Silica sol as a nanoglue: Flexible synthesis of composite aerogels, Science (80-.). 284 (1999) 622–624. https://doi.org/10.1126/science.284.5414.622.

[126] N.C. Bigall, A.K. Herrmann, M. Vogel, M. Rose, P. Simon, W. Carrillo-Cabrera, D. Dorfs, S. Kaskel, N. Gaponik, A. Eychmüller, Hydrogels and aerogels from noble metal nanoparticles, Angew. Chemie - Int. Ed. 48 (2009) 9731–9734. https://doi.org/10.1002/anie.200902543.

[127] W. Liu, A.K. Herrmann, N.C. Bigall, P. Rodriguez, D. Wen, M. Oezaslan, T.J. Schmidt, N. Gaponik, A. Eychmüller, Noble metal aerogels-synthesis, characterization, and application as electrocatalysts, Acc. Chem. Res. 48 (2015) 154–162. https://doi.org/10.1021/ar500237c.

[128] I. Introduction, (2) (3) 1.1., J. Non. Cryst. Solids. 100 (1988) 31–50.

[129] J.L. Gurav, I.K. Jung, H.H. Park, E.S. Kang, D.Y. Nadargi, Silica aerogel: Synthesis and applications, J. Nanomater. 2010 (2010). https://doi.org/10.1155/2010/409310.

[130] H. Hdach, T. Woignier, J. Phalippou, G.W. Scherer, Effect of aging and pH on the modulus of aerogels, J. Non. Cryst. Solids. 121 (1990) 202–205. https://doi.org/10.1016/0022-3093(90)90132-6.

[131] L.L. Hench, J.O.N.K. West, The Sol-Gel Process, Chem. Rev. 90 (1990) 33–72.

[132] L.A. Capadona, M.A.B. Meador, A. Alunni, E.F. Fabrizio, P. Vassilaras, N. Leventis, Flexible, low-density polymer crosslinked silica aerogels, Polymer (Guildf). 47 (2006) 5754–5761. https://doi.org/10.1016/j.polymer.2006.05.073.

[133] M.A. Einarsrud, E. Nilsen, A. Rigacci, G.M. Pajonk, S. Buathier, D. Valette, M. Durant, B. Chevalier, P. Nitz, F. Ehrburger-Dolle, Strengthening of silica gels and aerogels by washing and aging processes, J. Non. Cryst. Solids. 285 (2001) 1–7. https://doi.org/10.1016/S0022-3093(01)00423-9.

[134] J. Zarzycki, M. Prassas, J. Phalippou, Synthesis of glasses from gels: the problem of monolithic gels, J. Mater. Sci. 17 (1982) 3371–3379. https://doi.org/10.1007/BF01203507.

[135] P.H. Tewari, A.J. Hunt, K.D. Lofftus, Ambient-temperature supercritical drying of transparent silica aerogels, Mater. Lett. 3 (1985) 363–367. https://doi.org/10.1016/0167-577X(85)90077-1.

[136] J.P. Vareda, A. Lamy-Mendes, L. Durães, A reconsideration on the definition of the term aerogel based on current drying trends, Microporous Mesoporous Mater. 258 (2018) 211–216.

https://doi.org/10.1016/j.micromeso.2017.09.016.

[137] R. Du, X. Jin, R. Hübner, X. Fan, Y. Hu, A. Eychmüller, Engineering Self-Supported Noble Metal Foams Toward Electrocatalysis and Beyond, Adv. Energy Mater. 10 (2020). https://doi.org/10.1002/aenm.201901945.

[138] K. Loza, M. Heggen, M. Epple, Synthesis, Structure, Properties, and Applications of Bimetallic Nanoparticles of Noble Metals, Adv. Funct. Mater. 30 (2020). https://doi.org/10.1002/adfm.201909260.

[139] Y. Li, Y. Sun, Y. Qin, W. Zhang, L. Wang, M. Luo, H. Yang, S. Guo, Recent Advances on Water-Splitting Electrocatalysis Mediated by Noble-Metal-Based Nanostructured Materials, Adv. Energy Mater. 10 (2020) 1–20. https://doi.org/10.1002/aenm.201903120.

[140] L. Lu, R. Capek, A. Kornowski, N. Gaponik, A. Eychmüller, Selective fabrication of ordered bimetallic nanostructures with hierarchical porosity, Angew. Chemie - Int. Ed. 44 (2005) 5997–6001. https://doi.org/10.1002/anie.200501471.

[141] Y. Joseph, B. Guse, G. Nelles, Aging of 1,ω-alkyldithiol interlinked au nanoparticle networks, Chem. Mater. 21 (2009) 1670–1676. https://doi.org/10.1021/cm803407n.

[142] Y. Zhou, M. Kogiso, T. Shimizu, Necklace-Like chains of hybrid nanospheres consisting of Pd nanocystals and peptidic lipids, J. Am. Chem. Soc. 131 (2009) 2456–2457. https://doi.org/10.1021/ja809728c.

[143] J. Zheng, Y.M. Zhang, C.O. Rock, J.E. Cronan, J.K. Stoops, V.C. Joshi, J. Hofmann, A. Witkowski, a K. Joshi, S. Jenni, N. Ban, E. a Siess, L. Renner, F. Lynen, S.J. Kolodziej, J.P. Schroeter, J.P. Bretaudiere, S.J. Wakil, P. a Penczek, M. Leibundgut, T. Maier, C. Frick, D. Tsuchiya, T. Oyama, Y. Tsunaka, K. Morikawa, G. Merilainen, R.K. Wierenga, C.Y. Kim, I.I. Mathews, D.E. Cane, C. Khosla, E.C. Verbree, Z. Dauter, a R. Stuitje, Z.S. Derewenda, J. Straub, B. Rautenstrauss, M. Mittag, D. Stratmann, E. Schweizer, H. Schulz, a D. Arcy, G.E. Dale, S. Smith, S.W. White, a M. Haapalainen, J.K. Hiltunen, T. Glumoff, X. Liang, J.J. Kim, R.B. Johnston, E.D. Laue, R.N. Perham, S.R. Martin, E. Appella, S. Gutmann, E. Pohl, S. Russo, P. Afonine, Plastic and Moldable Metals by Self-Assembly of Sticky Nanoparticle Aggregates, Science (80-.). 316 (2007) 261–264.

[144] J. Schroers, C. Veazey, W.L. Johnson, Amorphous metallic foam, Appl. Phys. Lett. 82 (2003) 370–372. https://doi.org/10.1063/1.1537514.

[145] C. Zhu, D. Du, A. Eychmüller, Y. Lin, Engineering ordered and nonordered porous noble metal nanostructures: Synthesis, assembly, and their applications in electrochemistry, Chem. Rev. 115 (2015) 8896–8943. https://doi.org/10.1021/acs.chemrev.5b00255.

[146] T. Wang, D. La Montagne, J. Lynch, J. Zhuang, Y.C. Cao, Colloidal superparticles from nanoparticle assembly, Chem. Soc. Rev. 42 (2013) 2804–2823. https://doi.org/10.1039/c2cs35318k.

[147] H. Wang, Q. Fang, W. Gu, D. Du, Y. Lin, C. Zhu, Noble Metal Aerogels, ACS Appl. Mater. Interfaces. 12 (2020) 52234–52250. https://doi.org/10.1021/acsami.0c14007.

[148] R. Du, J.O. Joswig, X. Fan, R. Hübner, D. Spittel, Y. Hu, A. Eychmüller, Disturbance-Promoted Unconventional and Rapid Fabrication of Self-Healable Noble Metal Gels for (Photo-)Electrocatalysis, Matter. 2 (2020) 908–920. https://doi.org/10.1016/j.matt.2020.01.002.

[149] R. Du, W. Jin, R. Hübner, L. Zhou, Y. Hu, A. Eychmüller, Engineering Multimetallic Aerogels for pH-Universal HER and ORR Electrocatalysis, Adv. Energy Mater. 10 (2020). https://doi.org/10.1002/aenm.201903857.

[150] D. Wen, A.K. Herrmann, L. Borchardt, F. Simon, W. Liu, S. Kaskel, A. Eychmüller, Controlling the growth of palladium aerogels with high-performance toward bioelectrocatalytic oxidation of glucose, J. Am. Chem. Soc. 136 (2014) 2727–2730. https://doi.org/10.1021/ja412062e.

[151] W. Liu, A.-K. Herrmann, D. Geiger, L. Borchardt, F. Simon, S. Kaskel, N. Gaponik, A. Eychmüller, High-Performance Electrocatalysis on Palladium Aerogels, Angew. Chemie Int. Ed. 51 (2012) 5743–5747. https://doi.org/10.1002/anie.201108575.

[152] C. Zhu, Q. Shi, S. Fu, J. Song, H. Xia, D. Du, Y. Lin, Efficient Synthesis of MCu (M = Pd, Pt, and Au) Aerogels with Accelerated Gelation Kinetics and their High Electrocatalytic Activity, Adv. Mater. 28 (2016) 8779–8783. https://doi.org/10.1002/adma.201602546.

[153] H.G. Liao, L. Cui, S. Whitelam, H. Zheng, Real-time imaging of Pt3Fe nanorod growth in solution, Science (80-.). 336 (2012) 1011–1014. https://doi.org/10.1126/science.1219185.

[154] R. Du, X. Fan, X. Jin, R. Hübner, Y. Hu, A. Eychmüller, Emerging Noble Metal Aerogels: State of the Art and a Look Forward, Matter. 1 (2019) 39–56. https://doi.org/10.1016/j.matt.2019.05.006.

[155] F. Matter, A.L. Luna, M. Niederberger, From colloidal dispersions to aerogels: How to master nanoparticle gelation, Nano Today. 30 (2020) 100827. https://doi.org/10.1016/j.nantod.2019.100827.

[156] X. Gao, R.J. Esteves, T.T.H. Luong, R. Jaini, I.U. Arachchige, Oxidation-induced self-assembly of Ag nanoshells into transparent and opaque Ag hydrogels and aerogels, J. Am. Chem. Soc. 136 (2014) 7993–8002. https://doi.org/10.1021/ja5020037.

[157] K.G.S. Ranmohotti, X. Gao, I.U. Arachchige, Salt-mediated self-assembly of metal nanoshells into monolithic aerogel frameworks, Chem. Mater. 25 (2013) 3528–3534. https://doi.org/10.1021/cm401968j.

[158] X. Fan, B. Cai, R. Du, R. Hübner, M. Georgi, G. Jiang, L. Li, M. Samadi Khoshkhoo, H. Sun, A. Eychmüller, Ligand-Exchange-Mediated Fabrication of Gold Aerogels Containing Different Au(I) Content with Peroxidase-like Behavior, Chem. Mater. 31 (2019) 10094–10099. https://doi.org/10.1021/acs.chemmater.9b03121.

[159] R. Du, J.O. Joswig, R. Hübner, L. Zhou, W. Wei, Y. Hu, A. Eychmüller, Freeze–Thaw-Promoted Fabrication of Clean and Hierarchically Structured Noble-Metal Aerogels for Electrocatalysis and Photoelectrocatalysis, Angew. Chemie - Int. Ed. 59 (2020) 8293–8300. https://doi.org/10.1002/anie.201916484.

[160] D.R. Rolison, Catalytic nanoarchitectures - The importance of nothing and the unimportance of periodicity, Science (80-.). 299 (2003) 1698–1701. https://doi.org/10.1126/science.1082332.

[161] C.M.A. Parlett, K. Wilson, A.F. Lee, Hierarchical porous materials: Catalytic applications, Chem. Soc. Rev. 42 (2013) 3876–3893. https://doi.org/10.1039/c2cs35378d.

[162] B.E. Hayden, Particle size and support effects in electrocatalysis, Acc. Chem. Res. 46 (2013) 1858–1866. https://doi.org/10.1021/ar400001n.

[163] C.H. Cui, S.H. Yu, Engineering interface and surface of noble metal nanoparticle nanotubes toward enhanced catalytic activity for fuel cell applications, Acc. Chem. Res. 46 (2013) 1427–1437. https://doi.org/10.1021/ar300254b.

[164] S. Popović, M. Smiljanić, P. Jovanovič, J. Vavra, R. Buonsanti, N. Hodnik, Stability and Degradation Mechanisms of Copper-Based Catalysts for Electrochemical CO 2 Reduction , Angew. Chemie. 132 (2020) 14844–14854. https://doi.org/10.1002/ange.202000617.

[165] M. Hajnajafi, A. Khorshidi, M. Farsadrooh, A.G. Gilani, Nanoscale engineering of building blocks to synthesize a three-dimensional architecture of Pd aerogel as a robust self-supporting catalyst toward ethanol electrooxidation, Energy and Fuels. 35 (2021) 3396–3406. https://doi.org/10.1021/acs.energyfuels.0c04213.

[166] M. Abdinejad, M.K. Motlagh, M. Noroozifar, H.B. Kraatz, Electroreduction of carbon dioxide to formate using highly efficient bimetallic Sn-Pd aerogels, Mater. Adv. 3 (2022) 1224–1230. https://doi.org/10.1039/d1ma01057c.

[167] W. Wang, S. Gong, J. Liu, Y. Ge, J. Wang, X. Lv, Ag-Cu aerogel for electrochemical CO2 conversion to CO, J. Colloid Interface Sci. 595 (2021) 159–167. https://doi.org/10.1016/j.jcis.2021.03.120.

[168] Y. Wang, L. Cheng, Y. Zhu, J. Liu, C. Xiao, R. Chen, L. Zhang, Y. Li, C. Li, Tunable selectivity on copper–bismuth bimetallic aerogels for electrochemical CO2 reduction, Appl. Catal. B Environ. 317 (2022) 121650. https://doi.org/10.1016/j.apcatb.2022.121650.

[169] X. Wu, C. Ni, J. Man, X. Shen, S. Cui, X. Chen, A strategy to promote the ORR electrocatalytic activity by the novel engineering bunched three-dimensional Pd-Cu alloy aerogel, Chem. Eng. J. 454 (2022) 140293. https://doi.org/10.1016/j.cej.2022.140293.

[170] L. Lu, X. Sun, J. Ma, D. Yang, H. Wu, B. Zhang, J. Zhang, B. Han, Highly Efficient Electroreduction of CO 2 to Methanol on Palladium-Copper Bimetallic Aerogels, Angew. Chemie Int. Ed. 57 (2018) 14149–14153. https://doi.org/10.1002/anie.201808964.

[171] Y.X. Duan, F.L. Meng, K.H. Liu, S.S. Yi, S.J. Li, J.M. Yan, Q. Jiang, Amorphizing of Cu Nanoparticles toward Highly Efficient and Robust Electrocatalyst for CO2 Reduction to Liquid Fuels with High Faradaic Efficiencies, Adv. Mater. 30 (2018) 1–7. https://doi.org/10.1002/adma.201706194.

[172] W. Zhang, Q. Qin, L. Dai, R. Qin, X. Zhao, X. Chen, D. Ou, J. Chen, T.T. Chuong, B. Wu, N. Zheng, Electrochemical Reduction of Carbon Dioxide to Methanol on Hierarchical Pd/SnO2 Nanosheets with Abundant Pd–O–Sn Interfaces, Angew. Chemie - Int. Ed. 57 (2018) 9475–9479. https://doi.org/10.1002/anie.201804142.

[173] M. Favaro, H. Xiao, T. Cheng, W.A. Goddard, E.J. Crumlin, Subsurface oxide plays a critical role in CO2 activation by Cu(111) surfaces to form chemisorbed CO2, the first step in reduction of CO2, Proc. Natl. Acad. Sci.

U. S. A. 114 (2017) 6706–6711. https://doi.org/10.1073/pnas.1701405114.

[174] M. Le, M. Ren, Z. Zhang, P.T. Sprunger, R.L. Kurtz, J.C. Flake, Electrochemical Reduction of CO2 to CH3OH at Copper Oxide Surfaces, J. Electrochem. Soc. 158 (2011) E45. https://doi.org/10.1149/1.3561636.

[175] J.J. Lv, M. Jouny, W. Luc, W. Zhu, J.J. Zhu, F. Jiao, A Highly Porous Copper Electrocatalyst for Carbon Dioxide Reduction, Adv. Mater. 30 (2018) 1–8. https://doi.org/10.1002/adma.201803111.

[176] H. Zhou, K. Liu, H. Li, M. Cao, J. Fu, X. Gao, J. Hu, W. Li, H. Pan, J. Zhan, Q. Li, X. Qiu, M. Liu, Recent advances in different-dimension electrocatalysts for carbon dioxide reduction, J. Colloid Interface Sci. 550 (2019) 17–47. https://doi.org/10.1016/j.jcis.2019.04.077.

[177] C. Dinh, T. Burdyny, G. Kibria, A. Seifitokaldani, C.M. Gabardo, F.P.G. de Arquer, A. Kiani, J.P. Edwards, P. De Luna, O.S. Bushuyev, C. Zou, R. Quintero-Bermudez, Y. Pang, D. Sinton, E.H. Sargent, Sustained high-selectivity CO 2 electroreduction to ethylene via hydroxide-mediated catalysis at an abrupt reaction interface. Submitted to, Science (80-.). 787 (2018) 783–787. https://pubs.acs.org/sharingguidelines.

[178] M. Zoli, D. Roldán, H. Guzmán, M. Castellino, A. Chiodoni, K. Bejtka, N. Russo, S. Hernández, Facile and scalable synthesis of Cu2O-SnO2 catalyst for the photoelectrochemical CO2 conversion, Catal. Today. 415 (2023). https://doi.org/10.1016/j.cattod.2022.12.016.

[179] S.J. Cho, M.J. Uddin, P. Alaboina, Review of Nanotechnology for Cathode Materials in Batteries, Elsevier Inc., 2017. https://doi.org/10.1016/B978-0-323-42977-1.00003-0.

[180] A.V. Rane, K. Kanny, V.K. Abitha, S. Thomas, S. Thomas, Methods for Synthesis of Nanoparticles and Fabrication of Nanocomposites, Elsevier Ltd., 2018. https://doi.org/10.1016/B978-0-08-101975-7.00005-1.

[181] H. Guzmán, D. Roldán, N. Russo, S. Hernández, Ultrasound-assisted synthesis of copper-based catalysts for the electrocatalytic CO2 reduction: Effect of ultrasound irradiation, precursor concentration and calcination temperature, Sustain. Mater. Technol. 35 (2023). https://doi.org/10.1016/j.susmat.2022.e00557.

[182] S. Allahyari, M. Haghighi, A. Ebadi, S. Hosseinzadeh, Ultrasound assisted co-precipitation of nanostructured CuO-ZnO-Al 2O3 over HZSM-5: Effect of precursor and irradiation power on nanocatalyst properties and catalytic performance for direct syngas to DME, Ultrason. Sonochem. 21 (2014)

663–673. https://doi.org/10.1016/j.ultsonch.2013.09.014.

[183] R. Singh Yadav, I. Kuřitka, J. Vilcakova, T. Jamatia, M. Machovsky, D. Skoda, P. Urbánek, M. Masař, M. Urbánek, L. Kalina, J. Havlica, Impact of sonochemical synthesis condition on the structural and physical properties of MnFe2O4 spinel ferrite nanoparticles, Ultrason. Sonochem. 61 (2020) 104839. https://doi.org/10.1016/j.ultsonch.2019.104839.

[184] V. Jafari, A. Allahverdi, M. Vafaei, Ultrasound-assisted synthesis of colloidal nanosilica from silica fume: Effect of sonication time on the properties of product, Adv. Powder Technol. 25 (2014) 1571–1577. https://doi.org/10.1016/j.apt.2014.05.011.

[185] M.D. Luque de Castro, F. Priego-Capote, Ultrasound-assisted crystallization (sonocrystallization), Ultrason. Sonochem. 14 (2007) 717–724. https://doi.org/10.1016/j.ultsonch.2006.12.004.

[186] D. V. Pinjari, K. Prasad, P.R. Gogate, S.T. Mhaske, A.B. Pandit, Synthesis of titanium dioxide by ultrasound assisted sol-gel technique: Effect of calcination and sonication time, Ultrason. Sonochem. 23 (2015) 185–191. https://doi.org/10.1016/j.ultsonch.2014.10.017.

[187] M. Batzill, U. Diebold, The surface and materials science of tin oxide, Prog. Surf. Sci. 79 (2005) 47–154. https://doi.org/10.1016/j.progsurf.2005.09.002.

[188] Y. Zhao, C. Wang, G.G. Wallace, Tin nanoparticles decorated copper oxide nanowires for selective electrochemical reduction of aqueous CO2 to CO, J. Mater. Chem. A. 4 (2016) 10710–10718. https://doi.org/10.1039/c6ta04155h.

[189] S. Sarfraz, A.T. Garcia-Esparza, A. Jedidi, L. Cavallo, K. Takanabe, Cu-Sn Bimetallic Catalyst for Selective Aqueous Electroreduction of CO2 to CO, ACS Catal. 6 (2016) 2842–2851. https://doi.org/10.1021/acscatal.6b00269.

[190] Y. Li, F. Cui, M.B. Ross, D. Kim, Y. Sun, P. Yang, Structure-Sensitive CO2 Electroreduction to Hydrocarbons on Ultrathin 5-fold Twinned Copper Nanowires, Nano Lett. 17 (2017) 1312–1317. https://doi.org/10.1021/acs.nanolett.6b05287.

[191] C. Blanco-Andujar, D. Ortega, Q.A. Pankhurst, N.T.K. Thanh, Elucidating the morphological and structural evolution of iron oxide nanoparticles formed by sodium carbonate in aqueous medium, J. Mater. Chem. 22 (2012) 12498–12506. https://doi.org/10.1039/c2jm31295f.

[192] L. Lu, X. Sun, J. Ma, D. Yang, H. Wu, B. Zhang, J. Zhang, B. Han, Highly Efficient Electroreduction of CO2 to Methanol on Palladium–Copper Bimetallic Aerogels, Angew. Chemie - Int. Ed. 57 (2018) 14149–14153. https://doi.org/10.1002/anie.201808964.

[193] D.R.G. Mitchell, Circular Hough transform diffraction analysis: A software tool for automated measurement of selected area electron diffraction patterns within Digital Micrograph™, Ultramicroscopy. 108 (2008) 367–374. https://doi.org/10.1016/j.ultramic.2007.06.003.

[194] K.M. Reddy, S. V Manorama, A.R. Reddy, Bandgap studies on anatase titanium dioxide nanoparticles, Mater. Chem. Phys. 78 (2003) 239–245. https://doi.org/10.1016/S0254-0584(02)00343-7.

[195] L. Liu, W. Sun, W. Yang, Q. Li, J.K. Shang, Post-illumination activity of SnO2 nanoparticle-decorated Cu2O nanocubes by H2O2 production in dark from photocatalytic "memory," Sci. Rep. 6 (2016) 20878. https://doi.org/10.1038/srep20878.

[196] M. Schreier, J. Luo, P. Gao, T. Moehl, M.T. Mayer, M. Grätzel, Covalent Immobilization of a Molecular Catalyst on Cu2O Photocathodes for CO2 Reduction, J. Am. Chem. Soc. 138 (2016) 1938–1946. https://doi.org/10.1021/jacs.5b12157.

[197] D.H. Won, C.H. Choi, J. Chung, S.I. Woo, Photoelectrochemical production of formic acid and methanol from carbon dioxide on metal-decorated CuO/Cu2O-layered thin films under visible light irradiation, Appl. Catal. B Environ. 158–159 (2014) 217–223. https://doi.org/10.1016/j.apcatb.2014.04.021.

[198] N. Kamarulzaman, N.D. Abdul Aziz, M.F. Kasim, N.F. Chayed, R.H. Yahaya Subban, N. Badar, Anomalies in wide band gap SnO2 nanostructures, J. Solid State Chem. 277 (2019) 271–280. https://doi.org/10.1016/j.jssc.2019.05.035.

[199] M.C. Biesinger, L.W.M. Lau, A.R. Gerson, R.S.C. Smart, Resolving surface chemical states in XPS analysis of first row transition metals, oxides and hydroxides: Sc, Ti, V, Cu and Zn, Appl. Surf. Sci. 257 (2010) 887–898. https://doi.org/10.1016/j.apsusc.2010.07.086.

[200] M.C. Biesinger, B.R. Hart, R. Polack, B.A. Kobe, R.S.C. Smart, Analysis of mineral surface chemistry in flotation separation using imaging XPS, Miner. Eng. 20 (2007) 152–162. https://doi.org/10.1016/j.mineng.2006.08.006.

[201] D. Briggs, Handbook of X-ray Photoelectron Spectroscopy C. D. Wanger, W. M. Riggs, L. E. Davis, J. F. Moulder and G. E.Muilenberg Perkin-Elmer Corp., Physical Electronics Division, Eden Prairie, Minnesota, USA, 1979. 190 pp. $195, Surf. Interface Anal. 3 (1981) v–v. https://doi.org/10.1002/sia.740030412.

[202] J.T. Billy, A.C. Co, Reducing the onset potential of CO2 electroreduction on CuRu bimetallic particles, Appl. Catal. B Environ. 237 (2018) 911–918. https://doi.org/10.1016/j.apcatb.2018.06.072.

[203] J. Yuan, B. Xiao, C. Hao, Photoelectrochemical reduction of carbon dioxide to ethanol at Cu2O foam cathode, Int. J. Electrochem. Sci. 12 (2017) 8288–8294. https://doi.org/10.20964/2017.09.36.

[204] P. Chen, Y. Zhang, Y. Zhou, F. Dong, Photoelectrocatalytic carbon dioxide reduction: Fundamental, advances and challenges, Nano Mater. Sci. 3 (2021) 344–367. https://doi.org/10.1016/j.nanoms.2021.05.003.

[205] Y. Zhang, D. Pan, Y. Tao, H. Shang, D. Zhang, G. Li, H. Li, Photoelectrocatalytic Reduction of CO2 to Syngas via SnOx-Enhanced Cu2O Nanowires Photocathodes, Adv. Funct. Mater. 32 (2022). https://doi.org/10.1002/adfm.202109600.

[206] Y. Chen, N.S. Lewis, C. Xiang, Modeling and Simulation of the Spatial and Light-Intensity Dependence of Product Distributions in an Integrated Photoelectrochemical CO2 Reduction System, ACS Energy Lett. 1 (2016) 273–280. https://doi.org/10.1021/acsenergylett.6b00134.

[207] C.M. Hendy, G.C. Smith, Z. Xu, T. Lian, N.T. Jui, Radical Chain Reduction via Carbon Dioxide Radical Anion (CO2•-), J. Am. Chem. Soc. 143 (2021) 8987–8992. https://doi.org/10.1021/jacs.1c04427.

[208] H. Guzmán, F. Salomone, S. Bensaid, M. Castellino, N. Russo, S. Hernández, CO2Conversion to Alcohols over Cu/ZnO Catalysts: Prospective Synergies between Electrocatalytic and Thermocatalytic Routes, ACS Appl. Mater. Interfaces. 14 (2022) 517–530. https://doi.org/10.1021/acsami.1c15871.

[209] J.F. de Brito, A.R. Araujo, K. Rajeshwar, M.V.B. Zanoni, Photoelectrochemical reduction of CO2 on Cu/Cu2O films: Product distribution and pH effects, Chem. Eng. J. 264 (2015) 302–309. https://doi.org/10.1016/j.cej.2014.11.081.

[210] R. Kortlever, K.H. Tan, Y. Kwon, M.T.M. Koper, Electrochemical carbon dioxide and bicarbonate reduction on copper in weakly alkaline media, J.

Solid State Electrochem. 17 (2013) 1843–1849. https://doi.org/10.1007/s10008-013-2100-9.

[211] M. Dunwell, Q. Lu, J.M. Heyes, J. Rosen, J.G. Chen, Y. Yan, F. Jiao, B. Xu, The Central Role of Bicarbonate in the Electrochemical Reduction of Carbon Dioxide on Gold, J. Am. Chem. Soc. 139 (2017) 3774–3783. https://doi.org/10.1021/jacs.6b13287.

[212] C. Burda, X. Chen, R. Narayanan, M.A. El-Sayed, Chemistry and Properties of Nanocrystals of Different Shapes, 2005. https://doi.org/10.1002/chin.200527215.

[213] F. Zaera, Nanostructured materials for applications in heterogeneous catalysis, Chem. Soc. Rev. 42 (2013) 2746–2762. https://doi.org/10.1039/c2cs35261c.

[214] M.B. Gawande, R.K. Pandey, R. V. Jayaram, Role of mixed metal oxides in catalysis science - Versatile applications in organic synthesis, Catal. Sci. Technol. 2 (2012) 1113–1125. https://doi.org/10.1039/c2cy00490a.

[215] H. Wang, L. Chen, Y. Feng, H. Chen, Exploiting core-shell synergy for nanosynthesis and mechanistic investigation, Acc. Chem. Res. 46 (2013) 1636–1646. https://doi.org/10.1021/ar400020j.

[216] M.B. Gawande, A. Goswami, T. Asefa, H. Guo, A. V. Biradar, D.L. Peng, R. Zboril, R.S. Varma, Core-shell nanoparticles: synthesis and applications in catalysis and electrocatalysis, Chem. Soc. Rev. 44 (2015) 7540–7590. https://doi.org/10.1039/c5cs00343a.

[217] S.J. Oldenburg, R.D. Averitt, S.L. Westcott, N.J. Halas, Nanoengineering of optical resonances, Chem. Phys. Lett. 288 (1998) 243–247. https://doi.org/10.1016/S0009-2614(98)00277-2.

[218] R. Ghosh Chaudhuri, S. Paria, Core/shell nanoparticles: Classes, properties, synthesis mechanisms, characterization, and applications, Chem. Rev. 112 (2012) 2373–2433. https://doi.org/10.1021/cr100449n.

[219] Z. Wang, D. Luan, F.Y.C. Boey, X.W. Lou, Fast formation of SnO2 nanoboxes with enhanced lithium storage capability, J. Am. Chem. Soc. 133 (2011) 4738–4741. https://doi.org/10.1021/ja2004329.

[220] S.N. Zhang, M. Li, B. Hua, N. Duan, S. Ding, S. Bergens, K. Shankar, J.L. Luo, A Rational Design of Cu2O−SnO2 Core-Shell Catalyst for Highly Selective CO2-to-CO Conversion, ChemCatChem. 11 (2019) 4147–4153. https://doi.org/10.1002/cctc.201900395.

[221] P. Sawicka-Chudy, M. Sibiński, G. Wisz, E. Rybak-Wilusz, M. Cholewa, Numerical analysis and optimization of Cu2O/TiO2, CuO/TiO2, heterojunction solar cells using SCAPS, J. Phys. Conf. Ser. 1033 (2018) 0–10. https://doi.org/10.1088/1742-6596/1033/1/012002.

[222] A.T. Ravichandran, K. Dhanabalan, A. Vasuhi, R. Chandramohan, S. Mantha, Morphology, bandgap, and grain size tailoring in Cu2O thin film by SILAR method, IEEE Trans. Nanotechnol. 14 (2015) 108–112. https://doi.org/10.1109/TNANO.2014.2369438.

[223] M.H. Huang, Semiconductor nanocrystals possessing broadly size- and facet-dependent optical properties, J. Chinese Chem. Soc. 68 (2021) 45–50. https://doi.org/10.1002/jccs.202000267.

[224] A. Roy, H.S. Jadhav, J. Gil Seo, Cu2O/CuO Electrocatalyst for Electrochemical Reduction of Carbon Dioxide to Methanol, Electroanalysis. 33 (2021) 705–712. https://doi.org/10.1002/elan.202060265.

[225] W. Lv, R. Zhang, P. Gao, L. Lei, Studies on the faradaic efficiency for electrochemical reduction of carbon dioxide to formate on tin electrode, J. Power Sources. 253 (2014) 276–281. https://doi.org/10.1016/j.jpowsour.2013.12.063.

[226] T.Y. Chang, R.M. Liang, P.W. Wu, J.Y. Chen, Y.C. Hsieh, Electrochemical reduction of CO2 by Cu2O-catalyzed carbon clothes, Mater. Lett. 63 (2009) 1001–1003. https://doi.org/10.1016/j.matlet.2009.01.067.

[227] M. Hara, T. Kondo, M. Komoda, S. Ikeda, K. Shinohara, J.N. Tanaka, K. Domen, Cu2O as a photocatalyst for overall water splitting under visible light irradiation, Chem. Commun. 2 (1998) 357–358. https://doi.org/10.1039/a707440i.

[228] P.A. Cox, The electronic structure and chemistry of solids, Oxford Uni, Oxford [Oxfordshire], 1987.

[229] J.F. de Brito, A.R. Araujo, K. Rajeshwar, M.V.B. Zanoni, Photoelectrochemical reduction of CO2 on Cu/Cu2O films: Product distribution and pH effects, Chem. Eng. J. 264 (2015) 302–309. https://doi.org/10.1016/j.cej.2014.11.081.

[230] S. Nakayama, Highly selective determination of copper corrosion products by voltammetric reduction, SEI Tech. Rev. (2016) 96–101.

[231] G. Liu, F. Zheng, J. Li, G. Zeng, Y. Ye, D.M. Larson, J. Yano, E.J. Crumlin, J.W. Ager, L. wang Wang, F.M. Toma, Investigation and mitigation of degradation mechanisms in Cu2O photoelectrodes for CO2 reduction to ethylene, Nat. Energy. 6 (2021) 1124–1132. https://doi.org/10.1038/s41560-021-00927-1.

[232] Q. Li, J. Fu, W. Zhu, Z. Chen, B. Shen, L. Wu, Z. Xi, T. Wang, G. Lu, J.J. Zhu, S. Sun, Tuning Sn-Catalysis for Electrochemical Reduction of CO2 to CO via the Core/Shell Cu/SnO2 Structure, J. Am. Chem. Soc. 139 (2017) 4290–4293. https://doi.org/10.1021/jacs.7b00261.

[233] H. Kim, H. Lee, T. Lim, S.H. Ahn, Facile fabrication of porous Sn-based catalysts for electrochemical CO2 reduction to HCOOH and syngas, J. Ind. Eng. Chem. 66 (2018) 248–253. https://doi.org/10.1016/j.jiec.2018.05.036.

[234] C.W. Kohlpaintner, R.W. Fischer, B. Cornils, Aqueous biphasic catalysis: Ruhrchemie/Rhône-Poulenc oxo process, Appl. Catal. A Gen. 221 (2001) 219–225. https://doi.org/10.1016/S0926-860X(01)00791-8.

[235] R. Schäppi, D. Rutz, F. Dähler, A. Muroyama, P. Haueter, J. Lilliestam, A. Patt, P. Furler, A. Steinfeld, Drop-in fuels from sunlight and air, Nature. 601 (2022) 63–68. https://doi.org/10.1038/s41586-021-04174-y.

[236] A. Sacco, Electrochemical impedance spectroscopy as a tool to investigate the electroreduction of carbon dioxide: A short review, J. CO2 Util. 27 (2018) 22–31. https://doi.org/10.1016/j.jcou.2018.06.020.

[237] A. Sacco, Electrochemical impedance spectroscopy: Fundamentals and application in dye-sensitized solar cells, Renew. Sustain. Energy Rev. 79 (2017) 814–829. https://doi.org/10.1016/j.rser.2017.05.159.

[238] X. Lu, M. Rycenga, S.E. Skrabalak, B. Wiley, Y. Xia, Chemical synthesis of novel plasmonic nanoparticles, Annu. Rev. Phys. Chem. 60 (2009) 167–192. https://doi.org/10.1146/annurev.physchem.040808.090434.

[239] S.S. Skourtis, D.N. Beratan, Single-and Multi-Electron Transfer Processes, Electron Transf. Chem. 1 (2008) 109–125. https://doi.org/10.1002/9783527618248.ch3.

[240] J. Tyczkowski, Charge carrier transfer: A neglected process in chemical engineering, Ind. Eng. Chem. Res. 49 (2010) 9565–9579. https://doi.org/10.1021/ie101069w.

[241] M. Myronov, Molecular Beam Epitaxy of High Mobility Silicon, Silicon Germanium and Germanium Quantum Well Heterostructures, Elsevier Inc.,

2018. https://doi.org/10.1016/b978-0-12-812136-8.00003-7.

[242] D. Friedmann, C. Mendive, D. Bahnemann, TiO2 for water treatment: Parameters affecting the kinetics and mechanisms of photocatalysis, Appl. Catal. B Environ. 99 (2010) 398–406. https://doi.org/10.1016/j.apcatb.2010.05.014.

[243] D.W. Bahnemann, M. Hilgendorff, R. Memming, Charge carrier dynamics at TiO2 particles: Reactivity of free and trapped holes, J. Phys. Chem. B. 101 (1997) 4265–4275. https://doi.org/10.1021/jp9639915.

[244] G. Rothenberger, J. Moser, M. Gratzel, N. Serpone, D.K. Sharma, Charge carrier trapping and recombination dynamics in small semiconductor particles, J. Am. Chem. Soc. 107 (1985) 8054–8059. https://doi.org/10.1021/ja00312a043.

[245] C. Colbeau-Justin, M. Kunst, D. Huguenin, Structural influence on charge-carrier lifetimes in TiO2 powders studied by microwave absorption, J. Mater. Sci. 38 (2003) 2429–2437. https://doi.org/10.1023/A:1023905102094.

[246] M.P. De Haas, J.M. Warman, Photon-induced molecular charge separation studied by nanosecond time-resolved microwave conductivity, Chem. Phys. 73 (1982) 35–53. https://doi.org/10.1016/0301-0104(82)85148-3.

[247] M. Kunst, G. Beck, The study of charge carrier kinetics in semiconductors by microwave conductivity measurements, J. Appl. Phys. 60 (1986) 3558–3566. https://doi.org/10.1063/1.337612.

[248] T.J. Savenije, A.J. Ferguson, N. Kopidakis, G. Rumbles, Revealing the dynamics of charge carriers in polymer:fullerene blends using photoinduced time-resolved microwave conductivity, J. Phys. Chem. C. 117 (2013) 24085–24103. https://doi.org/10.1021/jp406706u.

[249] S.P. Berglund, F.F. Abdi, P. Bogdanoff, A. Chemseddine, D. Friedrich, R. Van De Krol, Comprehensive Evaluation of CuBi2O4 as a Photocathode Material for Photoelectrochemical Water Splitting, Chem. Mater. 28 (2016) 4231–4242. https://doi.org/10.1021/acs.chemmater.6b00830.

[250] M. Kölbach, I.J. Pereira, K. Harbauer, P. Plate, K. Höflich, S.P. Berglund, D. Friedrich, R. Van De Krol, F.F. Abdi, Revealing the Performance-Limiting Factors in α-SnWO4 Photoanodes for Solar Water Splitting, Chem. Mater. 30 (2018) 8322–8331. https://doi.org/10.1021/acs.chemmater.8b03883.

[251] A. Song, A. Chemseddine, I.Y. Ahmet, P. Bogdanoff, D. Friedrich, F.F. Abdi, S.P. Berglund, R. Van De Krol, Evaluation of Copper Vanadate (β-Cu2V2O7) as a Photoanode Material for Photoelectrochemical Water Oxidation, ACS Appl. Mater. Interfaces. (2020). https://doi.org/10.1021/acs.chemmater.9b04909.

[252] C.Y. Toe, M. Lamers, T. Dittrich, H.A. Tahini, S.C. Smith, J. Scott, R. Amal, R. Van De Krol, F.F. Abdi, Y.H. Ng, Facet-dependent carrier dynamics of cuprous oxide regulating the photocatalytic hydrogen generation, Mater. Adv. 3 (2022) 2200–2212. https://doi.org/10.1039/d1ma00934f.

[253] D. Credgington, F.C. Jamieson, B. Walker, T.Q. Nguyen, J.R. Durrant, Quantification of geminate and non-geminate recombination losses within a solution-processed small-molecule bulk heterojunction solar cell, Adv. Mater. 24 (2012) 2135–2141. https://doi.org/10.1002/adma.201104738.

[254] P. Lopez-Varo, J.A. Jiménez-Tejada, M. García-Rosell, S. Ravishankar, G. Garcia-Belmonte, J. Bisquert, O. Almora, Device Physics of Hybrid Perovskite Solar cells: Theory and Experiment, Adv. Energy Mater. 8 (2018) 1–36. https://doi.org/10.1002/aenm.201702772.

[255] O. Almora, Y. Zhao, X. Du, T. Heumueller, G.J. Matt, G. Garcia-Belmonte, C.J. Brabec, Light intensity modulated impedance spectroscopy (LIMIS) in all-solid-state solar cells at open-circuit, Nano Energy. 75 (2020). https://doi.org/10.1016/j.nanoen.2020.104982.

[256] H.L. Tan, F.F. Abdi, Y.H. Ng, Heterogeneous photocatalysts: An overview of classic and modern approaches for optical, electronic, and charge dynamics evaluation, Chem. Soc. Rev. 48 (2019) 1255–1271. https://doi.org/10.1039/c8cs00882e.

[257] E.A. Ponomarev, L.M. Peter, A generalized theory of intensity modulated photocurrent spectroscopy (IMPS), J. Electroanal. Chem. 396 (1995) 219–226. https://doi.org/10.1016/0022-0728(95)04115-5.

[258] F.F. Abdi, A. Chemseddine, S.P. Berglund, R. Van De Krol, Assessing the suitability of iron Tungstate (Fe2WO6) as a photoelectrode material for water oxidation, J. Phys. Chem. C. 121 (2017) 153–160. https://doi.org/10.1021/acs.jpcc.6b10695.

[259] J. Cen, Q. Wu, M. Liu, A. Orlov, Developing new understanding of photoelectrochemical water splitting via in-situ techniques: A review on recent progress, Green Energy Environ. 2 (2017) 100–111. https://doi.org/10.1016/j.gee.2017.03.001.

[260] G.O. Kim, K.S. Ryu, Dynamic response of charge transfer and recombination at various electrodes in dye-sensitized solar cells investigated using intensity modulated photocurrent and photovoltage spectroscopy, Bull. Korean Chem. Soc. 33 (2012) 469–472. https://doi.org/10.5012/bkcs.2012.33.2.469.

[261] A. Pockett, G.E. Eperon, T. Peltola, H.J. Snaith, A. Walker, L.M. Peter, P.J. Cameron, Characterization of planar lead halide perovskite solar cells by impedance spectroscopy, open-circuit photovoltage decay, and intensity-modulated photovoltage/photocurrent spectroscopy, J. Phys. Chem. C. 119 (2015) 3456–3465. https://doi.org/10.1021/jp510837q.

[262] N. Son, J.N. Heo, Y.S. Youn, Y. Kim, J.Y. Do, M. Kang, Enhancement of hydrogen productions by accelerating electron-transfers of sulfur defects in the CuS@CuGaS2 heterojunction photocatalysts, Catalysts. 9 (2019) 1–15. https://doi.org/10.3390/catal9010041.

[263] J.E. Thorne, J.W. Jang, E.Y. Liu, D. Wang, Understanding the origin of photoelectrode performance enhancement by probing surface kinetics, Chem. Sci. 7 (2016) 3347–3354. https://doi.org/10.1039/c5sc04519c.

[264] Y. Yang, K. Ri, A. Mei, L. Liu, M. Hu, T. Liu, X. Li, H. Han, The size effect of TiO2 nanoparticles on a printable mesoscopic perovskite solar cell, J. Mater. Chem. A. 3 (2015) 9103–9107. https://doi.org/10.1039/c4ta07030e.

[265] L. Zhang, T. Liu, L. Liu, M. Hu, Y. Yang, A. Mei, H. Han, The effect of carbon counter electrodes on fully printable mesoscopic perovskite solar cells, J. Mater. Chem. A. 3 (2015) 9165–9170. https://doi.org/10.1039/c4ta04647a.

[266] R. Miró Serra, H. Guzmán, C. Godard, A. Gual, F. Zammillo, T. Schubert, B. Iliev, A. Chiodoni, S. Hernández, M. Díaz de los Bernardos, Solar-driven CO2 reduction catalysed by Hybrid Supramolecular Photocathodes and enhanced by Ionic Liquids, Catal. Sci. Technol. (2023). https://doi.org/10.1039/C4CY00072B.

[267] H. Tian, Molecular Catalyst Immobilized Photocathodes for Water/Proton and Carbon Dioxide Reduction, ChemSusChem. 8 (2015) 3746–3759. https://doi.org/10.1002/cssc.201500983.

[268] M.F. Kuehnel, K.L. Orchard, K.E. Dalle, E. Reisner, Selective Photocatalytic CO2 Reduction in Water through Anchoring of a Molecular Ni Catalyst on CdS Nanocrystals, J. Am. Chem. Soc. 139 (2017) 7217–7223. https://doi.org/10.1021/jacs.7b00369.

[269] M. Schreier, J. Luo, P. Gao, T. Moehl, M.T. Mayer, M. Grätzel, Covalent Immobilization of a Molecular Catalyst on Cu2O Photocathodes for CO2 Reduction, J. Am. Chem. Soc. 138 (2016) 1938–1946. https://doi.org/10.1021/jacs.5b12157.

[270] H. Kumagai, G. Sahara, K. Maeda, M. Higashi, R. Abe, O. Ishitani, Hybrid photocathode consisting of a CuGaO2 p-type semiconductor and a Ru(II)-Re(i) supramolecular photocatalyst: Non-biased visible-light-driven CO2 reduction with water oxidation, Chem. Sci. 8 (2017) 4242–4249. https://doi.org/10.1039/c7sc00940b.

[271] B. Zhang, L. Sun, Artificial photosynthesis: Opportunities and challenges of molecular catalysts, Chem. Soc. Rev. 48 (2019) 2216–2264. https://doi.org/10.1039/c8cs00897c.

[272] J.T. Kirner, R.G. Finke, Water-oxidation photoanodes using organic light-harvesting materials: A review, J. Mater. Chem. A. 5 (2017) 19560–19592. https://doi.org/10.1039/c7ta05709a.

[273] H.L. Wu, X.B. Li, C.H. Tung, L.Z. Wu, Recent Advances in Sensitized Photocathodes: From Molecular Dyes to Semiconducting Quantum Dots, Adv. Sci. 5 (2018). https://doi.org/10.1002/advs.201700684.

[274] N. Elgrishi, M.B. Chambers, X. Wang, M. Fontecave, Molecular polypyridine-based metal complexes as catalysts for the reduction of CO2, Chem. Soc. Rev. 46 (2017) 761–796. https://doi.org/10.1039/c5cs00391a.

[275] B. Reuillard, K.H. Ly, T.E. Rosser, M.F. Kuehnel, I. Zebger, E. Reisner, Tuning Product Selectivity for Aqueous CO2 Reduction with a Mn(bipyridine)-pyrene Catalyst Immobilized on a Carbon Nanotube Electrode, J. Am. Chem. Soc. 139 (2017) 14425–14435. https://doi.org/10.1021/jacs.7b06269.

[276] A. Wang, J. Li, T. Zhang, Heterogeneous single-atom catalysis, Nat. Rev. Chem. 2 (2018) 65–81. https://doi.org/10.1038/s41570-018-0010-1.

[277] A. Nakada, H. Kumagai, M. Robert, O. Ishitani, K. Maeda, Molecule/Semiconductor Hybrid Materials for Visible-Light CO2Reduction: Design Principles and Interfacial Engineering, Accounts Mater. Res. 2 (2021) 458–470. https://doi.org/10.1021/accountsmr.1c00060.

[278] B. Gholamkhass, H. Mametsuka, K. Koike, T. Tanabe, M. Furue, O. Ishitani, Architecture of supramolecular metal complexes for photocatalytic CO2 reduction: Ruthenium-rhenium bi- and tetranuclear complexes, Inorg.

Chem. 44 (2005) 2326–2336. https://doi.org/10.1021/ic048779r.

[279] Y. Kuramochi, O. Ishitani, H. Ishida, Reaction mechanisms of catalytic photochemical CO2 reduction using Re(I) and Ru(II) complexes, Coord. Chem. Rev. 373 (2018) 333–356. https://doi.org/10.1016/j.ccr.2017.11.023.

[280] T. Li, B. Shan, T.J. Meyer, Stable Molecular Photocathode for Solar-Driven CO2 Reduction in Aqueous Solutions, ACS Energy Lett. 4 (2019) 629–636. https://doi.org/10.1021/acsenergylett.8b02512.

[281] S. Tougaard, Practical guide to the use of backgrounds in quantitative XPS, J. Vac. Sci. Technol. A. 39 (2021) 011201. https://doi.org/10.1116/6.0000661.

[282] S. Dong, Y. Xie, G. Cheng, Cyclic voltammetric and spectroelectrochemical studies of copper in alkaline solution, Electrochim. Acta. 37 (1992) 17–22. https://doi.org/10.1016/0013-4686(92)80005-7.

[283] M. Scherzer, F. Girgsdies, E. Stotz, M.G. Willinger, E. Frei, R. Schlögl, U. Pietsch, T. Lunkenbein, Electrochemical Surface Oxidation of Copper Studied by in Situ Grazing Incidence X-ray Diffraction, J. Phys. Chem. C. 123 (2019) 13253–13262. https://doi.org/10.1021/acs.jpcc.9b00282.

[284] M. Hijazi, V. Stambouli, M. Rieu, V. Barnier, G. Tournier, T. Demes, J.P. Viricelle, C. Pijolat, Synthesis and characterization of tin dioxide thick film modified by APTES in vapor and liquid phases, J. Mater. Sci. 53 (2018) 727–738. https://doi.org/10.1007/s10853-017-1541-4.

[285] R. Miró, H. Guzmán, C. Godard, A. Gual, F. Zammillo, T.J.S. Schubert, B. Iliev, A. Chiodoni, S. Hernández, M.D. de los Bernardos, Solar-driven CO2 reduction catalysed by hybrid supramolecular photocathodes and enhanced by ionic liquids, Catal. Sci. Technol. (2023). https://doi.org/10.1039/d2cy01523d.

[286] X. Li, J. Yu, M. Jaroniec, X. Chen, Cocatalysts for selective photoreduction of CO2 into solar fuels, Chem. Rev. 119 (2019) 3962–4179. https://doi.org/10.1021/acs.chemrev.8b00400.

[287] I. Dutta, S. Chatterjee, H. Cheng, R.K. Parsapur, Z. Liu, Z. Li, E. Ye, H. Kawanami, J.S.C. Low, Z. Lai, X.J. Loh, K.W. Huang, Formic Acid to Power towards Low-Carbon Economy, Adv. Energy Mater. 12 (2022) 1–17. https://doi.org/10.1002/aenm.202103799.

[288] L. Guo, J. Cao, J. Zhang, Y. Hao, K. Bi, Photoelectrochemical CO 2 reduction by Cu 2 O/Cu 2 S hybrid catalyst immobilized in TiO 2

nanocavity arrays, J. Mater. Sci. 54 (2019) 10379–10388. https://doi.org/10.1007/s10853-019-03615-4.

Appendix

A1. Bare Carbon Paper PEC CO_2RR tests

To assess the potential contribution of the electrodes support (Carbon paper) to the results, we performed different kind of PEC test onto the bare electrode. First, we tested the bare electrode (1 cm^{-2} active area) under solar illumination but with no CO_2 bubbling into the cell into the setup previously described (Section 2.3.2). Then, we performed the same testing procedure under illumination and with the CO_2 flux reaching the cell onto the same kind of bare electrode. Results are showed in Figure A.1. From the Cyclic voltammetry test (Figure A.1a) it was possible to observe in both the environments the very low current density values reached (lower than –0.4 mA cm^{-2}). The same was true for LSV curves pattern (Figure A.1b). They show a current density value almost zero for the test carried out in N_2 and a definitively low activity value for the CO_2-bubbling test, about one order of magnitude lower than during the tests with the catalytic ink. Moreover, as expected, even if the electrode was exposed to the chopped light, there were no signs of photoactivity in LSV or in Chronoamperometry curves. The latter (Figure A.1c) was conducted setting the same value of potential (–250 mV) with respect to the test with Cu_2O-SnO_2 in order to compare the two experiments. No significant differences are observable in the two curves reported in Figure A.1c. The response obtained under CO_2 flow almost overlapped to that recorded under N_2 and the main value of current density reached is more than 200 times lower than the test with the catalyst (Figure 4.8d). We also performed the 2-hours chronopotentiometry tests into the two different environments in order to detect products. Faradaic efficiencies are shown in Figure A.1d. The values related to the test in N_2 are on the left part of the graph, instead the ones obtained during the test in CO_2 environment are placed on the right. The applied current density value is reported onto the *x*-axis for each test, and all of them were carried out under illumination. Therefore, from the results of N_2-bubbling tests and the ones in CO_2 with a lower current density applied, it is possible to conclude that without the catalyst particles only HER occured. In fact, only Hydrogen was detected from these three tests, with a slightly increase from –1mA cm^{-2} to –3mA cm^{-2}. However, it can be observed in the rightmost part of the Figure, a very small

amount of CO_2 reduction products were present after the test carried out in CO_2 environment at –3mA cm^{-2}. The total faradaic efficiency is <5.5%, with a higher contribution due to Formate (3.91%).

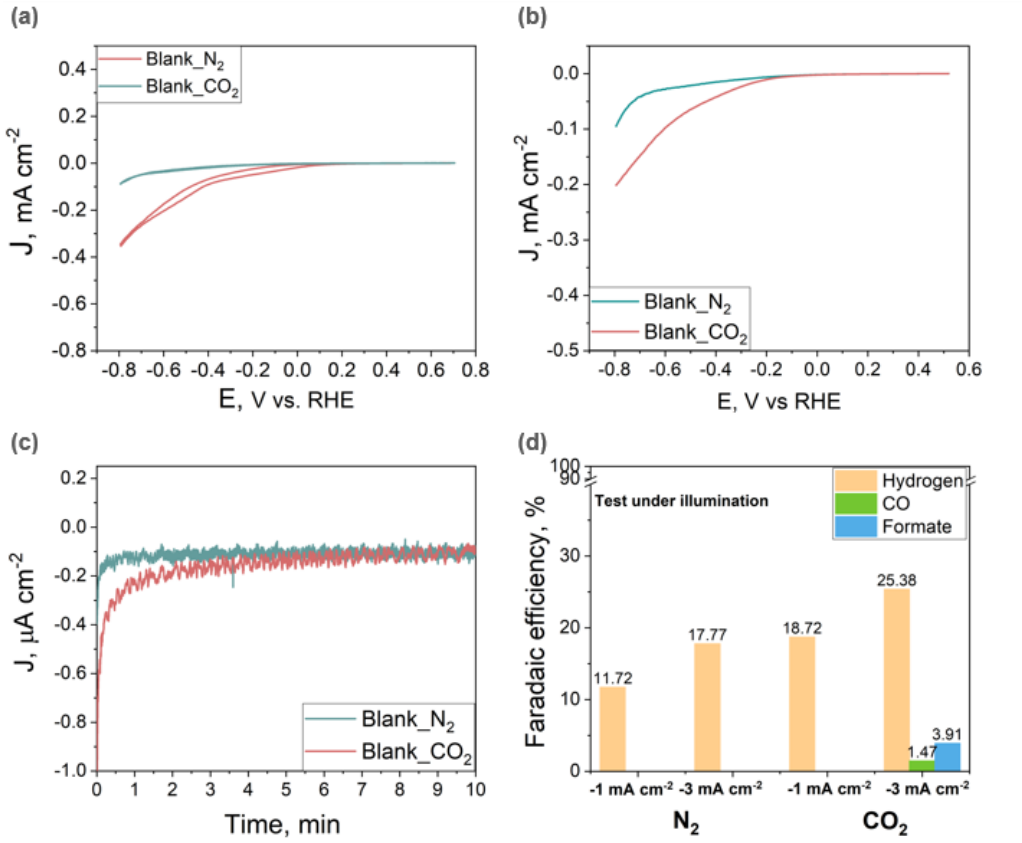


Figure A.1 – PEC test of a bare carbon paper based electrode; (a) Cyclic Voltammetry performed in N_2 and CO_2 ; (b) Linear Sweep Voltammetry performed both in N_2 and CO_2-environment with chopped light (2sec); (c) Chronoamperometry test performed at –250mV, chopped light each 1 minute (d). FEs of gas and liquid products detected after a 2-hours Chronopotentiometry in 0.1 M $KHCO_3$ aqueous electrolyte in two different environment (N_2 on the left and CO_2 on the right part of the graph) at two different current density values (–1 mA cm^{-2} and –3 mA cm^{-2}). All the tests were carried out under illumination.

A2. Co-precipitation obtained Cu_2O PEC CO_2 reduction test

A bare Cu_2O catalyst was also synthesized and evaluated as CO_2RR photo-electrocatalyst. The synthesis method was similar to that described in Section 4.3.2, the only difference was the absence of the Sn precursor added into the reaction flask. The so prepared catalyst was labelled bare Cu_2O. To assess the success of the synthesis, this sample was physico-chemically characterized by XRD of the powder. The diffractogram can be found in Figure A.2.

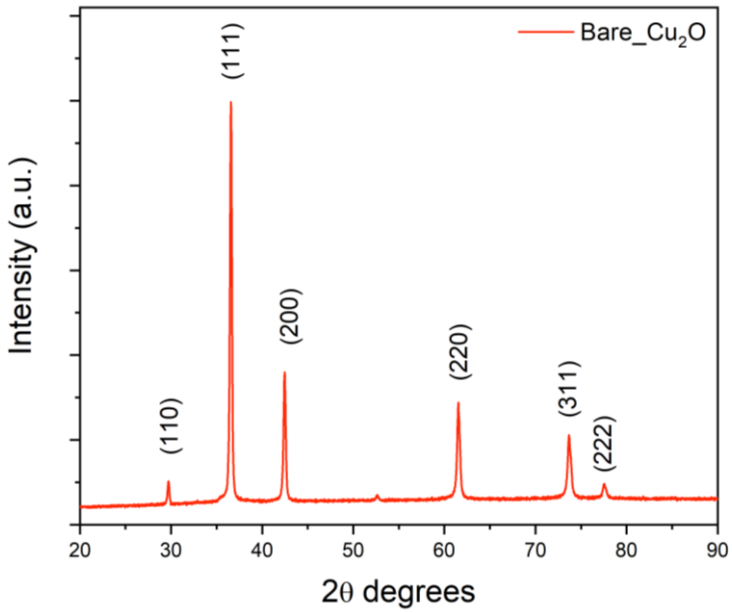


Figure A.2 – XRD pattern of the bare Cu_2O catalyst.

The cubic crystalline phase (cuprite) of Cu_2O (JCPDS 01-077-0199) is the only evident pattern that can be recognized. No peaks related to CuO or metallic Cu were observed in the diffraction pattern. The bare Cu_2O catalyst was deposited onto carbon paper by following the same procedure described into the manuscript for the photo-electrodes preparation (Section 4.3.4). Then, the photo-electrocatalytic CO_2 reduction test was conducted to compare the bare catalyst with the Cu_2O-SnO_2 one. Figure A.3 shows the results of PEC test onto both, the bare Cu_2O (red line) and the Cu_2O-SnO_2 (green line) catalysts.

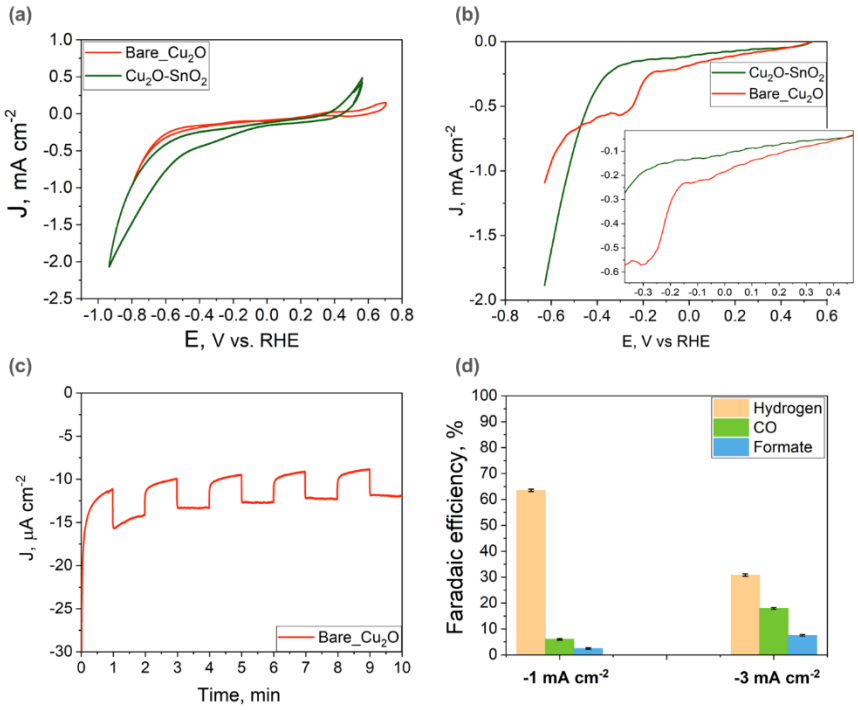


Figure A.3 – Comparison of bare Cu_2O (red line) and Cu_2O-SnO_2 (green line) PEC CO_2 reduction results; (a) Cyclic Voltammetry performed in CO_2; (b) Linear Sweep Voltammetry performed in CO_2-environment with chopped light (2sec), in the inset there is an enlargement of the photoactivity evidence revealed from the curve; (c) Chronoamperometry test (10 minutes) performed at –250mV, chopped light each 1 minute for bare Cu_2O (red); (d). FEs of gas and liquid products detected after a 2-hours Chronopotentiometry under illumination in 0.1 M $KHCO_3$ aqueous electrolyte in CO_2-environment of bare Cu_2O at two different current density values (–1 mA cm^{-2} and –3 mA cm^{-2}).

From the CV curves (Figure A.3a), it is possible to notice that the two catalysts have almost the same onset potential, at around –0.5 V vs. RHE, suggesting a similar activity towards the CO_2RR. Instead, the current density value reached by the bare Cu_2O was about half of the one of the Cu-Sn-based catalyst (–1 mA cm^{-2} and –3 mA cm^{-2}, respectively). A significant difference can be observed in Figure A.3b, since from the LSV curves a reduction peak is present at –0.3V vs. RHE, which may come from a slight reduction of the copper oxide in the electrode material ($Cu_2O \rightarrow Cu$), as detected by Guo *et al.* in their work on a Cu_2O based catalyst immobilized in TiO_2 [288]. Herein, the absence of the same or a similar peak in the Cu_2O-SnO_2 LSV curve is a further proof of its higher stability due to the SnO_2 protection. The results from CA test (Figure A.3c) were recorded with a different timing of "dark-light" alternance with respect to the

experiment carried out on the Cu-Sn-based catalyst, reported in Figure 4.8d of the manuscript. The difference in photocurrent gain for the two catalysts is evident: –8 μA cm^{-2} as a main value for bare Cu_2O with respect to the value of –18 μA cm^{-2} reported for the Cu-Sn-based catalyst during the 1-hour lasting stability test (shown in Figure 4.8b). As an potential explanation, even the very photoactive species Cu_2O, going through the test protocol described in Section 4.5.1 could progressively reduce from Cu^+ to to Cu^0, losing part of its photoactivity. Such reduction process is partially hindered for the Cu_2O-SnO_2 catalyst, thanks to its SnO_2 protection layer. Otherwise, it can be also expected an improved separation of charge carriers in the Cu-Sn-based catalyst that contributes to enhance its photoactivity.

Finally, the CP test in CO_2-environment Figure A.3d) were performed to compare the Faradaic efficiency results with respect to the ones of the Cu-Sn-based catalyst. The two tests were conducted only under illumination. The trend is quite the same for both the catalysts. At the lowest applied current density of –1 mA cm^{-2}, the hydrogen reached a higher Faradaic efficiency with respect to the test at higher current density, while the CO was the main reaction product in the test at –3 mA cm^{-2}. With the bare Cu_2O, the FE_{H2} decreased from 63.5% to 30.81%, while the Cu-Sn-based catalyst reported significant lower values: 35.83% of H_2 at –1 mA cm^{-2} and 20.7% of H_2 at –3 mA cm^{-2}. Instead, the CO increased from 6.01% to 17.94% following the increase of the applied current density. The same behaviour was detected with the Cu-Sn-based catalyst tests, for which the increase was about 4 times. The main difference for the bare Cu_2O was the formate production. The formate faradaic efficiency values always remained low, passing from 2.48% to 7.53% in the two tests with the bare Cu_2O, while for the Cu-Sn-based catalyst, the FE to formate at –3mA cm^{-2} was about 3 times higher. Such a result can be ascribed to the very strong SnO_2 selectivity towards formate product.

A3. Cu_2O Nanocubes, preliminary synthesis study

Starting from the method reported by Zhang *et al.* for the synthesis of Cu_2O nanocubes,[220] a first attempt was made to synthesize copper oxide by varying the concentrations and volumes of the reagents to increase the mass of obtained Cu_2O. The samples obtained were named as follows: Cu_2O-*x*-*y*-*z*-*w*, where *x* was the molarity of $CuCl_2$ (the copper precursor), *y* was the molarity of NaOH (the precipitating agent), *z* was the molarity of $C_6H_8O_6$ (the reductant agent) and *w* was the total volume of the reagent solution. In particular, in Cu_2O-0.01-2-0.6-300 nothing changed with respect to the method reported in literature. In Cu_2O-0.01-3-0.6-300 the molarity of the precipitating agent was increased by 50%. Cu_2O-0.01-2-0.9-300 showed a 50% increase in the molarity of the reducing agent. On the other hand, in Cu_2O-0.01-3-0.9-300 both the precipitating and reducing agents increased by 50%. These samples were synthesized with volumes of the solutions equal to those of the starting synthesis. Then, the changes refferred to the volume of the reagents. Cu_2O-0.01-3-0.9-600 and P1-Cu_2O-0.02-6-1.8-600 were synthesized with doubled volumes, the former maintaining the initial molarities, while the latter doubling their values. Table A.1 summarizes the molarities and volumes of the solutions used for the syntheses.

Table A.1 – Molarity and volumes of the reagents involved for the synthesis.

Sample	Molarity and Volume	$CuCl_2$	NaOH	$C_6H_8O_6$
Cu_2O-0.01-2-0.6-300	M	0.01	2	0.6
	mL	250	25	25
Cu_2O-0.01-3-0.6-300	M	0.01	3	0.6
	mL	250	25	25
Cu_2O-0.01-2-0.9-300	M	0.01	2	0.9
	mL	250	25	25
Cu_2O-0.01-3-0.9-300	M	0.01	3	0.9
	mL	250	25	25
Cu_2O-0.01-3-0.9-600	M	0.01	3	0.9
	mL	500	50	50

Cu_2O-0.02-6-1.8-600	M mL	0.02 500	6 50	1.8 50

The amounts of copper precursor and that of Cu_2O, obtained from each synthesis, were used to calculate the yield percentages. The yields were evaluated in terms of the ratio between the amount of copper in the precursor and amount of copper in the Cu_2O particles obtained. The Equation 42 used to calculate the yield:

Equation 42 – Production Yield of Cu_2O nanoparticles

$$\eta = \frac{Cu_2O \text{ amount (g)}}{\frac{CuCl_2 \text{ amount (g)}}{CuCl_2 \text{molecular weight (g/mol)}} \cdot \frac{1}{2} \cdot Cu_2O \text{ molecular weight (g/mol)}}$$

The resulting yields are reported in Figure A.4. Following the best result, slightly near to 100%, the decision was to implemented the doubled concentration values and volumes to carry out the final synthetic method for the creation of Cu_2O nanocubes.

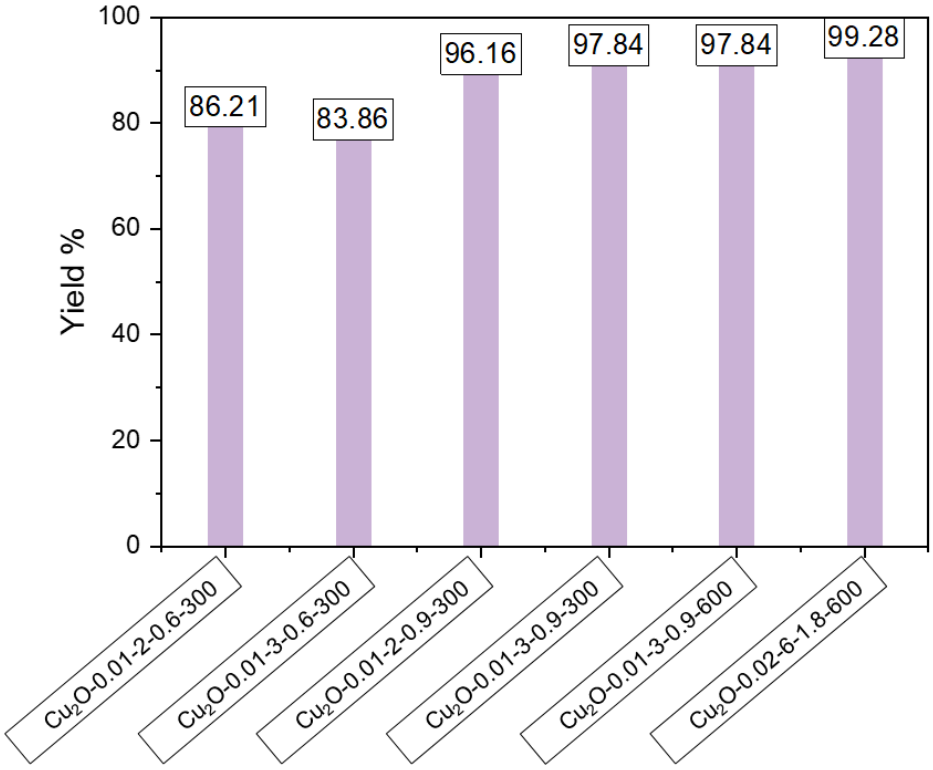


Figure A.4 – Reported yields percentage for the Cu_2O produced nanoparticles.

A4. IMVS plots

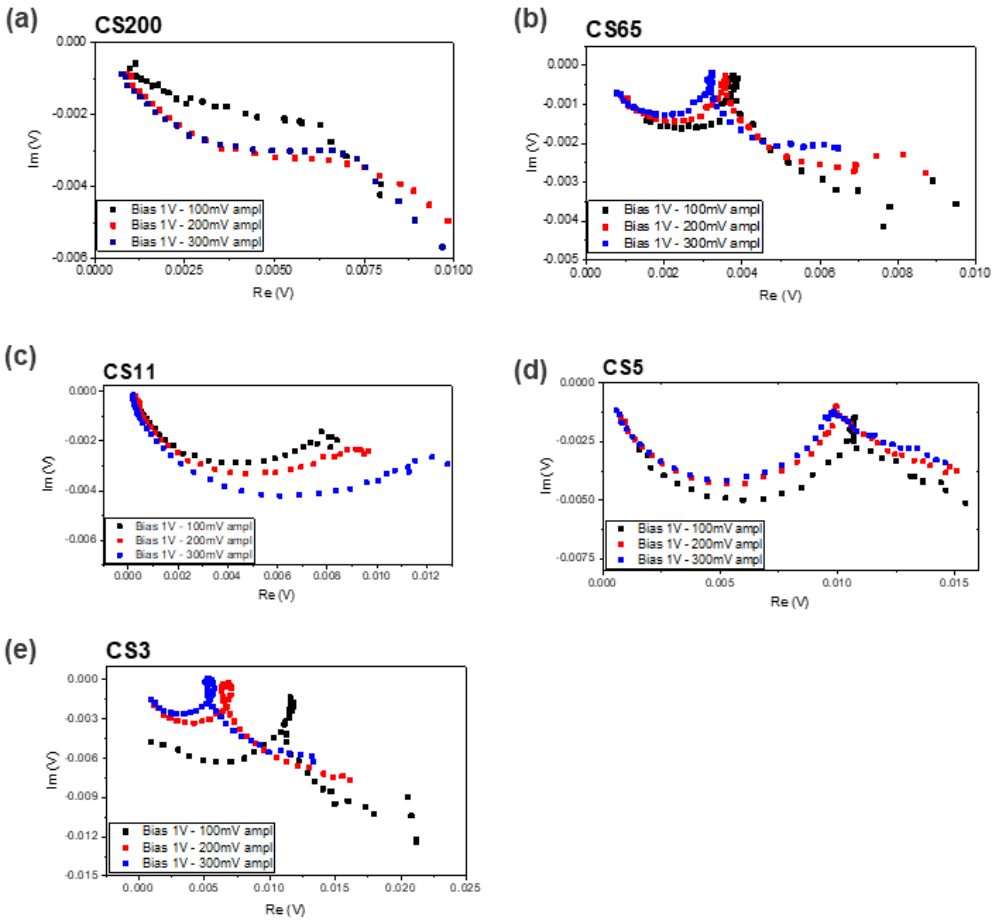


Figure A.5 – IMVS plots obtained with an applied bias of 1 V and varying the amplitude from 100 to 200 and 300 mV. Experiments carried out without CO_2 bubbling. The samples analyzed were: (a) CS200, (b) CS65, (c) CS11, (d) CS5, and (e) CS3.

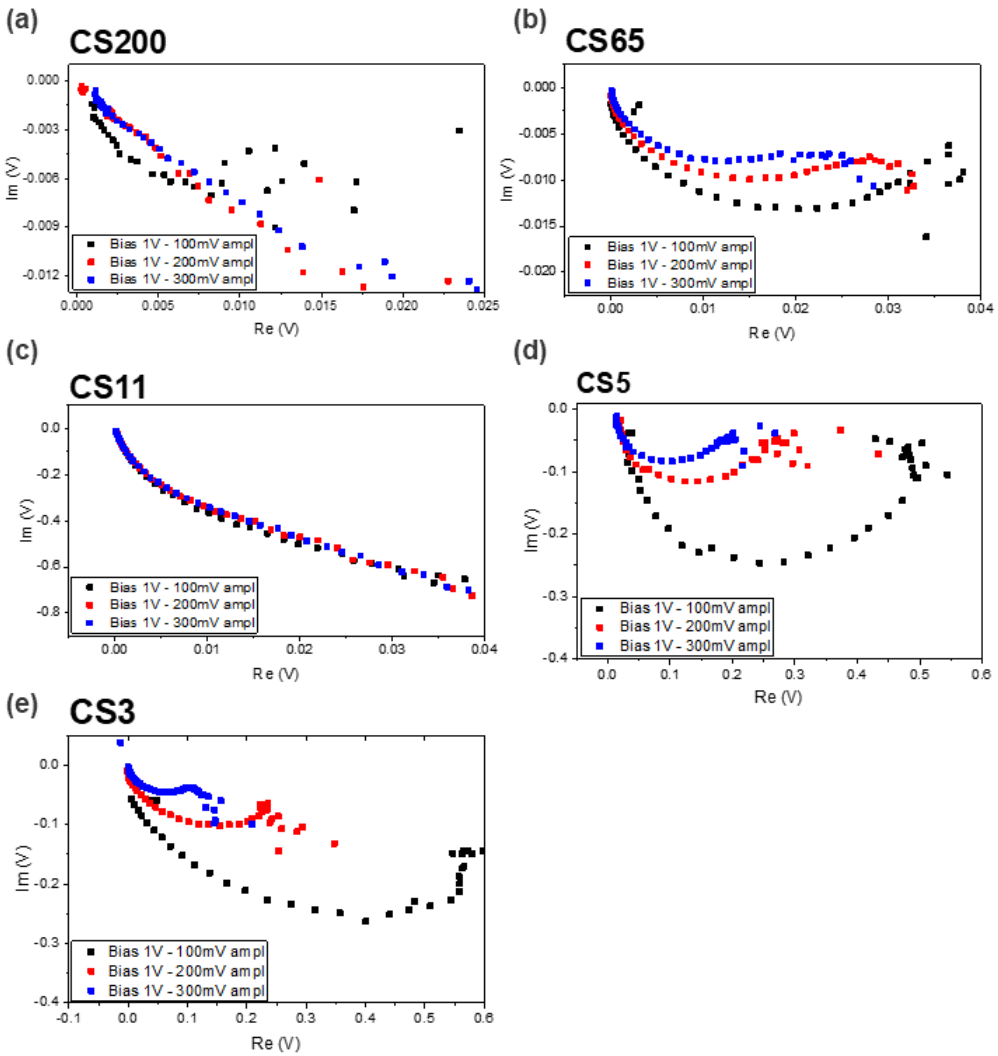


Figure A.6 – IMVS plots obtained with an applied bias of 1 V and varying the amplitude from 100 to 200 and 300 mV. Experiments carried out with CO_2 bubbling. The samples analyzed were: (a) CS200, (b) CS65, (c) CS11, (d) CS5, and (e) CS3.

A5. Characterization of Cu_2O-SnO_2 core-shell catalysts obtained with the standardized synthesis

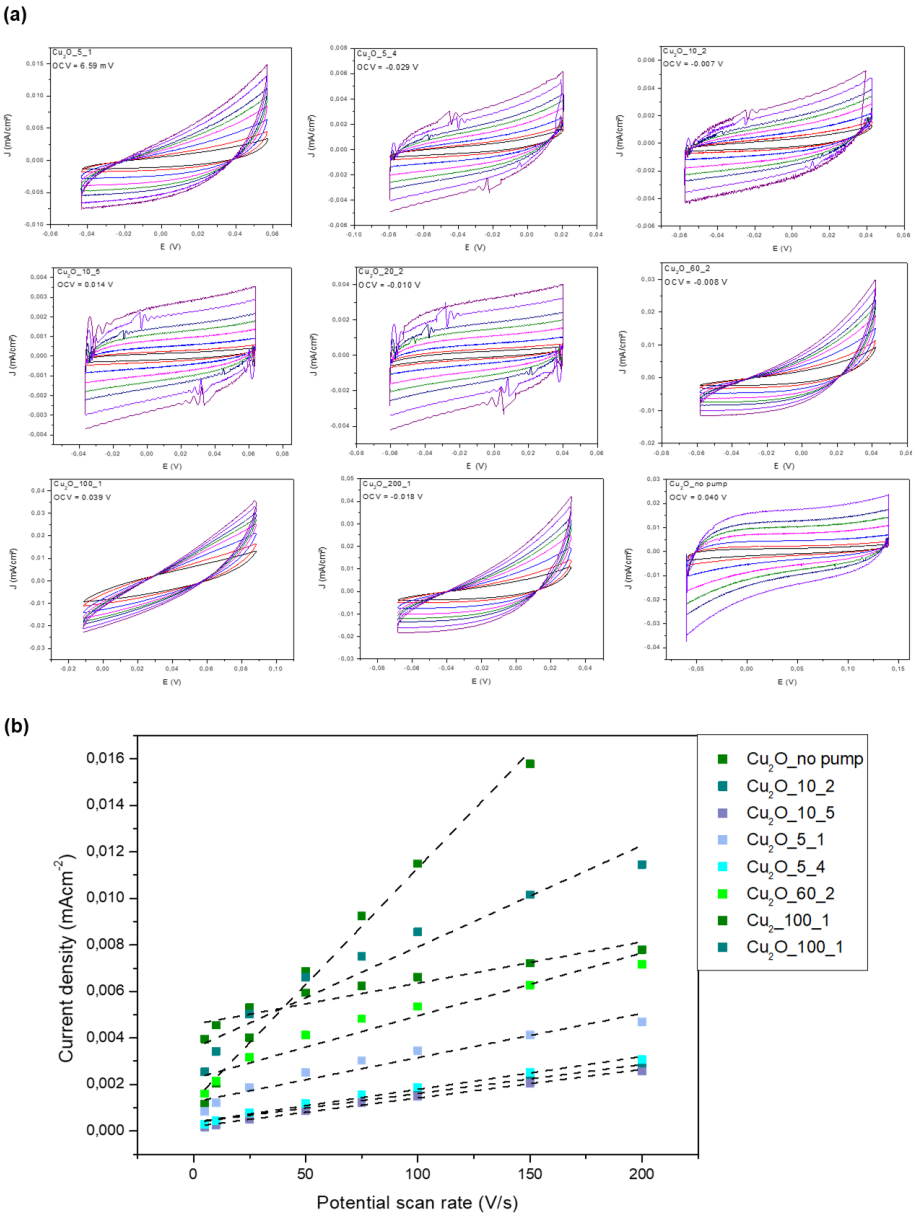


Figure A.7 – Electrocatalytic surface area analysis of Cu_2O bare samples, in particular: (a) Cyclic voltammetries of Cu_2O core samples and, (b) linear fitting of the current densities mean value obtained for Cu_2O samples.

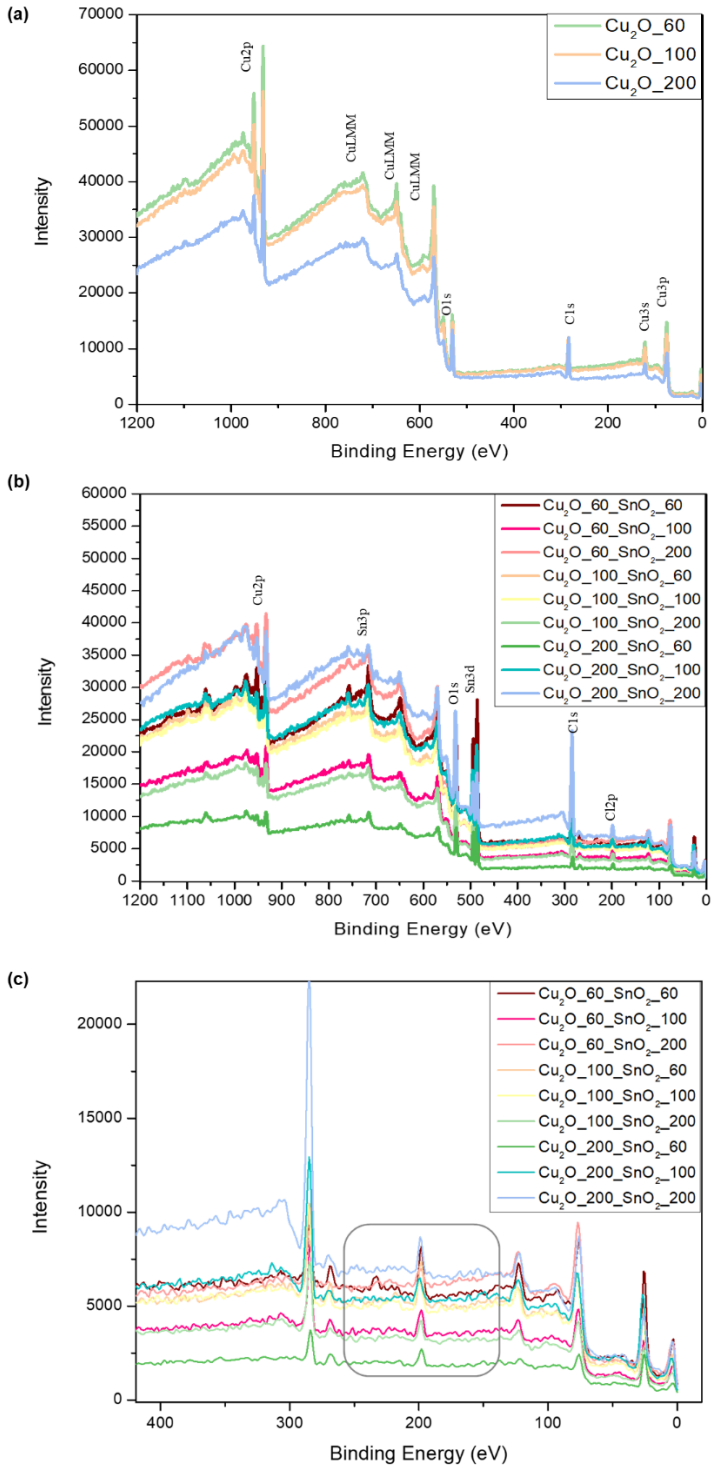


Figure A.8 – XPS analysis of the samples, in detail: (a) Cu_2O survey spectra, to be compared with (b) Cu_2O-SnO_2 survey spectra (both the images reported various samples obtained with different delivery velocities), and (c) HR Cl2p peak with flat background highlighted in the box for the various Cu_2O-SnO_2 samples.

Table A.2 – Atomic percentage of Cu, O, Sn, C and Cl in $Cu_2O_SnO_2$ samples obtained with different delivery velocities.

Samples	Cu at.%	O at.%	Sn at.%	C at.%	Cl at.%
$Cu_2O_60_SnO_2_60$	14.9	43.3	7.4	28.6	5.8
$Cu_2O_60_SnO_2_100$	10.6	31.5	4.0	49.1	4.8
$Cu_2O_60_SnO_2_200$	15.6	40.3	5.1	36.2	2.8
$Cu_2O_100_SnO_2_60$	10.8	34.5	4.7	44.4	5.6
$Cu_2O_100_SnO_2_100$	11.4	32.5	4.9	46.1	5.1
$Cu_2O_100_SnO_2_200$	9.3	31.7	3.6	51.9	3.5
$Cu_2O_200_SnO_2_60$	11.4	38.4	7.3	36.9	6.0
$Cu_2O_200_SnO_2_100$	7.4	34.9	4.6	50.5	2.6
$Cu_2O_200_SnO_2_200$	4.2	26.5	1.5	65.8	2.0